Synthesis and Characterization of Ag Doped TiO$_2$, CdS, ZnS Nanoparticles for Photocatalytic, Toxic Ions Detection, and Antimicrobial Applications

Submitted by

SIDDHARTHA SANKAR BOXI

Roll No-511CH602

To the department of Chemical Engineering in partial fulfilment of the requirements for the award of degree of Doctor of Philosophy in Chemical Engineering

Under the guidance of

Dr. SANTANU PARIA

Department of Chemical Engineering

National Institute of Technology Rourkela

Orissa-769008, India

Dedicated

to

My Family

Department of Chemical Engineering

National Institute of Technology

Rourkela - 769008, India

Certificate

This is to certify that the thesis entitled "**Synthesis and characterization of Ag doped TiO$_2$, CdS, ZnS Nanoparticles for Photocatalytic, Toxic Ions Detection, and Antimicrobial Applications**" submitted by Mr. Siddhartha Sankar Boxi (Roll No. 511CH602) in partial fulfilment of the requirements for the award of degree of Doctor of Philosophy in Chemical Engineering at National Institute of Technology, Rourkela is an authentic work carried out by him under my supervision.

To the best of my knowledge, the matter embodied in this thesis has not been submitted to any other University/Institute for the award of any degree or diploma.

Date- 21.07.2015

Dr. Santanu Paria

Associate Professor
Department of Chemical Engineering
National Institute of Technology,
Rourkela–769008

Acknowledgement

Abstract

The progresses of nanoparticles (NPs) research have been passed through several advancements, such as simple spherical NPs to different shapes (anisotropic), hollow, core/shell, doped, movable core/shell or yolk shell, etc. These NPs have more advanced properties in several applications, such as catalysis, biomedical, electronics, solar cells, sensors, and so on because of high surface area to volume ratio, the presence of more loosely bound surface atoms, etc. When the particles are made of multimaterials it's not only show improved property of the main material but also developed multifunctionality. Because of these reasons the multimaterials NPs are continuously drawing significant research attentions in the recent years. Under the multi-materials nanoparticles category, doped nanoparticles are also considered as an important class. This thesis is focused on synthesis, characterization, properties, and applications of Ag doped semiconductor nanoparticles. More specifically, TiO_2, CdS, and ZnS were considered as the host materials and Ag as the dopant to form single, core/shell, hollow, and hollow bi-layer NPs for the applications in visible light induced photocatalytic degradation of organic compounds (nitrobenzene, metronidazole, methylene blue dye), antifungal agent (against *Fusarium solani* and *Venturia inaquaelis*), and sensor for the detection of arsenic and fluoride ions in aqueous media. The abstracts of the studied works are organized sequentially in the following paragraphs.

Continuous increasing consumption of antibiotics in health care results to increase concentration of these compounds in surface water through wastewater treatment systems, which in turn, cause adverse effects on the aquatic ecosystems of the receiving water bodies, because of the intrinsic biological activity of these compounds. However, there are limited efforts on remediation of water pollution because of antibiotics using an effective and clean technology. In this study, photocatalytic activity of TiO_2, CdS, and ZnS semiconductor nanoparticles were employed to degrade the metronidazole antibiotic in visible light irradiation. The particle size of pure TiO_2, CdS, and ZnS was 33.39 ± 1.67, 4.06 ± 0.63, and 5.85 ± 0.5 nm, respectively. The particle size of Ag doped TiO_2, CdS, and ZnS was 27.6 ± 2.08, 3.44 ± 0.76, and 4.91 ± 0.45 nm, respectively. The maximum degradation efficiencies of the pure TiO_2, CdS and ZnS nanoparticles were 80.78, 82.46, and 81.66%, respectively. These particles were also modified by silver doping to improve its degradation efficiency. Doping of silver greatly enhanced the degradation efficiency of these nanoparticles. The particular concentrations of silver dopant were 1.00, 1.5, and 1.25% for TiO_2, CdS, and ZnS nanoparticles for achieving the maximum degradation efficiency and the corresponding

maximum degradation efficiencies were 94.39, 94.9%, and 95.11%. The basic mechanism of doping and the photocatalytic processes was explored in detail. A kinetic study of the degradation reaction shows first order kinetics fits well for all three cases. The reusability and stability of these photocatalyst were confirmed by the cyclic degradation test.

In addition to the antibiotics, contamination of water because of other organic pollutants, especially synthetic dyes, causes severe environmental problems because of its toxic nature to microorganisms, aquatic life, and human beings. In this regard, an effective and clean remediation process for the remediation of dye contaminated effluent waters becomes more demanding to reduce the environmental impact. This section reports the photocatalytic behaviour of methylene blue using pure and silver doped semiconductor heterogeneous nanocatalysts (TiO_2, CdS, and ZnS) under visible light. The photodegradation studies show there is a significant enhancement in degradation efficiency of all three nanoparticles after silver doping. For all nanoparticles, there is an optimum doping concentration to get the maximum degradation efficiency, which again depends on the material. The maximum degradation efficiencies for the three Ag doped TiO_2, ZnS, and CdS nanoparticles were 95.9, 95.33, and 94.99% for 1.00, 1.25, and 1.50% Ag, respectively. The first order rate constant value of 1.00% Ag doped TiO_2, 1.5% Ag doped CdS, and 1.25% Ag doped ZnS is 5.21, 5.72, and 7.71 times higher compared to their respective pure nanoparticles. The maximum degradation efficiency with minimum doping concentration among all three materials studied here was again found for TiO_2.

Further, silver doped hollow TiO_2 (Ag-h-TiO_2) nanoparticles were also synthesized by a sacrificial core (AgBr) method to enhance the surface area for higher photocatalytic activity. The Ag doping and the core removal was done simultaneously during the dissolution of the core in $(NH_4)OH$ solution. The mean particle size of synthesized Ag-h-TiO_2 nanoparticles was 17.76 ± 2.85 nm with the wall thickness ~2.5 nm. The hollow structured nanoparticles have the specific surface area of 198.3 m^2/g, where as solid TiO_2 nanoparticles have the specific surface area of 95.1 m^2/g. The suitability of this synthesized hollow nanoparticles as photocatalyst were tested for the photocatalytic degradation of three important different classes of organic compounds such as nitrobenzene (NB), metronidazole (MTZ) antibiotic, and methylene blue dye (MBD) in aqueous solution under irradiation of visible light. The maximum NB degradation was obtained 95.5%, and the metronidazole degradation efficiency was found to be 96.55 and 94.77% under the irradiation of visible light for the initial MTZ concentration of 15 and 30 mg/L with catalyst dose of 0.5 g/L. Photodegradation studies show there is a significant enhancement of the degradation

efficiency of the TiO_2 after the hollow structure formation and silver doping. The recycling tests of the catalysts show only ~ 10% decrease in efficiency for NB and MTZ degradation after sixth cycle of reuse. The light emission capacity in terms of quantum yield (QY) is enhanced by 18.7% for Ag-h-TiO_2 than that of pure TiO_2 nanoparticles.

The above mentioned hollow TiO_2 NPs were also used as photoinduced antifungal agent. The chemical based pesticides are widely used in agricultural farming to protect crops from insect infestation and diseases. However, the excessive use of highly toxic pesticides causes several human health (neurological, tumour, cancer) and environmental problems. So, nanoparticles based green pesticides are of special importance in recent years. Antifungal activities of the pure and Ag doped (solid and hollow) TiO_2 nanoparticles were studied against two potent phytopathogens, *Fusarium solani* (causing Fusarium wilt disease to potato, tomato etc.) and *Venturia inaquaelis* (causing apple scab disease) and found hollow nanoparticles are more effective than other two. The antifungal activities of the nanoparticles enhanced further under visible light exposure against these two phytopathogens. Fungicidal effect of the nanoparticles depends on different parameters, , such as particle concentration, and intensity of visible light. The minimum inhibitory dose of the nanoparticles for *V.inaquaelis* and *F.solani* are 0.75 and 0.43 mg/plate. Presence of Ag as a dopant helps to the formation of stable Ag-S and di-sulfide bond (R-S-S-R) in cellular protein, which leads to the cell damage. During photocatalysis generated $^{\bullet}OH$ radicals loosen the cell wall structure and finally lead to the cell death. The mechanisms of fungicidal effect of nanoparticles against these two phytopathogens are supported by biuret and triphenyl tetrazolium chloride analyses, and field emission electron microscopy. Apart from the fungicidal effect, at very low dose (0.015 mg/plate) the nanoparticles are successfully arrest production of toxic napthoquinone pigment for *F.solani* which is related to the fungal pathogenecity. The nanoparticles are found to be effective to protect spoiling of potato affected by *F.solani* or other fungus.

The doped nanoparticles can also be used effectively for the easy detection of toxic ions in water. In this regard, fluoride ion detection has taken a considerable research interest in recent years because of its typical nature. It is an essential anion for biological and medical systems, as well as for some industrial applications. But, the fluoride ions above its permissible level can cause different diseases, such as fluorosis, urolithiasis, kidney failure, cancer, and even leading to death. Because of this reason a simple and low cost method is highly desirable for the detection of fluoride ion. In this study a fluorometric method based

on Ag-CdS/Ag-ZnS nanoparticle is developed for the fluoride ion detection. The developed nanoparticles were of size range 5.92 ± 0.76 nm with shell layer of 0.75 nm and it showed the quantum yield of 77.57%. The method was tested in aqueous solution at different pH. The selectivity and sensitivity of the fluorescence probe was checked in the presence of other anions (Cl^-, Br^-, I^-, OH^-, NO_3^- SO_4^{2-}, HCO_3^-, HPO_4^{2-}, CH_3COO^-, $H_2PO_4^-$). The fluoride ion concentration was varied in the rage $190 - 22,800$ µg/L and the lower detection limit was obtained as 99.7 µg/L.

Arsenic poisoning from drinking water is also an important global issue in recent years. Because of high level toxicity of arsenic to human health, an easy, inexpensive, and low level and highly selective detection technique is of great importance to take any early precautions. This study reports the synthesis of Ag doped hollow CdS/ZnS bi-layer (Ag-h-CdS/ZnS) nanoparticles for easy fluorometric determination of As(III) ions in aqueous phase. The hollow bi-layer structures are synthesized by a sacrificial core method using AgBr as the sacrificial core and the core is removed by dissolution in ammonium hydroxide solution. The synthesized nanoparticles were characterized by using different instrumental techniques. The particle size of Ag-h-CdS/ZnS nanoparticles is $\sim 76.02 \pm 2.47$ nm with the shell thickness of CdS layer is 1.5 nm and ZnS layer is 1.8 nm. The QY of the Ag-h-CdS/ZnS nanoparticles is 88.14%. A good linear relationship is obtained between fluorescence quenching intensity and the As(III) concentration in the range of $750 - 22500$ ng/L at neutral pH with a limit of detection as low as 226 ng/L.

Key words: Nanoparticles, Doping, Semiconductor, Ag, TiO_2, CdS, ZnS, Core/shell, Hollow, Band gap, Quantum yield, Photodegradation, Antifungal, Sensor.

Contents

Chapter 4. Visible Light Induced Enhanced Photocatalytic Degradation of Organic Pollutants in Aqueous Media using Ag Doped Hollow TiO$_2$ Nanospheres   69

Chapter 5. Applications of Ag Doped Hollow TiO$_2$ Nanoparticles as an Effective Green Fungicide Against *Fusarium Solani* and *Venturia Inaequalis* Phytopathogens   90

List of Figures

concentration of the As(III) ions are in the range of 750 – 22500 ng/L. Linear plot of quenched fluorescence intensity of the L-cysteine capped Ag-h-CdS/ZnS nanoparticles with the increasing concentration of As(III) is shown in the inset. F_0 and F are the fluorescence intensities of L-cysteine capped Ag-h-CdS/ZnS nanoparticles in absence and presence of As(III) ions.

Scheme No	**Title**	**Page No**

List of Tables

List of Symbols

Greek Symbols

η_S : Refractive index of the sample

η_R : Refractive index of the reference (phenol)

ζ : Zeta potential

English Symbols

C   : Concentration of reactant T time t

C_0 : Concentration of reactant at the beginning

k   : Reaction rate constant, S^{-1}

t   : Time, s

F_0 : Fluorescence intensity without analyte

F   : Fluorescence intensity with analyte

Abbreviations

$AgNO_3$: Silver nitrate

BET   : Brunauer–Emmett–Teller

CdS   : Cadmium sulfide

CMC   : Critical Micellar Concentration

DLS   : Dynamic Light Scatter

DSSC   : Dye Sensitized Solar Cell

EDX   : Energy-dispersive X-ray spectroscopy

FE-SEM   : Field Emission Scanning Electron Microscope

FT-IR   : Fourier Transform infrared

JCPDS   : Joint Committee on Powder Diffraction Standards

LUMO   : Lowest unoccupied orbital

MBD   : Methylene blue dye

MTZ   : Metronidazole

LCMS   : liquid chromatography mass spectrometry

NB   : Nitrobenzene

PL   : Photoluminescence

QY   : Quantum yield

SDBS   : Sodium dodecylbenzenesulfonate

CTAB   : Cetyltrimethyl ammonium bromide

TBOT   : Titanium (IV) butoxide

TEM   : Transmission electron microscope

HR-TEM   : High resolution Transmission electron microscope

SAED   : Selected area electron diffraction

TiO_2 : Titanium dioxide/Titania

UV   : Ultra-violet

XRD   : X-ray diffraction

XPS   : X-ray photoelectron spectroscopy

ZnS   : Zinc sulphide

LOD   : Limit of detection

WHO   : World Health Organization

Chapter 1

Introduction

1.1 Introduction

Materials in the nanometer range have attracted much research interest over the last decades because of high surface area to volume ratio, the presence of more loosely bound surface atoms compared to that of bulk materials. Nanoparticle (NP) is defined as a small object in the order of 1 to 100 nm. The progress of nanoparticles research passed through several advancements (shown in Figure 1.1) such as simple spherical nanoparticles to different shapes (anisotropic), hollow, core/shell, doped, movable core/shell or yolk shell etc because of more advanced properties. When the nanoparticles are made of multi-materials, they not only show improved the properties than the main materials but also developed multi-functionality. Under the multi-materials nanoparticles category, doped nanoparticles are also considered as an important class. The process of intentionally incorporation of an impurity atom into the lattices of a pure material for tuning its properties is called as doping. In this process, the impurity atom is known as dopant. Doping is mostly used for the production of semiconductor materials, where dopant (impurity) is introduced into an extremely pure semiconductor material for the purpose of modulating electrical properties. Over the last two decades, several elements from the periodic table have been doped into different semiconductor nanoparticles and found a great success in improving their properties over the pure nanoparticles. [1-3]
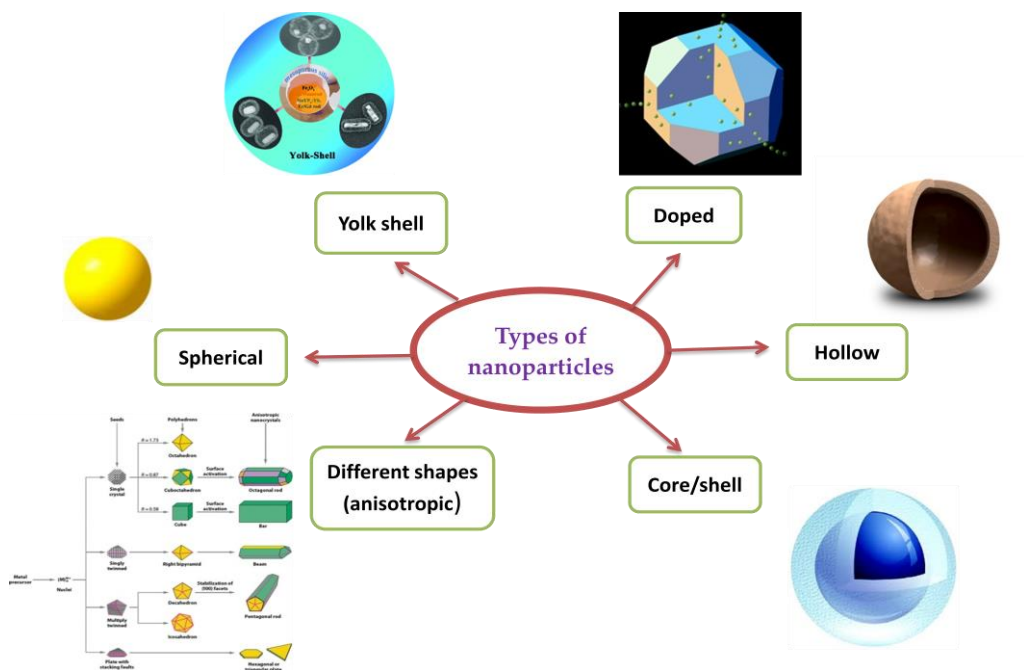
Figure 1.1. Types of nanoparticles.

Different dopant elements, such as metals, non-metals, and metalloids have been used for modulating the properties of nanoparticles. While the hollow and core/shell nanoparticles show much more improved properties than that of single nanoparticles, doping on similar structures also further show much improved properties than that of their original respective structures. [4,5] Figure 1.2 shows the statistical data of the research papers published in the area of doped nanoparticles collected from *'SciVerse-Scopus'* using the keywords 'doped nanoparticles', which indicates the increasing trend of the research papers published in this field.
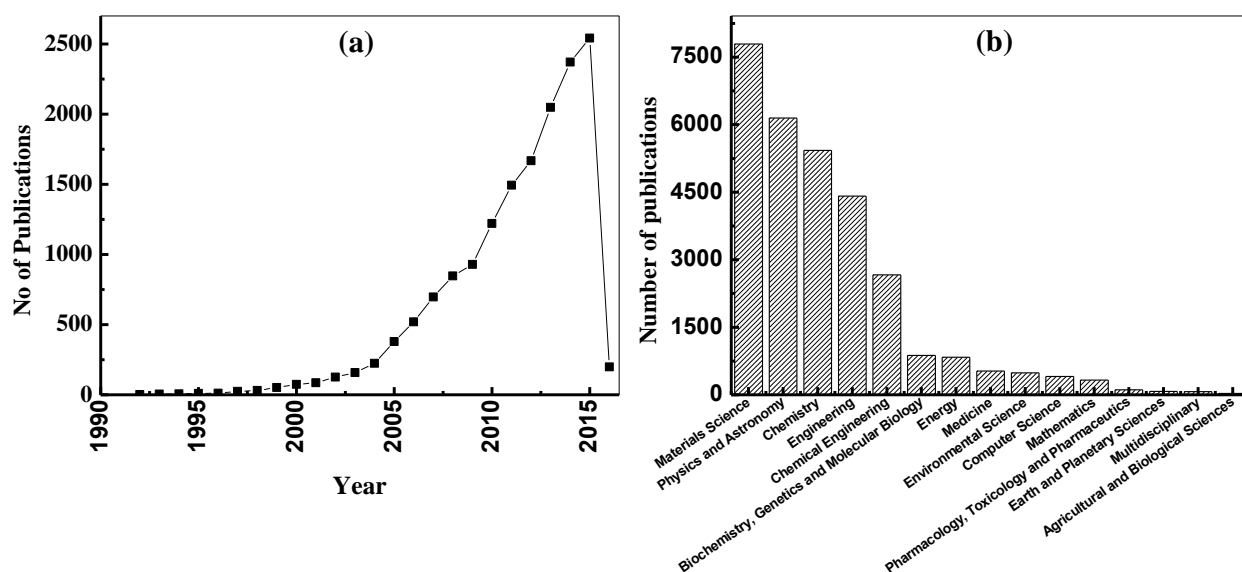
Figure 1.2. Research papers publications on doped nanoparticles (a) year wise and (b) in different subject area during the period 1992 to 12th January, 2016 (collected from *'SciVerse-Scopus'*).

1.2 Principle of Doping

According to the Octec-rule, atoms are accept or share neighbouring atom's outer shell electron to achieve eight electrons in their valence shell and accordingly n-type and p-type doping are achieved. Based on that principle, doping was mostly used to control the electrical conductivity of the semiconductors. Doping of silicon with pentavalent element like phosphorous and trivalent element like boron is shown in the Figure 1.3 as n-type and p-type doping respectively. Doping of Cu and Ag to InAs lattices is presented in Figure 1.4. Here Cu is doped in the interstitial site of the lattices and donates valence electrons to InAs, and n-type doping is achieved. In case of Ag doping, it is doped by substitution of principle reactant component and introduces two electron acceptor sites, which is a p-type doping. [6]
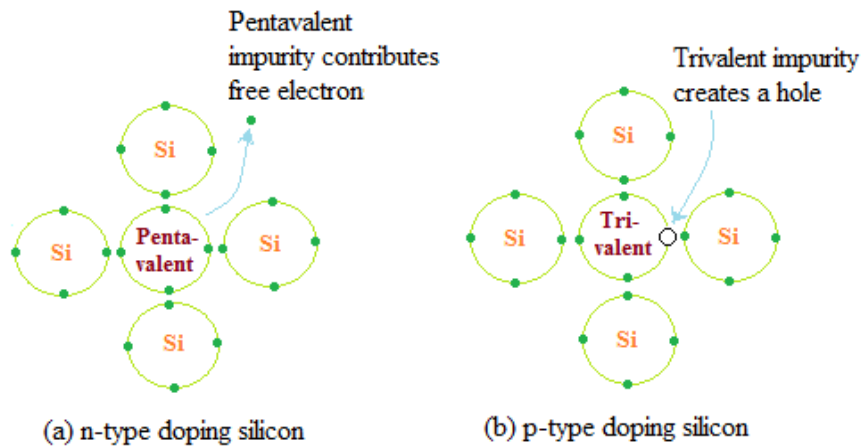
Figure 1.3 (a) n-type silicon doping with phosphorous and (b) p-type silicon doping with boron.
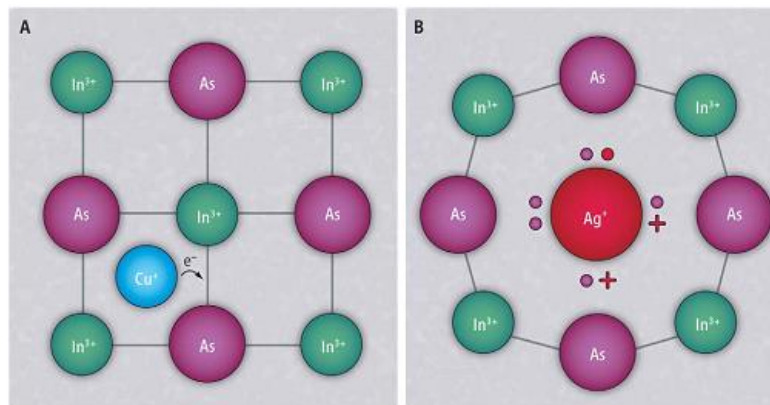
Figure 1.4 (A) Cu impurity in an interstitial site in the InAs lattice, which donates valence electrons to induce n-type doping. (B) Substitutional Ag occupying an In site in the InAs lattice, which introduces two electron acceptor sites resulting in a deficiency of valence electrons and p-type doping. Plus sign indicates the lack of an electron in a bonding orbital. [6]

1.2.1 Effects of doping to the energy band of the host material

When a semiconductor is doped with another element there is a change happens in the energy level in the energy band of the semiconductors. In n-type doping the weakly bound excess electron easily liberates from the dopant atom. The energy of the liberated electron lies close to the conduction band. In p-type doping the energy of the acceptor atoms lies close to the valence band and as a result the band gap of the original host material will change. During doping Fermi level position shifts near to the conduction band with increasing the donor impurities and it goes close to the valence band with increasing the hole concentration in the p-type doping. The shifting of Fermi level during doping is shown in Figure 1.5.
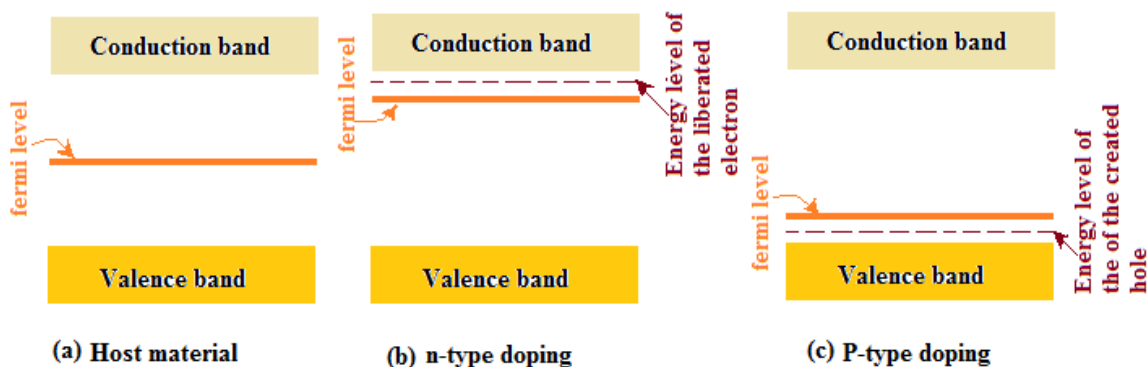
Figure 1.5 Position of the Fermi level and introduced energy level in band diagram in (a) host material, (b) n-type doping, (c) p-type doping.

1.3   Doping to Nanomaterials

Incorporation of dopant to nanomaterials opens up new possibility of broad applications of these materials because of broadening in their properties beyond what is possible in pure nanomaterials. From Figure 1.3 it is seen that there is shifting of Fermi level as well as intermediate energy level in the energy band of the semiconductors after n-type or p-type doping. As a result the band gap of the host material changes and because of intermediate energy state there is a possibility of tuning light emission from the host material. From various research studies on doping to nanomaterials it has been found that the success or failure of doping, and the quantity of doping achieved depend on the different factors, such as crystalline structure, shape, surface morphology of the host material, temperature, and the presence of surfactant (helps to change the adsorption binding energy of dopant with the adsorbing surface) in the growth solution. [7,8] These kinetic factors mainly control the host and dopant growth during synthesis. General synthetic approaches of nanocrystal doping are presented in Scheme 1.1. [9] Four different approaches are there (i) growth doping, (ii) nucleation doping, (iii) tuning ligand-metal bond strength, and (iv) ion diffusion approach. In the growth doping approach (Scheme 1.1b) the dopants are adsorbed on the nanocrystal surfaces. In nucleation doping approach (Scheme 1.1c), the dopant and host precursors are added during the nucleation step, where the nucleation of dopant is first. The tuning ligand-metal bond strength approach (Scheme 1.1d) depends on the relative Lewis acidity of the dopant and the host precursors. In doping through ion diffusion approach (Scheme 1.1e) the dopants are introduced in preformed nanocrystals through diffusion.

5
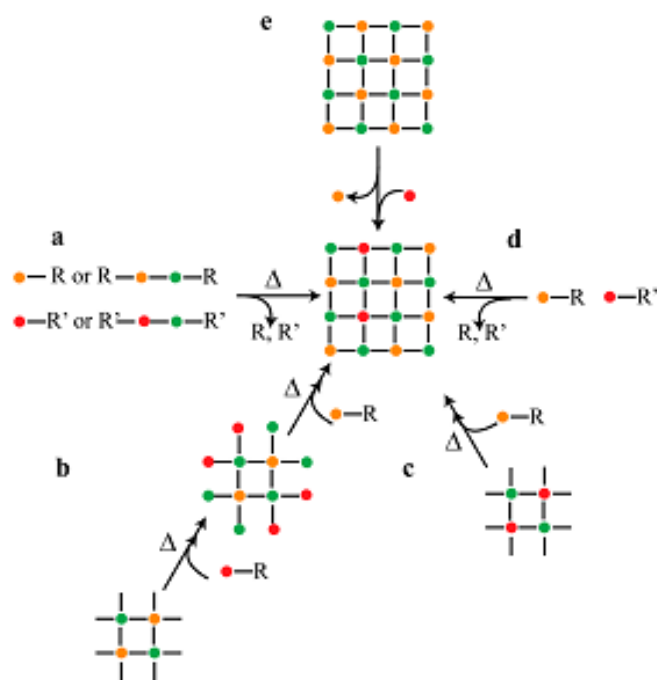
Scheme 1.1. Synthetic approaches to colloidal nanocrystal doping. (a) Source precursors, (b) growth doping, (c) Nucleation doping, (d) Tuning ligand-metal bond strength, (e) ion diffusion. [9]

1.3.1 Location of Dopant in the Host material

Location of dopant in host material should be confirmed to analyze the properties of the doped materials properly. In general there are three possible location of dopant in the host material such as (i) the surface of the host materials, (ii) substitution of principle reactant of the host material, and (iii) the interstitial sites of the host material. [10] In the first case dopants are deposited on the surface of the host materials. Substitutional doping depends on the ionic radius of dopant and principle reactant in the host material. If the ionic radius of principle reactant component is comparable with dopant ionic radius, it will be substituted by the dopant. In the third case the dopant position is in the interstitial sites of the host material. For doped core/shell nanostructure the dopant location may be (i) in the core, (ii) in the shell, (iii) in both core/shell, and (iv) in the interface of core/shell. The radial position doping in the core/shell structure can be controlled by step wise synthesis of host material with subsequently dopant growth followed by host shell growth and by separating unreacted dopant-species from the growth solution before host-shell growth. [11] The distribution of dopant in the nanocrystals was described by Bryan et al in the form of binomial expression (equation 1). [2] Where n is total no of dopant ions per nanocrystal, N is the total number of cation sites available for substitution, and x is the mole fraction of dopant.

$$P(n/N) = \frac{(N)!}{n!(N-n)!}(xN)^n(1-(xN))^{N-n} \qquad (1)$$

For n≪N, P(n/N) simplifies to P(n), the Poisson distribution

$$P(n) = \frac{(xN)^n e^{-xN}}{n!} \qquad (2)$$

The statistical dopant distribution per nanocrystals for various dopant level of 5.0 nm CdSe nanocrystals is presented in Figure 1.6. This model of statistical dopant distribution is esily expanded for desired nanocrystal size distribution.
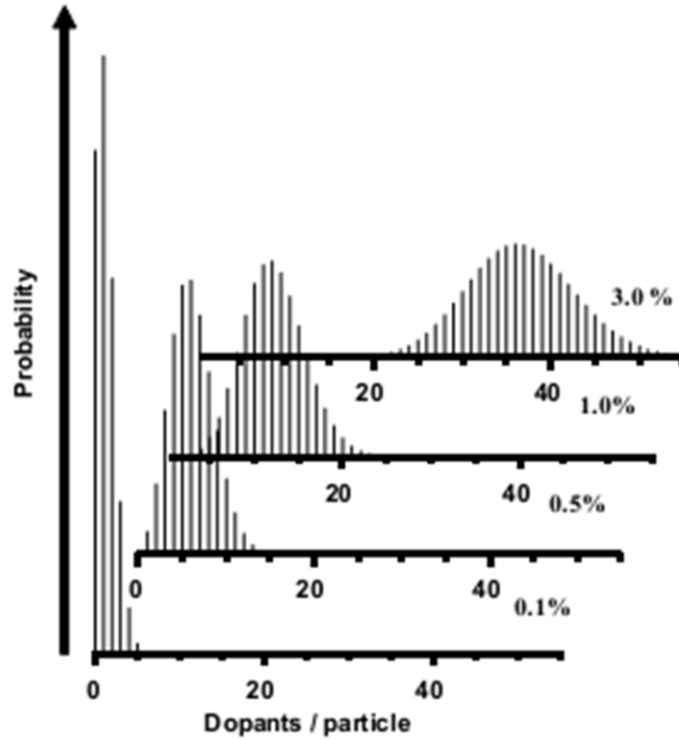
Figure 1.6 Statistical distributions of dopant ions per nanocrystal for various dopant levels (x %) in ensembles of 5.0 nm CdSe nanocrystals. [2]

1.4 Different Classes of Doped Nanomaterials

Doped nanoparticles are combination of host and dopant materials material. So, the doped nanoparticles can be classified based either on dopant or host materials. The host material is the base material and its properties can be modified in the presence of dopant as per their applications. Depending on the host materials type the doped nanoparticles are classified as (i) single host material, (ii) multiple host material. Again the single host materials are classified as (i) solid, (ii) hollow. The multiple host materials are classified as (i) core/shell, (ii) composite. The detail of classification of doped nanomaterials is shown in the schematic 1.2.
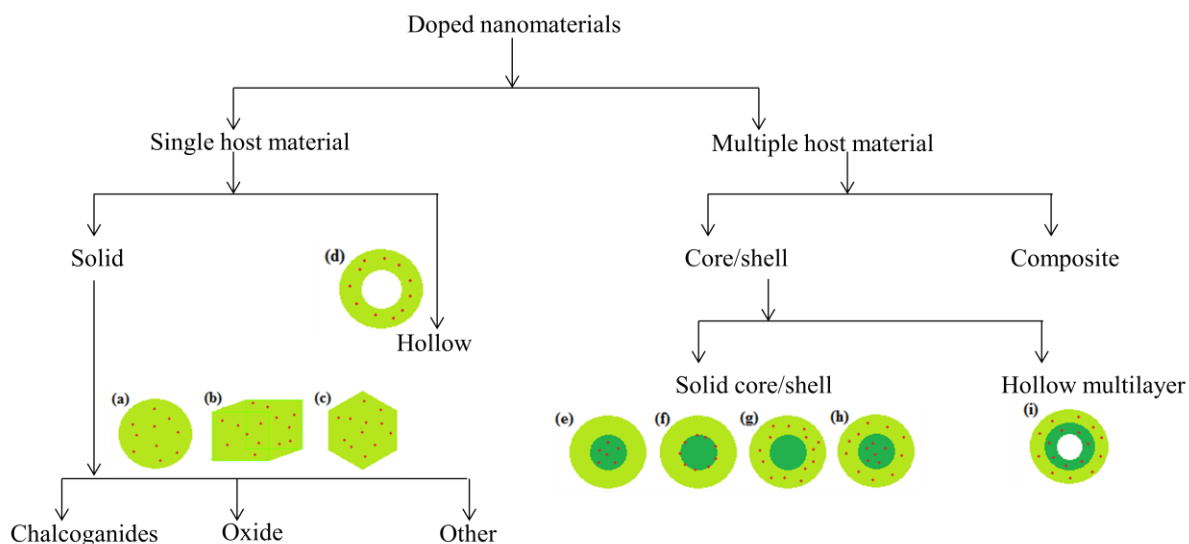
Scheme 1.2. Classification of doped nanomaterials based on host material type. Cartoon of doped nanoparticles: (a) doped spherical, (b) doped cubic, (c) doped hexagonal, (d) doped hollow, (e) doped core/inert shell, (f) core/shell particle with dopant at the interface, (g) inert core/doped shell, (h) doped core/doped shell, (i) doped hollow bi-layer.

1.5 Importance of Doped Nanomaterials

Nanomaterials are well known for their better performances than the bulk material in several applications such as catalysis, biomedical, electronics, solar cells, and so on. In general, doping to any material helps to change their electronic structure and transition probabilities and subsequently enhances the properties of the material or helps to achieve new born properties. [12] Doping to nanoparticles makes the the original band gap of the material under control and helps to tune their stabilization energy and substrate charge transfer, etc which intern makes the nanoparticles suitable for visible light photocatalytic applications. [13,14] Sometimes depending on the dopant an intermediate energy state is developed within the band gap of the host material, which subsequently controls the emission wavelength of the host material within the visible or IR regions. Here dopant acts as a photoluminescence activator. Doping may introduce some new born properties to a particular nanoparticles, for instance TiO_2 nanoparticles itself is having the photo catalytic activities but it can show good antibacterial activities along with photo catalytic activities after doping with Ag. [15] Quantity of doping is also an important parameter for improving particular properties of a host material; for an example, the magnetization of ZnO can be controlled by Ni dopant ratios, at lower dopant ratios Ni-ZnO shows ferromagnetic behaviour but at higher dopant ratios it shows paramagnetic behaviour. [16] Selective and appropriate element doping to a nanoparticle

can not only enhances the properties of the base material but also improves the multi-functionality of the nanoparticles. Apart from single material nanoparticles, recently, doping to core/shell and hollow structure nanoparticles have also been highlighted significantly for the noble applications because of their good thermal stability, dispersibility, enhanced surface area, porous shell structure along with the advantages of doping. Doped core/shell and hollow nanoparticles have promising applications in visible light photocatalysis, drug delivery properties, bio molecule sensing, telecommunication, and photovoltaics. [17-20]

1.6 Motivation of the Project

Among several semiconductor nanoparticles TiO_2, CdS, and ZnS nanoparticles are important because of their potential applications in different areas, such as catalysis, biomedical, sensors, electrical, electronics. The photocatalytic application of these nanoparticles under visible light depends mainly on their band gap, electron hole recombination, surface area, and crystallinity. So, the development of a cheap and efficient photocatalyst is still a promising job from the fundamental and industrial perspective. In spite of the fact that the photocatalysts are mostly used to degrade organic pollutants in aqueous media, however, the visible light induced photocatalytic activity of the catalysts can also be utilized as green antifungal agent or green pesticide for agricultural applications. The semiconductor nanoparticles are also used for the spectrometric detection or analysis of several ions, which may be simple and cheap than the conventional analytical methods. The development of suitable nanoparticles for ultralow and selective detection some important toxic ions is also a challenging job in recent years. Finally, motivation of this project is to develop some novel doped semiconductor nanoparticles for the above mentioned applications. At the same time, if the materials are multifunctional, same materials can be used for different applications.

1.7 Organization of the Thesis

The total work has been organized in eight chapters in the thesis. Chapter − 1 is an introductory chapter which contains the basic definition, concept, classification and importance of doped nanoparticles. Chapter − 2 presents the background literature on different doped semiconductor nanoparticles in single, core/shell, and hollow structural form. Chapter − 3 contains the synthesis and characterization of pure and silver doped TiO_2, CdS, and ZnS nanoparticles for the photocatalytic degradation of metronidazole antibiotic and methylene blue dye. Chapter − 4 presents synthesis and characterization of silver hollow TiO_2

nanoparticles for the photocatalytic degradation of nitrobenzene, metronidazole, and methylene blue dye. Chapter – 5 focuses applications of Ag doped hollow TiO_2 nanoparticles as an effective green fungicide against Fusarium solani and Venturia inaequalis phytopathogens. Chapter – 6 focuses synthesis and characterization of silver doped CdS/ZnS core/shell nanoparticles for the detection of F^- concentration in the aqueous media. Chapter – 7 contains the synthesis and characterization of silver doped hollow CdS/ZnS bi-layer nanoparticles for the ultra low detection of arsenic concentration in the aqueous media. Finally, Chapter – 8 contains the summary of the overall works, major findings, and the suggestions for the future work.

Chapter 2

Background Literature
Doped Solid, Hollow, and Core/Shell Nanomaterials

2.1 Classifications of Doped Nanomaterials

Doped nanomaterials consist of dopant and the host. Studies are available on doped nanomaterials of different kinds by the combination of different kinds of dopants and hosts, so, it is difficult to classify them. However, in a broad way doped nanomaterials are classified based on the host material, such as (i) single host material, (ii) multiple host material. Single host material is again classified based on their structure, as solid material and hollow material. Solid material is further classified based on the types of the materials, as chalcoganides, oxides, and other solid materials. Under multiple hosts material categories the materials are classified as core/shell and composite. The core/shell material is again classified as solid core/shell and hollow multilayer. Dopants are of different types, such as alkali metal, [21,22] alkaline earth metal, [23-26] transition metal, [27-29] lanthanide, [30-33] non metal, [34-36] and metalloid. [37-39] The total development in doped nanomaterials is discussed here in details in different sections under different categories.

2.1.1 Single Host Materials

Single host material is basically consists of one material (element/compound) only. Rapid advances in synthesis techniques of nanomaterials make possible to easy synthesis of different shape nanomaterials (anisotropic) apart from spherical, such as cubic, hexagonal, triangle, prism, rod, wire, tube, etc. These anisotropic nanomaterials have some quite different properties over the spherical nanoparticles. [40-43] As surface area is one important parameter of nanomaterials, researchers have also tried to develop porous or hollow structured nanoparticles. The porous or hollow structure nanomaterials have much more surface area compared to solid one. Because of high surface area these types of nanomaterials are highly desirable for the important applications, such as catalysis, adsorptions, drug delivery, and electrochemical applications. [44-46] The overall single host materials can be categorised based on their structure, as solid material and hollow material.

2.1.1.1 Solid Particles

Solid materials are of different kinds; here we have classified the overall solid materials in three different categories such as, chalcoganides, oxides, and other solid materials. Nanoscale chalcoganides (CdS, ZnS, $CdSe$, $ZnSe$, $CdTe$), oxides (TiO_2, ZnO, CdO, SiO_2, SnO_2), others solid materials ($NaYF_4$, MgB_2, CaF_2, Sb_2Se_3, $BaYF_5$, $BaMgF_4$, $Y_3Al_5O_{12}$) have been studied extensively because of the applications in photoluminescence material, photocatalysis, bio-imaging, antimicrobial, and spintronics. [47-51] Over the last few years researchers have tried to

improve the properties of these materials by doping. Doping of these materials has been studied in the presence of single dopant as well as co-dopant (more than one dopant). [52-54] In general co-doping by more than one material is used for controlling some specific properties of the materials, such as multicolour emission of up-conversion materials, [55,56] bioimaging, [57,58] and catalytic performances. [59,60] Up-conversion emission properties of Yb, Er, Tm, and Ho co-doped BaYF$_5$ nanocrystals have been studied by Niu et al., [54] where the nanocrystals were synthesized by facile hydrothermal method. The up-conversion emission spectras of the nanocrystals under excitation at 980 nm wavelength are presented in Figure 2.1. The emission spectra of BaYF$_5$:Yb/Er (Figure 2.1a) shows the green, green, and red emission at the wavelength 521, 541, and 654 nm. There are five emission band blue, blue, red, red, red in the emission spectra of BaYF$_5$:Yb/Tm (Figure 2.1b) at the wavelength 464, 476, 648, 698 and 781 nm. In case of BaYF$_5$:Yb/Ho nanocrystals green emission is obtain at 542 nm and a red emission is obtained at 648 nm wavelength. From this study it is clear that for a particular material up conversion multicolour emission is possible in the presence of co-doping of more than one component.
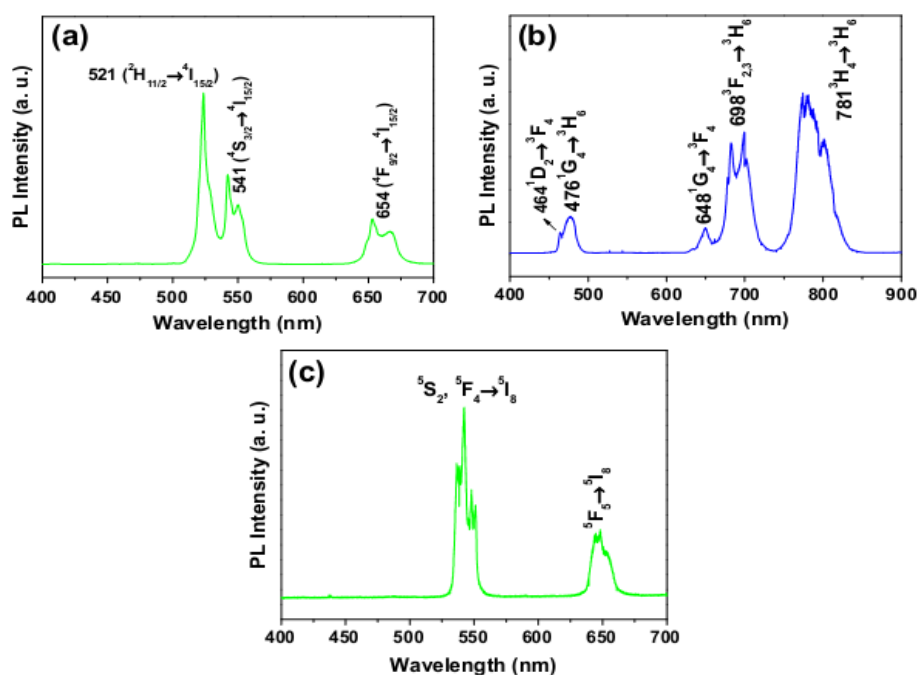
Figure 2.1. NIR-to-visible up-conversion emission spectra of (a) BaYF$_5$:Yb/Er, (b) BaYF$_5$:Yb/Tm, and (c) BaYF$_5$:Yb/Ho nanocrystals under 980 nm laser excitation. [54]

2.1.1.1.1 Chalcoganides

Chalcogenides are the compounds consisting of at least one chalcogen anion (sulfides, selenides, tellurides) and one electropositive element. Under the category of single solid

materials, different chalcoganides, such as CdS, ZnS, CdSe, ZnSe, CdTe, etc have attracted much attention in recent years because of their size and shape dependent electronic and optical properties, which in turn make them suitable for large possible applications such as nano-electronic devices, catalysis, sensor, and biological labelling.

Cadmium Sulphide:

Cadmium sulphide (CdS) is one of the important semiconductor materials with direct band gap of 2.42 eV. Because of its direct band gap, it has various promising applications in the fields of photoconducting cell, non-linear optics, photocatalysis, electroluminescence devices, gas sensor, laser, infrared detectors, and so on. [61–66] The band structure of nano sized CdS can be tuned by changing size/shape and chemical composition of the nanomaterials. [67,68] Doping of other element into a host semiconductor is one of the important techniques to change the properties of the host, for instances, doping of ions act as recombination centers for the excited electron-hole pairs and result in strong characteristic luminescence of the host lattices. [69,70] Different transition metal doping have been studied for tuning the properties of CdS nanoparticles, such as Cu, [71,72] Mn, [73,74] Ni, [75] Cr, [76] Zn, [77] Co, [78] Eu, [79] Ce, [80], Fe [81] to study its photoluminescence behaviour. Details studies of doped CdS nanoparticles are listed in Table 2.1 in different areas of applications. Different methods have been reported till date to synthesize doped CdS nanoparticles by different research groups, such as co-precipitation, [72,80,82,83] hydrothermal synthesis, [84] chemical bath deposition, [85] colloidal wet-chemical, [71,81] sol-gel. [86,87] Ag doping to CdS nanoparticles is important for photoluminescence materials because of their large potential difference between the conduction band of CdS (-1.0 V vs NHE) [88] and the Fermi level of the Ag (+0.15 V). [89] Ag-CdS hybrid particles have been studied to get the enhanced optical response from the inter particle electron transfer between Ag and CdS. [90-93] The fluorescence behaviour of Ag-CdS nanocolloids have been studied by Thakur et al. [93] The details mechanism of Ag-CdS formation is shown in equation (2.1-2.3). The Ag is doped by the substitution of Cd because of the comparable ionic radius of Cd^{2+} (0.97Å) and Ag^{2+} (0.94Å). Figure 2.2 shows the TEM image and the photoluminescence properties of the host CdS quantum dots in the presence of different percentages of silver doping. The photoluminescence emission of the quantum dots was increased with increasing the silver concentration from 1 to 3%, then for 4% silver concentration the emission intensity reduced because of the less availability of the binding sites.

$$\text{Nano CdS} + Ag^+ \xrightarrow{h\nu} CdS\,(e^-h^+) \cdots\cdots\cdots Ag^+ \tag{2.1}$$

$$CdS\,(e^-h^+) + Ag^+ \underset{O_2}{\leftrightarrow} CdS\,h^+ \ldots\ldots\ldots\ldots Ag^0 \leftrightarrow CdS\,(e^-\,h^+) + Ag^+ \tag{2.2}$$

$$\text{CdS } h^+ \ldots \ldots \ldots Ag^0 + Ag^+ \rightarrow \text{CdS } h^+ + Ag_2^+ \tag{2.3}$$
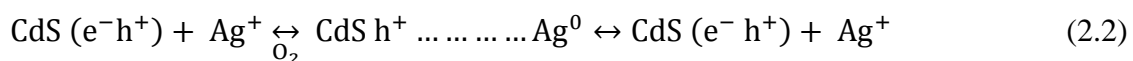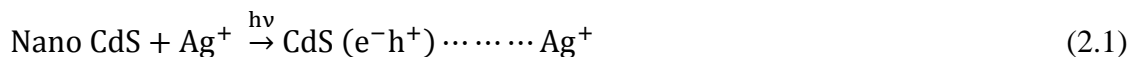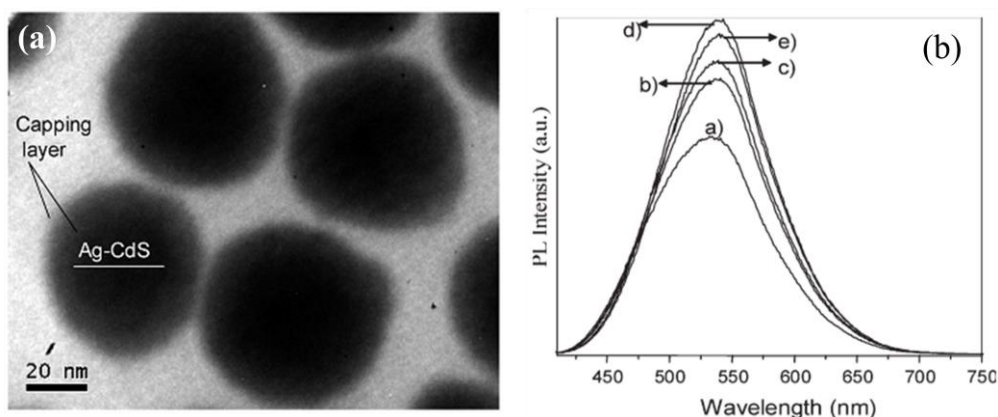
Figure 2.2. (a) TEM image of Ag-CdS. (b) Photoluminescence spectra of Ag-CdS quantum dots with different dopant concentrations: (a) 0, (b) 1, (c) 2, (d) 3, and (e) 4% silver. [93]

Table 2.1. List of doped CdS nanoparticles in the presence of different dopant with different properties

Dopant	Synthesis method	Particle size (nm)	Properties	Ref.
Mn	Chemical precipitation	2-6	Structural & optical	[73]
Mn	In aqueous solution	4±1.1	Photoluminescence	[70]
Mn	Chemical precipitation	3.8–4.3	Optical & thermal	[94]
Mn	Co-precipitation	3.1	Optical	[95]
Fe	Colloidal wet-chemical	4	Structural & optical	[81]
Co	Chemical co-precipitation	4-5	Optical & magnetic	[78]
Co, Al	Co-precipitation	4-5	Optical & magnetic	[96]
Cu	Chemical synthesis	2.7-8.7	Optical	[97]
Cr	Chemical co-precipitation	3-4	Characterization	[98]
Ag	Colloidal	-	Fluorescence	[93]
Ni	Chemical co-precipitation	-	Optical	[63]

Eu	Two-step chemical synthesis route	9.5 ±3.0	Photoluminescence	[79]
Er	Sol-gel	10	Up-conversion emissions	[99]
Gd	Wet chemical route	1-6	Luminescence	[100]
Ce	Co-precipitation	3	Structural & optical	[80]

Zinc Sulphide:

Zinc sulphide (ZnS) is another one of important II-IV semiconductor with a wide and direct band gap of 3.36 eV. Applications of ZnS nanoparticles include photoconductor, flat panel displays, catalysis, photoluminescence, reflectors, light-emitting diodes (LEDs), solar cells, and so on. [101–104] Regarding photoluminescence, pure ZnS nanoparticles have fluorescence emission in UV region but the emission can be made in visible region by doping with a suitable dopant element, where the dopant can acts as recombination centres for the excited electron-hole pairs and as a result a strong and characteristic luminescence is possible. ZnS has been activated or doped with variety of metal which provides an intermediate energy state within the band gap, and alters the wavelength of emission and the photophysical relaxation processes of the carriers in the host. The tuning of the intermediate state can help to control the emission wavelength within the visible and IR region. Successful studies have been done on doped ZnS nanoparticles in the presence of Ba, [105] Mn, [106–108] Co, [109,110] Cr, [111] Fe, [112] Cu, [102,113,114] Ti, [115] Ni, [116,117] Pb, [118] etc. Doping of Nobel metal, such as Ag to ZnS makes them possible for the potential applications in efficient photoluminescence material, [119] nanophosphor based display devices, [104] production of hydrogen by solar light, [120] and supramolecular devices. [121] Table 2.2 presents a list of doped ZnS nanoparticles in the presence of different dopant for the applications in different areas.

Table 2.2. List of doped ZnS nanoparticles in the presence of different dopant with various properties

Dopant	Synthesis method	Particle size (nm)	Properties	Ref.
Mn	Chemical route	3-5	Mechano luminescence & thermo luminescence	[122]
Mn	Surface initiated polymerization	12	Drug delivery	[106]

Mn	Chemical precipitation	2.8	PL enhancement	[107]
Mn	Chemical process	1.8-2.0	Size control	[123]
Mn	Inverse micro -emulsion	3-18	Photoluminescence	[124]
Co	Hydrothermal	7	Optical	[109]
Cr	Chemical co-precipitation	3-6	Structural & optical	[111]
Fe	Chemical co-precipitation	3.3-5.5	Photoluminescence & magnetic	[112]
Cu	Chemical precipitation	4-6	Synthesis & optical	[113]
Cu	Coordination chemistry	20	Optical	[114]
Cu	Chemical synthesis	1.8-3	Photoluminescence	[102]
Ni	Chemical co-precipitation	2-2.5	Luminescence	[116]
Ni	Chemical co-precipitation	2–3	Ferromagnetism	[117]
Pb	Aqueous chemical	2.8 ± 0.3	pH dependent photoluminescence	[118]
Ag, Al	Co-precipitation	5	Blue photoluminescence	[104]

2.1.1.1.2   Oxides

Apart from chalcoganides, different oxide nanomaterials, such as TiO_2, ZnO, CdO, have been studied a lots for different applications, such as photocatalysis, antibacterial agent, photovoltaic cells, optoelectronics, sensor, etc. Especially TiO_2, a semiconductor material, has long been studied for its wide range of applications in photocatalysis, solar cell, hydrogen gas production, bio applications, and so on. For the catalytic point of view TiO_2 has been regarded as an excellent semiconductor photocatalyst for its high performance, low toxicity, low cost, easy availability, and outstanding chemical stability. [125-127] But, because of its wide band gap (3.2 eV for anatase and 3.06 eV for rutile) [128] TiO_2 acts efficiently as a photocatalyst under UV light irradiation only. Since only a small fraction (3-5%) of solar light corresponds to UV region, so, it is expected that merely 3-5% of whole radiant solar energy is useful for the photocatalyst purpose. It is also well known that there is a high rate recombination between the excited electron and positive hole in case of pure TiO_2. [129] Research interest came to the scenario on the development of efficient TiO_2 photocatalyst to utilize the solar or indoor visible light for the photocatalytic degradation of organic compounds. Several steps have been taken for improving the visible light photocatalytic

response of TiO_2 nanoparticles, such as transition metal doping, [130–134] deposition of noble metal, [135–138] dye photosensitization on the TiO_2 surfaces. [139–141]. Modification of TiO_2 by impurities doping can produce high Schottky barrier that facilitates electron capture, [129] that may produce longer electron-hole pair separation life time and reduce the recombination of electron-hole pair separation. A detail studies on doped TiO_2 nanoparticles are listed in Table 2.3 in the presence of different dopant element. Incorporation of noble metal like Ag enhances the photocatalytic activities of TiO_2 by lowering the recombination rate of its photo-excited charge carrier and/or providing more surface area for adsorption. [138,142–144] Apart from this silver itself has antibacterial activities, [145–147] and it was seen that Ag doped TiO_2 has highly improved photocatalytic inactivation capabilities of bacteria. [148–150] For silver doped nanoparticles silver ions could be produced either by reduction or by decomposition of silver precursor compound. Reduction of silver precursor compound could be achieved in presence of a reducing agent or by irradiation with light. Decomposition could also be achieved through calcinations of the sol-gel product via the decomposition of silver precursor compound. [151]

Table 2.3. List of different doped TiO_2 nanoparticles in different studies areas by different researchers

Dopant	Synthesis method	Particle size (nm)	Properties	Ref.
Fe	Aqueous environment	2-4	Photocatalytic	[151]
Fe	Sol-gel	60 - 70	Photocatalytic	[152]
Fe	Sol–gel	15–40	Ferromagnetism	[153]
Mn	Sol-gel	7	Photocatalyst	[154]
Ag	Miniemulsion	25	Photoactivity	[136]
Co	Chemical route	10–15 & 27	Magnetic behavior	[155]
Co	Hydrothermal hydrolysis	5.3	Solubility & dispensability	[156]
Zr	Sol–gel	12	Nonlinear optical properties	[157]
Zn	Sol–gel	13–33	Optical	[158]
Nb	Solvothermal	4-15	Self-assemble & electrical conductivity	[159]

Y	Sol-gel	-	Photocatalytic activity	[160]
Al	Vapor-phase oxidation	18.9-29	Morphology & crystal structure	[161]
Zr, Y	Homogenous hydrolysis	2–3 μm	Phase and surface stability	[162]
Nb, Fe	Thermal plasma	30-74	Magnetic	[163]
Fe, Ni	Alcohol-thermal	14	H_2 evolution	[164]
Fe, C	Solvo-thermal	8	Visible-light photocatalyst	[165]
Sm	SGACS	-	Visible light photocatalyst	[166]
Eu	TPOLPM	30-83	Structural & luminescence	[167]
Ce	Hydrothermal	22	Photocatalytic	[168]
Pr	Sol–gel	10-50	Photocatalysis	[169]
La, Eu	Sol-gel	40–60	Photocatalytic	[170]

2.2.1.1.3   Other Materials

Apart from chalcoganides and oxide host materials, some other single host materials, such as MgB_2, [171] CaF_2, [172-174] BaF_2, [175] GaN, [176] GdF_3, [177] $NaYF_4$, [178,179] Sb_2Se_3, [54] $BaYF_5$, [55] $BaMgF_4$, [56] $Y_3Al_5O_{12}$, [180] KY_3F_{10}, [181] $Y_7O_6F_9$ [182] have been reported to show the effect of doping on their properties. Doping of these types of material mainly studied in the presence of lanthanide element, such as Ce, Yb, Gd, Er, Tm, Eu, Nd, Sm, etc, and some transition metal, such as Ni, Mn, Ag. These materials are mainly used for the applications in antibacterial agent, [183] magnetic material, [184] optical material, [185,186] and bioimaging purposes. [187]

2.1.1.2 Hollow Particles

Hollow nanomaterials are important over the solid nanomaterials because of their remarkable properties, such as higher surface area, low density, higher quantum yield, [188] high saturation magnetization, [189] efficient adsorption, [190] and so on. Sacrificial core method is one important technique for the synthesis of hollow nanoparticles, where the core is removed by calcinations or by dissolution. More advanced nanoparticles, such as doped hollow

nanoparticles have attracted recently because of its new and improved properties over the hollow nanoparticles. Diverse applications of doped hollow nanoparticles include chemical and biological sensors, [191] air and water purification, [192] advanced flat panel displays, [193] drug delivery, [194] low-cost fuel cell cathodic catalyst, [195] optical devices. [196] Synthesis of doped hollow nanoparticles was carried out using both template route [192,193] as well as template free route [196-198] by different researchers. Studies of different doped hollow nanoparticles in different areas by different research groups are listed in Table 2.4. From the reported studies it can be noted that mainly TiO_2, Gd_2O_3, and C were mainly studied as the host material for the doped hollow structure formation, where C was used as the core which was removed by calcinations. Different element, such as Bi, N, Sn, Yb, Er, Nd were used as the dopant.

Table 2.4. List of different doped hollow nanoparticles in different areas of application.

Dopant	Host material (Shell)	Core	Removal of core		Doped hollow	Properties	ref.
			dissolution	calcination			
Yb/Er	Gd_2O_3	C		800°C, 2 h in air	Gd_2O_3:Yb/Er	Structure & morphology	[199]
N, Ce	TiO_2	C		500°C, 4 h in air	TiO_2: N, Ce	Photocatalysis	[200]
Nd	TiO_2	C		500°C, 3 h in air	TiO_2: Nd	Photocatalysis	[201]
N	C	C	oxidative HNO_3	-	C:N	Fuel cell catalyst	[195]
Sn	TiO_2	C		500°C, 3 h in air	TiO_2: Sn	Photocatalysis	[202]
N	TiO_2	ZnO		550°C, 2 h in air	TiO_2: N	Photocatalysis	[203]
Bi	TiO_2	C		500°C, 4 h in air	TiO_2:Bi	Photocatalysis	[204]

Some reported studies on doped hollow nanoparticles are presented here. One method is developed by Chen et al. [115] for the synthesis of Polystyrene/(rare-earth-doped nanoparticles) (PS/REDNPs) hybrid hollow spheres via the in situ diffusion of organic core

into inorganic shell under strong capillary force. The details procedure is presented in Scheme 2.1.
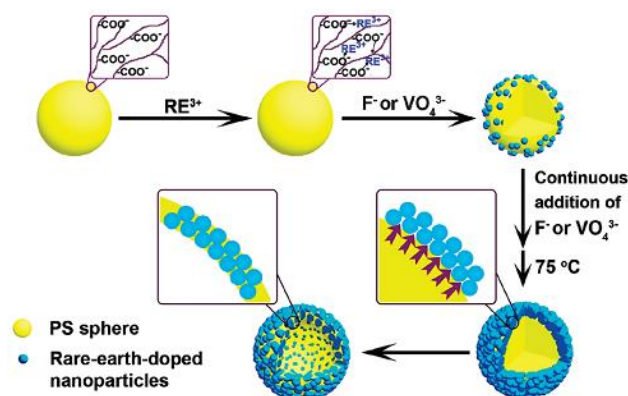
Scheme 2.1. Schematic Diagram for the Formation of PS/REDNPs Hybrid Spheres [115]

The corresponding TEM and SEM images of the PS/REDNPs hybrid hollow spheres (Figure 2.3) shows that after the deposition of REDNPs the diameter of the sphere increases from 280 to 340 nm and exhibits a rough surface. Figure 2.3(a-c) shows uniform hollow structure having strong contrast between the dark ring and the pale centre. The presence of broken sphere in the SEM image (Figure 2.3d,e) confirms the formation of hollow sphere. [115]
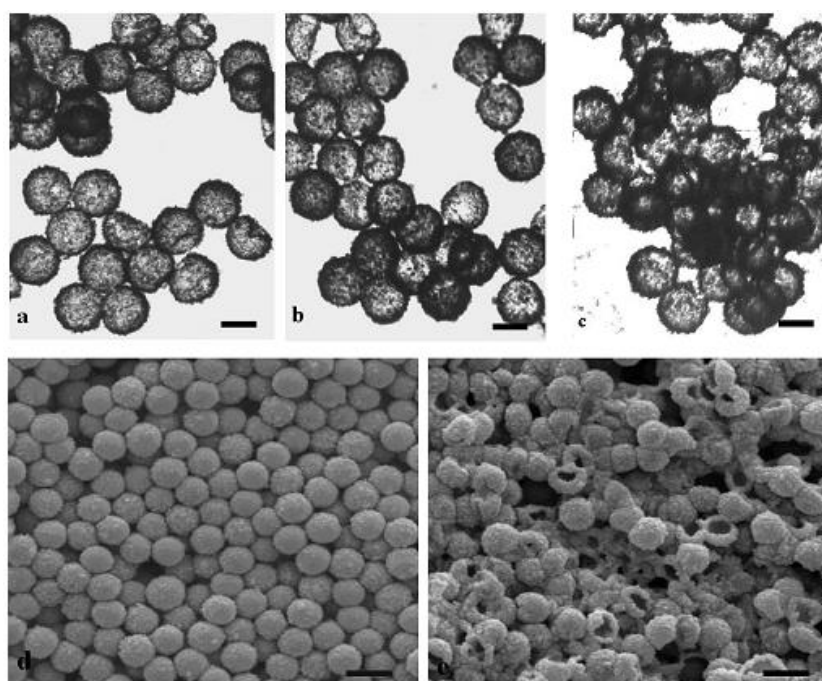
Figure 2.3. TEM images of (a) PS/LaF$_3$:Eu^{3+}, (b) PS/LaF$_3$:Ce^{3+}-Tb^{3+}, (c) PS/YVO$_4$:Dy^{3+}. The SEM image of (d) PS/LaF$_3$:Eu^{3+}, (e) artificially broken PS/LaF$_3$:Eu^{3+} hollow spheres. [115]

Ma et al. synthesized nitrogen doped hollow carbon nanoparticles (N-HCNPs) by detonation-assisted chemical vapor deposition (DCVD) technique. [195] The obtained N-HCNPs have excellent oxygen reduction performances. The TEM and HRTEM images (Figure 2.4a-e) of the hollow carbon NPs (HCNPs) and N-HCNPs show that both the HCNPs and N-HCNPs are of core/shell type with the entirely hollow cavities encapsulated by 2-5 nm thick carbon shells. The XPS spectra of N-HCNPs (Figure 2.4e) shows a dominant narrow graphitic C 1s peak at 284 eV, an N 1s peak at ~ 400 eV, and a weak O 1s peak at 531 eV, proves the incorporation of N atoms in the graphitic structure of N-HCNPs. Whereas the XPS spectrum of HCNPs shows only two peaks at 284 and 531 eV belonging to C 1s and O 1s photoelectron excitation, respectively. The high-resolution N 1s XPS spectrum in Figure 2.4f shows the presence of three peaks at binding energies of 398.6, 399.8, and 401 eV, corresponding to the pyridinic, pyrrolic, and quaternary like nitrogen bonding configurations, and the pyridinic like nitrogen is dominant in N-HCNPs.
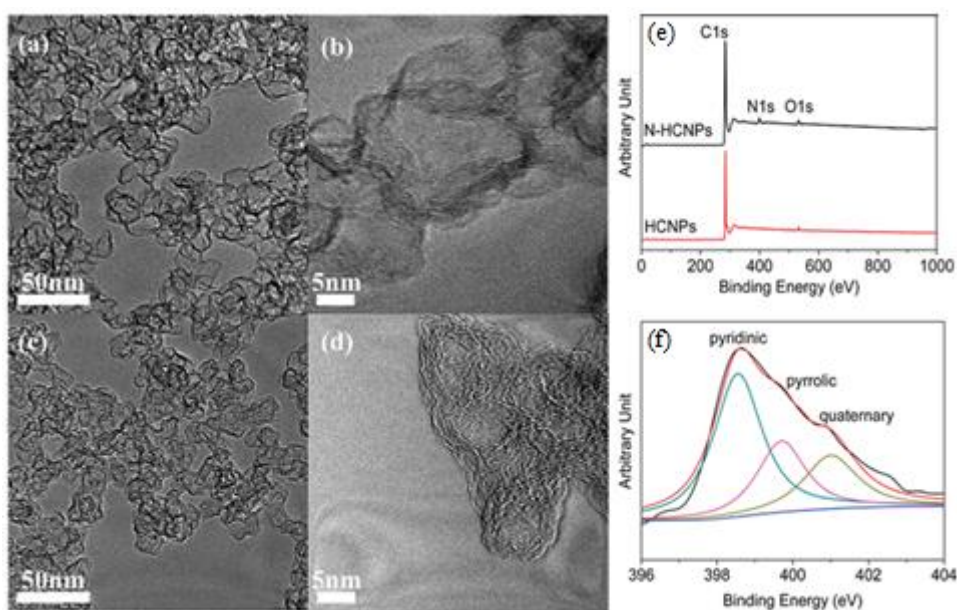
Figure 2.4. TEM images of (a) N-HCNPs, (c) HCNPs and HRTEM images of (b) N-HCNPs, (d) HCNPs, (e) XPS survey spectrum of N-HCNPs and HCNPs and (f) deconvoluted N 1s XPS spectrum of N-HCNPs. [195]

From the overall literature on doped hollow nanoparticles it is seen that synthesis of doped hollow nanopartices mainly includes three steps (i) synthesis of core material, (ii) synthesis of core/doped shell, (iii) removal of core material. Considering economic of the synthesis process, one step synthesis approach is most desirable for the synthesis of doped hollow nanoparticles, where doping will be achieved during the removal of the core. The method is economic because no extra precursors are needed for doping, in addition the

method is easy and less time consuming. Literature shows that core removal by dissolution method is more desirable compared to calcinations method, where complete removal of core with desired doping may be achieved. However, a very little attention has been given in this approach.

2.1.2 Multiple Host Materials

Over the last few decades researchers have found that nanoparticles made of more than one material have better efficiency in several applications over the single material nanoparticle. Some multi-material nanoparticles, such as heterogeneous, composite, and core/shell nanoparticles have attracted a considerable research interest because of some unique properties, such as multi-functionality and chemical stability. [205-207] The materials of core/shell and composite form have been studied between metal-metal, metal-compound, and compound-compound. The properties of these types of material are because the combined effect of the consisting materials. When a material is costly it can be formed as composite or core/shell with some cheap material for getting desired properties, which reduces material cost. In the core/shell form important core material can be protected from the environment by coating a very thin layer shell, where the material properties will not be hampered. Doping to this type of multiple host material further opens up a new scope for these materials because of the advantages of doping.

2.1.2.1 Core/Shell Materials

Amoung different multi-material nanoparticles core/shell nanoparticles are considered as important one because of their highly stable and dispersible properties. Different shaped core/shell nanoparticles are there, such as spherical core/shell, hexagonal core/shell, multiple small core coated by single shell, core/multishell, and movable core/shell. The properties of a core/shell nanoparticles is the combining effect of both the core and shell, and the overall properties can be controlled by the core to shell ratio. [208] Semiconductor/semiconductor core/shell nanoparticle is one important class of core/shell nanomaterials because of the importance of semiconductors. For this type of core/shell nanoparticles band gap of the core and shell is very important for getting the desired light emission properties of the materials. From various studies it has been seen that the particle made of higher band gap shell material is having higher quantum yield (QY) and higher stability against photobleaching of the core compared to the reverse case, where shell thickness is also one important parameter. [209,210] Core/shell materials may be further classified as (i) solid core/shell and (ii) hollow multilayer.

For hollow multilayer nanoparticles synthesis the core can be removed by the calcinations or dissolution method similar to the hollow nanostructure formation.

2.1.2.1.1 Solid Core/Shell Materials

Materials of core/shell structure have attracted a lot over the last two decades over the single material because of their diverse applications in various fields, such as catalysis, biomedical, electronics, and so on. Recently, researchers are interested about the some more advanced material like doped core/shell nanoparticles because of their outstanding properties, such as up-conversion emission intensity, [211] high and tunable photocatalytic activity, [212] and ferromagnetism. [213] These promising material are mainly used in medical diagnosis, [214] labels for biological molecules, [215] forster resonant energy transfer (FRET), [216] telecommunication, [217] photovoltaic, [218] and so on. Depending on the position of dopant in the core/shell structure the doped core/shell nanoparticles are divided as (i) doped core/inert shell, (ii) inert core/doped shell, (iii) doped core/doped shell nanoparticles. Synthesis of core/shell nanoparticles is a two steps process; (i) synthesis of core material and followed by (ii) uniform shell coating on the core. For doped core/shell nanoparticles synthesis, the dopant precursor is added during subsequent synthesis of core and shell, respectively. With the progress of doped core/shell nanoparticles doping is also studied for core/shell/shell structure nanoparticles. These types of material have promising upconversion fluorescence properties and are applicable for making bio-probes [219] and imaging purposes. [220] Successful studies of doped core/shell nanoparticles by different researchers are listed in Table 2.5.

Table 2.5. List of different doped core/shell shell nanoparticles in different application areas.

Dopant	Host	Core/shell	Properties	Ref.
Tb	$CePO_4$	$CePO_4$:Tb/ $LaPO_4$	Photoluminescence Quantum Yield	[221]
Tb	CeF_3	CeF_3:Tb/LaF_3	Luminescence & energy transfer	[215]
Tb	CeF_3	Fe_3O_4/CeF_3:Tb	Bi-functional luminescent & magnetic	[222]
Mn	ZnS	CdS/ZnS:Mn	Mechanism study	[223]
Mn	ZnS	CdS/ZnS:Mn	Color-tunable dual emissions	[224]
Mn	ZnS	ZnSe/ZnS:Mn	Chemical sensing	[225]
Cu, Pb	ZnS	ZnS:Cu, Pb/ZnS	Spectroscopic investigations	[226]

B, P	Si	Ge/Si: B, P	Transport modulation	[227]
B	Si	Ge/Si:B	Electronic transport	[228]
P	Ge	Si/Ge:P		
Eu	LaPO$_4$	LaPO$_4$:Eu/ LaPO$_4$	Identification of dopant sites	[229]
Ce,Tb	LaPO$_4$	LaPO$_4$:Ce,Tb/ LaPO$_4$	Luminescent	[230]
Co, Mn	ZnSe	ZnSe: Co, Mn /CdSe	Magneto-optical	[231]
Yb, Er	NaYF$_4$	NaYF$_4$:Yb,Er/ NaGdF$_4$	Up-conversion optical	[211]
Yb, Er	NaYF$_4$	NaYF$_4$:Yb,Er/ NaYF$_4$	FRET	[216]
Er, Yb	NaYF$_4$	NaYF$_4$: Er, Yb/ NaYF$_4$	Up-conversion luminescence	[232]
Yb, Er	NaYF$_4$	NaYF$_4$:Yb, Re/ NaYF$_4$	Up-conversion Luminescence	[233]
Er, Yb	NaGdF$_4$	NaGdF$_4$:Er, Yb/ NaGdF$_4$:Yb	Up-conversion Luminescence	[234]
Yb	NaGdF$_4$			
Ce,Tb	NaGdF$_4$	NaGdF$_4$:Ce,Tb/ NaYF$_4$	Luminescence	[235]
Eu	Y$_2$O$_3$	Fe/Fe$_3$O$_4$/Y$_2$O$_3$:Eu	Magnetic/fluorescent	[236]
Eu^{3+}	Ga$_2$O$_3$	Ga$_2$O$_3$/SiO$_2$	Electroluminescence	[237]
Eu^{2+}	GaN	GaN/SiO$_2$		
Er, Yb, Gd, Tm	NaYF$_4$	NaYF$_4$:Er, Yb, Gd/NaYF$_4$:Tm, Yb/NaGdF$_4$:Gd	Bi-functional up-conversion	[220]
Yb, Er(Tm)	NaYF$_4$	NaYF$_4$:Yb,Er(Tm)/Na YF$_4$/Polymer	Up-conversion Fluorescence	[219]

Abbreaviations: Diethyl zinc [(C$_2$H$_5$)$_2$Zn], Hexamethyldisilathiane [(CH$_3$)$_3$SiSSi(CH$_3$)$_3$], tetraethyl orthosilicate (TEOS).

In doped core/inert shell nanoparticle the role of the inert shell is basically to protect the luminescence core where as doped shell (active shell) can help to transfer the absorbed energy from the pump source to the core material. [234] From the reported literature it has been seen that most of the studies on doped core/shell nanoparticles are available on lanthanide materials. Some reported studies are presented here on doped core/shell materials. Figure

2.5a shows a schematic of doped core/doped shell ($NaGdF_4$:Er^{3+},Yb^{3+}/$NaGdF_4$:Yb^{3+}) nanoparticles. Here the Yb^{3+} doping helps to absorb the NIR light and subsequently transfer this energy to the Er^{3+}/Yb^{3+} co-doped core and which finally leads to three up-converted emissions, such as blue, green, and red emissions. The colloidal solution of the nanoparticles was excited at 980 nm and the digital photographs are presented in Figure 2.5b. Figure 2.5c shows up-conversion emission spectra of doped core, doped core/inert shell, and doped core/doped shell nanoparticles upon excitation at 980 nm. In every case up-converted emissions are observed in blue, green, red, and NIR region, but very low red emission observed in case of doped core/doped shell $NaGdF_4$ nanoparticles because of the emission from higher energy $^2H_{9/2}$ excited state to the $^4I_{11/2}$ excited state.
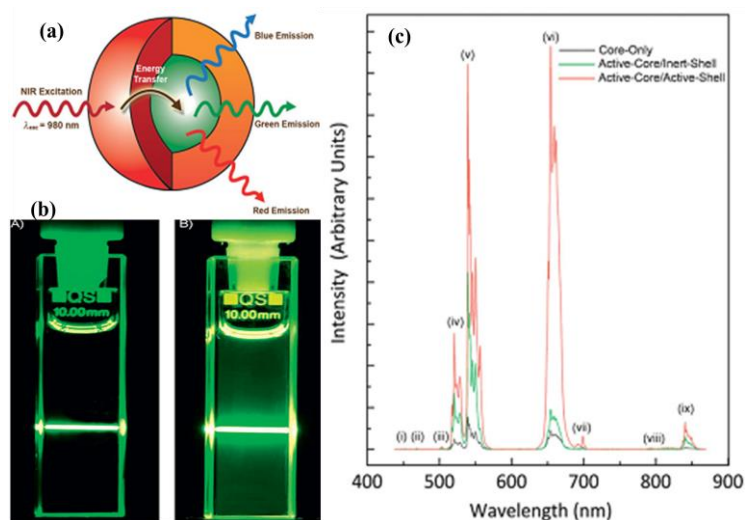
Figure 2.5. a) Schematic of an active core/active shell nanoparticles including red for Yb^{3+} doped shell and green for Er^{3+}/Yb^{3+} co-doped core. (b) Photographs of colloidal solutions of A) $NaGdF_4$:Er^{3+},Yb^{3+}/$NaGdF_4$ and B) $NaGdF_4$:Er^{3+},Yb^{3+}/$NaGdF_4$:Yb^{3+} nanoparticles in toluene. c) Up-conversion luminescence spectra of colloidal $NaGdF_4$:Er^{3+},Yb^{3+}, $NaGdF_4$:Er^{3+},Yb^{3+}/$NaGdF_4$ and $NaGdF_4$:Er^{3+},Yb^{3+}/$NaGdF_4$:Yb^{3+} nanoparticles. [234]

A study of inert core/doped shell (ZnSe/ ZnS:Mn) nanoparticles by Thakur et al. concluded that doping to shell is an effective way to get bright and emissive nanocrystals. [225] The absorption and emission spectra of core ZnSe, ZnSe/Mn-ZnS, and ZnSe/Mn-ZnS/ZnS nanocrystals are presented in Figure 2.6. There is a red shifting of the absorption with the shell layer addition and the emission intensity is increased by several hundred folds from the surface passivation. The inset Figure 2.6 is showing the digital photograph of the dispersed nanoparticles in water in room light and UV light irradiation.
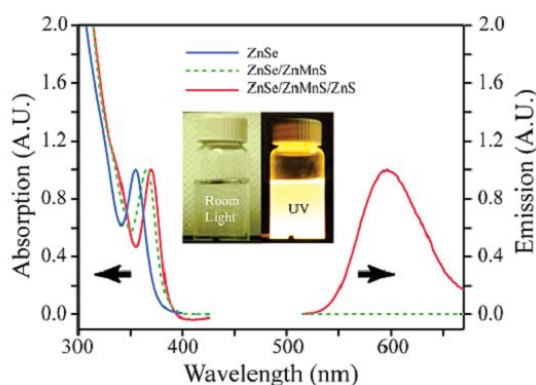
Figure 2.6. Absorption and emission spectra of ZnSe, ZnSe/ZnMnS, and ZnSe/ZnMnS/ZnS nanocrystals. Inset: ZnSe:Mn^{2+} nanocrystals solubilized in water under room light and UV irradiation. [225]

Ehlert et al. studied the effect of Cu and Pb doping on the photoluminescence properties of ZnS/ZnS core/shell nanoparticles. [226] The corresponding photoluminescence spectras in Figure 2.7 show the blue luminescence for undoped ZnS, green luminescence for ZnS:Pb core, ZnS:Cu,Pb core, and ZnS:Cu, Pb/ZnS core/shell and white luminescence for ZnS:Pb/ZnS core/shell nanoparticles. The undoped shell material (ZnS) reduces the effect of surface defects and quenching of the luminescence.
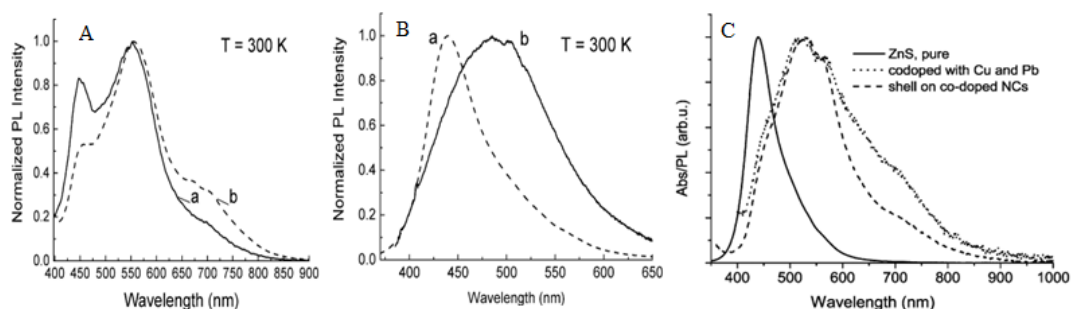
Figure 2.7. Photoluminescence spectra of (A) ZnS:Pb core (a) and ZnS:Pb/ZnS (b) nanocrystals with excitation wavelength 351 nm, (B) undoped (a) and Cu-doped (b) core-type ZnS nanoparticles with excitation wavelength 351 nm, (C) bare ZnS, ZnS:Cu,Pb core and ZnS:Cu,Pb/ZnS core/shell nanocrystals with excitation at 312 nm. [226]

The effect of Mn doping on the photoluminescence properties of CdS/ZnS core/shell nanoparticles has been studied by Yang et al. and it was seen that the photoluminescence emission was dependent on Mn concentration and it was maximum for the Mn concentration of 0.44% as is shown in Figure 2.8a. [223] The TEM image in Figure 2.8b shows the particle with nearly mono dispersed with a standard deviation of 6%. The photoluminescence (PL) quantum yield (QY) of the Mn emission increases with increasing the Mn-doping level and it quenched at Mn doping level of 0.44% (Figure 2.8c). The QY of the Mn emission with

varying the Mn position (δ) from 0 to 4.0 ML inside the ZnS shell is presented in Figure 2.8d. It has been seen that the QY is also dependent on the position of the Mn inside the ZnS shell and the maximum QY up to 56% is achieved at δ of 3.2 ML, and then the QY decreases with the further increase of δ.
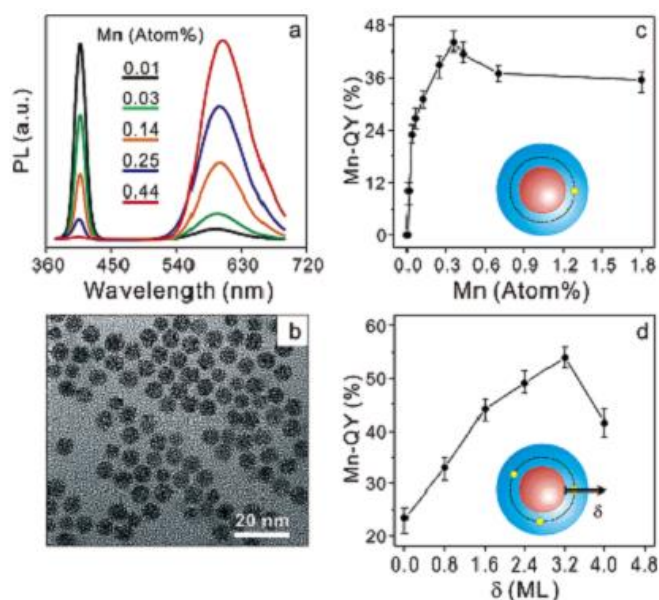
Figure 2.8. (a) Normalized PL spectra of Mn-doped CdS/ZnS core/shell nanocrystals with different doping levels. (b) TEM image of the Mn-doped core/shell nanocrystals. (c) Plot of Mn QY as a function of doping level for these nanocrystals. (d) Plot of Mn QY as a function of Mn position (σ) in the ZnS shell of the core/shell nanocrystals with a doping level of 0.36%. [223]

2.1.2.1.2   Hollow Multilayer Nanoparticles

As discussed in the previous section (2.2.1.2) that the hollow structure nanomaterials is much more important over the solid nanomaterials. When the materials are of multilayer with hollow structure then they have important properties, such as high surface area, low density, high dispersibility and stability. Because of these properties the materials can be used for photocatalysis, antifungal agent, molecular sensor, drug delivery, and spintronics applications. [238-240] There are still some lagging in the properties of such kind of materials, such as high band gap and electron hole recombination. Because of these reason this materials have some limited applications in visible light photocatalysis and fluorescence emission. When doping is introduced to this kind of nanomaterials, it is expected that the

problem can be solved. But, till date there are almost studies are available on doped hollow multilayer nanoparticles.

2.1.2.2 Composite Materials

Design of composites is one versatile method in advanced material development. Compostes can be made between compound-metal, compound-compound, and metal-metal. The formations of composite not only helps in surface modification [241] but also can effectively reduce band gap of the material, and makes the photogenerated electron/hole recombination under control. [242,243] Over the last few years synthesis of nano composite along with doping are attracted for the applications in different areas such as, photocatalysis, [244,245] photoluminescence, [246,247] antibacterial, [248,249] etc because of specific surface area, presence of interface between particles or polymer matrix, and quantum size effect. Table 2.6 shows a list of some doped composite nanomaterials for the applications in different areas.

Table 2.6. List of some doped composite nanoparticles with different applications.

Dopant	Composite	Properties	Ref
B	$Ag-TiO_2$	Photocatalysis	[250]
Ce	$TiO_2-Fe_3O_4$	Photocatalysis	[251]
N	$Ag-TiO_2$	Photocatalysis	[252]
Sm	$Ag-TiO_2$	Fluorescent	[247]
Eu, Tb	CdS/ZrO_2	Luminescence	[253]
Sm	SiO_2/CdS	Fluorescent	[254]
Zn	$CdS-TiO_2-ZnO$	Electrode efficiency	[255]

2.2 Synthesis Approaches of Doped Nanomaterials

Different approaches have been taken for the synthesis of doped nanomaterials and it is difficult to categorise the overall synthesis approaches. However in broad way the synthesis approaches are categorise in two ways, such as wet-method and dry-method. Each method has some advantages as well as some disadvantages. Scheme 2.1 shows different approaches of doped nanomaterials synthesis.
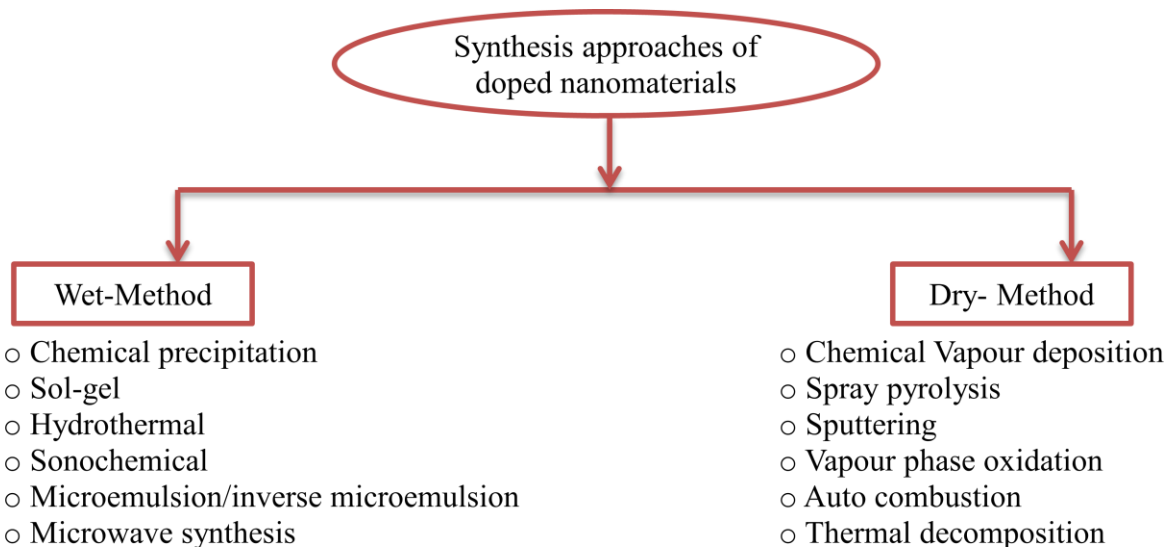
Scheme 2.2. Synthesis techniques of doped nanomaterials.

2.2.1 Chemical Precipitation Method

Chemical precipitation method is one easiest and most convenient wet chemical method for the synthesis of varieties of nanoparticles. This method is mainly consists of three steps, namely nucleation, growth, and agglomeration. In this method the water soluble salts react with each other to form insoluble salt and precipitated out from the reaction media. After the reaction in the liquid phase embryos are generated. Then the solid particle starts to form after crossing the critical radius (nucleus). In the growth step the embryos diffuses to the nuclei surface and finally the larger size particles are formed due to agglomeration. Chemical precipitation method has been used for the synthesis of Ba, Mn, Co, Cu, Yb doped ZnS; Mn, Cr, Fe, Ni, Ce, doped CdS; Ni doped CdSe; [256] Ag doped CdZnS; [257] Co, [258] Ni [259] doped ZnO; Co doped SnO_2; [260] Eu doped SiO_2; [261] Ni doped In_2O_3 [262] nanoparticles. Chemical precipitation method has some advantages over other synthesis method; such as the methods are simple, less time consuming, inexpensive, high yield process, size controllable, and un-agglomerated particles can be obtained.

2.2.2 Sol-gel Method

This process of nanoparticles synthesis is a two step process, (i) hydrolysis and (ii) polycondensation. Different metal oxide nanoparticles are synthesized using this method. Initially the metal salts (precursors) are hydrolyzed to form hydrated metal hydroxides in aqueous media, which are then formed as oxo bridge (-M-O-M-) through condensation and then sol is formed. Then a three dimentional network structured (gel) is formed with time,

which is then kept for aging. Then it is kept for drying to remove the liquid part. After the particle formation through this method heat treatment is required to improve the particle crystallinity. Sol-gel method has been used for the synthesis of different types of doped nanoparticles, such as Eu doped CdSe; [263] Zr, [264] Co, [265] Cu, [266] Ti, [267] Cd, [268] Fe, [269] V, [270] doped ZnO; Fe, Mn, Mg, Ag, Au, Pt, Cd, doped TiO_2; Ni, [271] Mn, [272] F, [273] Er [274] doped SnO_2; Ce doped SiO_2; [275] Fe doped Al_2O_3, [276] Eu doped $La_2Ti_2O_7$; [277] Eu doped $BaTiO_3$. [278]

2.2.3 Hydrothermal Method

Hydrothermal method is used mainly for the synthesis of hydrophilic nanoparticles at high temperature and pressure. In this method the reaction between the solids is more favourable because of the improved solubility of the solid in the reaction media. Hydrothermal method has been successfully used for the synthesis of Co-ZnS; Sn doped ZnO; [279] Fe, Co, Nb, Sm, Eu, Er, Nd, Ce doped TiO_2; Al doped SnO_2; [280] Co doped CeO_2; [281] Li doped $BaTiO_3$; [282] F doped $LiFePO_4$. [283] The advantages of this method are (i) size and shape controllable nanoparticles can be obtained and (ii) appropriate dopant concentration can be obtained. The disadvantage of the process is the impossibility of the nanocrystal growth processes. [284]

2.2.4 Microemulsion/Inverse Microemulsion Method

Microemulsion is basically oil-in-water (O/W) system and inverse microemulsion is water-in oil (W/O) system. This method of nanomaterials synthesis is attracted because of advantages, such as good size control and narrow particle size distribution can be obtained. This methods have been used for the synthesis of Mn-ZnS, Cu doped CeO_2, [285] Eu doped Y_2O_3, [286] Yb, Er co-doped CaF_2, [287] Nd doped BaF_2, [288] La doped $CoFe_2O_4$. [289] This method has some disadvantages such as complicated method, huge surfactants consuming, because of oil phase separation and purification is difficult.

Apart from these methods some other wet and dry methods are also there for the synthesis of doped nanomaterials, such as sonochemical, [290] microwave synthesis, [291] chemical vapour deposition, [292-294] auto combustion, [295-297] and thermal decomposition techniques. With the advantages of these methods some disadvantages are there, such as these methods are expensive, low purity of product, less size controlled, aggregation of the particles.

2.3 Different Shaped Doped Nanomaterials

Properties of the nanomaterials not only depend on the size of the material but also depend on the shape of the materials. Because of this reason apart from spherical type nanomaterials different shape nanomaterials, such as hexagonal, cubic, triangle, prism, rod, tube, wires, and needle like have also been synthesized. Here we have discussed about the different shape doped nanomaterials. From the literature it has been seen that different shape doped nanomaterials, such as doped- nanotube, [298-300] nanowires, [301-303] nanorod, [304,305] and bamboo [306] structured have been synthesized for advanced applications like logic circuits, radial junction thin film solar cells, nano-wire -based solar cells, nonenzymatic glucose biosensor, supercapacitors, and so on. Table 2.7 shows a list of different shape doped nanomaterials with their synthesize method and application areas.

Table 2.7. Different shaped doped nanomaterials with synthesis approaches and applications

Host	Doped	Synthesis method	Shape of the material	Properties	Ref
GaN	Cu	HWCVT	Wires	Magnetism	[307]
C	Ag	CCVD	Multiwall tube	Antibacterial	[308]
TiO_2	Ag	CCT	Film	Optical absorption	[309]
TiO_2	Fe	MHSM	Rod	Photocatalysis	[310]
TiO_2	P	hydrothermal	Tubes	Photocatalytic	[311]
TiO_2	Ni	Spin-coating	Thin films	Photoluminescence	[312]
SiO_2	Ag	Sol-gel	Thin film	Optical absorption	[314]
SiO_2	NiO	Sol-gel	Thin films	Gas sensing	[315]
TiO_2, SiO_2	Au	SCT	Thin films	Optical	[316]
CeO_2	Fe	Co-precipitation	Rod	Synthesis	[317]
BN	Si	CAP	Bamboo type	Morphologies & structures	[306]
ZnO	Cr	Solvothermal	Rod	Gas sensing	[318]
ZnO	Cr	Solvothermal	Wires	Photocatalysis	[319]
ZnO	Al, Ga, In, Ag	Sol-gel	Thin films	Optical & electrical	[320]
ZnO	Co	SSGM	Films	Photoluminescence	[321]

ZnO	Co	MCBDT	Rods	Optical absorption	322
CdO	Ni	SGSC	Thin films	Optical	323
C	N	MPCVD	Tubes	IR studies	324
NaGdF$_4$	Gd, Yb, Er, Tm, Ho	Hydrothermal	Rod	Up-conversion emissions & magnetic	325

Hot-wall chemical vapor transport (HWCVT) system, catalytic chemical vapour deposition (CCVD), colloidal crystal as template (CCT), 4-hydroxy-2,2,6,6-tetramet hylpiperidinyloxy [C$_9$H$_{18}$NO$_2$], tetraethyl orthosilicate (TEOS), boron nitride (BN), catalyst -assisted pyrolysis (CAP), boron-containing polymeric precursor (BCPP), Microwave Plasma Chemical Vapor Deposition (MPCVD) technique, bis-(acetylacetonate)platinum(II) [Pt(acac)$_2$], titanium tetrai-sopropoxide (TTIP), tetraethyl orthosilicate (TEOS), modified hydrothermal & solvothermal method (MHSM), modified chemical bathdeposition technique (MCBDT), sol gel spin coating (SGSC), simple solution growth method (SSGM), spin-coating techniques (SCT).

Some case studies of different shaped doped nanomaterials are presented here. Silicon-doped boron nitride bamboo structure was synthesized via pyrolysis of a polymeric precursor. [306] The corresponding TEM, HRTEM and EDX spectra are shown in Figure 2.9. Two types silicon doped boron nitride bamboo structures are formed. Type I (Figure 2.9A) which consists of a hollow compartment, re-sembling the structure of bamboo with no encapsulated catalytic particles and type II (Figure 2.9B) in which the tip of every compartment contains an encapsulated catalytic particle. The EDX spectra conformes the presence of B, N and Si.
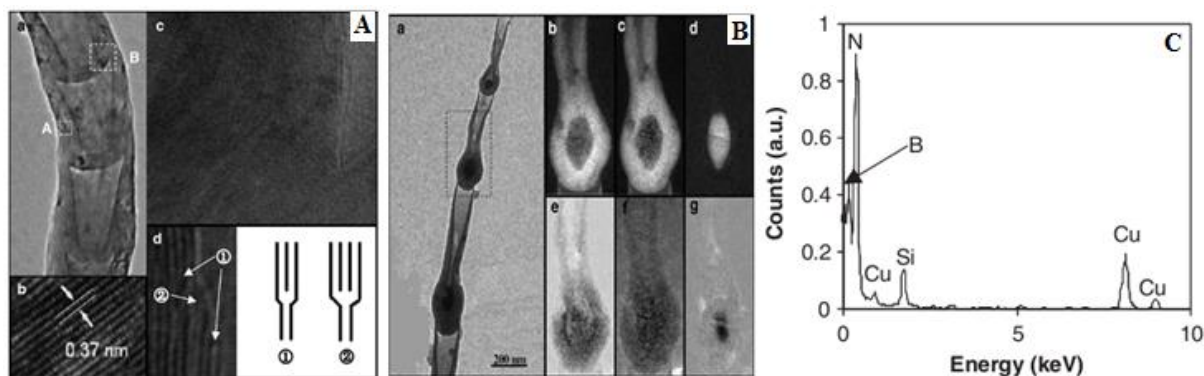
Figure 2.9. (A). (a) A TEM bright-field image of the type I boron nitride nanotube; (b) high-resolution micrograph recorded from area marked A in (a); (c) HRTEM image recorded from area marked B in (a) and (d) enlarged HRTEM image of the joining area between side wall

and tip, showing edge dislocations containing one and two half atomic planes, as indicated by ① and ②, respectively. (B) (a) A transmission electron microscopy bright-field image of the type II boron nitride nanotube; and (b–g) elemental distribution maps of N, B, Fe, Si, C and O, respectively. (C) energy dispersive X-ray spectroscopy spectrum of the nanotube showing that the tube consists of boron, nitrogen and silicon. [306]

Nitrogen doped carbon nanotube (NCNTs) was synthesized using melamine as a C/N precursor. [317] The TEM image of the synthesized products from detonation of the 2,4,6-trinitrophenol-C_6H_{12} (TNP-C_6H_{12}) mixture is shown in Figure 2.10a. Figure 2.10b and 2.10c show TEM and HRTEM image of the nanotubes obtained from the TNP-melamine mixture and the inset in Figure 2.10b presents a typical closed tube end with a hollow core. The raman spectrum of the tubes obtained from the TNP-melamine mixture is shown in Figure 2.10d. Here the strong G-band indicates a graphitic structure and the D-band suggests the presence of structural defects.
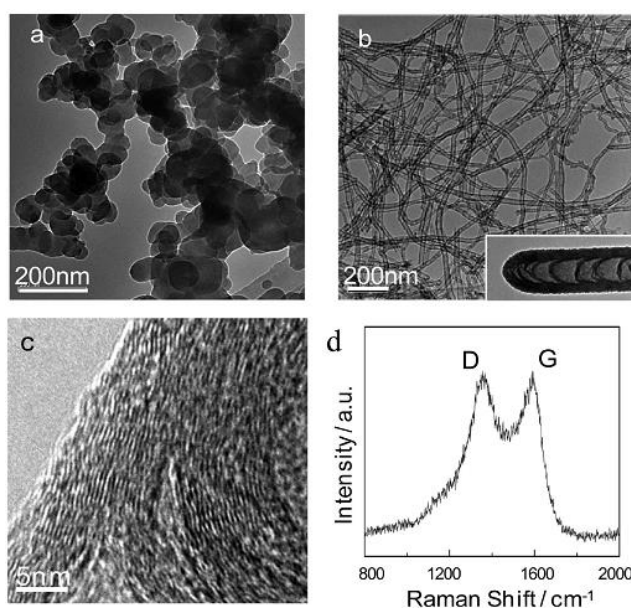
Figure 2.10. (a) TEM image of the products obtained from detonation of the TNP-C_6H_{12} mixture. (b) TEM and (c) HRTEM of the tubes obtained from the TNP-melamine mixture. Inset of panel b shows a typical closed tube end with a hollow core. (d) Raman spectrum of the tubes obtained from the TNP-melamine mixture. [317]

The morphology of the NCNTs produced from melamine was bamboo-like, which is due to rich nitrogen atoms were incorporated into the carbon networks, which is shown in Figure 2.11a. Elemental mapping along the bamboo-like tubules is shown in Figure 2.11b,

where the nitrogen atoms are relatively rare at the straight sections and instead concentrated at the curved joints between different compartments. The X-ray photoelectron spectrum (XPS) of the nanotubes in Figure 2.11c shows a strong signal relative to N1s photoelectron excitation peak, corresponding to an atomic percent of 19.88%. High-resolution N1s XPS spectrum of the N-doped tubes is presented in Figure 2.11d, which is broad and asymmetric, indicating different binding configurations.
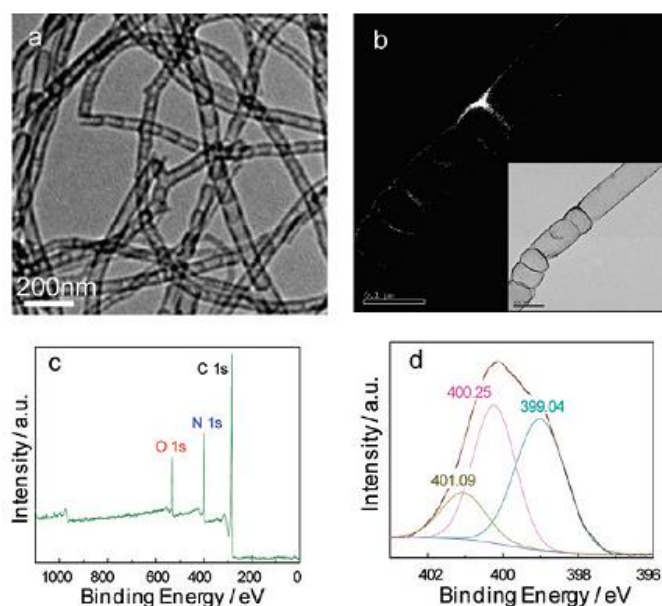
Figure 2.11. NCNTs produced from melamine: (a) bamboo-like morphology of the tubes; (b) N-mapping of the individual tube shown in the inset; (c) survey XPS spectrum; (d) high-resolution N1s XPS spectrum. [317]

Ag NPs anchored N-doped carbon nanotubes was synthesized using a chemical route synthesis method. [326] The TEM image and EDX in Figure 2.12 confirms the tube like structure with the presence of Ag. The SEM and STEM image of this sample both in dark and bright field in Figure 2.13 shows the coating of mono disperse Ag NPs, having diameter 5-10 nm, on the multiwall nanotube is more uniform in N-doped nanotubes than that of undoped nanotube. And there is no uniformity in coating of undoped multiwall nanotube with Ag cluster, having the diameter 10-20nm, which has a tendency to agglomerate with each other, which might be due to the lack of reactivity.
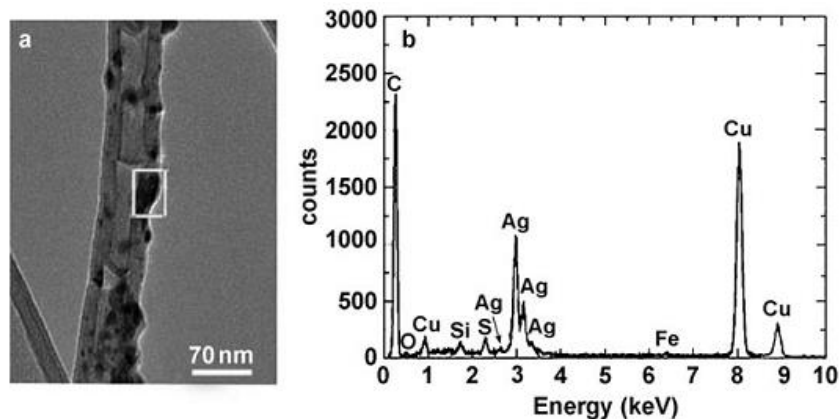
Figure 2.12. a) TEM image of a CNx MWNT decorated with Ag NPs, EDX spectrum of the region shown in (a). [326]
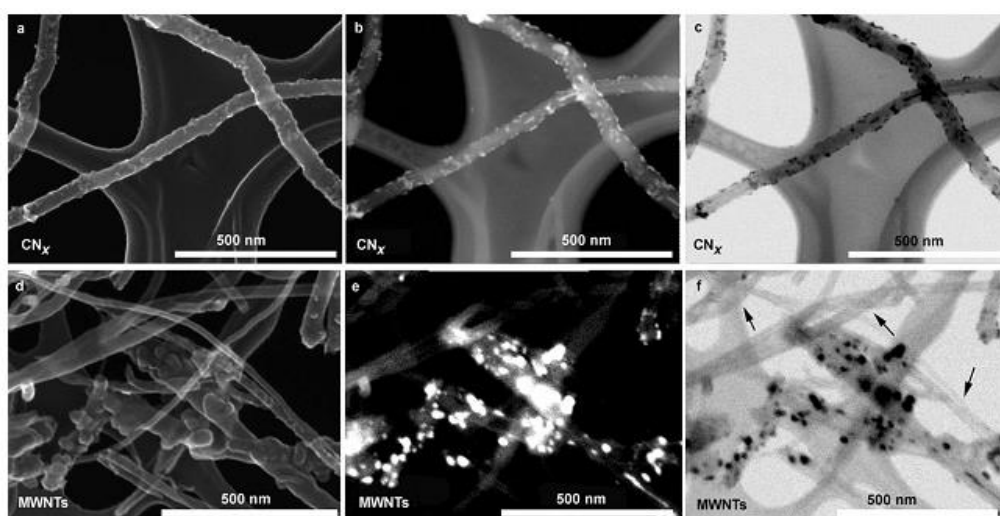
Figure 2.13. SEM and STEM images (bright- and dark-field) of carbon nanotubes decorated with Ag-NPs. The first row (a–c) corresponds to CNx MWNTs and the second row (d–f) depicts MWCNTs. Images (b) and (e) correspond to the dark-field images of (a) and (d), respectively. Bright-field (using the transmission mode) images are depicted in (c) and (f). Arrows in (f) indicate that various undoped MWNTs do not show any Ag NPs on their surface. This also demonstrates that MWNTs are not capable of uniformly anchoring Ag NPs. [326]

2.4   Applications of Doped Nanomaterials

Doping to nanomaterials reduces the bandgap of the material and creates an intermediate energy state in the energy level of the materials. Reduction of band gap helps the material for the applications as the photocatalysis under the visible light irradiation. The intermediate energy state in the material helps to control the emission properties of the base material. Doped nanomaterials have the potential applications in different areas, such as

photocatalysis, [327,328] solar cell, [329-331] fuel cell, [332-334] light emitting diodes, [335-337] laser, [338] and rechargeable batteries. [339,340] Here some important applications of the doped nanomaterials are discussed in details.

2.4.1 Photocatalytic Degradation of Organic Compounds

Environmental pollution because of organic pollutants is a major environmental problem today. Different classes of organic compounds, such as dyes, pharmaceutical products, aromatics, volatile organic compounds, etc are responsible for the water, soil, and air pollution. Presence of these organics in water causes serious problems to aquatic life as well as human beings. Therefore removal of these organics from the environment is very necessary. The sources of these organic compounds, their toxic effect to the environment, and the conventional methods available for the degradation of these compounds are discussed here in details.

2.4.1.1 Degradation of Pharmaceutical Products

Pharmaceutical compound is one important class of toxic organic pollutants, which causes mainly soil and water pollution. Some specific classes of pharmaceutical compounds, such as antibiotics, antipyretic, etc are used in huge quantity and the excess quantity are discharged to the environment. Some classes of antibiotics, such as nitroimidazole (metronidazole, ronidazole, tinidazole), fluoroquinolones (ciprofloxacin), are widely used in human and veterinary medicine. Like different pharmaceutical compounds these antibiotics are not completely metabolized in the body and released to the environment. The major sources of the pharmaceutical contaminants are the sewage treatment plant of pharmaceutical industries and the municipal waste water. The presence of pharmaceutical products, for instance antibiotics in the environment, even at low concentrations, causes the growth of antibiotic-resistant bacteria [341,342] and creates microbial population, [343,344] which may cause of ineffectiveness of the present forms of treatment and major epidemics. For this reason complete removal of this kinds of organics from the environment is very necessary. Some conventional method, such as advanced oxidation processes (AOP), namely electrochemical oxidation, ultra sound radiation, ozonation, are already been used for the degradation of these pharmaceutical compounds. Complete removal of antibiotics from the environment by conventional method is still difficult because of the low degradability efficiency of the methods and high solubility of the antibiotics in water.

2.4.1.2 Degradation of Dyes

Dye contamination is another critical environmental problem and addressed by several researchers till now. The sources of synthetic dyes in wastewater are from different industries such as, textile, dye and dye intermediates, paper and pulp, printing, colour photography, petroleum industries, and so on. [345,346] In the textiles dyeing processes a wide variety of synthetic dyes such as, azo, polymeric, anthraquinone, triphenyl-methane, and heterocyclic dyes are used. In most of the textile dying process, almost 15% of synthetic dyes are unutilized, which are released into the waste water stream. [347,348] Continuous discharge of dye-bearing effluents from these industries into natural stream and rivers poses severe environmental problems as toxic to useful microorganisms, aquatic life, and human beings. So, suitable and efficient techniques are highly essential for the treatment of these industrial effluents. Different physical, chemical, and biological methods have been developed for the removal of dyes from the waste water. However complete removal of the dyes from the water by these conventional methods is difficult because some drawbacks, such as low degradation efficiency, high cost method, and complex structure of some organic compounds. Nanoparticles based dye degradation are attracted over the last few years because of their complete removal efficiency of organics from the contaminated water. These methods are easy, low cost, less time consuming, and environmentally friendly. [349-352]

2.4.1.3 Degradation of Aromatic Compounds

Different classes of aromatics, such as benzo compounds, phenolic compounds, naphthalene, trinitrotoluene, etc are responsible for the environmental pollution. The benzo compounds such as nitrobenzene are highly toxic organic compound mainly used for the production of aniline, paper and pulp, pesticides, dyes, explosives, cosmetics, pharmaceuticals, and so on. [353–355] The long term exposure of nitrobenzene to the environment, even at low concentration, causes risks to human, such as liver or kidney damage, lung irritation, increase heart rate, skin problem, vomiting, etc. Therefore, removal of nitrobenzene from the environment is a major concern. Degradation of nitrobenzene in effluent water is difficult by conventional chemical method because of the nitro group which has strong electron withdrawing property and inhibits its oxidation, or by biological method because of its toxic and mutagenic effect on the biological systems. [356,357]

Over the last few decades semiconductor nanomaterials have attracted a lot as the photocatalyst for the degradation of organic pollutants in the contaminated water. The main objective of the process is to convert the toxic compounds to the non-toxic or usefull products. Efficient photocatalyst should have some specific characteristics, such as high surface area, visible light active, more electron and hole generator, low recombination rate, reusability, and so on. Among different semiconductor nanomaterials, TiO_2, CdS, ZnS are generally recognized as the photocatalyst because of their strong oxidizing power, low cost, chemical stability, and low cost. Pure semiconductor nanomaterials have the electron hole recombination problem and are active mainly under UV-light irradiation because of high band gap. Since only a small fraction (3-5%) of solar light corresponds to UV region, so, it is expected that merely 3-5% of whole radiant solar energy is use full for the photocatalysis purposes. For this reason For a particular photocatalyst dopant helps to gain those specific properties, for instances doping can change the band gap of the host material and as a result the photo catalytic activity of the host material will enhance due to the presence of more photo generated electrons and holes. Doping of noble metal, such as silver to TiO_2 improves the anatase crystallinity, surface area, lowering the band gap and makes the TiO_2 as an environmentally sustainable efficient photocatalyst for the degradation of persistent organic pollutants. [135,328] Doping of samarium ions to TiO_2 improves the specific surface area, separation efficiency of electron-hole pairs and prevents the recombination tendency of the photoinduced electron and holes, as results the overall photocatalytic activity for methylene blue degradation of TiO_2 improves significantly. [166] Fe doping to TiO_2 helps to obtained high specific surface areas, small crystal sizes, mesoporous structure, as well as a large amount of surface adsorbed water and hydroxyl groups, which contribute to their high photocatalytic activity for the degradation of XRG dye. [358] Fluorine doping to TiO_2 powders enhances the surface acidity, creation of oxygen vacancies, an increase of active sites, and finally the Vis-light photocatalytic activity of TiO_2 powders has been achieved. [35] Doping of other materials, such as Sn, [359] Si, [38] and F–B–S tri-doping [360] to TiO_2 nanoparticles promote the UV-induced photodecomposition activities of TiO_2, visible light photocatalytic activity, much larger specific surface area, relatively shorter duration of photocatalytic cleaning reactions, inhibiting the recombination of photogenerated electrons and holes, and so on. Apart from TiO_2, other photocatalyst such as ZnO, CdS and ZnS, Nb_2O_3 and others have been studied in presence of different doping element for improving their photocatalytic performances. [93,327,361]

2.4.2 Antifungal Agent

Wastage of crops because of fungal infection and diseases is a major global problem in agricultural farming. The fungal phytopathogens affect on the plants and crops both and rotting the crops, as a results farmers do not get proper value. For agricultural based countries this is a big problem. Some potent fungal phytopathogens, such as *Fusarium solani* is responsible for wilt disease to potato, tomato etc; *Venturia inaquaelis* is responsible for apple scab disease. [362] Antimicrobial agents kill or inhibit the growth of the microorganisms. To protect crops from such type of phytopathhogens different types of Pesticides embrace insecticides, herbicides, and fungicides chemical base pesticides are used. But these types of chemical pesticides are highly toxic and cause not only health problems, but also responsible for air, water and soil pollution. Antimicrobial agents are not only used in farming, but also used in different industrial applications, such as food packaging, synthetic textiles, health care, cosmetics, sunscreen, and medicine production. Over the last few years researchers have tried to use nanoparticles as the antimicrobial agent against different types of potent phytopathogens because of their suitable physical, chemical and biological properties over the chemical based pesticides. This approach is not only economic, but also environmentally friendly and green because of its nontoxic in nature. Some used nanoparticles as the antifungal/antibacterial agent with incubation time, temperature, and minimum inhibitory concentration (MIC) are listed in Table 2.8.

Table 2.8. List of different nanoparticles used as antifungal/antibacterial agent

Pathogenic Bacteria/Fungi	Nanoparticle used	Incubation	MIC	Ref
Candida albicans	ZnS	30°C, 48 h	300 µg/ml	[363]
Staphylococcus aureus *Escherichia coli*	ZnO	37°C, 24 h	0.08 g/L	[364]
Staphylococcus aureus	Cu	35°C, 24 h	3.75 µg/ml	[365]
Candida albicans	TiO_2/ZnO	37°C, 24 h	-	[366]
Candida albicans	TiO_2	37°C for 48 h	5.14 µg/ml	[367]
Candida albicans	Au	27°C, 24 h	250 µg/ml	[368]
Staphylococcus aureus	NFC/PPy-Ag	37°C, 24 h	-	[369]
S. mutans *S. gordonii*	BisBAL	37°C, overnight	5 µM	[370]

			10 µM	
Candida albicans			10 µM	
S. aureus, *E. Coli*	ZrO$_2$	37°C, 24 h		[371]
Candida spp.	Ag	37°C, 36 h	0.05 µg/ml	[372]

Minimum inhibitory concentration (MIC), bismuth dimercaptopropanol (BisBAL), nanofibrillated cellulose/polypyrrole-silver (NFC/PPy-Ag)

2.4.3 Molecular Sensor

Contamination of water because of different molecules, such as metal ions (As(III)/As(V), Hg^{2+}, Cr^{3+}), anions (F$^-$, Cl$^-$, Br$^-$, I$^-$), explosives (2,4,6-trinitrotoluene (TNT)), [373,374] drugs (paraceutamol, albendazole), [375,376] aromatics (nitrobenzene, phenol), [377] etc is major environmental problem. There is a permissible limit of each ion in water as per the World Health Organization (WHO). If the molecules are present in water above this permissible limit it will effect on the aquatic life as well as human beings. Water contamination because of some metal ions (As(III/V)) and anions (F$^-$) are becoming a serious environmental issue in recent years because of their dangerous effect on the environment above the permissible limit in water. For this reason detection of these kinds of molecules in water before use is very necessary.

2.4.3.1 Detection of Metal Ions

Detection of metal ions, such as As(III/V), [378] Cr(VI), Hg^{2+}, [379-381] Cu^{2+}, [382-384] Fe^{2+}, [385] Fe^{3+}, [386] Zn^{2+}, [387] Al^{3+}, [388] etc in drinking water are important because of their serious environmental and health concern. The permissible limit of different metal ions in drinking water are discussed in details by Kumar et al. [389] Concentration of these ions in drinking water above the permissible limit can cause several environmental and health problems. For this reason detection of these metal ions in drinking water is essential. Amoung different metal ion in water arsenic is considered as the most unsafe elements because of the high level toxicity of arsenic to human health. According to WHO the permissible limit of arsenic in drinking water should be 0.01 – 0.05 mg/L. [390] Contamination of arsenic in drinking water above the permissible limit causes skin diseases, respiratory problem, lungs, and even it can also lead to cancer in skin, lungs, liver, and kidney. [391,392] For this reason very low level detection of arsenic in drinking water is very essential. Various analytical methods have been developed for this purpose, such as atomic absorption spectroscopy (AAS), [393] hydride generation atomic absorption spectrometry (HG-AAS), [394] polarographic technique, [395]

inductively coupled plasma (ICP), [396] ICP atomic emission spectrometry (ICP-AES), ICP mass spectrometry (ICP-MS), [397] high performance liquid chromatography (HPLC) with optical spectrometric detection, [398] and voltammetry study. [399,400] But these methods are costly, complicated in nature, selectivity problem, and lagging of low level and accuracy of the detection. As an alternative nanoparticle based fluorometric detection of arsenic becomes in research interest recently. Nanoparticles based fluorescence sensing of arsenic is easy, less time consuming, and low cost method. [379,402-404]

2.4.3.2 Detection of Anions

Different anions species, such as F^-, cyanide, Cl^-, I^-, SO_4^{2-}, NO_3^-, CO_3^{2-} play a major role in a broad range of applications in chemical, biological, and medical processes. Amoung different anions fluoride is considered as one important anion species because of its physical and chemical important. Fluoride is the smallest anions and having some unique properties, such as high charge density, high electronegativity, and high polarizing ability. [405-407] Because of this fluoride ions have important role in biological systems. Fluoride ions are widely used as additives in toothpaste for protecting the dental health and as pharmaceutical agents to treat dental cavities, [408] osteoporosis. [409,410] It is added in the drinking water to maintain the optimum level of the fluoride ion in the human body. [411] Fluoride is also used for manufacturing nuclear weapons. [412,413] In addition, the increasing number of industries on fluorine products is causing the fluorine contamination in the environment. However, high concentration of fluoride may cause fluorosis, [414,415] urolithiasis, [416] kidney failure, [417] cancer, [418] and even leading to death. The maximum permissible limit of fluoride ion in drinking water is 1.5 mg/L according to World Health Organization (WHO). [419] For this reason qualitative and quantitative detection of fluoride ions in drinking water is essential. Some available methods are there to detect the fluoride ions in water, such as desilylation, [420-422] fluoride-hydrogen bonding, [423,424] boron-fluoride complexation, [405,426] colorimetric changes, [427-429] fluorescence quenching, [430] and fluorescence enhancing. [419,421,432,433] However, fluorescence based fluoride anion sensing method is important because of its low cost, simplicity, sensitivity, and high selectivity towards the anion species.

2.5   Concluding Remarks

Some important semiconductor materials, such as chalcoganides (CdS, ZnS, CdSe, ZnSe), oxides (TiO$_2$, ZnO) have been studied extensively because of their wide ranges of applications in photocatalysis, solar cells, antimicrobial agents, bio-imaging, hydrogen gas generation, and sensors. The performances of these semiconductor NPs in suitable

applications such as photocatalysis under visible light, antimicrobial activity, photoluminescence behaviour, and molecular sensors can be further improved by tuning of band gap and recombination of electron hole pair. These modifications are done in the presence of different element as doping, such as transition metals (Fe, P, Mn, Mg, Cr, Ni, Co, Cu, Al, Ag, Pt, Au), lanthanides (Ce, Yb, Er, Eu, Nd, Sm, Pr), non metals (S, N, P, F), metalloids (Sb, Si, As, Ge). From the photocatalytic perspective doping to TiO_2, CdS, ZnS NPs helps to reduce their original band gap, which in turn, makes the photocatalyst active under visible light exposure. The visible light induced photocatalyst makes the industrial process economic and green. As a photoluminescence activator doping provides an intermediate energy state within the band gap of a base material, which subsequently alters the wavelength of emission and the photophysical relaxation processes of the carriers in the host material. The tuning of the intermediate state can also help to control the emission wavelength within the visible and IR regions. The tuning fluorescence emission properties of these materials make them suitable for the advanced applications, such as fluorometric sensors, upconversion fluorescence material, and bio-imaging. Apart from single NPs, doping to core/shell NPs have been studied recent years because of their outstanding properties, such as up-conversion emission, high and tunable photocatalytic activity, and ferromagnetism etc. Doped hollow NPs have also equally attracted recently because of their new and improved properties over the hollow NPs itself, such as higher quantum yield, high saturation magnetization, higher adsorption capacity, high catalytic activity, and so on. Applications of these nanomaterials are very important in organic compound degradation as photocatalysis, antimicrobial agent, and sensing of toxic ions in water.

2.6 Objectives

The specific objectives of the project are:

o   To study the effect of Ag doping on the properties of some selective semiconductor nanoparticles, such as TiO_2, CdS, ZnS, etc.

o   To see the effect of Ag doping on solid, hollow, core/shell, and bi-layer hollow structures for photocatalytic and toxic ion detections applications.

o   To study the effect of Ag doping on TiO_2 as a green pesticide against phytopathogens for agricultural applications.

Synthesis and Characterization of Ag Doped TiO$_2$, CdS, and ZnS Nanoparticles for the Photocatalytic Degradation of Metronidazole Antibiotic and Methylene Blue Dye Under Visible Light

3.1 Introduction

The presence of pharmaceutical components in the surface and groundwater is a growing environmental concern in recent years. Different classes of numerous pharmaceutical compounds have been shown to pass through sewage treatment plants (STPs) of industry and municipality, which in turn contaminate the aquatic environment. [434,435] In general, pharmaceutical compounds present in industrial wastewater are difficult to degrade because of their complicated structure. The commonly used antibiotics in health care such as penicillin, metronidazole, streptomycin, chloramphenicol, chlortetracycline, neomycin, erythromycin, ciprofloxacin, and so on, are contaminating surface as well as groundwater. Their main sources are discharged of pharmaceutical sewage treatment plants (STPs) and municipal waste water. [436-438] Veterinary antibiotics, which are used for animal husbandry for growth promotion and therapeutic use, have become a serious concern for the environment. [439,440] The presence of antibiotics in the environment, even at low concentrations, causes the growth of antibiotic-resistant bacteria [341,342,442] and creates microbial population, [443,343,344] which may cause of ineffectiveness of the present forms of treatment and major epidemics. As the consumption of antibiotics gradually increases, development of the new technique for the treatment of antibiotics in wastewater is highly essential. Metronidazole (MTZ), a nitroimidazole based antibiotic, is primarily used for the infectious diseases caused by anaerobic bacteria and protozoa (such as giardia infections, amebic liver abscess, amoebic dysentery, bacterial vaginosis, carriers of trichomonas and trichomonas vaginal infections, and so on). It is soluble in water, not easily-biodegradable, [444] highly mobile, and weakly adsorbed on soil. [445] Elimination of MTZ from the effluent of the waste water treatment plant before discharging become a significant issues as it is potentially carcinogenic and mutagenic in nature. [446]

Different technologies were reported to degrade MTZ present in drinking and industrial waste water such as ultraviolet (UV) irradiation, [447] Oxidation processes using UV, UV/H_2O_2, H_2O_2/Fe^{2+}, and UV/H_2O_2/Fe^{2+}, [448] etc. In general these processes are expensive and complicated. [449] Biodegradation of antibiotics by Closed Bottle Test (CBT) is another method to degrade antibiotics; however, most of the antibiotics have below 60% degradation efficiency even after 28 days of incubation time, and MTZ has only 25.6% degradation. [450] Biodegradability test was also conducted by another research groups for the degradation of metronidazole antibiotic and they also concluded the lag of biodegradation of metronidazole. [451.452] As an alternate route to microbial degradation, solar simulator was used for the degradation of MTZ residues in naturals waters. [453] Apart from these methods catalytic

photodegradation of MTZ (10 mg/L) using micron sized Zn_2GeO_4 hollow sphere (1g/L) under UV light irradiation was also reported. [454] The $ZnSnO_3$ hollow nanospheres/reduced graphene oxide (RGO) hybrid nanocomposite (1 g/L) was also used as a photocatalyst for the degradation of metronidazole solution (5 mg/L), where they found only 72.5% degradation after 3h of visible light irradiation. [455] The metal nanoparticles prepared from pickling waste water liquor was employed for the degradation of MTZ under nitrogen flow, and the degradation efficiency was pH dependent. [456] From the background literature, it has been found there are limited studies available on MTZ antibiotic degradation, so visible light induced photocatalytic degradation of antibiotics is a promising task.

Apart from pharmaceutical components, water pollution because of another organic contaminants is also become a major global problem in recent years. The major sources of organic contaminated water are from industrial effluents. Among several organic pollutants present in the industrial wastewater, dye contamination is a critical environmental problem. The sources of synthetic dyes in wastewater are from different industries such as, textile, dye and dye intermediates, paper and pulp, printing, colour photography, petroleum industries, and so on. [457-459,345] In the textiles dyeing processes a wide variety of synthetic dyes such as, azo, polymeric, anthraquinone, triphenyl-methane, and heterocyclic dyes are used. In most of the textile dying process, almost 15% of synthetic dyes are unutilized, which are released into the waste water stream. [347,348] Similarly, other industries also release the significant amount of dyes through the effluent water. Continuous discharge of dye-bearing effluents from textile industries into natural stream and rivers poses severe environmental problems as it is toxic to microorganisms, aquatic life, and human beings. [460] Moreover, synthetic dyes can also hinder penetration of sunlight through the water, leading to the eutrophication and the die-off of plants and animals. [461] Since the significant amounts of dyes are present in the effluent stream in the soluble form, suitable and efficient techniques are highly essential for the treatment of these industrial effluents.

Different physical, biological, and chemical methods, such as, adsorption, biodegradation, [462,463] chlorination, ozonation [464] are frequently been used for the removal of different organic pollutants. However, semiconductor-based nano-photocatalyst for the degradation of dyes has been attracted considerable attention in the field of environmental remediation and solar energy utilization. During last few decades, heterogeneous photocatalysis using semiconductor nanomaterials is chosen as the advanced oxidation process for the removal of dye pollutants from the waste water. [465] Doped nanoparticles such as Fe-TiO_2, [349] Sm-TiO_2, [466] and Ce-, Cu-, Mn-, Sn-TiO_2 [350] were also reported as the

photocatalyst for the degradation of methylene blue dye under the UV light irradiation. Visible light active doped photocatalysts such as C-TiO_2, [467] Fe-CdS, [468] Cu-ZnS, [351] N-, S-TiO_2, [469,352] and Mn-, Ni-, Cu-ZnS [470] were also shown to be very efficient. Some other visible light active catalysts such as Pt-TiO_2, [471] Si-, Fe-TiO_2, [472] and $NaYF_4$:Yb-,Tm-TiO_2 [473] were employed for MB degradation where the catalyst dose was maintained at 1.0 g/l, and the initial dye concentration was 10, 20 and 15 mg/l, respectively. In recent years, the visible light induced photodegradation of dyes using nanoparticles are drawing more research interest to make the process more effective, green, and economical. Most of these researches are focused on the enhancement of photocatalytic efficiency by using different doped nanoparticles, mesoporous high surface area materials, etc.

The objective of this study was to develop an efficient pathway for the degradation of metronidazole antibiotic. Some semiconductor nanoparticles, such as TiO_2, CdS, and ZnS as the photocatalyst were introduced for the degradation of metronidazole (MTZ) and methylene blue dye (MBD) in visible light irradiation. These particles were modified by silver doping to enhance their catalytic efficiency. Studies were conducted with low catalyst dosing and the high initial metronidazole concentration compared to the studies reported till now. The basic mechanism of doping and the photocatalytic process was explained in details. Kinetic study was performed to measure the degradation rate constant of the MTZ and MBD solutions. The optimum doping percentage was identified for getting maximum catalytic efficiency of these nanoparticles. The reusability of these catalysts was also checked by cyclic degradation test. To our knowledge this is the first study, where three semiconductor nanoparticles in its pure and silver doping condition, were employed in one time for degrading MTZ and MBD solution in visible light.

3.2   Materials and Methods

3.2.1   Chemicals and Materials

Reagent-grade silver nitrate (99.9%) was purchased from Rankem. Anionic surfactant sodium dodecylbenzene sulphonate (SDBS) (technical grade, Cat No. 28995-7) and titanium (IV) butoxide (Ti[O(CH_2)$_3CH_4$]$_4$) (TBOT) (97%) were obtained from Sigma Aldrich. Zinc acetate, cadmium acetate, sodium sulphide, nitric acid (69% GR), and methylene blue dye were purchased from Merck. Metronidazole antibiotic was supplied by J B Chemicals Pvt. Ltd. All the chemicals were used as it was received without any further purification. Ultrapure water of 18.2 MΩ.cm resistivity and pH 6.4–6.5 were used for all experiments.

3.2.2 Synthesis of TiO₂ and Ag Doped TiO₂ Nanoparticles

Silver doped and pure TiO_2 nanoparticles were synthesized by the sol-gel method in aqueous SDBS media in the presence of acidic pH (pH = ~ 2, adjusted by HNO_3). A 0.5 mM TBOT concentration was used for synthesis of TiO_2, and for silver doping the $AgNO_3$ concentration was maintained at 0.5, 1.0, 1.25, and 2.0% of TBOT concentration. Henceforth these doped NPs are termed as 0.5-Ag-TiO₂, 1.0-Ag-TiO₂, 1.25-Ag-TiO₂ and 2.0-Ag-TiO₂. Finally, all these particles were separated by centrifugation at 25000 rpm for 20 min, washed thrice using ethanol-water (2:1 ratio) mixture and dried in a hot air oven at 60°C for overnight. The particles were then calcined at 450°C for 2 h to improve the crystallinity.

3.2.3 Synthesis of CdS and Ag Doped CdS Nanoparticles

Silver doped CdS nanoparticles were synthesized in SDBS media, where the equimolar concentration (0.5 mM) of both cadmium acetate and Na_2S were used. The $AgNO_3$ concentrations used were 1.0, 1.5, 1.75, and 3.0% of cadmium acetate concentration for different doping dose. The concentration of surfactant (SDBS) was maintained at 1.5 times of CMC of SDBS (1.8 mM). Initially, cadmium acetate was mixed with aqueous SDBS solution, followed by drop wise addition of freshly prepared Na_2S under constant stirring. The reaction was continued for about 45 min for complete formation of CdS NPs. During the whole reaction, the sample was irradiated using a 200 watts incandescent light bulb. The finally formed particles were then separated by centrifugation at 25000 rpm for 20 min, washed thrice using ethanol-water (2:1 ratio) mixture and dried in a hot air oven at 60°C for overnight. Depending on the $AgNO_3$ concentration the samples were denoted as 1.0-Ag-CdS, 1.5-Ag-CdS, 1.75-Ag-CdS and 3.0-Ag-CdS.

3.2.4 Synthesis of ZnS and Ag Doped ZnS Nanoparticles

Pure and silver doped ZnS nanoparticles were synthesized using the same procedure as was followed for synthesizing CdS. The $AgNO_3$ concentration was maintained at 1.0, 1.25, 1.5, and 2.0 % of zinc acetate concentration, and accordingly the samples were named as 1.0-Ag-ZnS, 1.25-Ag-ZnS, 1.5-Ag-ZnS and 2.0-Ag-ZnS.

3.2.5 Particle Characterization

The light absorbance properties of the nanoparticles were characterized by UV–Vis–NIR Spectroscopy (Shimadzu-3600). The crystallinity of synthesized particles was characterized using X-ray diffraction (XRD) (Philips, PW 1830 HT) with scanning rate of 0.01°/S in the 2θ range from 20° to 70°. Fourier transform infrared spectroscopy (FT-IR) was carried out using a FT-IR (Thermo Fisher Scientific, Nicolet iS10). The size and shape of the particles were observed under a transmission electron microscope (TEM) and high resolution-TEM (HR-

TEM) (FEI, Tecnai S-twin and JEOL, JEM 2100). The chemical composition of the samples and the valence states of various elements were analyzed by X-ray photoelectron spectroscopy (XPS) (PHI 5000 Versa Probe II scanning XPS microprobe, ULVAC-PHI, Inc.) employing a monochromatic Al Kα X-ray source (hν=1486.6 eV).

3.2.6   Photocatalytic Degradation

The photocatalytic activities of the synthesized nanoparticles were studied by the photo-degradation of MTZ and MBD in aqueous solution at 30°C and neutral pH. For MTZ degradation the initial concentration of the MTZ and catalyst dose was maintained to 15 mg/L and 0.5 g/L respectively. For MBD degradation the initial concentration of the MBD solution was 25 mg/L and the catalyst concentration was 0.25 g/L. The degradation studies were conducted in a photoreactor equipped with a 125 W high pressure mercury vapor lamp (λ=435.8 nm, light intensity 27000 LUX) placed about 12 cm above the solution under constant stirring. Prior to each test, the lamp was turned on and warmed up for about 10 min in order to get a constant light output. The samples were magnetically stirred for 20 min in the dark to allow physical adsorption equilibrium of MTZ on catalyst particles. Then the solution was exposed to visible light irradiation under constant stirring condition. The sample was then taken out and centrifuged to remove the nanoparticles after each 20 minutes interval for MTZ and 30 minutes interval for MBD. Then the concentration of the MTZ and MBD solution was analyzed using a UV-Vis-NIR Spectrophotometer at its maximum absorbance wavelength of λ=320 nm for MTZ and 661 nm for MBD.

3.3 Results and Discussion

3.3.1   Characterization of Pure and Ag Doped TiO_2 Nanoparticles

The optical absorption properties of pure and Ag doped TiO_2 nanoparticles were studied using UV-vis spectroscopy and the spectrum are presented in Figure 3.1a. It is noticed that the optical absorption edges of TiO_2 shifted toward the visible region in presence of Ag doping. With increasing the silver content there was a red shifting of the absorption peak for up to 1% of $AgNO_3$ concentration, then with increasing $AgNO_3$ concentration the absorption peak shifted from higher visible region to lower visible region. This shifting of the optical absorption peak originates from changing of the band gap energy of TiO_2 in presence of silver doping. The band gap energy was calculated using the equation $E_g = 1239.8/\lambda$, [474] where E_g is the band gap (eV) and λ is the wave length of the absorption edges in the UV–Vis spectrum. And the band gap is found to be 3.29, 2.88, 2.27, 2.64, and 3.05 eV for pure TiO_2,

0.5-Ag-TiO$_2$, 1.0-Ag-TiO$_2$, 1.25-Ag-TiO$_2$, and 2.0-Ag-TiO$_2$ nanoparticles, respectively. These results clearly indicate that in the presence of Ag doping the band gap reduces up to 1.0% of Ag doping and then it increases with further increasing the doping percentage. Point is also to be noted that the absorption intensity is high for Ag doped TiO$_2$ compared to pure TiO$_2$. Since the particle concentration of all the samples were same so, the possible reason may be due to the lowering the particle size in presence of Ag doping. The absorption intensity is maximum for 1.0-Ag-TiO$_2$ which is having lowest band gap energy. So, it can be concluded that 1% AgNO$_3$ concentration was the optimum value of silver precursor for getting maximum visible light absorption in Ag doped TiO$_2$ NPs. The crystallographic phases of pure and Ag doped TiO$_2$ nanoparticles were identified by X-ray diffraction (XRD) technique. The XRD spectra of pure TiO$_2$ (Figure 3.1b) shows the TiO$_2$ anatase peak at 2θ 25.1, 36.5, and 62.3°, corresponding to the planes (101), (103), and (204) (JCPDS card no.71-1169), and the rutile peaks (2θ) 27.3, 54.1, and 68.6°, corresponding to the planes (110), (211), and (301) (JCPDS card no.76-0319). For Ag doped TiO$_2$ nanoparticles (Figure 3.1c), the anatase peaks (2θ) were obtained at 25.35, 37.87, 48.12, 53.78 and 62.84°, corresponding to the planes (101), (004), (200), (105) and (204) (JCPDS card no. 84-1285). It was also found that the major anatase peak of (101) plane shifted from 25.1° to 25.35° after doping with silver and the rutile peak (2θ) 27.3° was found to be absent in case of Ag doped TiO$_2$. The shifting of the anatase peak and the phase change might be due to the doping of the Ag to TiO$_2$. Since, there is no separate peak of pure Ag, which indicates that the doping is achieved through substitution of principle reactant component of the host material. In general, the substitution doping is favourable when the ionic radii of two elements are comparable. The ionic radii of Ag^{2+}, Ag^{3+}, Ti^{4+}, and O^{2-} are 0.94, 0.74, 0.605, and 1.4 Å respectively. As the ionic radius of Ag^{3+} is closer to Ti^{4+} compared to O^{2-}, as a result, Ti^{4+} is substituted by Ag^{3+}. The nanoparticles were also examined by FTIR spectroscopy to check the functional groups present and the spectrum are shown in Figure 3.1d. For Ag doped TiO$_2$ the absorption peak at 3399 cm^{-1} is attributed to the O-H stretching vibration and its corresponding bending vibration occurs at 1629 cm^{-1} due to the hydroxyl groups of water molecules present, where as for pure TiO$_2$ the bending vibration occurs at 1618 cm^{-1}. The absorption peak at 2360 cm^{-1} for pure TiO$_2$ and 2389 cm^{-1} for Ag doped TiO$_2$ are due to the symmetric stretching vibration of the –OH group of absorbed water molecules. The broad absorption peaks in the range 400-1000 cm^{-1} for pure TiO$_2$ are the contribution of anatase phase Ti-O, but for Ag-doped TiO$_2$ one sharp peak obtained at 1053 cm^{-1}. In silver doped TiO$_2$ the peaks of the functional groups are shifting to higher wave numbers, which might be due to silver doping to TiO$_2$ molecules.
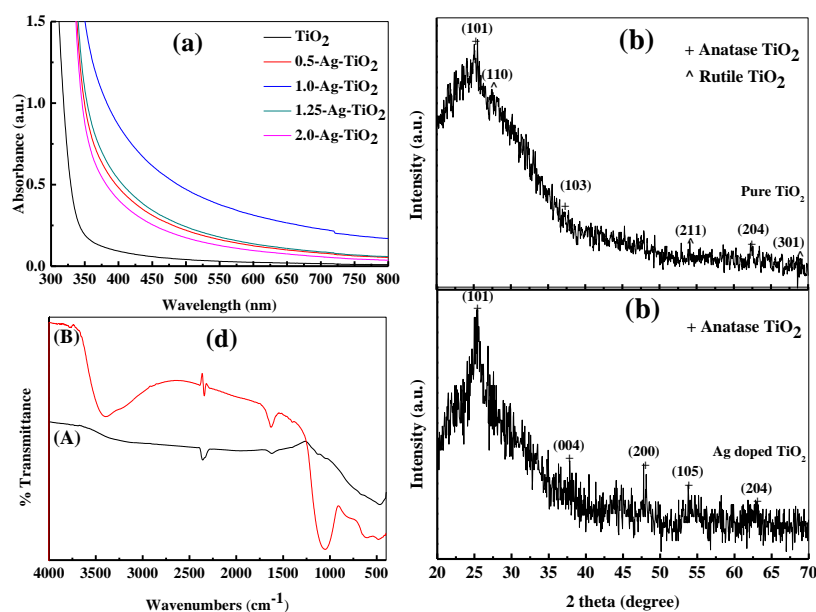
Figure 3.1. (a) UV –Vis spectra of as synthesized TiO_2, 0.5-Ag-TiO_2, 1.0-Ag-TiO_2, 1.25-Ag-TiO_2 and 2.0-Ag-TiO_2 nanoparticles. X-ray diffraction pattern of (b) pure TiO_2 and (c) 1.0-Ag-TiO_2 nanoparticles. (d) FTIR spectrum of (A) pure and (B) 1.0-Ag-TiO_2 nanoparticles.

The particles were further characterized by TEM to study the structure and morphology of the pure and silver doped TiO_2 nanoparticles. The TEM image of pure TiO_2 and 1.0-Ag-TiO_2 nanoparticles are presented in (a) and (b) parts of Figure 3.2. The spherical type particles are in the size range 33.39 ± 1.67 and 27.6 ± 2.08 nm for TiO_2 and 1.0-Ag-TiO_2 nanoparticles. There is a reduction of TiO_2 particle size in case of Ag doping; this is because of prevention of nucleation growth during formation of particles in presence doping. Figure 3.2c shows the HR-TEM image of the 1.0-Ag-TiO_2 nanoparticles, which shows the lattice fringes with spacing of TiO_2 is 0.67 nm.
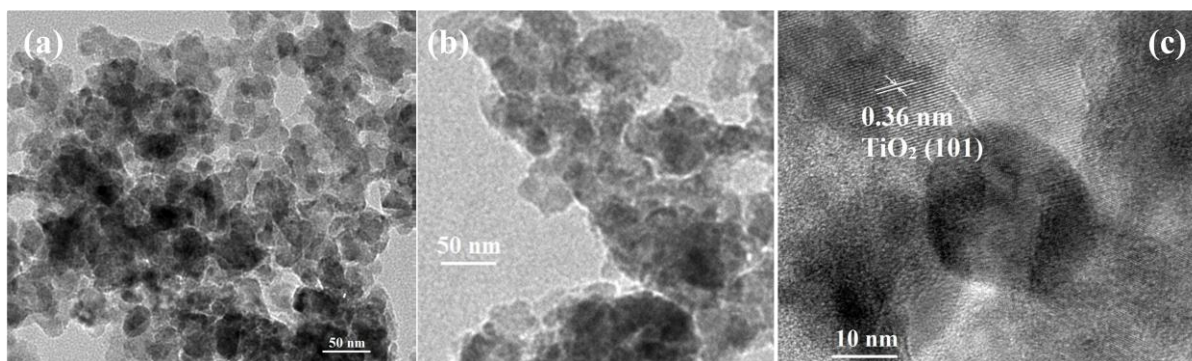
Figure 3.2. Transmission electron microscopic image of (a) pure TiO_2, (b) 1.0-Ag-TiO_2 nanoparticles. (c) HR-TEM image of 1.0-Ag-TiO_2 nanoparticles.

The surface composition and the chemical states of Ag doped TiO_2 nanoparticles were studied by XPS analysis. The high resolution XPS spectra Ti (2p) in Figure 3.3a indicates peak at 463.5 eV corresponds to Ti $2p_{1/2}$, and 457.625 eV corresponds to Ti$2p_{3/2}$. The slitting between Ti$2p_{1/2}$ and Ti $2p_{3/2}$ is 5.875 eV which indicates the normal state of Ti^{4+} in the mesoporous anatase TiO_2. [475] The XPS peak (Figure 3.3b) at ~530.875 eV corresponds to the lattice oxygen of TiO_2 crystal. Figure 3.3c shows the Ag $3d_{5/2}$ and Ag $3d_{3/2}$ peaks at the binding energy of 372.375 and 366.5 eV, respectively with a slitting of the 3d doublet of 5.875 eV, which suggest the ionic Ag instead of elemental Ag within the material. So, it is clear that there is neither elemental Ag deposition to the surface of the TiO_2 nor the Ag presence in the interstitial sites of the TiO_2. The only possibility of Ag doping is through the substitution of principle reactant of the TiO_2, which again confirmed the substitution doping of Ag to the TiO_2.
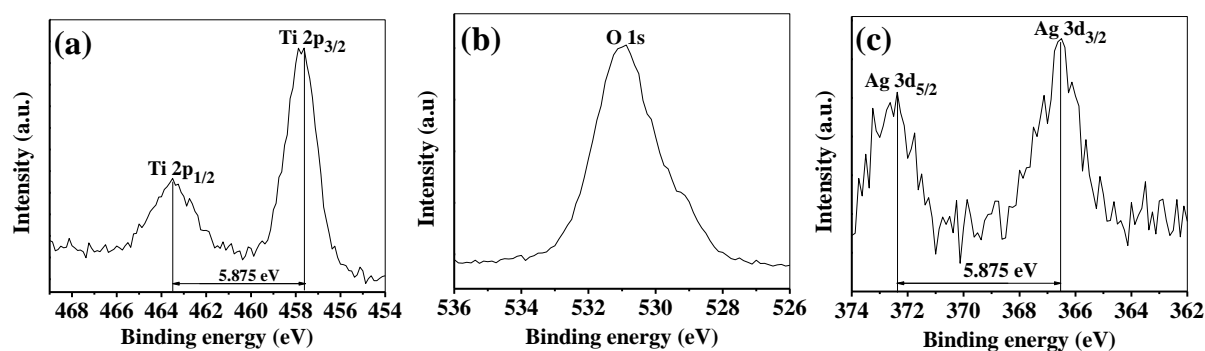
Figure 3.3. High resolution XPS narrow scan spectrum of (a) Ag(3d), (b) Ti(2p), and (c) O(1s) for 1.0-Ag-TiO_2 nanoparticles.

3.3.2 Characterization of Pure and Ag Doped CdS Nanoparticles

The optical properties of pure and Ag doped CdS nanoparticles were studied by UV-Vis-NIR spectroscopy and the spectras are presented in Figure 3.4a. It is seen that the maximum absorption occurs in the wavelength range of 475-200 nm and there is red shifting of the increasing absorption edges of CdS after Ag doping. The maximum red shifting of the absorption spectra occurs for 1.5% $AgNO_3$ concentration, then with the increasing $AgNO_3$ concentration the blue shifting of the absorption edges starts again. This shifting of the absorption edges is due to the change in band gap of the CdS in presence of Ag doping. The calculated band gaps are 2.48, 2.41, 2.2, 2.43, and 2.41 eV for CdS, 1-Ag-CdS, 1.5-Ag-CdS, 1.75-Ag-CdS, and 3-Ag-CdS nanoparticles. These results clearly indicate that there is reduction in band gap energy after doping with Ag and the lowest band gap was obtained in case of 1.5-Ag-CdS. The maximum absorption intensity was also obtained for 1.5-Ag-CdS

nanoparticles. Figure 3.4b shows the XRD spectra of pure CdS and 1.5-Ag-CdS nanoparticles. It shows the peaks at 2θ value of 26.69, 43.02, 52.13, 54.29, and 63.63° for CdS; and 27.02, 44.02, 52.47, 54.79, and 64.37° for Ag-CdS nanoparticles, corresponding to (111), (220), (311), (222), and (400) planes respectively, of the cubic structural phase of CdS (JCPDS card no.75-1546). Similar to the previous case, no peak of elemental silver is present here, which means there is no simple deposition of elemental Ag. But there is a shifting of XRD peaks of cubic CdS after doping with Ag, which might be because of the substitution of principle reactant by Ag. The ionic radius of Ag^{2+} (0.94 Å) is more comparable with Cd^{2+} (0.95 Å), but there is a significant difference with S^{2-} (1.84 Å). So, there is a fare possibility of substitution of Cd^{2+} by Ag^{2+}.
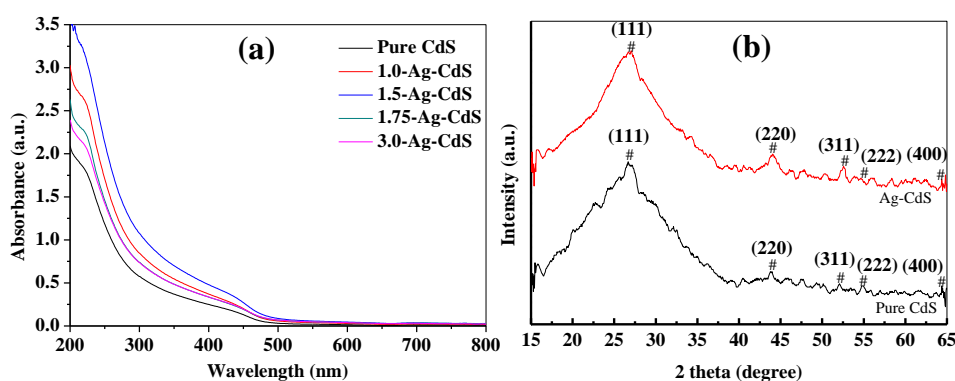
Figure 3.4. (a) UV –Vis-spectroscopy image of as synthesized pure CdS, 1.0-Ag-CdS, 1.5-Ag-CdS, 1.75-Ag-CdS and 3.0-Ag-CdS nanoparticles. (b) X-Ray diffraction patterns of pure CdS and 1.5-Ag-CdS nanoparticles.

The TEM images (Figure 3.5a,b) show the spherical type particles with size distribution in the range of 4.06 ± 0.63 and 3.44 ± 0.76 nm for pure CdS and 1.5-Ag-CdS nanoparticles, respectively. Figure 5c shows the HR-TEM image of 1.5-Ag-CdS nanoparticles, which clearly indicates the lattice fringes with spacing of CdS is 0.33 nm and confirms the crystallinity nature of the CdS NPs. The inset Figure 3.5c presents the selected area electron diffraction (SAED) pattern of this particle obtained by focusing the electron beam on individual nanoparticles; the ring like diffraction pattern again confirms the crystalline nature of 1.5-Ag-CdS NPs. The particle composition was also studied by energy-dispersive X-ray (EDX) study and the spectra in Figure 3.5d confirm the presence of Ag with Cd and S.
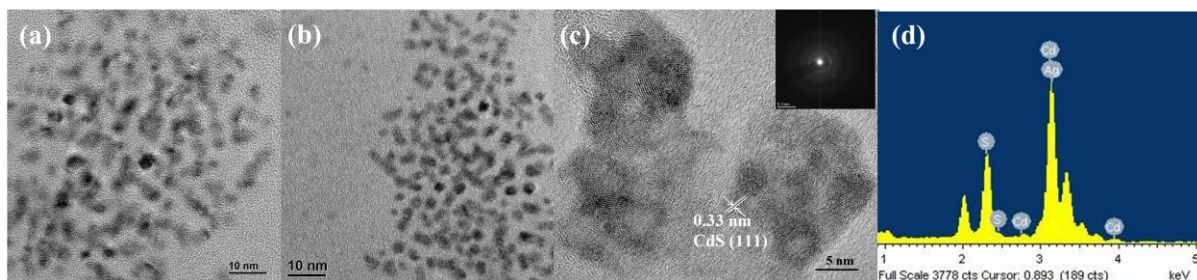
Figure 3.5. Transmission electron microscopic (TEM) images of (a) pure CdS and (b) 1.5-Ag-CdS nanoparticles; (c) High resolution TEM image and (d) EDX pattern of 1.5-Ag-CdS nanoparticles. The inset shows the SAED pattern of 1.5-Ag-CdS nanoparticles.

3.3.3 Characterization of pure and Ag doped ZnS Nanoparticles

The UV-Vis absorption spectra of pure and Ag doped ZnS is presented in Figure 3.6a. The intensive absorption was in the UV region and there is red shifting of the absorption peak in presence of Ag doping to ZnS nanoparticles. The absorption intensity increased in the visible region after doping of Ag to ZnS and it is maximum for 1.25-Ag-ZnS nanoparticles. The obtained band gaps are 3.75, 3.61, .3.2, 3.44, and 3.51 eV for ZnS, 1.0-Ag-ZnS, 1.25-Ag-ZnS, 1.5-Ag-ZnS, and 2.0-Ag-ZnS nanoparticles. The XRD pattern in Figure 3.6b shows the peak at 2θ value of 28.91, 33.43, 48.27, 56.53, and 59.65° for pure ZnS and 28.97, 33.56, 48.2, 57.17, and 59.73° for 1.25-Ag-ZnS nanoparticles. The peaks have been identified corresponding to the plane (111), (200), (220), (311) and (222), respectively, of the cubic structural phase of ZnS (JPCDS card no.80-0020). Similar to the previous two cases, here no peak of elemental silver is obtained. The ionic radii of Ag^{2+}, Zn^{2+}, and S^{2-} are 0.94, 0.74, and 1.84Å respectively. As the ionic radius of Ag^{2+} (0.94 Å) is very close to Zn^{2+} (0.74 Å) compared to S^{2-} (1.84 Å), silver can easily substitute the Zn in the ZnS lattices.
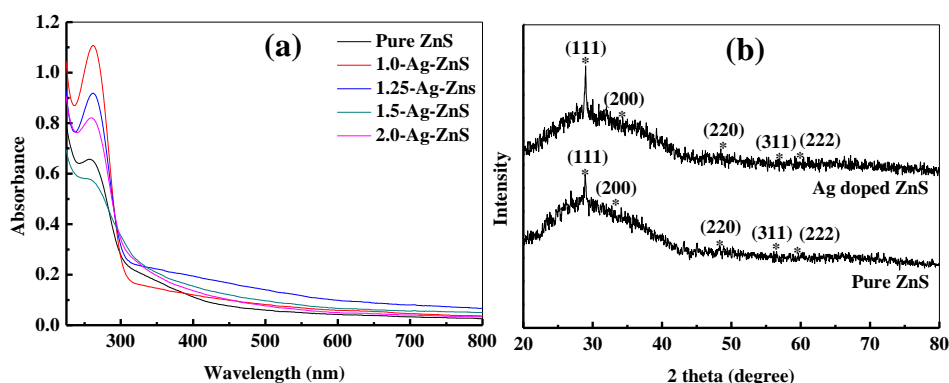
Figure 3.6. (a) UV–Vis spectra of pure ZnS, 1.0-Ag-ZnS, 1.25-Ag-ZnS, 1.5-Ag-ZnS and 2.0-Ag-ZnS nanoparticles. (b) X-ray diffraction pattern of pure ZnS and 1.25-Ag-ZnS nanoparticles.

The TEM images (Figure 3.7a,b) show the spherical type particles with size range of 5.85 ± 0.5 and 4.91 ± 0.45 nm for pure ZnS and 1.25-Ag-ZnS nanoparticles. The HR- TEM image in Figure 3.7c presents the lattice fringes spacing of 0.31 nm corresponding to the (111) plane of cubic ZnS. Figure 3.7d shows the SAED pattern of the particle and the ring like diffraction pattern confirms the crystalline nature of 1.25-Ag-ZnS nanoparticles.
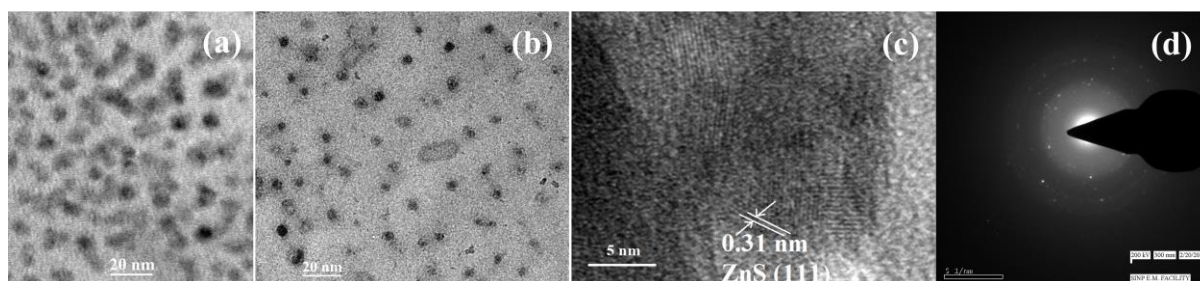
Figure 3.7. Transmission electron microscopic image of (a) pure ZnS and (b) Ag doped ZnS nanoparticles. (c) SAED pattern and (d) HR-TEM image of 1.25-Ag-ZnS nanoparticles.

3.3.4 Photocatalytic Activity of Pure TiO$_2$, CdS, and ZnS Nanoparticles

3.3.4.1 Degradation of Metronidazole Antibiotic

The degradation studies were carried out for two hours duration in the presence of pure TiO$_2$, CdS, and ZnS nanoparticles under the visible light irradiation as shown in Figure 3.8a. It has been found that the degradation process reached a plateau level after 2 hours of exposure time in the presence of visible light. The maximum degradation percentages of MTZ were 80.78, 82.46, and 81.66 % for TiO$_2$, CdS, and ZnS nanoparticles, respectively. All particles are having degradation efficiency of more than 80% with very close values. The experimental results of the degradation reaction were tried to fit with different kinetic models, and it was found that the first order kinetics fits well for all three materials. The final form of the equation is presented as follows:

$$\ln(C_0/C) = kt \tag{3.1}$$

Where, C_0 and C are the concentrations of MTZ at the beginning and t time respectively, k is the degradation rate constant. The rate constant values for photocatalytic degradation are 0.0142, 0.015, and 0.0145 min^{-1} for TiO$_2$, CdS, and ZnS nanoparticles respectively (Figure 3.8b).

For each degradation study, two sets of reference studies, (i) MTZ solution + catalyst in dark and (ii) only MTZ solution under visible light irradiation were carried out. There was no significant change in the concentration of MTZ indicates the concentration change in the presence of light and catalyst is mainly because of degradation of MTZ.
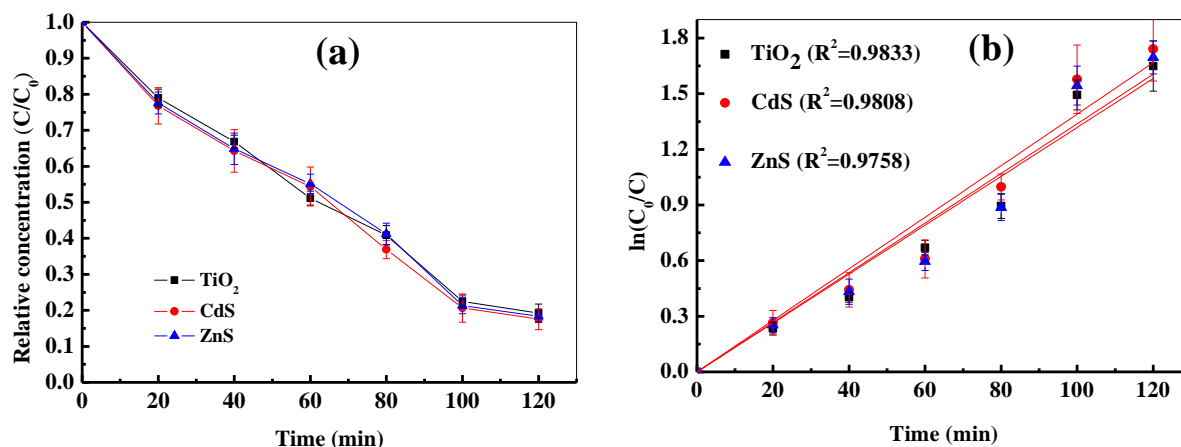
Figure 3.8. (a) Photocatalytic degradation and (b) kinetic data for the degradation of MTZ solution in the presence of pure TiO$_2$, CdS and ZnS nanoparticles.

3.3.4.2 Degradation of Methylene Blue Dye

The studies of MBD degradation were carried out in the presence of these three semiconductor nanoparticles TiO$_2$, CdS and ZnS under visible light irradiation. The degradation results presented in Figure 3.9b clearly indicate that the degradation process reached the plateau level after 3 h of exposure time in the presence of visible light. The maximum degradation of MBD obtained as 49.73, 41.4, and 34.9% for pure TiO$_2$, CdS, and ZnS nanoparticles, respectively. Here pure TiO$_2$ nanoparticles showed maximum degradation efficiency compared to pure CdS and ZnS nanoparticles. The physical appearances of MBD solution before and after photodegradation under different nanoparticles are presented in Figure 3.9a. These degradation results were also tried to fit with different kinetic models, and it was found that the first order kinetics fits well for all three materials. The first order rate constants of photocatalytic degradation under pure TiO$_2$, CdS, and ZnS nanoparticles are 0.0038, 0.0032, and 0.0024 min^{-1}, respectively (Figure 3.9c).

Similar to the MTZ degradation two sets of reference studies were also conducted here, (i) MBD solution + catalyst in dark and (ii) only MBD solution under visible light irradiation were carried out. There was no significant change in the concentration of MBD indicates the concentration change in the presence of light and catalyst is mainly because of degradation of MBD.
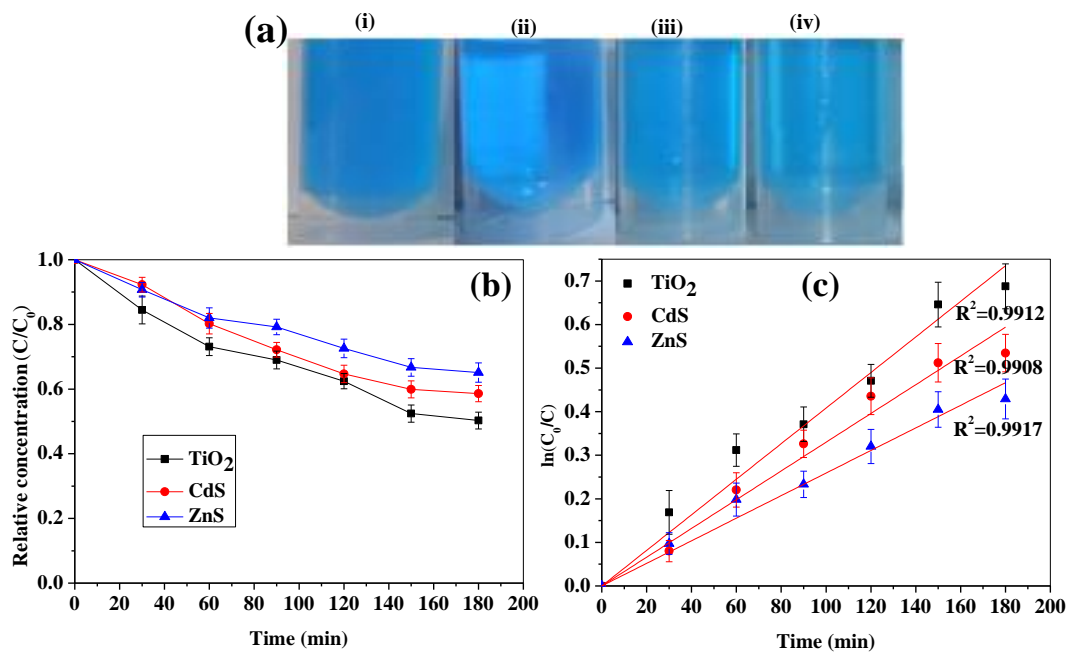
Figure 3.9. (a) The images of pure methylene blue solution (i), and after degradation under HPMV lamp light using pure TiO_2 (ii), pure CdS (iii), pure ZnS (iv). (b) Photocatalytic degradation and (c) Kinetic data for the degradation of MBD solution using pure TiO_2, CdS, and ZnS nanoparticles.

3.3.5 Photocatalytic Activity of Ag Doped TiO_2 Nanoparticles

3.3.5.1 Degradation of Metronidazole Antibiotic

The degradation of MTZ was carried out in the presence of different silver doped TiO_2 nanoparticles, to see the effect of silver doping on the photocatalytic process, as presented in Figure 3.10a. From the Figure one can see that in the presence of doped nanoparticles degradation efficiency increases significantly compared to that of pure TiO_2 nanoparticles. The degradation efficiencies are 92.82, 94.39, 89.15, and 83.36% for 0.5-Ag-TiO_2, 1.0-Ag-TiO_2, 1.25-Ag-TiO_2, and 2.0-Ag-TiO_2 nanoparticles respectively. These results clearly indicate the degradation efficiency is maximum in the presence of 1% dopant concentration, and the efficiency decreases above and below this concentration. The first order rate constant values (Figure 3.10b) of photocatalytic degradation in the presence of 0.5-Ag-TiO_2, 1.0-Ag-TiO_2, 1.25-Ag-TiO_2, and 2.0-Ag-TiO_2 nanoparticles are 0.022, 0.0236, 0.019, and 0.016 min^{-1}, respectively. So, the value of rate constant in the presence of 1.0-Ag-TiO_2 is about 1.66 times higher than that of pure TiO_2. As 1.0-Ag-TiO_2 NPs show highest MTZ degradation efficiency, the re-usability of this material was also tested by cyclic degradation tests under the same condition, and these results are presented in Figure 3.10c. The results show there is a ~12% decrease (94.39 to 82.14%) in degradation efficiency after sixth cycles. Noteworthy

to mention that, after 6th cycle of the degradation study, it was found that the photocatalytic efficiency of the catalyst was still comparable to that of pure TiO_2.
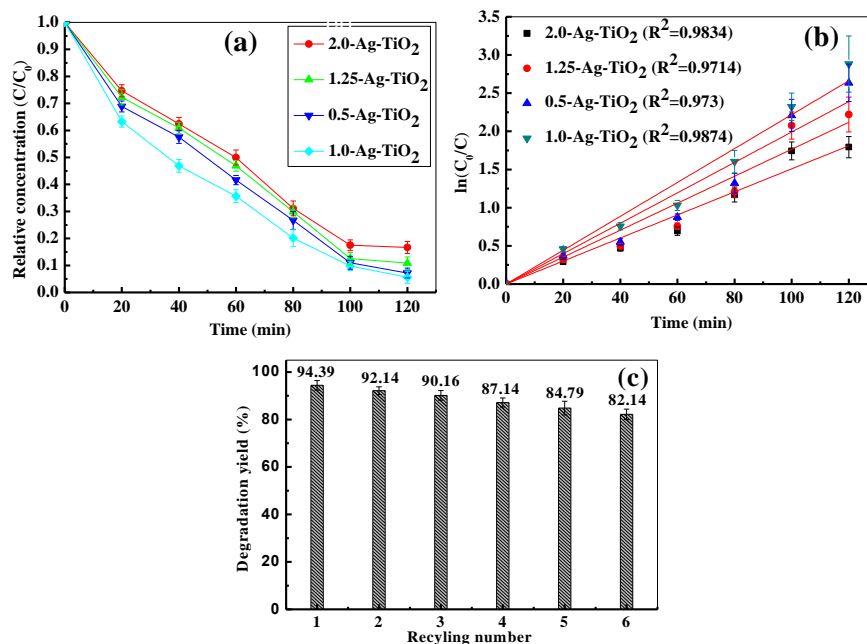
Figure 3.10. (a) Photocatalytic degradation and (b) Kinetic data for the degradation of MTZ solution over 0.5-Ag-TiO$_2$, 1.0-Ag-TiO$_2$, 1.25-Ag-TiO$_2$ and 2.0-Ag-TiO$_2$ nanoparticles. (c) Recycling test of 1.0-Ag-TiO$_2$ for the degradation of MTZ solution.

3.3.5.2 Degradation of Methylene Blue Dye

The degradation of MBD was carried out in the presence of different quantity silver doped TiO_2 nanoparticles, to see the effect of doping on the photocatalytic property. The degradation results using silver doped TiO_2 nanoparticles are presented in Figure 3.11b. It was found that, in the presence of silver dopant, the degradation efficiency increases significantly compared to that of pure TiO_2 NPs. The degradation efficiencies are 95.38, 95.9, 82.54, and 60.3% for 0.5-Ag-TiO$_2$, 1.0-Ag-TiO$_2$, 1.25-Ag-TiO$_2$, and 2.0-Ag-TiO$_2$ NPs, respectively. These results clearly show the degradation efficiency is maximum in the presence of 1% silver dopant concentration, and the efficiency decreases above and below this concentration. The images of dye solutions before and after the light irradiation under different silver doped TiO_2 photocatalyst are presented in (*i*) - (*iv*) of Figure 3.11a. The rate constants of photocatalytic degradation under 0.5-Ag-TiO$_2$, 1.0-Ag-TiO$_2$, 1.25-Ag-TiO$_2$, and 2.0-Ag-TiO$_2$ nanoparticles are 0.0187, 0.0198, 0.0104, and 0.0051 min^{-1}, respectively, as is presented in Figure 3.11c. The results show the first order rate constant in 1.0-Ag-TiO$_2$ photocatalytic process is about 5.21 times higher than that of pure TiO_2 photocatalytic process.
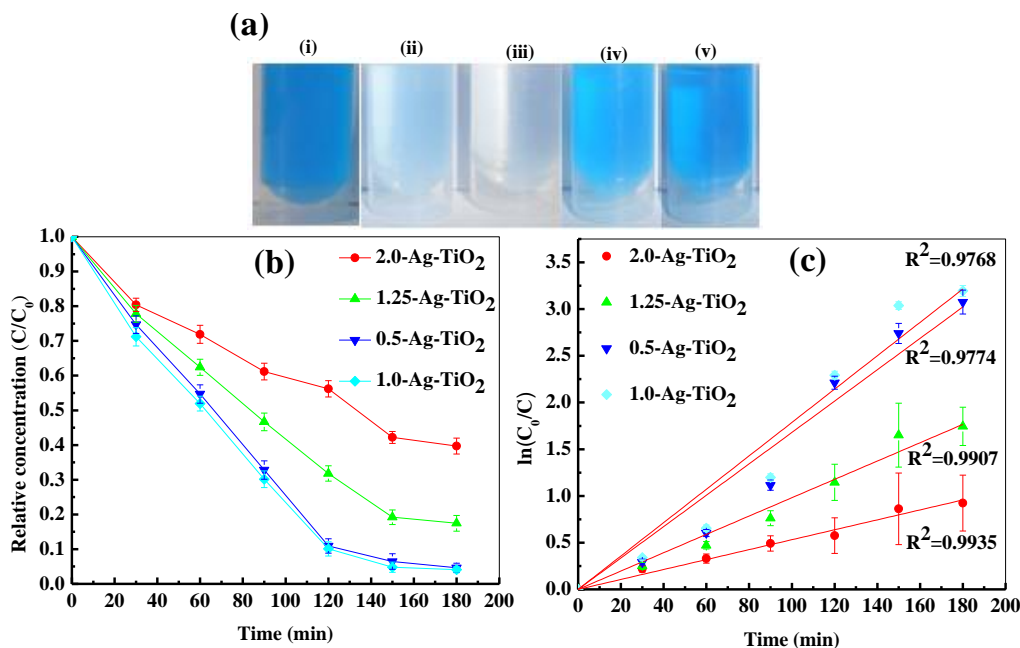
Figure 3.11. (a) The images of pure methylene blue solution before (i), and after degradation using 0.5-Ag-TiO$_2$ (ii), 1.0-Ag-TiO$_2$ (iii), 1.25-Ag-TiO$_2$ (iv), 2.0-Ag-TiO$_2$ (v). (b) Photocatalytic degradation and (c) Kinetic data for the degradation of MBD solution using 0.5-Ag-TiO$_2$, 1.0-Ag-TiO$_2$, 1.25-Ag-TiO$_2$ and 2.0-Ag-TiO$_2$ NPs.

3.3.6 Photocatalytic Activity of Ag Doped CdS Nanoparticles

3.3.6.1 Degradation of Metronidazole Antibiotic

Photodegradation of MTZ was also carried out using Ag doped CdS nanoparticles. Figure 3.12a shows the photocatalytic degradation of MTZ in the presence of silver doped CdS nanoparticles. It can be seen that the 1.0-Ag-CdS, 1.5-Ag-CdS, 1.75-Ag-CdS, and 3.0-Ag-CdS nanoparticles degraded 93.89, 95.11, 90.88, and 86.67% of MTZ from the solution after 2 hours of visible light irradiation. Among all particles used here, 1.5-Ag-CdS NPs have the highest degradation efficiency. Degradation results among these materials indicate that with the increasing silver nitrate concentration the efficiency increases up to 1.5% of silver nitrate concentration, and then the degradation efficiency decreases. Figure 3.12b depicts the linear fitting of the first order kinetics of the experimental data. The first order rate constant values of photocatalytic degradation using 1.0-Ag-CdS, 1.5-Ag-CdS, 1.75-Ag-CdS, and 3.0-Ag-CdS are 0.0227, 0.0252, 0.02, and 0.017 min^{-1}, respectively. The first order rate constant in the presence of 1.5-Ag-CdS photocatalytic reaction is about 1.68 times higher than that of pure CdS. The above results reveal that 1.5-Ag-CdS has the highest photocatalytic efficiency among pure and other silver doped CdS nanoparticles. Similar to the previous study, this sample was also further selected for cyclic efficiency test under the same condition, and

results are plotted in Figure 3.12c. These results show there is a reduction in efficiency of ~ 11% (95.11 to 85.22%) after sixth cycle of photodegradation; however, the final efficiency is still higher than that of pure CdS.
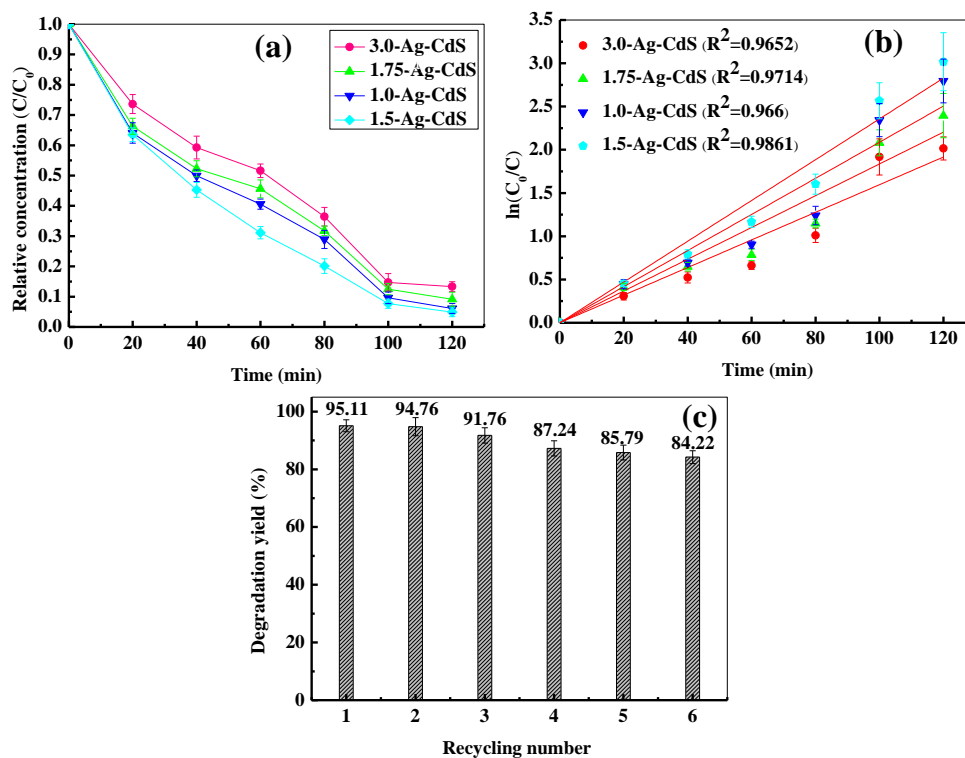
Figure 3.12. (a) Photocatalytic degradation and (b) first order kinetic plot for the degradation of MTZ solution over 1.0-Ag-CdS, 1.5-Ag-CdS, 1.75-Ag-CdS and 3.0-Ag-CdS. (c) Recycling test of 1.5-Ag-CdS for the degradation of MTZ solution.

3.3.6.2 Degradation of Methylene Blue Dye

In this section, silver doped CdS nanoparticles were employed as the photocatalyst for the degradation of methylene blue dye. The degradation results in Figure 3.13b shows that after 3 h of visible light irradiation the 1.0-Ag-CdS, 1.5-Ag-CdS, 1.75-Ag-CdS, and 3.0-Ag-CdS NPs degraded 89.72, 95.33, 60.18, and 49.79% of MBD from the solution. The degradation results using different Ag doped CdS indicates that with the increasing concentration of the silver the degradation efficiency increases up to 1.5% of silver concentration, and then the degradation efficiency decreases. So, the degradation of MBD solution is the maximum in case of 1.5-Ag-CdS NPs. The images of methylene blue solutions before and after 3h light irradiation under different silver doped CdS photocatalyst are presented in (i) – (iv) parts of Figure 3.13a. The first order rate constants of photocatalytic degradation using 1.0-Ag-CdS, 1.5-Ag-CdS, 1.75-Ag-CdS, and 3.0-Ag-CdS nanoparticles are 0.0132, 0.0183, 0.0054, and 0.0042 min^{-1}, respectively (Figure 3.13c). In the case of maximum degradation efficiency

(1.5-Ag-TiO$_2$), the first order rate constant is 5.72 times higher than that of pure CdS nanoparticles. The above results reveal that 1.5-Ag-CdS nanoparticles hold higher photocatalytic activity among pure and other silver doped CdS nanoparticles.
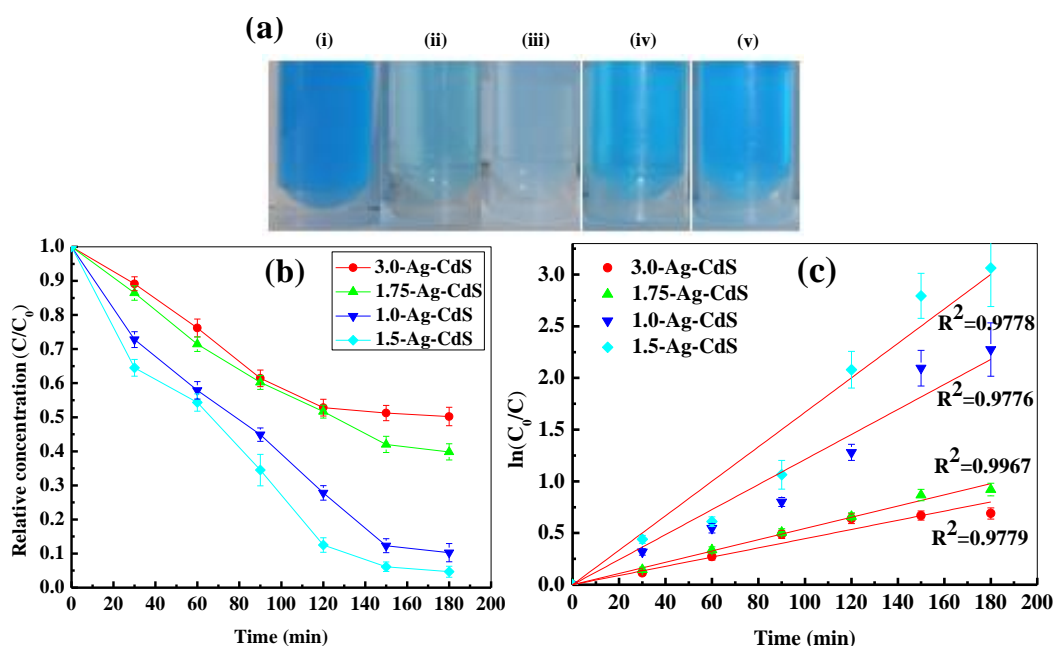
Figure 3.13. (a) The images of pure methylene blue solution before (i), and after degradation using 1.0-Ag-CdS (ii), 1.5-Ag-CdS (iii), 1.75-Ag-CdS (iv), 3.0-Ag-CdS (v). (b) Photocatalytic degradation and (c) First order kinetic plot for the degradation of MBD solution using 1.0-Ag-CdS, 1.5-Ag-CdS, 1.75-Ag-CdS and 3.0-Ag-CdS nanoparticles.

3.3.7   Photocatalytic Activity of Ag Doped ZnS Nanoparticles

3.3.7.1 Degradation of Metronidazole Antibiotic

In this section, different percentages silver doped ZnS nanoparticles were employed for photo-degradation MTZ from aqueous solutions. For the degradation study, the same experimental procedure was followed for this case and results are presented in Figure 3.14a. For the Ag doped ZnS catalyzed systems the relative degradation rate of MTZ can be ranked as: 1.25-Ag-ZnS > 1.0-Ag-ZnS > 1.5-Ag-ZnS > 2.0-Ag-ZnS. The maximum degradation (94.9%) of MTZ was achieved in 1.25-Ag-ZnS photocatalytic process after 2 hours of degradation time. Whereas, 1.0-Ag-ZnS, 1.5-Ag-ZnS, and 2.0-Ag-ZnS nanoparticles degraded 93.55%, 90.64% and 86.29% of MTZ respectively. The first order reaction rate constant values of photocatalytic degradation (Figure 3.14b) using 1.0-Ag-ZnS, 1.25-Ag-ZnS, 1.5-Ag-ZnS, and 2.0-Ag-ZnS are 0.0219, 0.0242, 0.0197, and 0.0174 min^{-1}, respectively. The k value for 1.25-Ag-ZnS photocatalytic process is about 1.71 times higher than that of pure ZnS photocatalytic process. Further, results of cyclic degradation test show

there is a decrease in efficiency of ~ 10% (94.90 to 84.61%) after sixth cycle of photodegradation (Figure 3.14c).
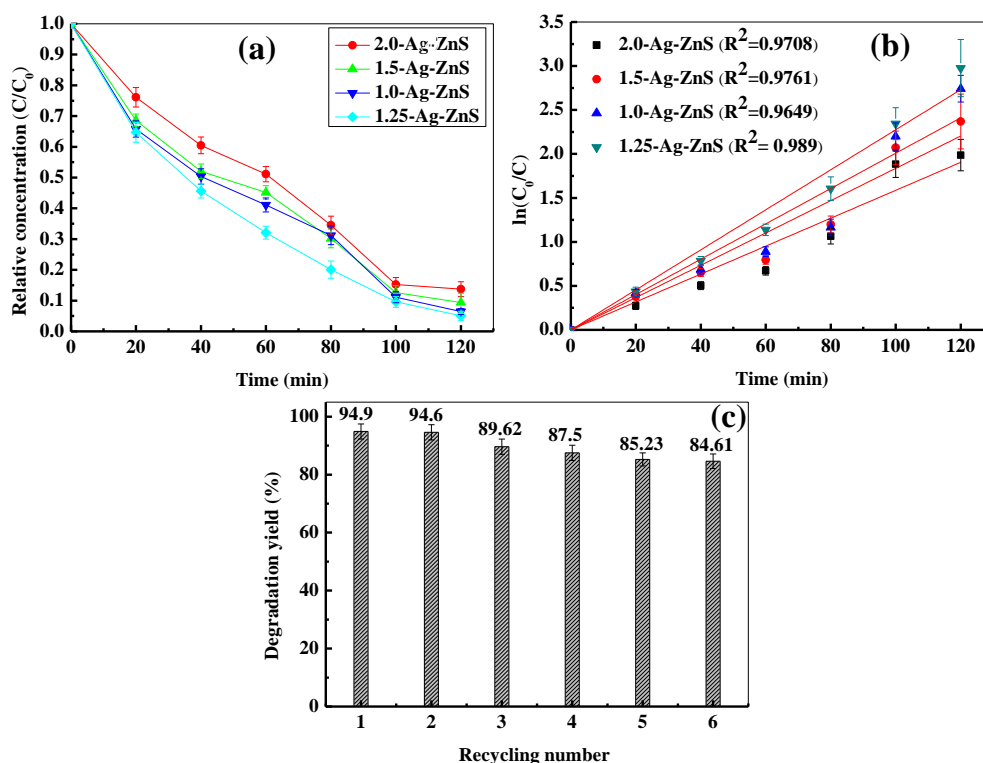
Figure 3.14. (a) Photocatalytic degradation and (b) Kinetic data for the degradation of MTZ solution over 1.0-Ag-ZnS, 1.25-Ag-ZnS, 1.5-Ag-ZnS and 2.0-Ag-ZnS. (c) Recycling test of 1.25-Ag-ZnS for the degradation of MTZ solution.

3.3.7.2 Degradation of Methylene Blue Dye

Silver doped ZnS NPs were also employed as the photocatalyst for removing MBD from the aqueous solution. The degradation results (Figure 3.15b) clearly indicate that the relative degradation rate of MBD to be ranked as: 1.25-Ag-ZnS > 1.0-Ag-ZnS > 1.5-Ag-ZnS > 2.0-Ag-ZnS. The maximum removal of MBD was achieved 94.99% for 1.25-Ag-ZnS NPs process after 3 hrs of degradation time. Whereas, 1.0-Ag-ZnS, 1.5-Ag-ZnS and 2.0-Ag-ZnS nanoparticles degraded 85.38, 59.43 and 50.8% of MBD from the solution. The physical appearance of methylene blue solutions for different silver doped ZnS NPs are presented in Figure 3.15a (i-iv). The kinetic data for the MBD photocatalytic degradation using 1.0-Ag-ZnS, 1.25-Ag-ZnS, 1.5-Ag-ZnS and 2.0-Ag-ZnS NPs are 0.0118, 0.0185, 0.005 and 0.004 min^{-1}, respectively, as presented in Figure 3.15c. The rate constant (k) value for 1.25-Ag-ZnS photocatalytic process was about 7.71 times higher than that of pure ZnS photocatalytic process. So, 1.25-Ag-ZnS NPs was the highest efficient photocatalyst among pure and other silver doped ZnS photocatalytic process.
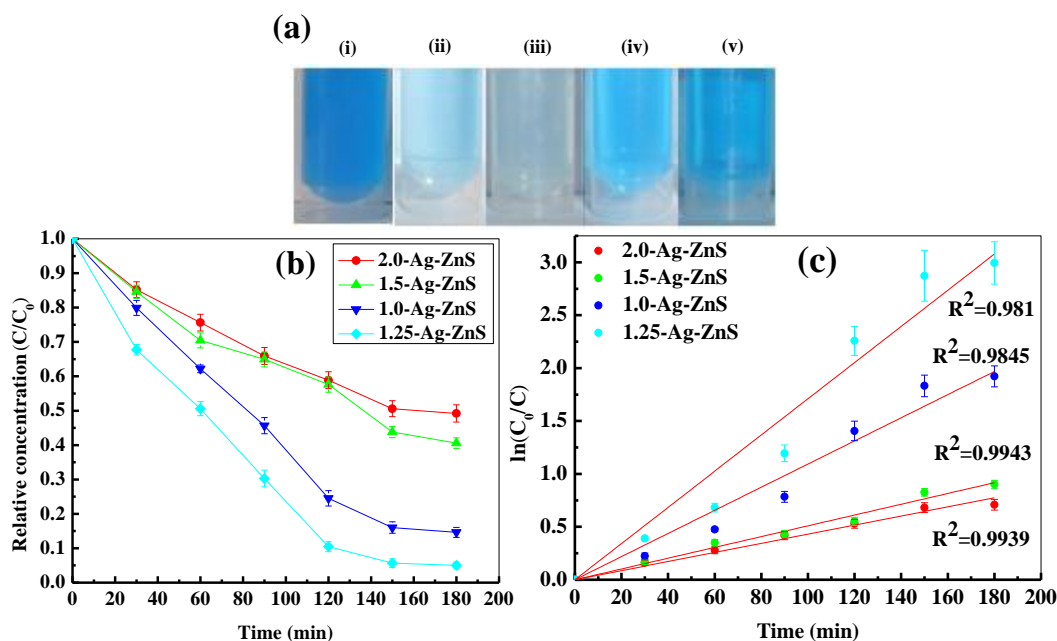
Figure 3.15. (a) The images of pure methylene blue solution before (i), and after degradation using 1.0-Ag-ZnS (ii), 1.25-Ag-ZnS (iii), 1.5-Ag-ZnS (iv), 2.0-Ag-ZnS (v). (b) Photocatalytic degradation and (c) Kinetic data for the degradation of MBD solution using 1.0-Ag-ZnS, 1.25-Ag-ZnS, 1.5-Ag-ZnS and 2.0-Ag-ZnS nanoparticles.

3.3.8 Mechanism of Photocatalytic Degradation

During the photocatalytic process, the incident photons excite the valence band electrons of photocatalyst to the conduction band, thus generating the electron-hole pairs (reaction 3.2). The dissolved O_2 molecules in the suspension capture the electron in the conduction band (reaction 3.3).The H_2O molecules are adsorbed (reaction 3.4 to 3.7) on the surface of the catalyst and interact with the generated valence band hole to produce the $^\bullet OH$ radicals, which subsequently participate in antibiotic oxidation. The yield of $^\bullet OH$ radicals depends on the oxidation of the surface water molecules by holes and electron-hole recombination according to reaction 3.8. Recombination of charge carriers occur mainly because of abundant surface trapping sites and the lack of driving the force for the separation of electron-hole pairs, which is the opposing factor for the $^\bullet OH$ radical formation and finally decreases degradation efficiency. Suggested general reaction schemes are presented below:

$$NP \rightarrow NP^* (e_{CB}^- + h_{VB}^+) \tag{3.2}$$

$$e_{CB}^-(NP) + O_2 \rightarrow {}^\bullet O_2^- \tag{3.3}$$

$$H_2O_{ad} + h_{VB}^+(NP) \rightarrow OH^\bullet + H^+ \tag{3.4}$$

$$^\bullet O_2^- + H^+ \rightarrow HOO^\bullet \tag{3.5}$$

$$HOO^\bullet + e^-_{CB} + H^+ \rightarrow H_2O_2 \rightarrow 2^\bullet OH \qquad (3.6)$$

$$\text{Antibiotic} + {}^\bullet OH \rightarrow \text{Degraded products} \qquad (3.7)$$

$$e^-_{CB}(NP) + h^+_{VB}(NP) \rightarrow NP \text{ (Recombination)} \qquad (3.8)$$
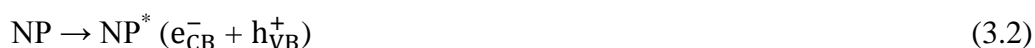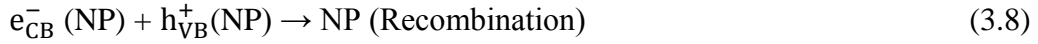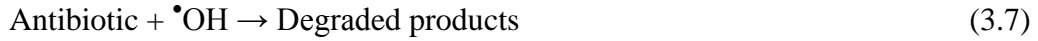
During the photodegradation process using silver doped nanoparticles, the dopant accepts the photoinduced electrons and holes, which in turn act as electron/hole traps (reaction 3.9 to 3.12). In general, electron or hole traps prevent the recombination of the charge carriers by increasing the separation efficiency of the electron-hole pairs effectively, and eventually the degradation efficiency increases. If n and p are valences of the dopant ion and principle reactant (P) of the host material, these processes can be represented as follows:

$$Ag^{n+} + e^-_{CB}(NP) \rightarrow Ag^{(n-1)+} \text{ (reduction) (electron trap)} \qquad (3.9)$$

$$Ag^{(n-1)+} + P^{m+} \rightarrow Ag^{(n)+} + P^{(m-1)+} \qquad (3.10)$$

$$Ag^{n+} + h^+_{VB}(NP) \rightarrow Ag^{(n+1)+} \text{ (oxidation) (hole trap)} \qquad (3.11)$$

$$Ag^{(n+1)+} + OH^- \rightarrow Ag^{(n)+} + {}^\bullet OH \qquad (3.12)$$
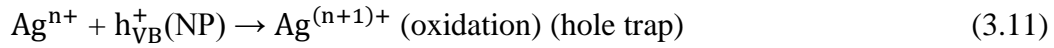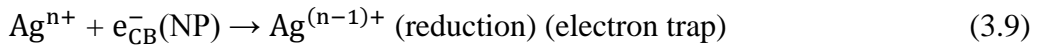
However, with the increasing doping concentration, after a particular limit of doping concentration there is a possibility of destroying the lattice structure of host material because of serious lattice mismatching and the loss of stoichiometry; which in turn leads to quantum tunnelling and structural instability of the material. Additionally, at higher doping concentration the electron-hole pairs will try to recombine again through quantum tunnelling because of higher trapping of charge carriers according to reactions 3.13 to 3.16, which finally leads to decrease in the photocatalytic activity.

$$Ag^{(n-1)} + h^+_{VB}(NP) \rightarrow Ag^{n+} \qquad (3.13)$$

$$Ag^{(n+1)+} + e^-_{CB}(NP) \rightarrow Ag^{n+} \qquad (3.14)$$

$$Ag^{(n+1)+} + Ag^{(n-1)} \rightarrow 2Ag^{n+} \qquad (3.15)$$

$$Ag^{(n+1)+} + P^{(m-1)+} \rightarrow P^{m+} + Ag^{n+} \qquad (3.16)$$
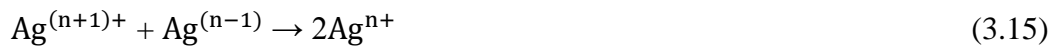
The degradation results show that, for doped nanoparticles the maximum photocatalytic efficiency is possible at a particular concentration of doping. While comparing the maximum degradation efficiency for three Ag doped nanoparticles it has been found that the corresponding concentrations of $AgNO_3$ are 1.5, 1.25, and 1.0% for CdS, ZnS, and TiO_2 host materials respectively. This is because of the combined effect of ionization energy of dopant ion and different ionic radius of principle reactant and dopant component. While comparing

CdS and ZnS NPs, as the difference in ionic radius between Ag^{2+} (0.94 Å) and Cd^{2+} (0.95 Å) is less than that of Zn^{2+} (0.74 Å) doping % of CdS is more than that of ZnS. However, while comparing ZnS and TiO_2 the difference in ionic radius for TiO_2 (ionic radius of Ti^{4+} is 0.605) is low, but the doping% for maximum degradation is also low; which can be attributed to the fact of higher energy of ionization of Ag^{3+} (3361 kJ/mol) than that of Ag^{2+} (2070 kJ/mol).The overall degradation results show that, all three materials are having very close maximum degradation efficiency but the doping% of silver is low for TiO_2 compared to CdS and ZnS nanoparticles. As it is well known that, TiO_2 has some excellent properties such as low toxicity, low cost, easy availability, and outstanding chemical stability, compared to CdS and ZnS; it can be concluded that, among these three semiconductor nanoparticles, Ag doped TiO_2 may have some better applicability for the degradation of metronidazole antibiotic and methylene blue dye depending on the actual requirement of the process.

While comparing with the literature, it is seen that degradation of MTZ antibiotic by ultraviolet (UV) irradiation, [447] Oxidation processes using UV, UV/H_2O_2, H_2O_2/Fe^{2+}, and $UV/H_2O_2/Fe^{2+}$ [448] are expensive and complicated. [449] Use of Closed Bottle Test (CBT) for MTZ degradation is also not effective because of its low degradation efficiency (25.6%) even after 28 days of incubation time. [450] Apart from these conventional method, use of photocatalyst were also studied as listed in Table 3.1. It shows lower degradation rate in visible light irradiation, 100% degradation was only achieved in UV-light irradiation and in high catalyst dose. In this regards our approach of MTZ degradation is noble compared to the reported conventional method as well as photocatalytic degradation approach.

Table 3.1. Comparison of the present work of metronidazole degradation with the published literatures

Catalyst	catalyst dose (g/L)	Initial MTZ conc (mg/L)	Light source	parameters	Time (min)	% deg.	Ref.
Ag-TiO$_2$, CdS, ZnS	0.5	15	125 W, visible light (λ=435.8 nm)	-	120 min	94.39-95.11	our case

catalyst	catalyst dose (g/L)	initial MBD conc (mg/L)	Light sources	parameters	Time (min)	% deg	ref.
nZVM	0.1	100	-	251°C, pH dependent, O_2 flow	-	84	[456]
ZnSnO$_3$/RGO	1	5	500 W, visible lamp		180 min	72.5	[455]
Zn$_2$GeO$_4$	1	10	UV light lamp (λ = 253.7 nm)	-	80 min	~100	[454]

From the reported literature for methylene blue degradation (Table 3.2) it is seen that above 90% MBD degradation achieved either in UV-light or in visible light with high catalyst dose and low initial dye concentration. Some reported studies showed ~100% dye degradation efficiency with specific reaction conditions, such as pH of the reaction media, temperature, and irradiation by high wattage UV or NIR light. Whereas our synthesized photocatalyst showed good photocatalytic activity in visible light, neutral pH media, room temperature, low catalyst dose, and high initial dye concentration.

Table 3.2. Methylene Blue degradation in presence of different nanoparticles as the photocatalyst

catalyst	catalyst dose (g/L)	initial MBD conc (mg/L)	Light sources	parameters	Time (min)	% deg	ref.
Ag-TiO$_2$, CdS, ZnS	0.25	25	125 W, visible light (λ=435.8 nm)	-	180	94.99-95.9	our case
Mn, Ni, Cu-ZnS	0.15	5	500 W HL	pH=11	30	87.3-95.6	[470]
Sm-TiO$_2$	1.0	100	160 W HPMVL (UV)	-	120	95	[466]
N, S- TiO$_2$	0.2	9	500 W ML	pH=3	240	90.61	[469]
Ce, Cu, Mn, Sn-	0.0375	10	UV light, 254 nm	-	90	~97	[476]

TiO$_2$							
Fe-TiO$_2$	0.5	100	300 W HPMVL (365 nm)	-	65	~ 75	[349]
Cu-ZnS	1.0	10	1000 W HL	pH=6.5	180	100	[351]
Fe-ZnO	0.448	32	UV/sun light	-	105/75	41/91	[477]
C-TiO$_2$	1.0	10	solar light	pH=10	100	100	[467]
SnO$_2$-MgO	1.5	8	sun light	pH=9.5	40	98	[478]
Pt/TiO$_2$	1	10	300 W XL	-	50	~95	[471]
Co, Fe, Mn-TiO$_2$	0.5	50	UV-Hg/XL	temp 20°C	120	96-100	[479]
Nd, I-TiO$_2$	0.5	10	ITL (≥760 nm)	31 ± 1°C	150	~100	[480]
Si, Fe, TiO$_2$	1.0	20	500 W LAXL	-	180	82.51	[472]
NaYF$_4$:Yb,Tm/TiO$_2$	1.0	15	DL (980 nm)	-	14 h	65	[473]
Ag-C-TiO$_2$	1.0	18.4	150 W HPXL (420 nm)	-	8 h	38.6	[481]
Fe-CdS	1	10	1000 W HL	pH=6.5	180	100	[468]

Abbreaviation: high-pressure xenon lamp (HPXL), high-pressure mercury vapour lamp (HPMVL), halogen lamp (HL), xenon lamp (XL), mercury lamp (ML), iodine tungsten lamp (ITL), long-arc xenon lamp (LAXL), diode laser (DL).

3.4 Conclusions

In summary, the TiO$_2$, CdS, and ZnS nanoparticles were synthesized in aqueous surfactant media. The particle size was in the range of 33.39 ± 1.67 and 27.6 ± 2.08 nm for pure and Ag doped TiO$_2$, 4.06 ± 0.63 and 3.44 ± 0.76 nm for pure CdS and 1.5-Ag-CdS, and 5.85 ± 0.5 nm and 4.91 ± 0.45 nm for pure and Ag doped ZnS nanoparticles respectively. Ag doping is achieved through substitution of principle reactant component of the host material. The TiO$_2$, CdS, and ZnS nano catalysts showed 80.78, 82.46, and 81.66% MTZ degradation and 49.73,

41.4, and 34.9% MBD degradation efficiency under visible light irradiation. The degradation efficiency of these particles enhanced drastically while doped with silver, however, the optimum doping percentage is crucial to get highest efficiency. The maximum degradation efficiencies of 1.00, 1.5, and 1.25% Ag doped TiO_2, CdS, and ZnS nanoparticles were 94.39, 95.11, and 94.9% for MTZ and 95.9, 95.33, and 94.99% for MBD. In spite of the fact that, the maximum degradation efficiencies are similar for all three catalysts at the optimum doping content, but for TiO_2 low dopant concentration is required. Since TiO_2 is nontoxic and cheap, Ag doped TiO_2 will be useful for photodegradation of antibiotics and dye in waste water compared to other two catalysts studied here. The catalyst recycling study for the MTZ degradation also shows 10-12% reduction in degradation efficiency of the catalyst after sixth cycle of photodegradation, which indicates the re-usability of the catalyst. Overall our approach in the degradation of metronidazole antibiotics and methylene blue dye using different doped nanoparticles is expected to be an important technique for the remediation of antibiotic and dye contaminated waste water treatment. Additionally, as the degradation is possible in visible light, the process can also be considered as environmentally friendly or green.

Chapter 4

Visible Light Induced Enhanced Photocatalytic Degradation of Organic Pollutants in Aqueous Media using Ag Doped Hollow TiO$_2$ Nanospheres

4.1 Introduction

Metal oxide semiconductor nanoparticles play an important role in different areas of science and engineering such as photo catalysis, [133,482,483] solar cells, [484–486] Li-ion batteries, [487,488] piezoelectric devices, [489,490] fuel cells, [491] sensors, [492,493] and so on. The photo catalytic degradation of organic pollutants is considered as one of the advanced environmental remediation process in recent years over the conventional processes such as membrane filtration, adsorption. Among several metal oxide semiconductor nanoparticles TiO_2 is one of the promising photocatalysts because of its relatively higher efficiency, low toxicity, long term stability, low cost, photoinduced strong oxidation activity properties. [124,494,495] However, the application of pure TiO_2 as a photocatalyst is limited in visible light because of its high band gap (3.03 eV for rutile and 3.18 eV for anatase). Because of this reason, the development of visible light induced TiO_2 photocatalyst with higher efficiency is highly essential to make the industrial process more feasible and economic. Since the reduction of band gap enhance the photocatalytic activity of a photocatalyst under visible light, significant efforts have been made till now to dope different elements into the TiO_2 host lattices such as, Fe, [129,496] Mn, [497] Mg, [498] Cr, [130] Co, [132] Sn, [359] Sm, [499] Nd, [500] and so on. In addition to the band gap of a photocatalyst, the surface area is also extremely important to enhance the activity of a catalyst. In this regard, TiO_2 with different morphologies such as nanowires, [501] nanotubes, [502] nanorods [503] have been studied. More advanced material like hollow nanoparticles along with doping have attracted considerable interests because of its larger surface area along with some important properties, such as low density, good surface permeability and high light-harvesting efficiencies, [504–507] The TiO_2 photocatalysts are not only used for the remediation of contaminated water but also useful in air purification, [508] cathodic catalyst for low-cost fuel cell. [195] Some studies are also available on hollow TiO_2 nanoparticles doped with different elements such as Nd, [509] N and Ce, [510] Sn, [511] Bi, [512] in all these studies the C was used as the core and it was removed by calcination. The other template such as polystyrene was used for Sm^{3+} doped hollow TiO_2 structure. [513] Sulfur doped hollow sphere TiO_2 was also synthesized by our group, where S was doped during the removal of the sacrificial S core. [514] Considering catalytic properties of TiO_2, incorporation of noble metal like Ag to hollow TiO_2 structure is important because of its unique characteristics in resonant collective oscillations of the conduction electrons by electromagnetic radiation and the localized surface plasmon resonance (SPR). [515,516] Since nanoscale silver has good antibacterial property, [145,517] Ag doped TiO_2 nanoparticles also show similar property. [148,149,518] Silver-TiO_2 composite hollow nanoparticles was reported by template free method

[519] and PSA latex templated method [520] as a visible light active photocatalyst. Recently, Ag and AgCl doped TiO_2 hollow nanoparticles were synthesized using polystyrene particles as template for getting a visible light active photocatalyst. [521]

It has been noted from most of the literature that the doped hollow structure was formed after removing the core, and the doping was achieved in the presence of some extra precursor. However, a single step method for the core removal and doping could make the process simple.

As mentioned before, a significant fraction of research activities is going on environmental remediation of organic pollutants using TiO_2 nanoparticles. The main advantage of this process over the other conventional separation processes is toxic pollutants can be converted to useful or nontoxic compounds. Different classes of organic compounds such as aromatics (benzo compounds, phenolic compounds, naphthalene, trinitrotoluene, etc), phermaceutical products (antibiotics, antipyretic etc.), dyes (synthetic dyes, reactive dyes, azo dyes, basic cationic dyes etc.), some volatile organic compounds (formaldehyde, methylene chloride, ethylene glycol, etc) can be degraded using this catalysts. The benzo compounds such as nitrobenzene are highly toxic organic compound mainly used for the production of aniline, paper and pulp, pesticides, dyes, explosives, cosmetics, pharmaceuticals, and so on. [353–355] The long term exposure of nitrobenzene to the environment, even at low concentration, causes risks to human, such as liver or kidney damage, lung irritation, increase heart rate, skin problem, vomiting, etc. Therefore, removal of nitrobenzene from the environment is a major concern. Degradation of nitrobenzene in effluent water is difficult by conventional chemical method because of the nitro group which has strong electron withdrawing property and inhibits its oxidation, or by biological method because of its toxic and mutagenic effect on the biological systems. [356,357] Apart from aromatic compounds, the presence of pharmaceutical products for instance antibiotics in the environment, even at low concentrations, causes the growth of antibiotic-resistant bacteria [341,342] and creates microbial population, [343,344] which may cause of ineffectiveness of the present forms of treatment and major epidemics. Metronidazole (MTZ) is one such type of antibiotic which is primarily used for the infectious diseases caused by anaerobic bacteria and protozoa. Complete removal of metronidazole from the environment by conventional method is difficult because of its low degradability and high solubility in water. Dye contamination is another critical environmental problem and addressed by several researchers till now. The sources of synthetic dyes in wastewater are from different industries such as, textile, dye and dye intermediates, paper and pulp, printing, colour photography, petroleum industries, and so on.

[344,345] Continuous discharge of dye-bearing effluents from these industries into natural stream and rivers poses severe environmental problems as toxic to useful microorganisms, aquatic life, and human beings. So, suitable and efficient techniques are highly essential for the treatment of these industrial effluents.

In this study Ag-h-TiO$_2$ nanoparticles were synthesized through a sacrificial core technique using AgBr as the core. The core was removed under a mild condition by dissolving in ammonium hydroxide solution, and the silver doping was also achieved during the dissolution of the core without any addition extra dopant precursor. After Ag doping, pure anatase phase TiO$_2$ particles were obtained even after heating at 450 °C. The hollow structure nanoparticles have higher surface area (198.3 m^2/g) compared to solid TiO$_2$ nanoparticles (95.1 m^2/g) and hollow structures reported by other researchers. [522–526] To test the photocatalytic activity of the developed nanoparticles towards three important organic compounds such as nitrobenzene (NB), metronidazole (MTZ), and methylene blue dye (MBD) degradation studies were conducted with low catalyst dose and high initial MTZ concentration compared to the studies reported till now. The obtained TiO$_2$ particles are having low band gap, anatase phase, high surface area, good crystallinity, and efficient visible light induced photocatalytic property to degrade important organic compounds such as nitrobenzene, antibiotic, and dye.

4.2   Materials and Methods

4.2.1   Chemicals and Materials

Reagent-grade silver nitrate (99.9%) and potassium bromide (99.3%) were purchased from Rankem. Anionic surfactant sodium dodecyl benzene sulphonate (SDBS) (technical grade, Cat No. 28995-7) and titanium (IV) butoxide (Ti[O(CH$_2$)$_3$CH$_3$]$_4$ or TOBT, 97%) were obtained from Sigma Aldrich. Ammonium hydroxide (25%), nitric acid (69% GR), cyclohexane, and methylene blue dye were bought from Merck. Nitrobenzene was provided by Nice Chemicals Pvt. Ltd. Metronidazole was supplied by J B Chemicals & Pharmaceuticals Ltd. All the chemicals were used as it was received without any further purification. Ultrapure water of 18.2 MΩ.cm resistivity and pH 6.4–6.5 was used for all the experiments.

4.2.2   Methods

A sol-gel method was followed for the synthesis of silver doped hollow TiO_2 nanoparticles using AgBr as the sacrificial core (Scheme 4.1). The AgBr nanoparticles were synthesized in aqueous SDBS media according to the reported study.[527] The concentrations of both $AgNO_3$ and KBr were maintained at 0.1 mM. After the formation of AgBr NPs the suspension was sonicated using a bath sonicator for 20 min, TBOT was then added slowly under constant stirring condition for uniform coating on the core surface. After 5 minutes of addition of TBOT, HNO_3 was added to maintain the pH of ~2 and kept for 35 min under stirring condition. The $AgBr/TiO_2$ core/shell nanoparticles were then separated by centrifugation at 25,000 rpm for 20 min and washed thrice with ethanol and water mixture (2:1, v/v). Then the particles were dipped in ammonium hydroxide solution (2.5 mM) for 48 hrs for the dissolution of AgBr core. The particles were separated and calcined at 450°C for 2 hrs to improve the crystallinity. For quantum yield (QY) calculation of Ag-h-TiO_2 NPs, phenol was used as a reference (QY=0.14).
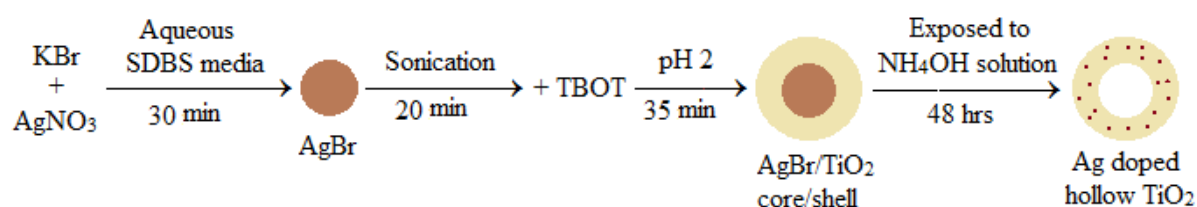
Scheme 4.1. Schematic presentation for the formation of Ag-h-TiO_2 nanoparticles.

4.2.3 Particles Characterization

The particle size was measured initially by dynamic light scattering (DLS) using a Malvern Zeta Size analyzer, (Nano ZS). The crystallinity of synthesized particles was characterized using powder X-ray diffraction (XRD) (Philips, PW 1830 HT) with scanning rate of 0.01°/s in the 2θ range from 20° to 70°. The size and shape of the particles were observed under a field emission scanning electron microscope (FE-SEM) (FEI, Nova NanoSEM NPE212) and transmission electron microscope (TEM) (FEI, Tecnai S-twin). The elemental composition of the sample was analyzed by energy-dispersive X-ray spectroscopy (EDX) (Oxford Instruments, model X-sight) attached to the HR-TEM (JEOL, JEM 2100). The light absorbance and luminescence properties were also characterized by UV–vis–NIR Spectroscopy (Shimadzu, UV-3600) and fluorescence spectroscopy (Hitachi, F-7000) respectively. Fourier transform infrared spectroscopy (FT-IR) was carried out using an FT-IR (Thermo Fisher Scientific, Nicolet iS10). The chemical composition of the samples and the valence states of various elements were analyzed by X-ray photoelectron spectroscopy (XPS,

ULVAC-PHI, Inc., PHI 5000 Versa Probe II.). The surface area of the nanoparticles was measured by Brunauer–Emmett–Teller (BET) technique (Quantachrome, USA).

4.2.4 Photocatalytic Degradation

The photocatalytic activity of the synthesized catalyst was tested by the degradation of NB, MTZ antibiotic, and MBD in aqueous solutions. For nitrobenzene degradation the initial concentration of nitrobenzene and catalyst dose were maintained 61.5 mg/L and 0.05 g/L. For MTZ degradation the initial concentration of the MTZ solution was maintained to 15 mg/L for all experiments and the catalyst concentration was 0.5 g/L. The MBD degradation was carried out with 25 mg/L initial concentration of dye and the catalyst concentration of 0.25 g/L. The degradation studies were conducted in a photoreactor equipped with a 125 W high pressure mercury vapour lamp (λ=435.8 nm, light intensity 27000 LUX, light energy 56 ± 2 w/m^2) placed about 12 cm away from the solution. The solutions were stirred continuously using a magnetic stirrer. Prior to each test, the lamp was turned on 10 min before in order to get a maximum light intensity. The samples were magnetically stirred for 20 min in the dark to allow physical adsorption equilibrium of NB, MTZ, and MBD on the catalyst surface. Then the suspension was exposed to visible light irradiation under constant stirring condition. The sample was then taken out and centrifuged to remove the nanoparticles after each 20 min interval for MTZ and 30 min interval for NB and MBD degradation. Then the concentration of the NB, MTZ, and MBD solution were analyzed using a UV-Vis-NIR Spectrophotometer at its maximum absorbance wavelength of $\lambda = 267$, 320, and 661 nm for NB, MTZ, and MBD, respectively. The cyclic degradation test was conducted to check the reusability of the photocatalyst. After each cycle of degradation the catalyst was separated by centrifugation and was used for the next cycle of degradation without any pre-treatment. The intermediate and final degraded products during nitrobenzene degradation were analyzed by liquid chromatography-mass spectrometry (LC-MS) (Flexar SQ 300 MS, Perkin Elmer). The sample was extracted with cyclohexane and 70% water/30% acetonitrile (v/v) mobile phase was used for the analysis.

4.3   Results and Discussion

4.3.1 Synthesis of Hollow TiO$_2$ Particles

The hollow particles were synthesized by the templated sacrificial core method using AgBr as a core. In aqueous media the surface charge of AgBr nanoparticles is -15 to -25 mV.

Addition of anionic surfactant (SDBS) makes the surface charge of AgBr more negative (-47.8 mV). The surface charge of TiO_2 nanoparticles is positive, so, it is expected that the TiO_2 will favourably coat on the AgBr core surface because of the electrostatic attraction. When ammonium hydroxide solution was added to the particle suspension, AgBr would try to dissolve in ammonium hydroxide through the formation of soluble complex according to equation 4.1. During the dissolution of AgBr, there is a chance of doping of Ag on TiO_2 shell.

$$AgBr \ (s) + 2 \ NH_3 \ (aq) \rightarrow Ag(NH_3)_2^+(aq) + Br^- \hspace{2cm} (4.1)$$
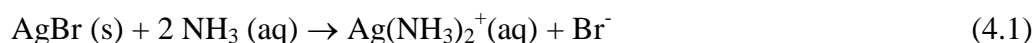
4.3.2 Characterization of Particles by UV-Vis Spectroscopy

UV-Vis spectroscopic study was done to investigate the light absorption property of the nanoparticles, and the results are presented in Figure 4.1. The Figure shows that the sharp peak of pure AgBr is present in the UV region (237 nm), and it disappears after the coating of external shell layer of TiO_2 on AgBr. Pure TiO_2 is having major absorption below 350 nm wavelength, and there is no absorption in the visible region, this is because of its high energy band gap (3.2 eV). However, the UV-Vis spectra of Ag-h-TiO_2 nanoparticles show a significant absorption in 300-650 nm wavelength range. The shifting of absorbance in the visible range is attributed to the fact of lowering of the band gap of the obtained nanoparticles because of doping of Ag. In addition, noteworthy to mention that, the absorption intensity of Ag-h-TiO_2 is higher compared to that of pure solid TiO_2 in both UV as well as in visible regions. The increase in absorbance is also attributed to the fact of porous hollow structure and formation of shell layer by the deposition of small particles. The band gap energy was calculated using the equation $E_g = 1239.8/\lambda$ [474] to support the above fact, where E_g is the band gap (eV) and λ is the wave length (nm) of the absorption edges in the UV –Vis spectrum. It has been found that the calculated band gaps are 2.69 and 3.29 eV for AgBr and TiO_2, which are in good agreement with the reported values of 2.7 eV [528] and 3.28 eV [529] respectively, whereas, 2.48 and 2.25 eV for AgBr/TiO_2 and Ag-h-TiO_2 nanoparticles respectively. Since the band gap of the TiO_2 is reduced after the formation of doped hollow structure, it is expected to be useful as good photocatalyst under the visible light irradiation, dye sensitized solar cells, or other electrochemical applications.
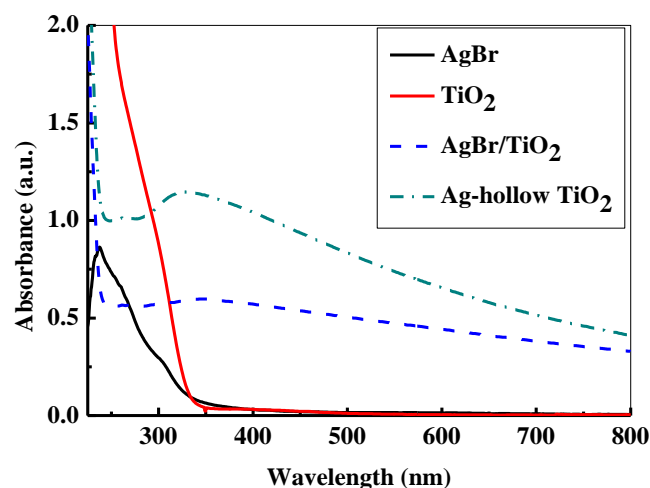
Figure 4.1. UV –Vis spectra of as synthesized AgBr, TiO$_2$, AgBr/TiO$_2$, and Ag-h-TiO$_2$ nanoparticles.

4.3.3 Characterization of Particles by X-ray Diffraction

The crystallographic phases of the nanoparticles were identified by XRD technique. The diffraction patterns of all particles are presented in Figure 4.2. For pure AgBr, the XRD pattern displays peaks at 2θ value of 26.6, 30.9, 44.3, 55.2, 64.5, and 73.3° corresponding to the planes (111), (200), (220), (222), (400), and (420) of cubic structure (JCPDS card no.79-0149). For pure TiO$_2$, the anatase peaks were obtained at 2θ value of 25.1, 36.5 and 62.3° corresponding to the planes (101), (103), and (204) (JCPDS card no.71-1169). The peaks rutile phase were obtained at 2θ values of 27.3, 54.1, and 68.6° corresponding to the planes (110), (211), and (301) (JCPDS card no.76-0319). For AgBr/TiO$_2$ core/shell nanoparticles the XRD pattern shows the peaks of both AgBr and TiO$_2$, but the peak intensity of AgBr is reduced and that of TiO$_2$ becomes more dominant mainly because of TiO$_2$ coating. For Ag-h-TiO$_2$ NPs the TiO$_2$ anatase peaks (2θ) were obtained at 25.6, 37.4, 48.6, and 63.2° corresponding to the planes of (101), (103), (200), and (204) (JCPDS card no. 75-1537) with the peaks of elemental silver at 2θ values of 44.3 and 64.7, corresponding to the planes (200) and (220) (JCPDS card no.03-0931) respectively. Additionally, another important observation is the rutile peak at 2θ = 27.3° is absent in the hollow structure, while compare with pure TiO$_2$ NPs. The XRD analysis also shows that the anatase TiO$_2$ peak (2θ) of (101) plane shifts from 25.1° to 25.6° after the formation of hollow structure, which attributed to the silver doping to TiO$_2$ lattices.
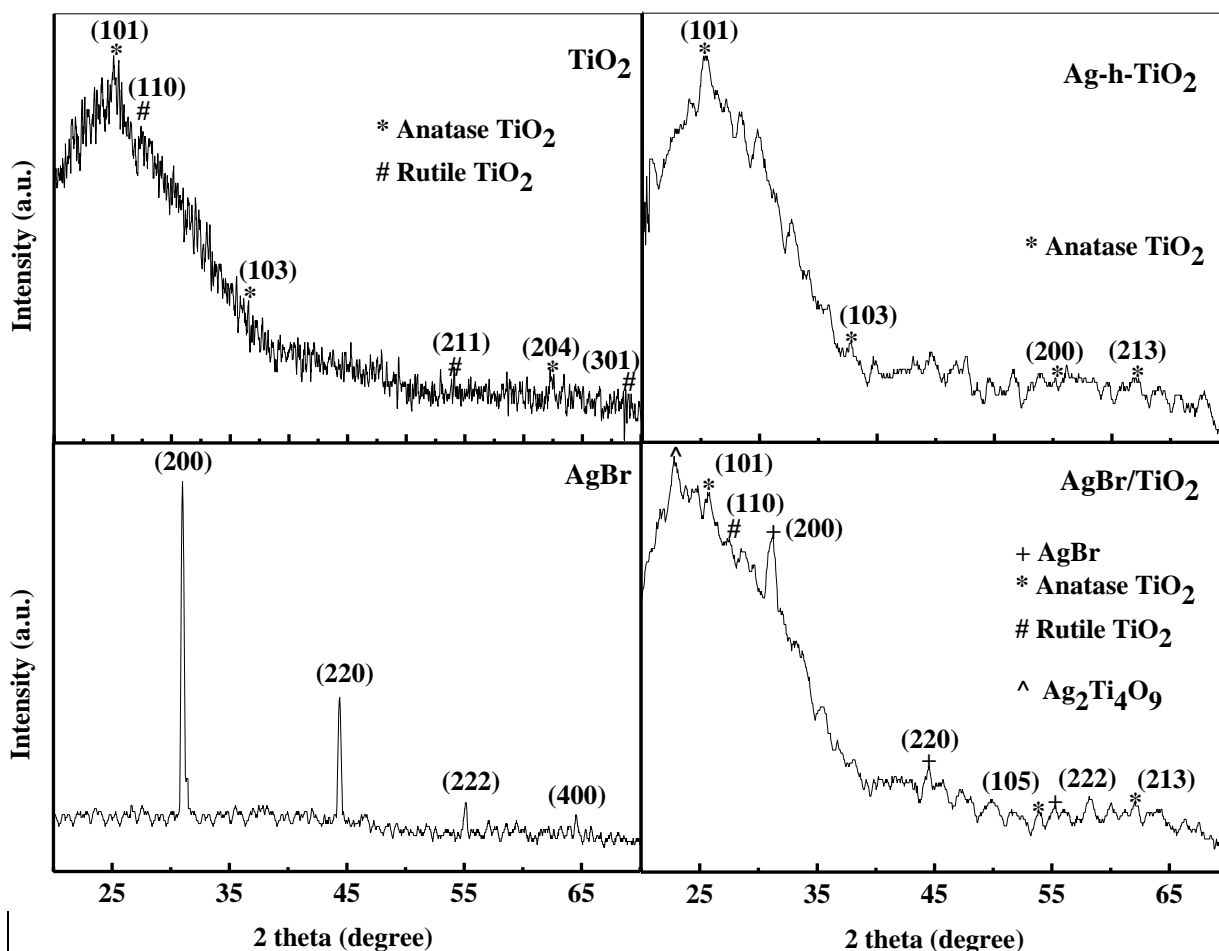
Figure 4.2. The X-ray diffraction patterns of AgBr, TiO_2, AgBr/TiO_2 core/shell, and Ag-h-TiO_2 nanoparticles.

4.3.4 Characterization of Particles by TEM and FE-SEM

The Figure 4.3a shows the TEM image of AgBr/TiO_2 core/shell nanoparticles before expose to ammonium hydroxide solution. The contrast difference between the core and shell in the image indicates the formation of core/shell structure. The particles are spherical in shape, and the size distribution is plotted in Figure 4.3c which indicates the mean particle size of 17.86 ± 2.46 nm and the shell thickness is ~ 2.5 nm. The TEM image of AgBr/TiO_2 core/shell particles after dissolution in ammonium hydroxide solution is presented in Figure 4.3b. The particle size distribution is plotted in Figure 4.3d which shows mean particle size of 17.76 ± 2.85 nm, which is almost same as it was before the dissolution. The FE-SEM image (Figure 4.4) clearly shows some of the broken hollow spheres. The TEM image of single contrast indicates the removal of core. So, the TEM and FE-SEM images confirm the formation of hollow TiO_2 particles after treatment with ammonia solution. The high resolution TEM image of Ag-h-TiO_2 nanoparticles (Figure 4.5a) shows lattice fringes spacing of 0.353 nm

corresponding to the (101) plane for anatase phase TiO_2 (JCPDS card no. 75-1537) previously confirmed by XRD. But there is no lattice fringe of rutile TiO_2 or Ag, which confirms 100% anatase phase of TiO_2 and no surface deposition of Ag. The Figure 4.5b shows the selected area electron diffraction (SAED) pattern of the hollow particle by focusing the electron beam on a single particle. The ring like diffraction pattern is indexed to (101) and (200) planes of TiO_2 together with (200) diffraction of silver, which confirms the presence of silver inside the crystal structure of TiO_2 nanoparticles. The EDX in Figure 4.5c further confirms the presence of silver, titanium, and oxygen atoms. Some extra peaks of Cu and C are mainly from TEM grids.
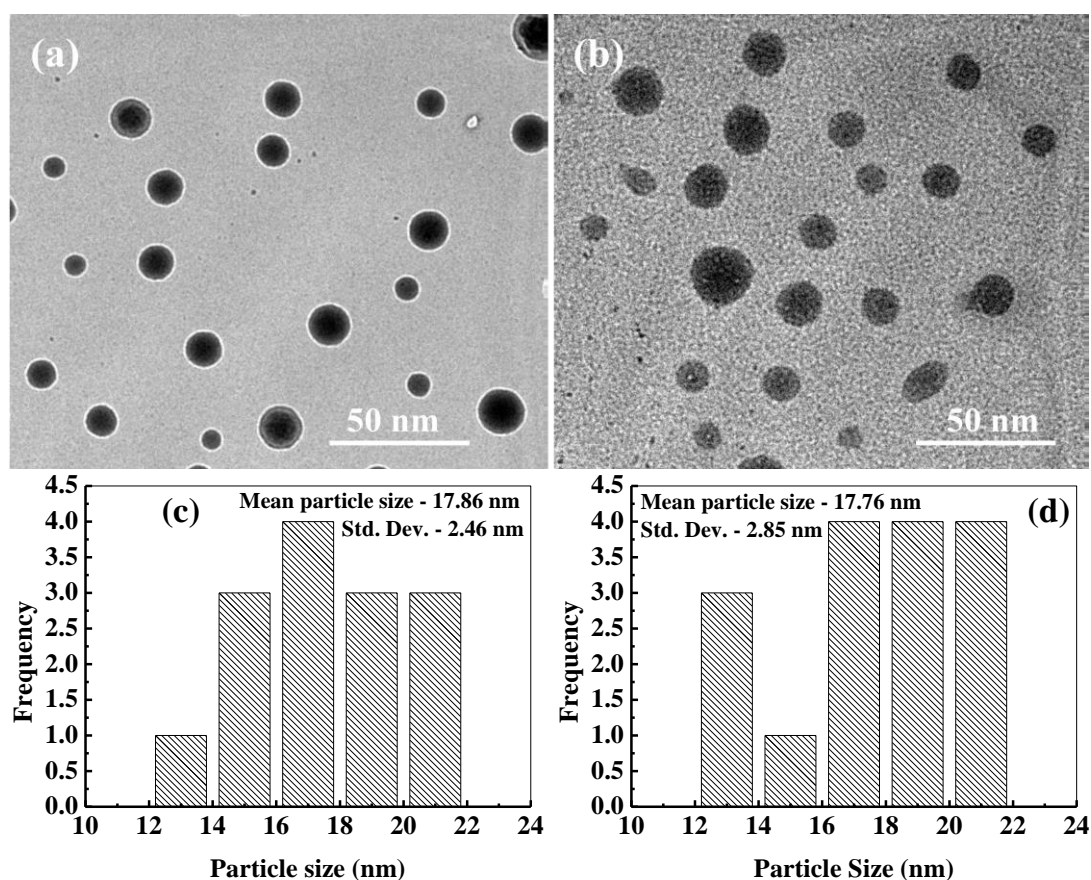
Figure 4.3. TEM images of (a) $AgBr/TiO_2$ core/shell, and (b) Ag-h-TiO_2 hollow nanoparticles. Particle size distributions of (c) $AgBr/TiO_2$ core/shell, and (d) Ag-h-TiO_2 nanoparticles.
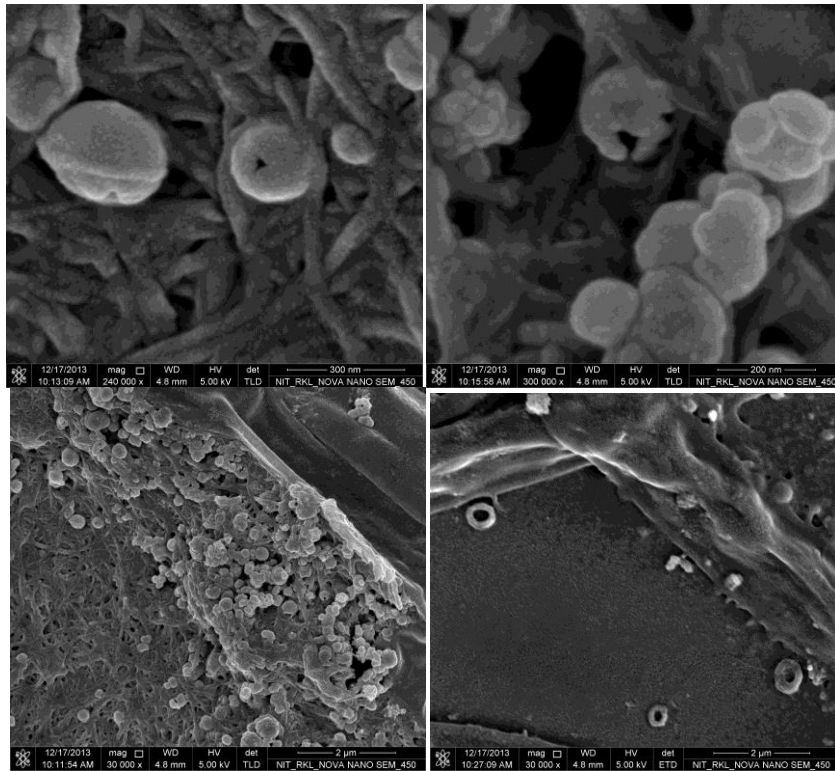
Figure 4.4. FE-SEM images of Ag-h-TiO$_2$ nanoparticles with some broken hollow structure.
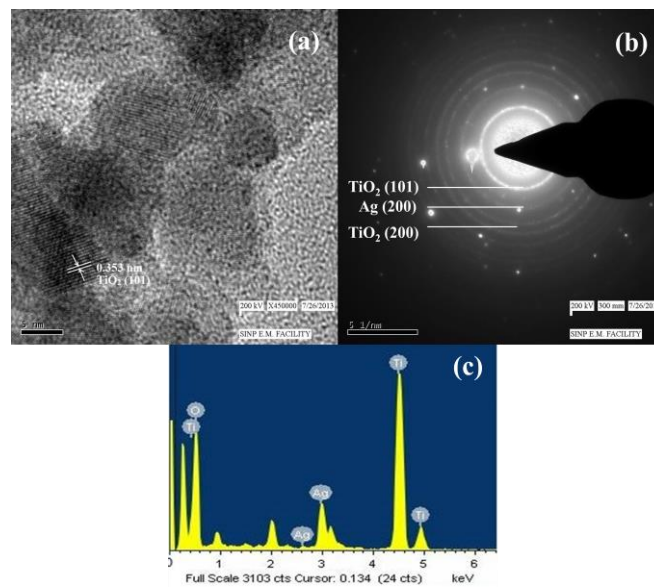
Figure 4.5. (a) HR-TEM image (b) SAED pattern, and (c) EDX pattern of Ag-h-TiO$_2$ nanoparticles.

4.3.5 Characterization of particles by XPS

For the further confirmation of the surface composition and the chemical states of Ag-h-TiO$_2$ nanoparticles, XPS analysis was carried out. The high resolution XPS spectra of Ag (3d), Ti (2p) and O (1s) are presented in Figure 4.6. The XPS peak at 462.9 eV corresponds to Ti 2p$_{1/2}$, and 457.2 eV corresponds to Ti 2p$_{3/2}$ in the Ti 2p region (Figure 4.6a). The slitting between Ti2p$_{1/2}$ and Ti 2p$_{3/2}$ is 5.9 eV which indicates the normal state of Ti^{4+} in the mesoporous anatase TiO$_2$. [475] The XPS peak (Figure 4.6b) at ~530 eV corresponds to the lattice oxygen of TiO$_2$ crystal and peaks at 532.1 and 531.7 eV correspond to the adsorbed oxygen on TiO$_2$ surface. Figure 4.6c shows the Ag 3d$_{3/2}$ and Ag 3d$_{5/2}$ peaks at the binding energy of 366.5 and 372.6 eV, respectively with a slitting of the 3d doublet of 6.1 eV, which suggest the zero valence silver instead of Ag$^+$ ions within the material. [530] So, the possible location of dopant is attributed as the surface or in the interstitial sites of the host material. The TEM or FE-SEM images confirm that there is no surface deposition of the silver on the particles. So, there is a fair possibility of the silver doping in the interstitial sites of the host material.
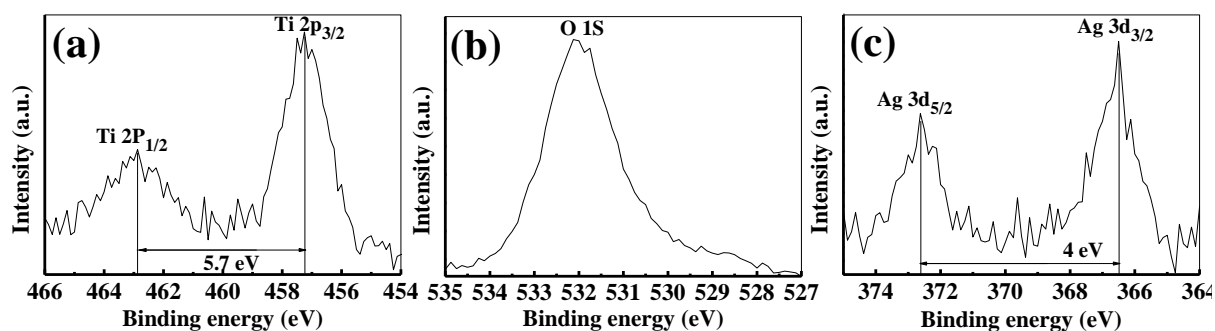
Figure 4.6. High resolution XPS narrow scan spectra of (a) Ti(2p), (b) O(1s), and (c) Ag(3d) for Ag-h-TiO$_2$ nanoparticles.

4.3.6 Characterization of particles by BET analysis

The specific surface area of the pure and hollow doped TiO$_2$ nanoparticles was measured by BET technique. Before the adsorption-desorption study the sample was degasified for 1 hr at 150°C temperature. The nitrogen adsorption-desorption isotherm of pure TiO$_2$ and Ag-h-TiO$_2$ nanoparticles are plotted in Figure 4.7a and 4.7b. The presence of broad hysteresis loop confirms the presence of mesopores. The BET surface area of solid TiO$_2$ and Ag-h-TiO$_2$ nanoparticles are 95.1 and 198.3 m^2/g respectively. The Ag-h-TiO$_2$ nanoparticles are having 103.2 m^2/g more surface area compare to that of solid TiO$_2$. The obtained surface area of

hollow structure TiO_2 is higher compared to the literature values of 38.9 - 123 m^2/g [62–66] This might be because of the core removal technique and the final particle size. In most of the literature the core was removed by calcinations but in our case the core is removed by dissolution at room temperature. The high surface area hollow structure TiO_2 is expected to be useful for the catalysis or other applications.
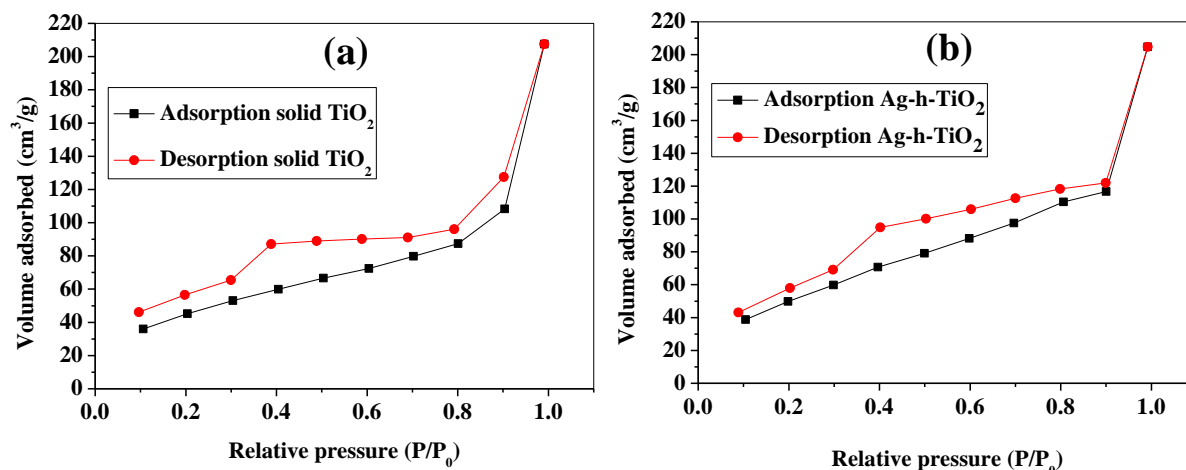
Figure 4.7. Nitrogen adsorption-desorption isotherm of (a) solid TiO_2 and (b) Ag-h-TiO_2 nanoparticles.

4.3.7 Photoluminescence activity of the synthesized nanoparticles

The photoluminescence (PL) properties of the synthesized nanoparticles were also checked by the fluorescence spectroscopy in terms of light emission. The light emission data was recorded between 500-600 nm wavelengths while excitation at 270 nm. The emission spectra of AgBr, TiO_2, AgBr/TiO_2, and Ag-h-TiO_2 NPs are presented in Figure 4.8. All the particles show emission in the visible region of wavelength $\sim$ 543.8 nm. The intensities of emission are in the following order: AgBr > Ag-h-TiO_2 > AgBr/TiO_2 > TiO_2. The pure TiO_2 have very low intensity compared to pure AgBr and the intensity increases after the formation of Ag-h-TiO_2 NPs.
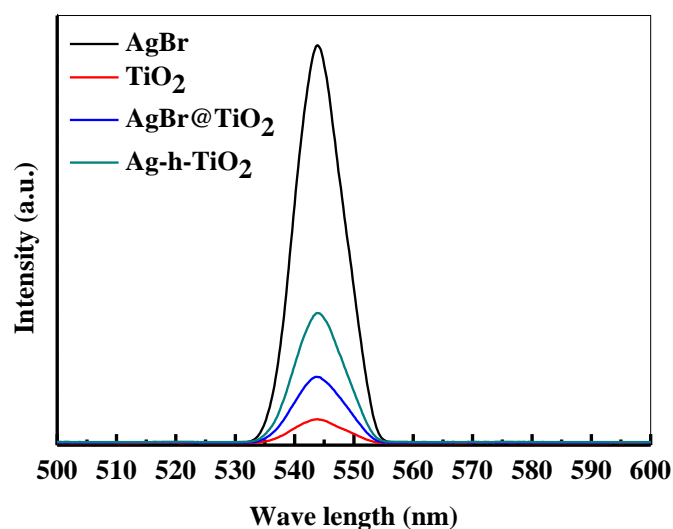
Figure 4.8. Light emission spectra of AgBr, TiO$_2$, AgBr/TiO$_2$, and Ag-h-TiO$_2$ NPs after excitation at 270 nm wavelength.

The quantum yield (QY) was calculated for these materials from UV and PL data (Equation 4.2) using phenol as the standard material (QY = 0.14). The QYs of TiO$_2$, AgBr, AgBr/TiO$_2$, and Ag-h-TiO$_2$ NPs are 0.29, 0.498, 0.36, and 0.477 respectively. So, the quantum yield of TiO$_2$ is enhanced by 18.7% after the formation of hollow structure and Ag doping. From these results it can be pointed out that the Ag–h-TiO$_2$ nanoparticles has enhanced light emission property and QY compared to that of pure TiO$_2$ nanoparticles. So, the light emission properties along with the catalytic properties could be utilized for better photocatalyst or dye sensitized solar cells applications.

$$Q.Y_S = Q.Y_R \left(\frac{Grad_S}{Grad_R} \right) \times \left(\frac{\eta_S}{\eta_R} \right)^2 \qquad 4.2$$

Where, Q.Y$_S$ – Quantum yield of the sample

Q.Y$_R$ – Quantum yield of the reference (Phenol)

Grad$_S$ – Slope of the Integrate intensity vs. absorbance line for sample

Grad$_R$ – Slope of the Integrate intensity vs. absorbance line for reference (Phenol)

η_S – Refractive index of the sample

η_R – Refractive index of the reference (Phenol)

4.3.8 Photocatalytic Applications of Synthesized Nanoparticles

4.3.8.1 Photodegradation of Nitrobenzene

The photocatalytic activities of the synthesized Ag-h-TiO$_2$ nanoparticles were first tested for the degradation of NB under the visible light irradiation. The degradation studies using pure and Ag doped solid TiO$_2$ (Ag-TiO$_2$) were also employed as the photocatalyst for the comparison purpose. The results of NB degradation in visible light are shown in Figure 4.9. It has been found that the degradation process reaches a plateau level after 3.5 hrs of light exposure time. The results show that at the plateau level, the degradation efficiencies of NB are 58.46, 89.61, and 95.5% in the presence of TiO$_2$, Ag-TiO$_2$, and Ag-h-TiO$_2$ NPs respectively (Figure 4.9a). The results clearly indicate that the maximum degradation of the NB was obtained in the presence of the Ag-h-TiO$_2$ NPs. The degradation results were also fitted with different kinetic models, and it was found that the first order kinetics fits well for all the materials. The Figure 4.9b presents the reaction kinetics of NB degradation. The rate constants (k) of the photocatalytic degradation reactions obtained from the experimental results are 0.0045, 0.0109, and 0.016 min^{-1} for TiO$_2$, Ag-TiO$_2$, and Ag-h-TiO$_2$ NPs respectively. The rate constant of Ag-h-TiO$_2$ photocatalytic process is about 3.6 and 1.5 times than that of pure TiO$_2$ and Ag-TiO$_2$ photocatalytic processes respectively. A comparison at 50% degradation times for NB shows 136.5, 41.5, and 27 min for TiO$_2$, Ag-TiO$_2$, and Ag-h-TiO$_2$ nanoparticles, respectively. These results reveal that Ag-h-TiO$_2$ nanoparticles have higher photocatalytic activity compared to that of pure TiO$_2$ and Ag-TiO$_2$ NPs. This is attributed to the fact that pure TiO$_2$ is having low yield of $^{\bullet}$OH radicals because of recombination of the charge carriers during photodegradation, which helps to oxidize the organic compound as stated in our previous study. [531] In Ag doped TiO$_2$ NPs the Ag dopant accepts the photoinduced electrons and holes, which in turn act as electron/hole traps and prevents the recombination of the charge carriers. In Ag-h-TiO$_2$ NPs, addition to Ag doping it is having more surface area (198.3 m^2/g as mentioned in the BET analysis) compared to solid TiO$_2$ (95.1 m^2/g), which is useful for better catalytic processes. Additionally, as mention in the XPS section, the presence of adsorbed oxygen on the TiO$_2$ surface allows the H$^+$ hydroxylation to form –Ti(OH)-O-Ti-(OH)- in the presence of water. During the photodegradation, this compound may help to generate the photogenerated hole (h$^+_{VB}$) and finally turn to $^{\bullet}$OH free radicals, which is beneficial for the photocatalysis. [532] While comparing the degradation efficiency and PL intensity, it can be seen that Ag-h-TiO$_2$ is having high degradation efficiency as well as PL intensity compared to that of pure TiO$_2$. In

general high PL intensity is due to the high recombination of electrons and holes. Our results can be attributed in the following way. In the presence of doping, the reduction in recombination continues up to the certain limit of doping percentage (optimum doping) and then again recombination starts increasing with the increasing doping %. [533,534] From the EDX study it is seen that 9.02% doping is achieved, which is higher compared to optimum doping percentage (1%) for TiO_2, [531] we believe because of that the PL intensity is high. At the same time, as the surface area of hollow particles is higher than solid TiO_2, the degradation efficiency is more because of more adsorption of dye molecules. The reusability of Ag-h-TiO_2 NPs was tested by recycling the catalyst under the same condition, and the results are plotted in Figure 4.9c. The results show there is a ~10.83% decrease (95.5 to 84.67%) in degradation efficiency after sixth cycles. The turn over number (TON) of the photocatalyst is calculated as 0.467, 0.716, and 0.763 mol/mol for the first cycle of the TiO_2, Ag-TiO_2, Ag-h-TiO_2, respectively.
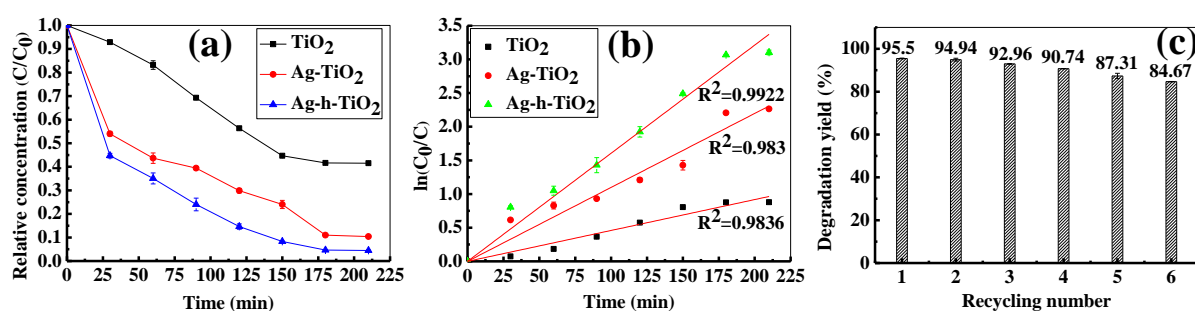
Figure 4.9. (a) Photodegradation kinetics of nitrobenzene under visible light of high pressure mercury vapour lamp using TiO_2, Ag-TiO_2 and Ag-h-TiO_2 NPs. (b) Fitting of first order kinetics with the experimental data. (c) Recycling test of Ag-h-TiO_2 for the degradation of nitrobenzene solution.

From the reported literatures (Table 4.1) it is has been found that more than 90% degradation efficiency of nitrobenzene was achieved either in the presence high catalyst dose, low organic concentration, in the presence of UV light irradiation, or in presence of some additives and at specific pH. In this regard, our catalytic process is more effective in normal visible light and in the absence of any additives than the already reported literatures.

Table 4.1. Comparison of the present work of nitrobenzene degradation with the published literature

Catalyst	catalyst dose	Initial NB conc	Light source	Time	parameters	% deg.	Ref.
N-Ce-TiO$_2$	1 g/L	50 mg/L	visible lamp, 300 W	4 hrs	30°C	53	[535]
TiO$_2$	0.2 g/L	50.1 mg/L	14 W UV lamp, 254 nm	3 hrs	air feeding of 150 mL/min	90	[536]
Nano crystalline TiO$_2$	0.2 g/L	49.94 mg/L	mercury vapour lamp	8 hrs	air purging	98%	[537]
Ce-TiO$_2$	0.1 g/L	25 mg/L	Visible lamp 500 W	7 hrs	pH 9	100	[538]
Pt/Cd$_2$Sb$_2$O$_{6.8}$	2.5 g/L	100.047 mg/L	Xenon lamp	3 hrs	CH$_3$OH	~100	[539]
TSA-MIP-TiO$_2$	0.1 g/L	6.153 mg/L	9 W UV lamp, 253.7 nm	90 min	-	>95	[540]

Further, to explore the degradation pathway of NB in the presence of TiO$_2$, Ag-TiO$_2$, and Ag-h-TiO$_2$ photocatalysts, LC-MS study was conducted to identify different photo degraded products. Based on the LC-MS results probable degradation path is proposed in Figure 4.10. During the photodegradation, the $^\bullet$OH radicals attack the nitrobenzene and subsequently produce some aromatic compounds, such as benzene, phenol, catechol, resorcinol, and hydroquinone. The hydroquinone again forms benzoquinone through the dehydrogenation. Further degradation of the aromatic compounds happens through the ring cleavage and some degraded product, such as propionic acid, n-butanol, di-ethyl ether, furan, orthoformic acid, propanol, and acetic acid are formed.
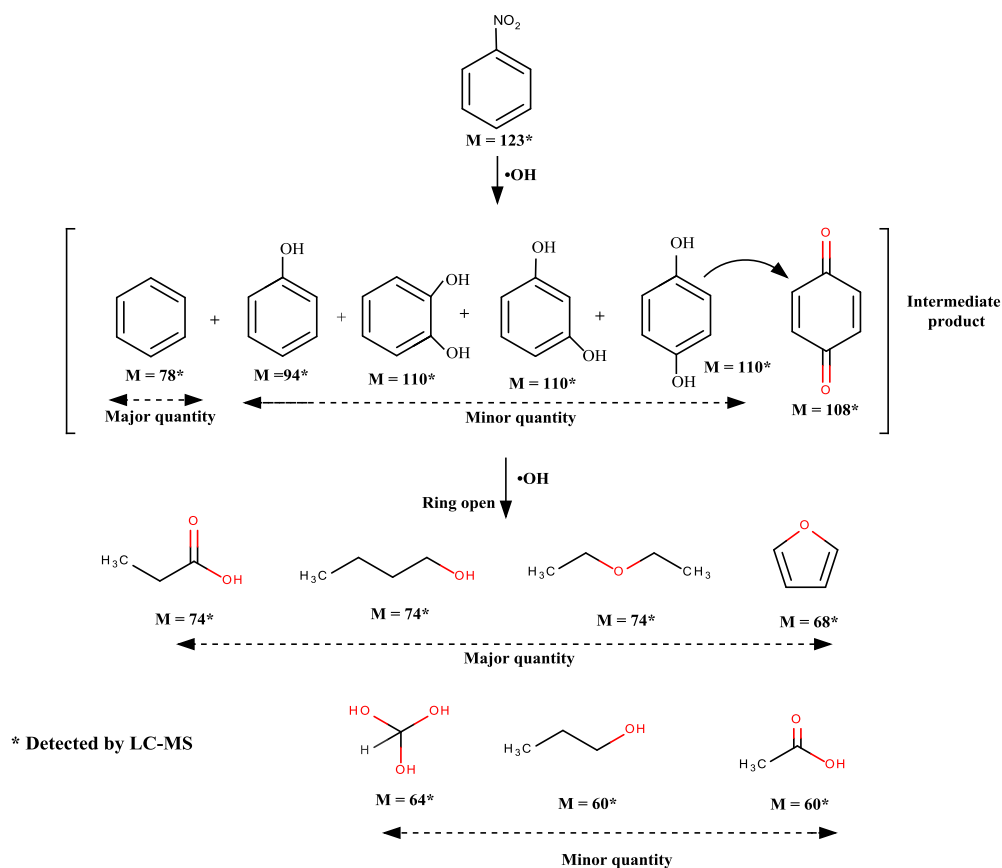
Figure 4.10. Probable pathway for the degradation of nitrobenzene under visible light in the presence of TiO_2, Ag-TiO_2, and Ag-h-TiO_2.

4.3.8.2 Photocatalytic Degradation of Metronidazole Antibiotic

Since the Ag-h-TiO_2 nanoparticles show good photocatalytic degradation against the NB, the same catalyst was also used to study the photodegradation efficiency on metronidazole antibiotic under the visible light irradiation. The degradation results (Figure 4.11a) show that at the plateau level the degradation of MTZ is 96.55% in the presence of Ag-h-TiO_2 NPs, while pure TiO_2 and Ag-TiO_2 degraded 80.78 and 94.39% of MTZ. [531] The rate constant of the photocatalytic degradation reactions obtained from the experimental results is 0.0269 min^{-1} for Ag-h-TiO_2 NPs. The results of reusability test of Ag-h-TiO_2 NPs (Figure 4.11b) show there is a ~10.76% decrease (96.55 to 85.79%) in degradation efficiency after sixth cycles. It can be noted that the difference between hollow and solid TiO_2 is not significant (~2%), in spite of significantly high surface area for hollow particles, which can be attributed to the low initial MTZ concentration. So, the initial concentration of MTZ was increased to 30 mg/L and it has been found that after 2 hrs the Ag-TiO_2 and Ag-h-TiO_2 NPs degraded 88.5 and 94.77% MTZ (Figure 4.11c) with rate constants 0.019 and 0.024 min^{-1} (Figure 4.11d) for Ag-TiO_2

and Ag-h-TiO$_2$ NPs respectively. These results indicate that, when the concentration of organic molecules is high hollow particles show better efficiency.
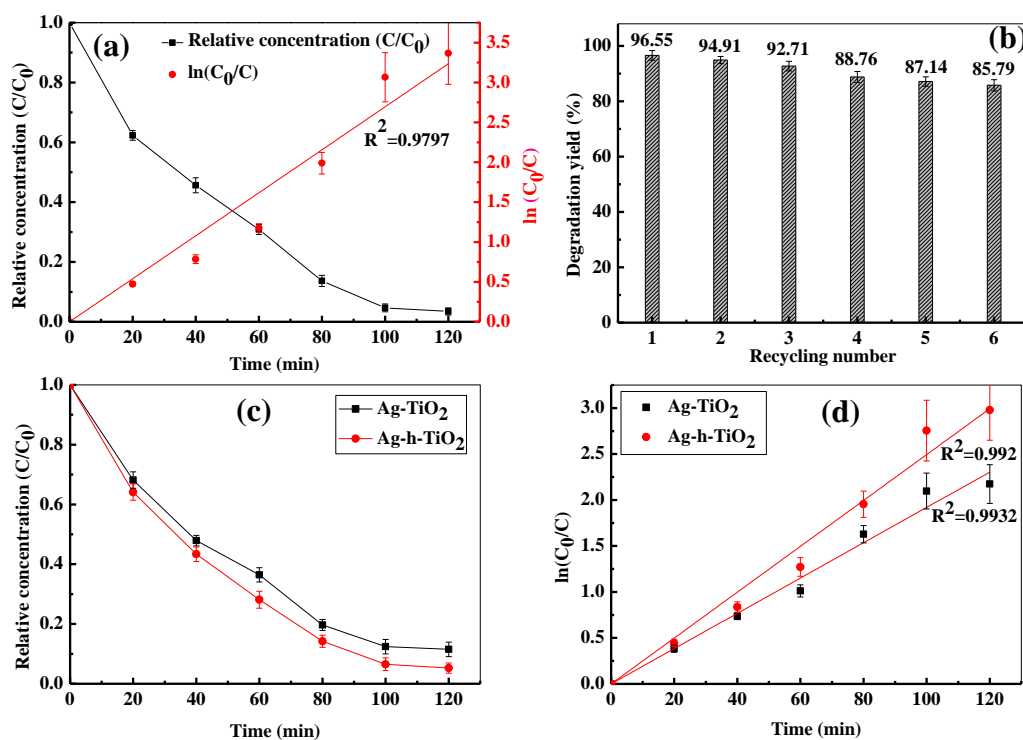
Figure 4.11. (a) Photodegradation kinetics and fitting of first order kinetics with the experimental data of MTZ degradation under visible light of high pressure mercury vapour lamp using Ag-h-TiO$_2$ NPs with 15 mg/L of initial MTZ concentration. (b) Recycling test of Ag-h-TiO$_2$ for the degradation of MTZ solution. (c) Photodegradation kinetics and (d) Fitting of first order kinetics with the experimental data of MTZ using Ag-TiO$_2$ and Ag-h-TiO$_2$ NPs with 30 mg/L initial concentration of MTZ.

4.3.8.3 Photocatalytic Degradation of Methylene Blue Dye

The nanocatalyst was further used for the degradation of MBD degradation under the visible light. The degradation results are presented in Figure 4.12. The dye degradation efficiency of Ag-h-TiO$_2$ is 96.77 % after 3 hrs exposure time (Figure 4.12b). The physical appearance of dye solutions before and after the light irradiation under Ag-h- TiO$_2$ photocatalyst is presented in Figure 4.12a. The rate constant of photocatalytic degradation of MBD under the visible lamp using Ag-h-TiO$_2$ NPs is 0.0216 min^{-1} (Figure 4.12c). Similar to previous study Ag-h-TiO$_2$ sample was further selected for cyclic degradation test under the same condition and found there is a decrease in efficiency of ~ 10.47% (96.77 to 86.3%) after sixth cycle of photodegradation (Figure 4.12d).
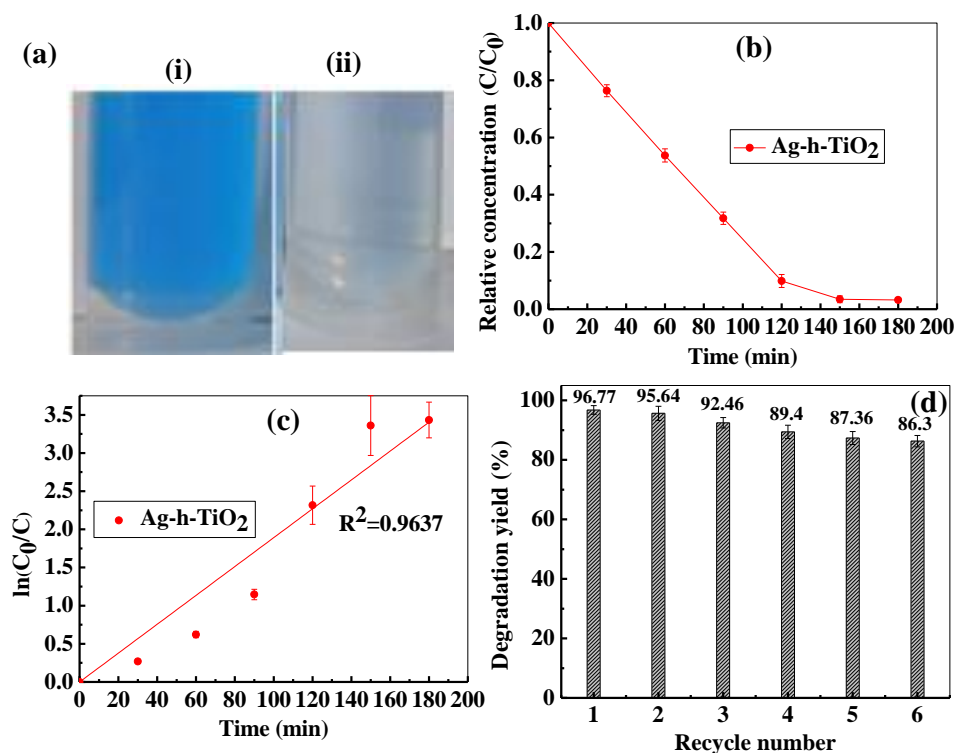
Figure 4.12. (a) The images of the methylene blue solution before (i) and after degradation under (ii: Ag-h-TiO$_2$). (b) Photocatalytic degradation and (c) Kinetic data for the degradation of MBD solution in high pressure mercury vapour lamp under Ag-h-TiO$_2$ NPs. (d) Recycling test of Ag-h-TiO$_2$ for the degradation of MBD solution under visible light.

For each type of organic compound degradation, two sets of reference studies, (i) organic solution + catalyst in dark and (ii) only organic solution under visible light irradiation were carried out. The first was to test only adsorption capacity. Since the catalyst concentration was low, there was no significant change found because of adsorption. So we confirmed that the concentration change was only because of degradation.

4.4   Conclusions

The hollow TiO$_2$ nanoparticles were synthesized by a sacrificial core method using AgBr as sacrificial core. During the removal of core, Ag was doped in the interstitial sites of the host TiO$_2$. The obtained Ag-h-TiO$_2$ nanoparticles are purely in anatase phase and good crystalline in nature. The mean particle size is 17.76 ± 2.85 nm with wall thickness of ~ 2.5 nm. The increase of surface area for hollow nanoparticles is 103.2 m^2/g more compared to that of solid TiO$_2$ nanopaticles. Apart from the surface area, the quantum yield of Ag-h-TiO$_2$ nanoparticles also increases to 18.7% compared to that of pure solid TiO$_2$ nanoparticles. The nanoparticles were used for the photo degradation of NB, MTZ antibiotic and MBD. The

maximum NB degradation was obtained 95.5% under visible light irradiation for 3.5 hr. The metronidazole degradation efficiency was found to be 96.55 and 94.77% under the irradiation of visible light for the initial MTZ concentration of 15 and 30 mg/L with catalyst dose of 0.5 g/L. The Ag-h-TiO$_2$ NPs show only 10.47% decrease in degradation efficiency even after sixth cycle of reuse. The synthesized Ag-h-TiO$_2$ nanoparticles may also be useful for dye sensitized solar cells and other electrochemical applications.

Applications of Ag doped hollow TiO$_2$ Nanoparticles as an Effective Green Fungicide Against *Fusarium Solani* and *Venturia Inaequalis* Phytopathogens

5.1 Introduction

Nanoparticle-based antimicrobial agents are emarging as a promising alternative over the traditional chemical-based antimicrobial agents in recent years because of their attractive and multidimentional physico-chemical properties and biological compatibility. [541,542] In most of the cases the disadvantage of the chemical-based antimicrobial agents is the microorganisms tend to develop resistance after a certain time. [543] On contrary, chances of developing resistance is much lower in case of nanoparticles-based agents. [544] The antimicrobial properties of Ag nanoparticles (NPs) are well known for long time because of its toxicity towards the microorganism cells. [545] But, Ag NPs are very expensive for large scale applications such as agricultural fields. As an alternative, the anitimicrobial properties of many other NPs are also explored in recent years. On the other hand, the photocatalytic degradation of organic molecules using semiconductor metal oxide nanoparticles is also an important area and drawing considerable attention. In this area, TiO_2 nanoparticles are mostly used as an eco-friendly and clean photocatalyst because of its low cost, good photocatalytic activity, chemical stability, and non-toxicity. [124,125,546] However, the major disadvantage of pure TiO_2 nanoparticles is its higher band gap (~ 3.2 eV), because of this pure TiO_2 nanoparticles are active in the UV region of the light wavelength. In recent years, many researchers have focused on the improvement of the photo-catalytic activity of the TiO_2 nanoparticles under visible light irradiation by doping with metallic and non-metallic elements, which in turn reduce the band gap of the doped TiO_2 NPs to make it more active in the visible light wavelengths. When TiO_2 NPs are doped with Ag, the doped particles not only show improved photocatalytic activity by reducing the band gap, but also expected to show good antimicrobial activity against a wide range of microorganisms because of the presence of Ag. [546,547]

Antimicrobial activity of Ag doped TiO_2 NPs under visible light irradiation [548] and under dark condition have been studied against pathogenic bacteria like *E.coli*, *S.aureous*, *P.aeruginosa*, *S. typhimurium, B. subtilis, Candida albicans* etc. by few researchers. [546,549,550] Toxicity of Ag doped TiO_2 is associated with the released Ag^+ ions. The antibacterial effect of Ag ion is also because of the free radical induced oxidative damage to the bacterial cell membrane. [548,551] It may also participate in catalytic oxidation reaction between cellular oxygen and thiol group that results in blockage of bacterial respiration and finally cell death. [552] But no research have been explored on the antifungal activity of the Ag doped TiO_2 NPs till date to the best of our knowledge.

Fungal phytopathogens causes huge loss to the annual production yield of various important fruits and vegetables, which in turn affect the economies of the agriculture-based countries. The fungal phytopathogens are not only affect the plants but also soil or plant born pathogens causing the rotting of many crops (potato tuber, tomato etc.) during the storage. Pesticides embrace insecticides, herbicides, and fungicides are used in the agricultural farming. The chemical pesticides are highly toxic, which not only cause several serious health problems while enter inside our body through the food chains, but also pollute air, water, and soil during and after the process of applications. Hence, the objective of this research work is to develop a nanoparticle based cheap fungicide that can be effective against a wide range of fungal phytopathogens as well as economically viable for the agricultural applications. In this purpose, *F. solani*, a potential phytopathogen causing Fusarium wilt to important vegetables such as tomato, potato etc. and *V. inaquaelis*, causing apple scab disease to worldwide popular apple fruit have been selected and tested their susceptibility against Ag doped TiO_2 NPs. This study, may be of extreme importance in formulating NPs-based fungicide which is effective in controlling both phytopathogens at a time. The eco-friendly nature of the nanoparticles nullifies the chances of altering the soil property when return to the soil from the plant leafs or exerting any harmful effect to the host plant body. Application of the as synthesized Ag doped TiO_2 NPs on fungal phytopathogens in the presence of light, aiming to the agricultural field applications have not been reported earlier, to the best of our knowledge.

5.2 Materials and Methods
5.2.1   Materials

Reagent-grade silver nitrate (99.9%) and potassium bromide (99.3%) were purchased from Rankem. Anionic surfactant sodium dodecyl benzene sulphonate (SDBS) (technical grade, Cat No. 28995-7) and titanium (IV) butoxide ($Ti[O(CH_2)_3CH_4]_4$ or TOBT, 97%) were purchased from Sigma Aldrich. Ammonium hydroxide (25%) and nitric acid (69% GR) were purchased from Merck. All the chemicals were used as it was received without any further purification. *F. solani* (MTCC9668) and *V. inaequalis* (MTCC1109) were purchased from MTCC, Chandigarh, India. Ultrapure water of 18.2 MΩ.cm resistivity and pH 6.4–6.5 was used for all the experiments.

5.2.2 Maintainance of Fungal Culture

F. solani (MTCC9668) and *V. inaequalis* (MTCC1109) were sub-cultured in potato dextrose agar (PDA) plates at 25°C temperature. The grown fungal cultures were stored at 4°C after 7 days. Fungal mycelia were freshly grown prior to every experiment.

5.2.7 Phytotoxicity Assay

5.2.7.1 Extraction of Naphthoquinone

The *F.solani* produces naphthoquinone mycotoxin (orange color compound) in PD media as an extracellular secondary metabolite. To generate napthoquinone, a 5 ml *F.solani* spore suspension (spore density of 5×10^6/ml) was inoculated into PDB media, and incubated at 25°C for 30 days. The napthoquinone was separated from the grown mycelia by filtration through a clean cotton cloth filter and the filtrate was repeatedly passed for thrice. The naphthoquinone containing filtrate was then autoclaved for 15 min to kill the fungal spores present (if any) in the extracted broth. The sterilized broth was then incubated at 25°C for 5 days prior to further experiment to confirm the absence of any fungal spores.

5.2.8 Toxicity Assay of Naphthoquinone on Potato Tuber

Phytopathogenecity of naphthaquinone was tested by applying the extracted PD broth to fresh potato tuber and incubated in a humidity cabinet for one month period at 25°C temperature. Control set was maintained by applying sterilized double distilled water instead of PD broth.

5.2.9 Fungicidal Assay

5.2.9.1 Growth Inhibition Test

The radial growth of the fungal colony grown on nanoparticle containing agar plates were measured. The nanoparticle induced growth inhibition was calculated with reference to the control experiment (devoid of NPs).

5.2.9.2 Protein Assay

Fungal mycelia plug of 4 mm diameter grown in the presence of different nanoparticle concentrations were taken and suspended into 1 ml sterile water followed by addition of 2 ml Biuret reagent (1 % $CuSO_4$ and 10 % NaOH). After 10 min incubation, the cellular protein released to the external environment changes the reagent color blue to purple. Mycelia free cellular extract was obtained by centrifugation without any physical disruption. The intensity of purple colour was measured at 520 nm wavelength using an UV-Vis spectrophotometer

(Shimadzu, UV -3600). Same study using only PDA disc without any fungal colony was measured and deducted from the all samples for final calculations. [362]

5.2.9.3 Fungicidal Test

Fungal mycelia plug of 4 mm diameter were incubated in 5 ml sterile distilled water at 25°C in the presence of different nanoparticle concentrations. After 24 h incubation, 200 μl of Triphenyl Tetrazolium Chloride (TTC) reagent (5 mg/ml) was incorporated into all the test tubes and incubated for further 12 h. The experiments were conducted under visible fluorescent tube light (8 watt, 2950 lux intensity) exposure (12 h/day). In this test, active TTC is reduced to red color Triphenyl formazan in the presence of dehydrogenase enzyme released from viable fungal cell which is detectable by UV –Vis spectroscopy at 570 nm wavelength. [553] Afterwards produced formazan was solubilized in 5 ml DMSO and the fungal biomass was separated by centrifugation and absorbance of the supernatant was measured spectrophotometrically.

5.2.10 Microscopic Analysis

Surface morphology of the fungal biomass before and after the NP treatment were studied using Field Emission Scanning Electron Microscopy (FE-SEM, Nova NanoSEM450). Presence of NP on the fungal surface after NP treatment was confirmed by associated Energy Dispersive Atomic X-ray (EDAX) analysis.

5.3 Results and Discussion
5.3.1 Fungitoxicity of Nanoparticles

Fungitoxicity or growth inhibitory potential of three different TiO_2 nanopaticles such as pure TiO_2, Ag-s-TiO_2, and Ag-h-TiO_2 were studied in dark and compared here. The same effect was also studied in the presence of light and discussed in the next section. A 0.015 mg/plate particle concentration was employed for fungitoxicity assay against *F.solani* and *V.inaquaelis*. Experiments were carried out under complete darkness at 25°C temperature for 10 days. Fungitoxicity of the NPs were determined by calculating their growth inhibitory effect with reference to the control plate (devoid of NPs). The results obtained for *F.solani* are shown in Figure 5.1.
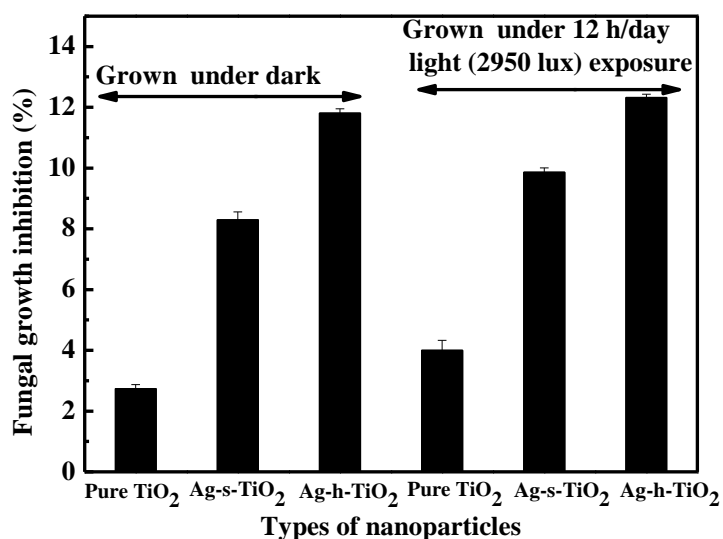
Figure 5.1. Growth inhibitory effect of nanoparticles on *F.solani*.

A comparison among three tested NPs shows Ag-h-TiO$_2$ NPs are most toxic while pure TiO$_2$ exert minimum toxicity towards *F. solani*. Figure 5.1 clearly shows that the growth inhibition capacity of Ag-h-TiO$_2$ NPs towards *F.solani* is nearly 4.5 times and 1.5 times higher than pure and Ag-s-TiO$_2$ respectively. The digital photograph of the plates depict *Fusarium* forms a smooth colony on PDA plate in the presence of Ag-h-TiO$_2$ rather than the characteristic cottony growth which is an indication of the nanoparticle induced morphological changes in the fungal species (Figure 5.2).
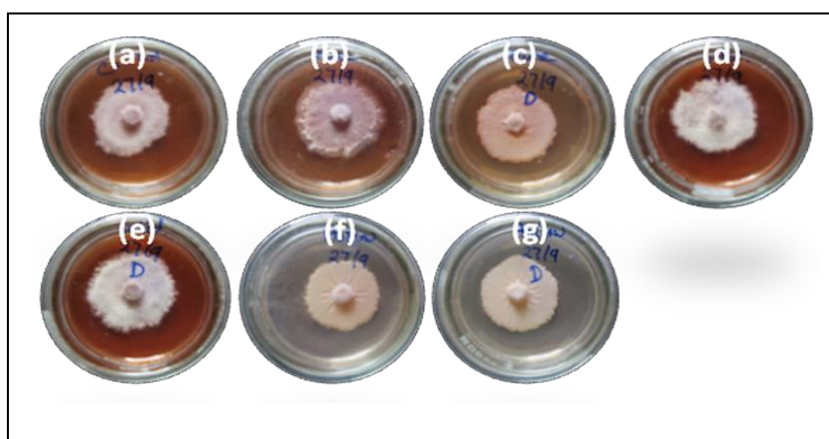
Figure 5.2. Digital photograph of the plates depict *Fusarium solani* grown in presence of different types of nanoparticles (0.015 mg/plate) in exposer of light and dark.

[(a) Control, (b) Pure TiO$_2$ (exposed to light), (c) Pure TiO$_2$ (in dark), (d) Ag-s-TiO$_2$ (exposed to light), (e) Ag-s-TiO$_2$ (in dark), (f) Ag-h-TiO$_2$ (exposed to light), (g) Ag-h-TiO$_2$ (in dark)].

Figure 5.3 shows the growth inhibitory effect of three different NPs on *V. inaquaelis*. Similar to *F. solani*, Ag-h-TiO$_2$ NPs are more effective towards growth inhibition of *V. inaquaelis*. In case of *V.inaquaelis*, Ag-h-TiO$_2$ NPs induced growth inhibition is almost 2 and 1.3 times higher than that of pure and Ag-s-TiO$_2$ NPs respectively. While comparing Figures 5.1 and 5.2, it is observed that *F.solani* is more sensitive to Ag doped TiO$_2$ than *V.inaquaelis*, but *V.inaquealis* is found to be more sensitive towards pure TiO$_2$ than that of *F.solani*.
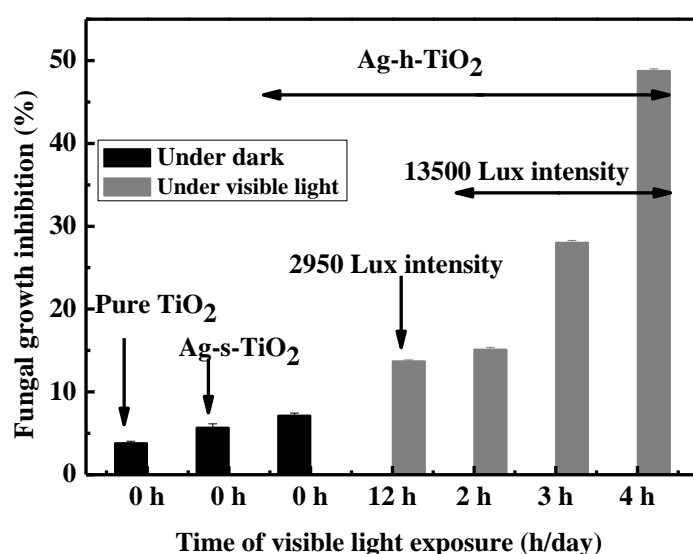
Figure 5.3. Growth inhibitory effect of different NPs on *V. inaquaelis* under dark and visible light exposure.

The growth inhibitory effect of nanoparticles are directly related to its high oxidizing property. The TiO$_2$ nanoparticles are positively charged in aqueous media, as a result, the nanoparticles are attracted towards the negatively charged fungal cell wall surface easily. While particles are in contact, they oxidize the fungal bodies leading to cell wall perforation and cell death.

Higher toxicity of the Ag doped TiO$_2$ is related to the additional antimicrobial activity of Ag. In aqueous media Ag doped TiO$_2$ releases the silver ions and shows microbial toxicity. [554] The antimicrobial activity of Ag can be attributed as: (i) formation of stable Ag-S bond (Equation. 5.1) between silver atoms and thiol groups (-SH) present in the cellularproteins. [555] Since, thiol group act as an active site for a number of important enzymes, the activity of those enzymes reduce or stop in the presence of Ag and finally blocks the significant biochemical pathways of the microbial cells. (ii) Formation of disulfide bond (R-S-S-R) by

96

coupling sulfur atoms of two thiol (-SH) groups (Equation 5.2). In this process Ag acts as a catalyst in the oxidation reaction between the oxygen molecules present in the cell and hydrogen atoms of thiol groups resulting the formation disulfide bond (R-S-S-R). [556] Formation of the disulfide bond induces structural deformities into protein structures especially the respiratory enzymes and finaly leads to cell death. In addition, the generated active oxygen in this reaction decomposes the protein, lipid and nucleic acids of the microbial cell.

$$Ag^+ + [-SH] \rightarrow Ag-S- \tag{5.1}$$

$$O_2 + [R-SH] \xrightarrow{\ Ag\ } H_2O + R-S-S-R + [O^-] \tag{5.2}$$
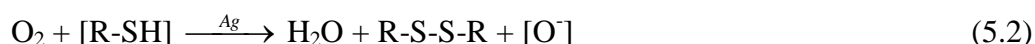
In general, thiol group [-SH] presents in different sulfur containing aminoacids such as methionine, cystine, and cysteine as a structural component is susceptible towards Ag toxicity.

Further, the greater fungitoxic effect of Ag-h-TiO$_2$ compared to that of Ag-s-TiO$_2$ is attributed to the higher surface area which in turn provides more surface atoms, a better contact with the fungal bodies and more availability of Ag atoms.

5.3.2 Photocatalytic Fungitoxicity of Nanoparticles

The TiO$_2$ NPs are well known for their photocatalytic activity. As a result, the photocatalytic degradation potency of the nanoparticles are exploited here for controlling the growth of fungal pathogens in the presence of visible light. To assess the combined inhibitiory activity of the NPs against *F.solani* and *V.inaquaelis*, previous fungitoxicity experiments were repeated under 12 h/day visible light exposure (2,950 and 13,500 lux light intensities). Light induced growth inhibitory effect of NPs on *F.solani* and *V.inaquaelis* with reference to their respective control experiments are also presented in Figures 5.1 and 5.3 respectively. These studies are also compared with the fungitoxic effect of the NPs in the absence of visible light. The Figures 5.1 and 5.3 show that the growth inhibitory effect of nanoparticles under the visible light exposure follow the desending order of Ag-h-TiO$_2$ > Ag-s-TiO$_2$ > pure TiO$_2$ which is similar to the fungitoxic effect of the NPs. Higher activity of Ag doped NPs is attributed to lower band gap (2.27 and 2.25 eV for Ag-s-TiO$_2$ and Ag-h-TiO$_2$ respectively) compared to that of pure nanoparticles (3.29 eV), which eventually leads to low photo generated electron – hole recombination rate.

NPs induced growth inhibitions of *F.solani* performed under complete darkness and 12 h/day visible light (2,950 lux intensity) exposure were compared for each NPs separately. It can be observed that, for each type of particles the fungal growth is less in case of visible light exposure for 12 h/day compared to that under complete darkness (Figure 5.1). While comparing two fungal pathogens, the photocatalytic growth inhibition is much prominent in the case of *V.inaquaelis*. Photocatalytic activity of Ag-h-TiO$_2$ causes only 0.5% more fungal growth reduction for *F.solani*, however, the growth reduction is 6.57% more in the case of *V.inaquaelis* (Figure 5.3). The results indicate that photocatalytic degradation of the fungal cell accompanied with fungitoxic effect of the NPs results in better growth reduction in the presence of visible light exposure. Under complete darkness though fungitoxicity of the particles retains, photocatalytic degradation is completely hindered.

Since the Ag-h-TiO$_2$ NPs are found to be the most fungitoxic among three studied NPs in the absence and presence of light, further, the effect of light intensity was also studied. In our first experiment the exposure time was 12 h/day, keeping in mind the natural exposure of sunlight towards plants, however, the difference of growth inhibition between the light and dark condition was not very significant mainly because of extremely low light intensity compared to that of sunlight intensity (> 100,000 lux). The reason of initial study was in the presence of low light intensity to see the sensitivity of the light effect. To analyze the light intensity dependent photocatalytic activity of the NPs, experiments were conducted under a high intensity visible light (metal halide lamp, 13,500 lux). The exposure time of the high intensity light and the NPs concentrations were varied in this study. The results are represented in Figures 5.3 and 5.4 for *V.inaquaelis* and *F.solani* respectively.
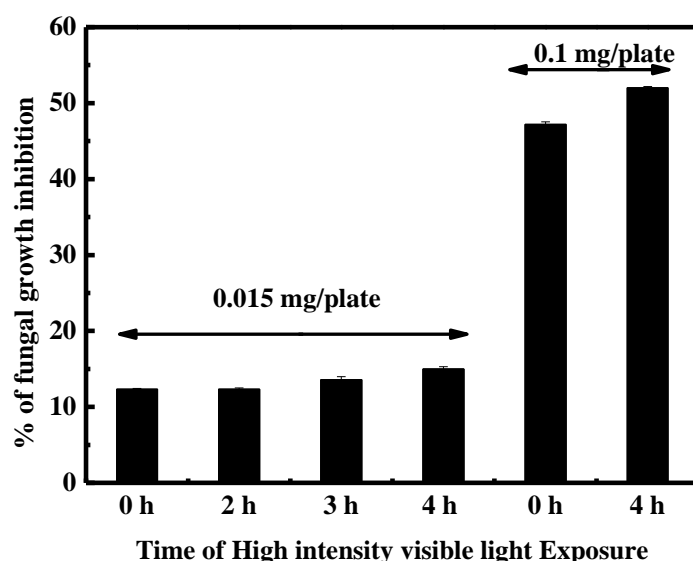
Figure 5.4. Photocatalytic growth retardation of *F.solani* in the presence of Ag-h-TiO$_2$.

Figures 5.3 and 5.4 exhibit a gradual increase in the fungal growth inhibition with the increasing exposure time of the high intensity light. After 2 h/day light exposure no significant growth inhibition was noticed. However, after 4 h/day of exposure time, visible reduction in fungal growth was observed. Similar to the low intensity light effect, photocatalytic activity of Ag-h-TiO$_2$ is more prominant on *V. inaquaelis* than that of *F. solani* under high intensity light. The results show after 4 h of light exposure 15% growth inhibition is achieved for *F.solani* (Figure 5.4) and almost 50% growth inhibition is noticed in the case of *V.inaquaelis* with respect to the control experiments (Figure 5.3). Unlike the fungitoxic property, photocatalytic activity of Ag-h-TiO$_2$ is more dominent to *V.inaquaelis* than that of *F.solani*. Time and intensity of the visible light exposed have much higher impact on controlling the growth of *V.inaquaelis*. Since both light intensity and exposure time used in this study are much lower compared to natural sunlight, we expect in real applications these NPs would be much more effective for both phytopathogens. The high intensity of visible light used in this study is of 13,500 lux and 20 Wm^{-2} energy. Whereas, the sunlight intesity is >100,000 lux in a bright sunny day and ~90,000 lux in a cloudy day. If the exposure time to the natural light is ~10 h/day, it is expected that the photocatalytic activity would enhance to much higher level, in that case complete inhibition of fungal growth is possible to achieve even at much lower NPs concentration.

The particle concentration effect shows that, with the increasing NPs concentration, the photocatalytic growth retardation also enhances. At 0.015 and 0.1 mg/plate NPs concentrations, growth inhibition of *F.solani* was enhanced upto 3 and 5% respectively when exposed to the high intensity light for 4 h/day (Figure 5.4).

The fact of photo catalytic growth inhibition can be explained by the similar mechanism of photocatalytic degradation organic compounds. [531] During the photocatalysis process $^\bullet$OH radicals are generated which subsequently decompose the microbial cell wall and cell membrane and leads to cell death. The $^\bullet$OH radical generation depends on the oxidation of surface water molecules by holes and the recombination of the electron-hole pairs. However, the growth inhibition is less in pure TiO_2, since the $^\bullet$OH radical generation is less because of the recombination of photoinduced charge carriers. The doping of Ag to TiO_2 reduces the recombination rate by accepting the photo induced electrons and holes as electron/hole traps, and increase the $^\bullet$OH radical generation. For this reason Ag doped TiO_2 is showing more growth inhibitory effect compared to that of pure TiO_2. In addition, Ag-h-TiO_2 is having higher surface area (198.3 m^2/g) compared to solid TiO_2 (95.1 m^2/g), which is also a favorable parameter for the maximum growth inhibitory effect of Ag-h-TiO_2.

5.3.3 Determination of Minimum Inhibitory Concentration for *F. solani*

To determine the minimum inhibitory concentration (MIC) of the Ag-h-TiO_2 nanoparticles against *F. solani*, a wide range of concentrations of 0.02, 0.04, 0.10, 0.27, 0.43, and 0.52 mg/plate were employed. All the experiments were conducted in the presence of visible light of 2950 lux intensity for 12 h/day. The radial growth of fungal colonies after 10 days of incubation were measured and represented in Figure 5.5a. The images of fungal colonies grown at different particle concentrations are shown in the inset of Figure 5.5(b-m).

Colonies of *F. solani*

Colonies of *V. inaquaelis*
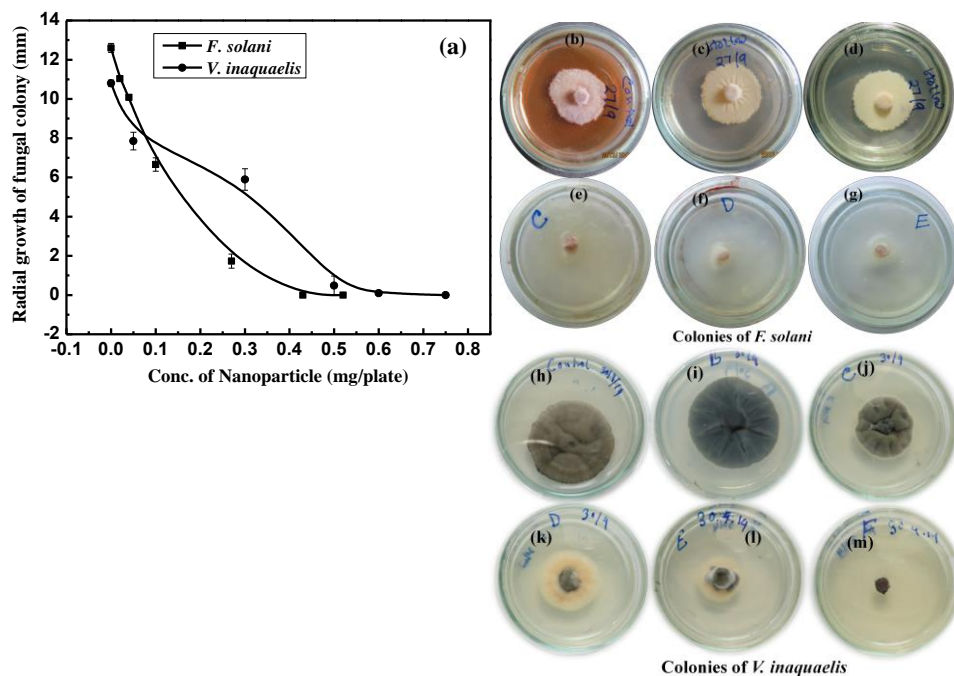
Figure 5.5. (a) MIC of Ag-h-TiO$_2$ for *F.solani* and *V.inaquaelis*. Photographs of growth of *F. solani* on agar plate in the presence of different concentrations of Ag-h-TiO$_2$ NPs: (b) Control (c) 0.02 mg/plate (d) 0.04 mg/plate (e) 0.1 mg/plate (f) 0.27 mg/plate (g) 0.43 mg/plate.

Photographs of growth of *V. inaquaelis* on agar plate in the presence of different concentrations of Ag-h-TiO$_2$ NPs: (h) Control (i) 0.05mg/plate (j) 0.3mg/plate (k) 0.5 mg/plate (l) 0.6 mg/plate (m) 0.75 mg/plate.

The Figure 5.5a clearly shows that at lower nanoparticle concentrations fungitoxicity of the NPs is not very prominant but with the increase in particle concentration a gradual increase in fungal growth inhibition is observed and finally at 0.27 mg/plate concentration 86.5% fungal growth is inhibited, while complete inhibition is noticed at 0.43 mg/plate concentration. In our previous study, it has been observed that SDBS surfactant used in nanoparticle synthesis does not exert any growth inhibition effect on *F.solani*. [362] Hence, it can be concluded that antifungal property is only for the presence Ag-h-TiO$_2$ nanoparticles. Noteworthy to mention that the MIC will vary with the change in light intensity.

Another interesting observation in this study is, at lower nanoparticle concentrations, although the growth inhibitory effect of Ag-h-TiO$_2$ is low, however, it successfully inhibits the pigment production. The orange color pigment (mainly naphthoquinone, as reported before) [557] production was observed in the case of control study as shown in Figure 5.5b. The pigment production is completely hindered in the presence of as low as 0.015 mg/plate (0.003 mg/ml) NPs concentration.

Naphthoquinone and its derivatives are potentent mycotoxin and highly associated with fungal pathogenecity. Phytotoxic effect of naphthoquinone is related to its interaction with the oxidative system of the plant cell. [558] Hence, inhibition of naphthoquinone production by *F.solani* fairly lowers the phytopathogenecity of the fungi. Phytotoxicity of naphthoquinone was confirmed in this study by potato tuber test in our laboratory. Digital and microscopic images of the naphthoquinone exposed potato tuber after 30 days of incubation time at 25°C temperature in the humidity cabinet are presented in Figure 5.6.
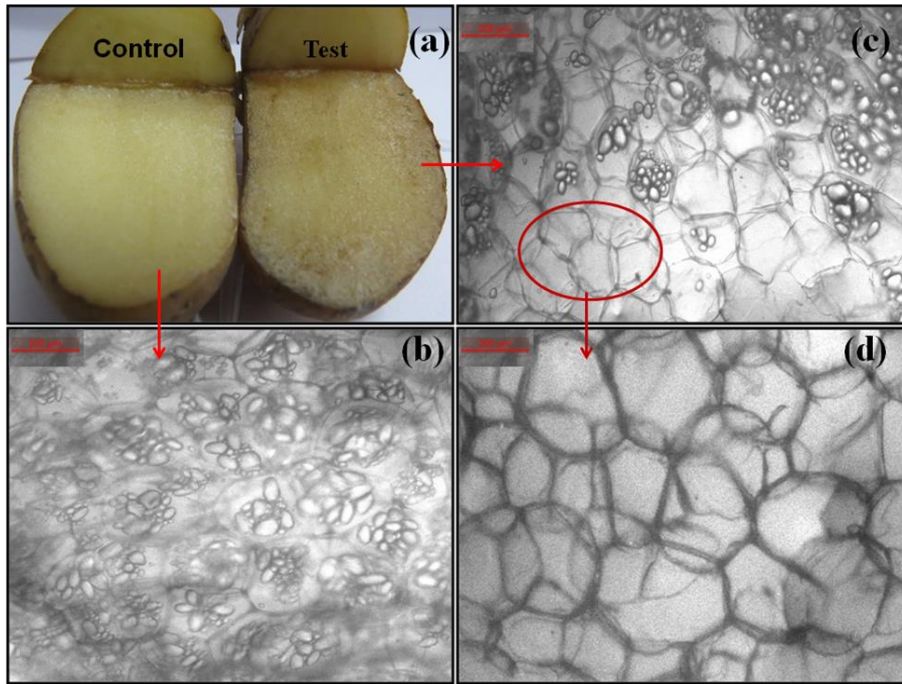
Figure 5.6. Phytotoxic effect of naphthoquinone on potato tuber after 30 days incubation: (a) Digital image of control and test potato tuber (b). Microscopic view of (c) control potato tuber, (d) test potato tuber, and (e) outer layer of test potato tuber.

Darkening and drying of the test potato tuber is clearly observed in Figure 6a compared to that of control indicates naphthoquinone induced infection to the potato tuber tissue. The microscopic images of the control and test potato tubers provide better evidence to the phytotoxic effect of the naphthoquinone. Figures 5.6b and 5.6c show the potato tissues of control and naphthoquinone treated tuber respectively. In control potato, cellular starch density is high and uniformly distributed. In contrast, scarcity of cellular starch globules is observed while treated with naphthoquinone. Additionally, the presence of starch globules in the inner cell layer from the outer surface (upper part of the image) are much more compared to the outer cell layer (down part of the image). Depletion of starch in cell indicates higher rate of respiration in tissue which is often considered as a diseased condition. Since the outer layer of the potato was more contact with the naphthoquinone, resulting more starch depletion in the outer layer compared to the inner tissues. Figure 5.6d represents the outer most layer of the test potato. Thickening of the cell wall and complete utilization of stored starch in outer most layer supports the evidence of naphthoquinone induced necrosis to the potato tissue. Starch depletion in naphthoquinone induced diseased lemon seedling has also been reported by previous researchers. [559]

5.3.4   MIC for *V.inaquaelis*

Similar to the previous section, Ag-h-TiO$_2$ NPs of different concentrations such as 0.05, 0.3, 0.5, 0.6, and 0.75 mg/plate along with all other similar physical parameters were used to determine the MIC against *V. inaquaelis* phytopathogen. The Figure 5.5 shows that the growth inhibitory effect of the NPs increases with the increase in concentration. It can be seen that, at 0.05 mg/plate concentration fungal growth inhibition is only ~ 30% but at 10 times higher nanoparticle concentration (0.5 mg/plate) the inhibition is more than 55%. At the same time, important observation in this study is that, at higher concentration the NPs are more active in delaying the sporulation rather than simply inhibiting the growth of the fungal colony. As an example, at 0.5 mg/plate nanoparticle concentration fungal growth inhibition is only ~ 10% higher than 0.3 mg/plate concentration, but significant effect in sporulation was observed (Figure 5.5). Fungal growth was completely arrested at 0.75 mg/plate concentration which can be considered as the MIC of Ag-h-TiO$_2$ nanoparticles against *V.inaquaelis* phytopathogen.

For better understanding, the growth inhibitory effect of NPs is also attributed in terms of molecular structure of the cell wall. The fungal cell wall of phylum Ascomycota group (includes both *F.solani* and *V.inaquaelis*) is composed of chitin and high amount of β-glucan. Chitin is composed of N-acetylglucosamine monomers linked by 1,4-glycosidic linkage. On the otherhand, β-glucans are the polysaccharides composed of D-glucose monomers linked by 1,3 and 1,6 glycosidic linkage (Figure 5.7). The $^•$OH radicals generated by the NPs in the presence of light (discussed in 3.2 section) cleave the glycosidic linkage by replacing the H atom at 1 position and the glycosidic bonds are converted to ester bonds, resulting loosening of the cell wall structure and allows the intracellular material to pass through the cell boundaries. It can also degrade the newly formed spore walls or may inhibit the sporulation affecting the sexual reproduction process of the fungus which can be confirmed by the delay in blackening (spore colour) of the *V.inaquaelis* colony (Figure 5.5) at higher concentration.
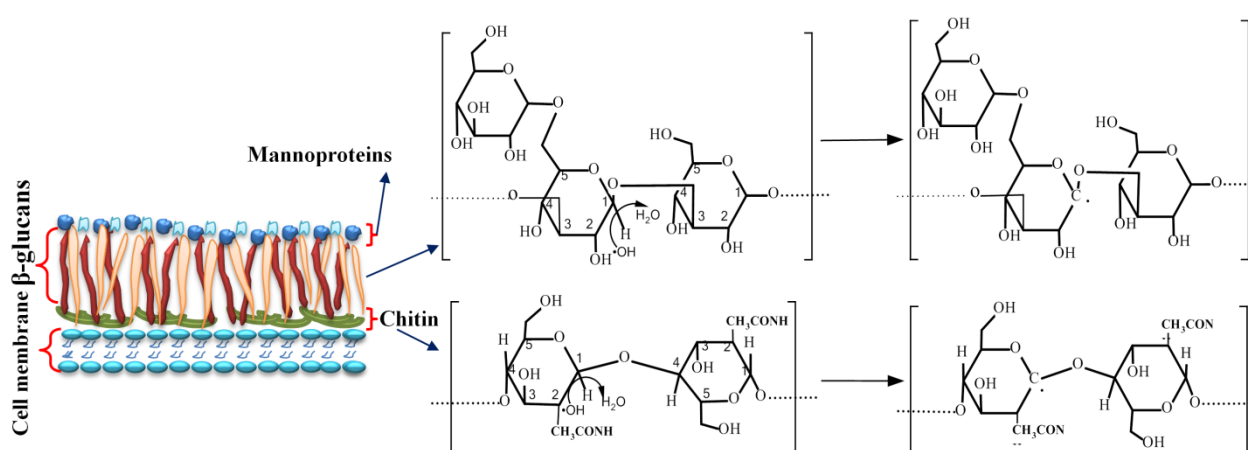
Figure 5.7. Mechanism of bond cleavage of glucan and chitin layers of fungal cell wall in the presence of $^\bullet$OH radicals generated by Ag-h-TiO$_2$ nanoparticles.

While comparing the effect of NPs on *F.solani* and *V.inaquaelis*, it is observed that, the NPs exert its toxic and photocatalytic effects on vegetative cells of *F.solani*; in contrast, the fungal spores are affected more than the vegetative cell in the case of *V.inaquaelis*. At the lower particle concentration, though the fungal growth of *F.solani* was not declined much but the naphthoquinone pigment production was hindered. As the pigment is toxic to the plant body, inhibition in pigment production can be considered as the partial loss of pathogenicity of the fungal body. In case of *V.inaquelis*, significant delaying in spore formation is observed only at higher NPs concentration. While expecting the photocatalytic activity, the growth inhibition potency of the NPs is highly dependent on the light intensity. In presence of the high intensity light (13500 lux), at low NPs concentration, *V.inaquaelis* is found to be more sensitive than *F.solani*. On the contrary, under low intensity visible light (2950 lux), minimum inhibitory concentration (MIC) for *V.inaquaelis* is higher than that of *F.solani*.

5.3.5 Biochemical changes of fungal mycelia in the presence of nanoparticles

In the previous sections we have mentioned that the growth inhibition of fungal body by Ag-h-TiO$_2$ NPs is mainly because of cell membrane damage, which in turn leads to the release of intracellular proteins to the external environment. To understand the antifungal mechanism and potency of the used NPs, the released protein was measured by the Biuret method. The absorbance values obtained from the spectroscopic measurements are considered to be directly proportional to the intracellular protein released and degree of cell membrane damage as well. The graphical expressions of the obtained results are presented in Figure 5.8. It can be seen that the release of intercelluar protein increases gradually with the increase in NPs concentration because of the cell membrane damage.
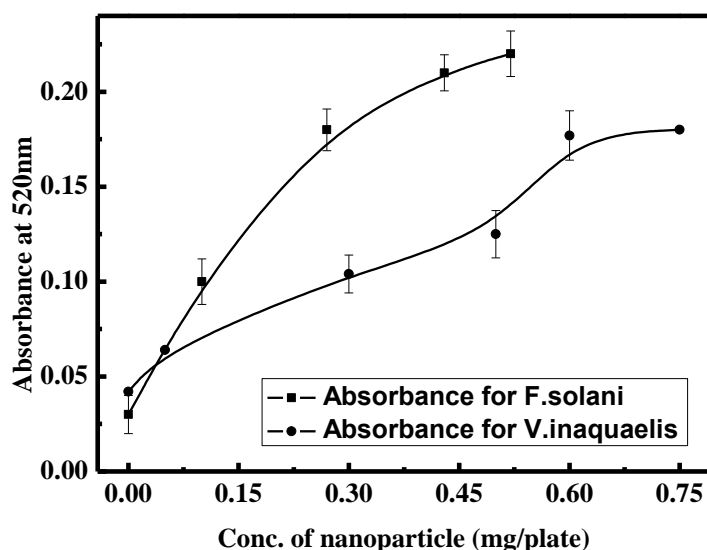
Figure 5.8. Effect of Ag-h-TiO$_2$ NPs on cellular protein release under low intensity (2950 lux) visible light exposure.

Figure 5.8 reveals that the release of cellular protein is increasing gradually with the increasing NPs concentrations for both *F. solani* and *V. inaquaelis* and the concentration is maximum at MIC. While comparing the results, it is observed that, in the absence of NPs *V. inaquaelis* release more (although not very significant) protein than that of *F. solani*; but in the presence of NPs, the amount of protein release in case of *F. solani* is higher than that of *V. inaquaelis*. This observation indirectly indicates that the damage of cell wall caused by Ag-h-TiO$_2$ nanoparticles is higher in the case of *F.solani* compared to that of *V. inaquaelis*. Since already discussed in section 5.3.2 and Figure 5.5 that the Ag-h-TiO$_2$ nanoparticles have a significant inhibitory effect on *V.inaquaelis* sporulation than damaging the vegetative cell boundaries at higher particle concentrations, which eventually the cause of less release of intercelluar protein.

5.3.6 Fungicidal assay of Ag-h-TiO$_2$

The release of the celluar protein to the external environment reduces the viability of the fungal biomass. Viability of the cell is often detected by dehydrogenase enzyme synthesis by the cell which is an indication of intracellular oxidative metabolism and associated with the viability of cell. [560] Declination in formazan formation is directly proportional to the reduced dehydrogenase production i.e. reduction in cell viability. Percentage of cell viability reduction is calculated in respect to the control experiment (devoid of NPs) and the results are shown in Figure 5.9.
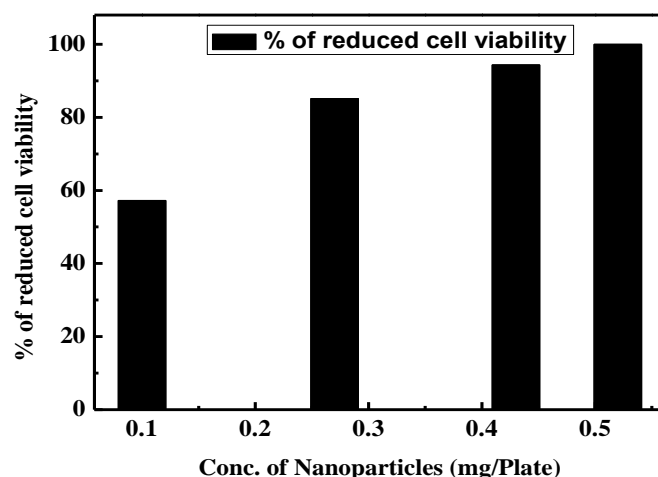
Figure 5.9. Effect of nanoparticles on cell viability of *F.solani*.

Figure 5.9 shows with the increase in nanoparticles concentration, the percentage of cell death also increases. This observation indicates that, at lower concentration the toxicity of nanoparticle is limited. Hence, cellular metabolism and dehydrogenase production is not affected severely. In contrast, at higher concentrations, nanoparticles exert strong toxic effect to the living cell as a result cellular metabolism is arrested and cell viability is reduced to a higher extend.

The TTC assay performed for *V.inaquaelis* shows similar results as *F.solani*, i.e. formazan formation is higher at lower nanoparticle concentration and reduces gradually with the increase in nanoparticle concentration. This test can be considered as the further evidence to the growth inhibiting effect of the Ag-h-TiO$_2$ on *V.inaquaelis* phytopathogen as discussed in section 5.3.4. The decreased fomazan formation is clearly shown in Figure 5.10.
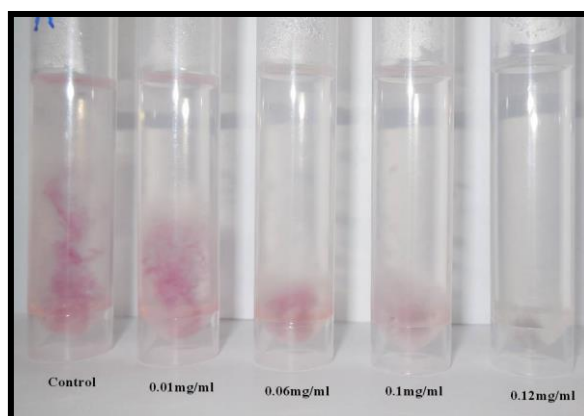
Figure 5.10. TTC assay of *V.inaquaelis* at different Ag-h-TiO$_2$ concentrations.

5.3.7 FE-SEM and EDX analysis

The morphologies of *F. solani* before and after the nanoparticles treatment were studied using FE-SEM and presented in Figure 5.11. Figure 5.11a shows the fungal hyphae prior to nanoparticles treatment and Figures 5.11(b-d) show the fungal hyphae and spores after the treatment with different concentrations of Ag-h-TiO$_2$ nanoparticles. A smooth fungal surface without morphological damage is observed before the nanoparticles treatment (Figure 5.11a), in contrast, roughening of the surface structure is observed after nanoparticles treatment (Figure 5.11(b-d)). Changes in the surface morphology is more prominent at 0.27 mg/plate concentration (Figure 5.11b) than that of 0.04 mg/plate (Figure 5.11c) or 0.1 mg/plate (Figure 5.11d) concentrations which is because of greater damage of the cell wall at higher nanoparticle concentration. The cell wall degradation potency of the NPs also increases significantly by exposure to high intensity (13,500 lux) visible light and the difference is clearly notices in the inset view of Figure 5.11c.
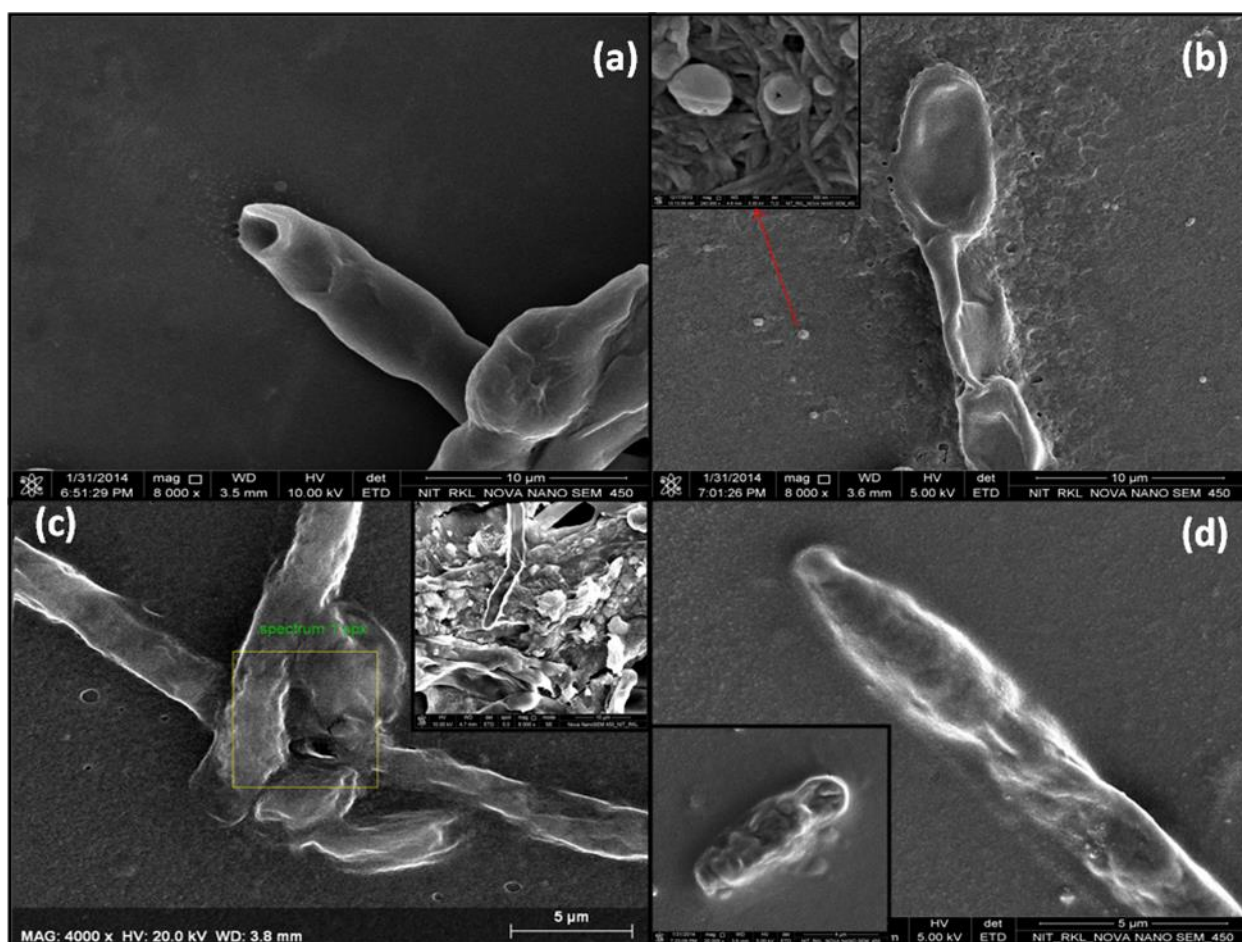
Figure 5.11. The FE-SEM micrographs of *F.solani* incubated: (a) in the absence of nanoparticles and (b-d) in the presence of nanoparticles. (b) 0.04 mg/plate NPs concentration

(Ag-h-TiO$_2$ attached on fungal hyphae in inset view), (c) 0.1 mg/plate NPs concentration (photocatalytic degradation of fungal hyphae under 13500 lux visible light exposure 4 h/day in inset view), (d) 0.27 mg/plate NPs (NPs treated fungal spore in inset view).

The inset image in Figure 5.11b shows the presence of Ag-h-TiO$_2$ NPs on the fungal hyphae which is further confirmed by the EDX analysis of the selected area of the fungal body. The EDX data shows the absence of Ti atoms in the control experiment, while fungal bodies grown in the presence of 0.04, 0.1, and 0.27 mg/plate NPs concentrations show gradual increase of Ti content (atomic%) on the selected area of fungal bodies as 0.0049, 0.01, and 2.203 respectively (Figure 5.12). The prominent increased in Ti atomic percentage on the fungal hyphae with the gradual increase of the NPs concentrations confirms the higher attachment of the Ag-h-TiO$_2$ nanoparticles to the fungus causing greater damage to cell structure. The toxicity of the used nanoparticle is not only towards the vegetative fungal hyphae but also towards the fungal spores which is evident in inset of Figure 5.11d.
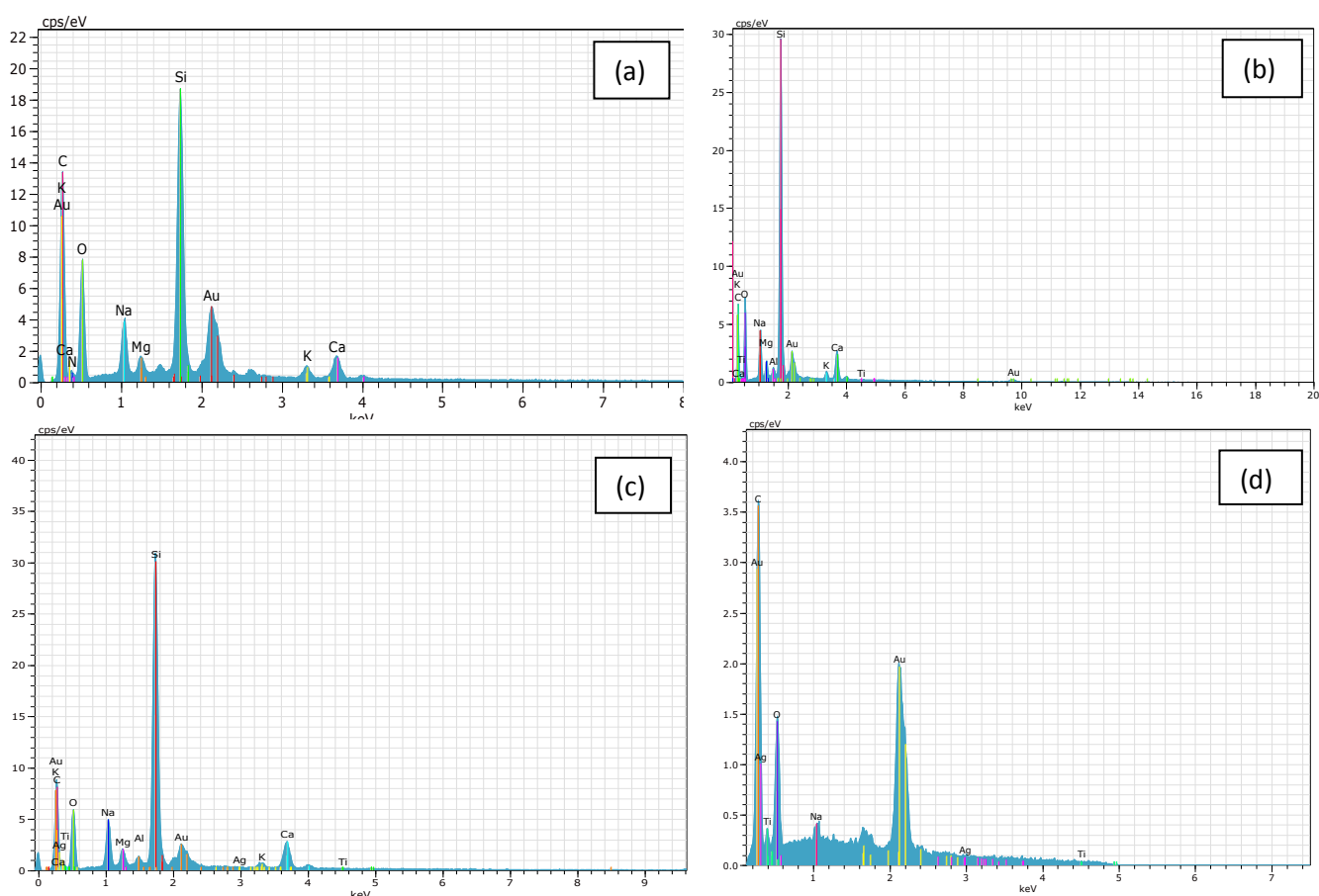
Figure 5.12. EDX analysis of the selected area of the *F-solani* fungal body in (a) control, in presence of (b) 0.04 mg/L, (c) 0.1 mg/L, and (d) 0.27 mg/L nanoparticles.

The Nanoparticles induced morphological changes on *V. inaquaelis* were also studied by FE-SEM analysis and represented in Figure 5.13 (a-e). Fungal hyphae grown in the absence of nanoparticle was found to have a smooth suface morphology (Figure 5.13a). When the fungal bodies are incubated in the presence of 0.3 mg/plate nanoparticles concentration, deposition of nanoparticles is clearly observed on the fungal surface and consequently the smooth appearance of the fungal surface (Figure 5.13b) is absent. As proposed in section 5.3.2, the antifungal effect of the nanoparticles increases by the exposure to the high intensity light (13,500 lux), which is further confirmed by the greater perforation and roughening of the cell surface presented in the inset view (Figure 5.13b). A 0.6 mg/plate concentration nanoparticles cause more damage to the fungal cell boundaries compared to lower nanoparticles concentration (Figure 5.13c). The cell wall damage imaged at high magnification is presented in the inset view for better understanding. Figures 5.13d,e represent the nanoparticle treated fungal spores at different concentrations. The higher shrinkage of spore wall in Figure 5.13e is because of the high nanoparticle concentration than that of Figure 5.13d.
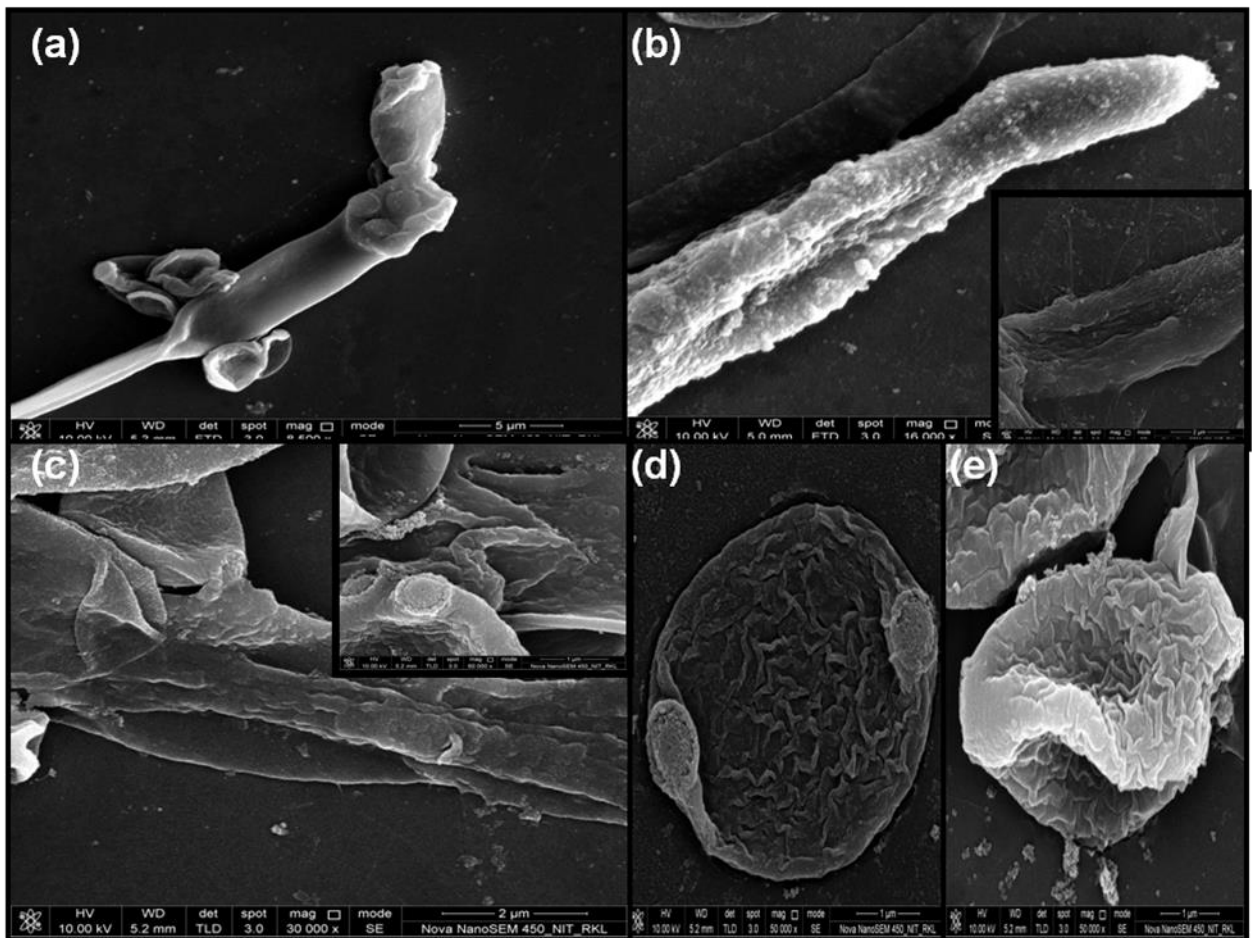
Figure 5.13. The FE-SEM micrographs of *V.inaquaelis*: (a) in the absence of nanoparticles (b-e) In the presence of nanoparticles. (b) treated with 0.3 mg/plate NPs concentration (exposed to 13,500 lux visible light for 4 h/day in inset view), (c) 0.6 mg/plate NPs concentration (image at high magnification in insert view). Fungal spores treated with (d) 0.3 mg/plate and (e) 0.6 mg/plate NPs concentrations.

The EDX analysis of the *V.inaquaelis* hypahe also shows the gradual increase of the atomic percentage of Ti and Ag (Figure 5.14) with the increasing NPs concentration, confirm better attachment of the NPs on the fungal surface at higher NPs concentrations; which inturn helps in better inhibition of the fungal growth.
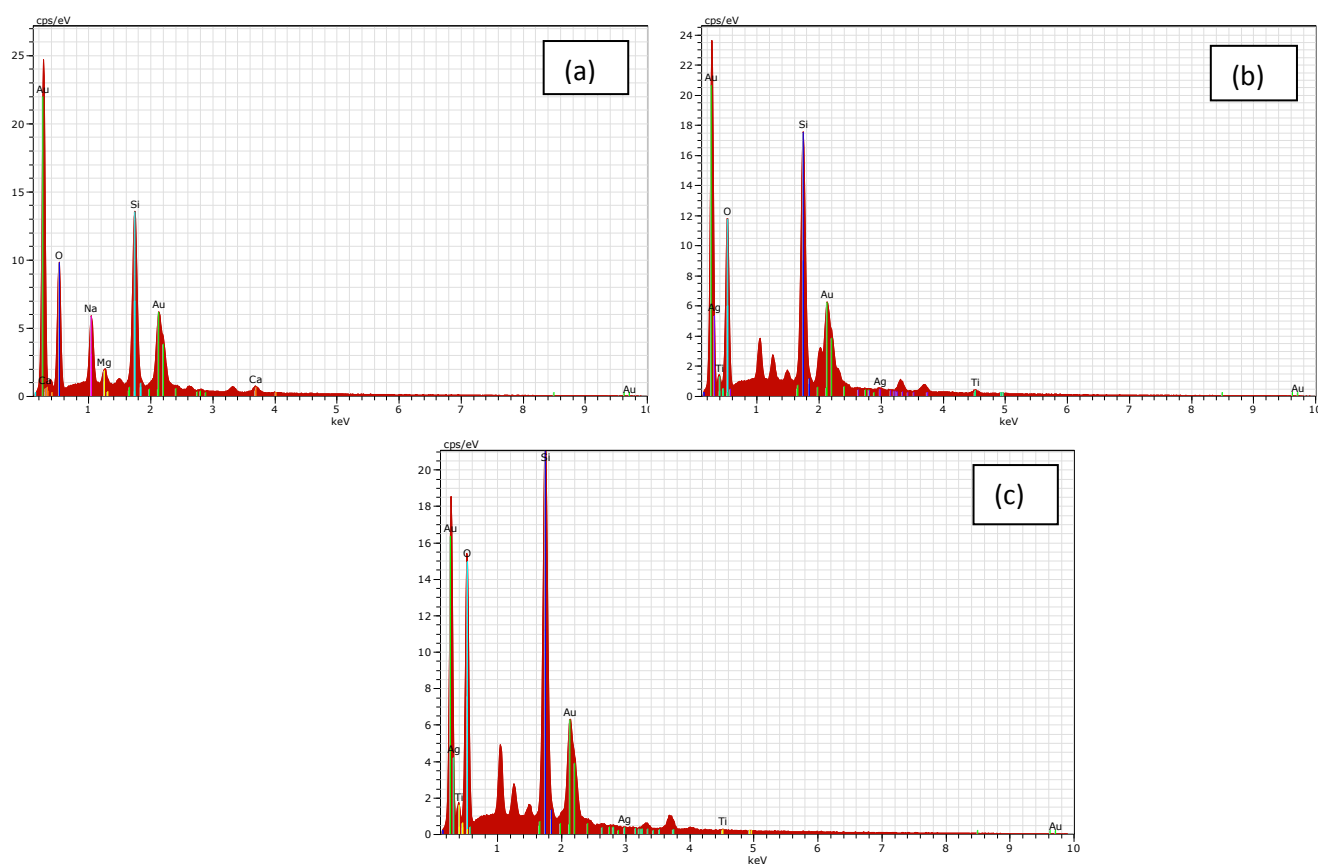
Figure 5.14. EDX analysis of the selected area of the *V.inaquaelis* fungal body in (a) control, in presence of (b) 0.3 mg/L, (c) 0.6 mg/L nanoparticles.

5.3.8 Fungicidal Activity of Ag-h-TiO$_2$ NPs on Potato Tuber

The antifungal potency of Ag-h-TiO$_2$ NPs was tested against *F.solani* infection on potato tuber to see the practical applicability. A potato tuber was washed with water and alcohol and treated with nanoparticles prior to inoculation of the *F.solani* inoculum. The control experiment was conducted without NPs treatment. Both potato tubers were then incubated at

25°C temperature in a humidity chamber for 2 weeks. The prominent growth of *F.solani* (white coloured fungal colony) on untreated potato tuber along with the rotten appearance was observed, while complete inhibition of the fungal pathogen with good condition was observed on the NPs treated potato tuber as shown in Figure 5.15. Blackening of the potato tuber was because of dehydration. This observation indicate that this NPs can also used for potato storage by avoiding the damage because of fungal attack.
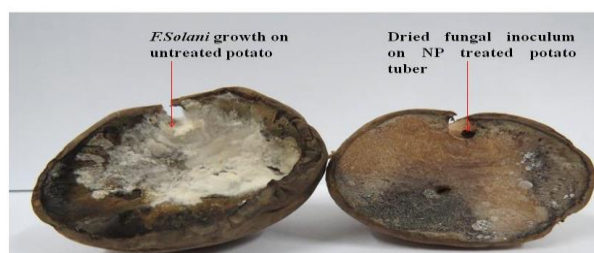
Figure 5.15. *F.solani* infection on potato tuber: (left) untreated, (right) treated with Ag-h-TiO$_2$ NPs.

5.4 Conclusions

The photocatalytic degradation property of Ag doped TiO$_2$ NPs has been successfully exploited for controlling the growth of *F.solani* and *V.inaquaelis* phytopathogens under the exposure of visible light. Fungal growth inhibition potency of three tested NPs under dark are showing the following order: Ag-h-TiO$_2$ > Ag-s-TiO$_2$ > TiO$_2$. At very low concentration (0.015 mg/plate), the Ag-h-TiO$_2$ NPs not only inhibit the growth of *F.solani* but also the production of orange color phytotoxic naphthoquinone during the growth. The MICs of the Ag-h-TiO$_2$ NPs for *F.solani* and *V.inaquaelis* are found to be 0.43 and 0.75 mg/plate respectively. At higher concentration, the NPs inhibit the sporulation process of *V.inaquaelis*. The antifungal activity of the used NPs is enhanced under the exposure of visible light and highly dependent on the intensity of the exposed light. A comparison of the fungal growth under complete darkness and 4 h/day visible light exposure (13,500 lux) shows the growth inhibition capacity of Ag-h-TiO$_2$ NPs is enhanced upto 15 and 50 % in case of *F.solani* and *V.inaquaelis* repectively with respect to the control experiments. The photo generated $^\bullet$OH radicals damage the compact chitin and β-glucan structure of the fungal cell wall, because of this intracellular proteins release out and leading to cell death. In case of Ag doped TiO$_2$ the formation of stable Ag-S bond and di-sulfide bond (R-S-S-R) in cellular protein also plays key role in cell damage. It is expected to improve the antifungal activity of the NPs to a much

higher extend and complete inhibition of the fungal pathogens can be achieved at much lower concentrations than the laboratory-based results under the exposure of sunlight for agricultural field applications. It is evident from the above research work that, Ag-h-TiO$_2$ NPs can effectively control both the phytopathogens at very low concentration, so this NPs can be utilized as a green fungicide for controlling a wide range phytopathogens. Additionally, the Ag-h-TiO$_2$ NPs can also be used effectively to prevent rotting of crops (potato, tomato etc.) because of fungal attacks during the storage.

Chapter 6

Synthesis and Characterization of Ag doped CdS/ZnS Core/Shell Nanoparticles for the Detection of Fluoride Ions Concentration in the Aqueous Media

6.1   Introduction

Over the last few years' semiconductor nanocrystals and nanoparticles have been investigated extensively because of their unique size dependent electronic and optical properties. Among which direct band gap semiconductor like CdS (2.42 eV) and ZnS (3.6 eV) are more important because of the application in gas sensor, [561] optical material, [562] electrochemical devices [563] and photochemical catalysis. [564] However continuous research on semiconductor NPs proposes that dual semiconductor systems give better luminescence and conductive properties due to the elimination of surface non-radiative recombination defects [565–567]. Therefore, designs of semiconductor/semiconductor core/shell nanoparticles have attracted much research interest in recent years. [568–571] For getting a higher fluorescence quantum yield and higher stability, core material can be coated with a higher band gap semiconductor material. [572] Further updated properties of core/shell nanoparticles, such as electronic, electrical and chemical properties can be tailored by the shell type and shell thickness. Surface passivation of a core material by wider band gap material gives more efficient and photostable luminescent nanocrystals because it reduces surface-related defect states and to the confinement of charge carriers in the core region due to the band offset potentials. [566,573,574] Applications of core/shell nanoparticles include telecommunication, biological imaging, and so on. Doping of semiconductor nanoparticles can create an opportunity for producing functional materials with enhanced or new born properties, which has been investigated to get basic information about the impurity states in quantum dots and their potential applications in novel light-emitting devices. [574] Doped core/shell structure nanoparticles have the properties, like enhanced sensitized dopant photoluminescence, [575–577] dual-mode bioimaging, [578] large radial pressure effects, [579] and modified dopant-carrier magnetic exchange coupling across the interface. [580] Physical properties of semiconductor nanocrystals also depend on the position of dopant in the core/shell structure, i.e. dopant inside the crystals or on their surface. Yang et al. studied that optical properties of Mn- doped CdS/ZnS core/shell nanoparticles depend on the radial position of Mn in the core/shell structure. [576] Depending on the position of dopant, doped core/shell nanoparticles can be classified as (i) doped-core/inert-shell, (ii) inert-core/doped-shell, (iii) doped-core/doped-shell nanoparticles. The role of the inert shell is basically to protect the luminescence core where as the active shell can help to transfer the absorbed energy from the pump source to the core material. [584] To date, variety of studied have been conducted on doped CdS/ZnS core/shell nanostructure to get enhanced photoluminescent material, such as Mn-CdS/ZnS, [581] CdS/Mn-ZnS, [582] ZnSe/Mn-ZnS, [577] ZnS-Cu, Pb/ZnS. [583] Silver nanoparticles has good

optical, catalytic, antimicrobial and optoelectronics properties. Use of silver nanoparticles for some specific applications in bare form is difficult because of its agglomeration tendency, where its activity gets prevented. This agglomeration problem can be reduced when silver is introduced in core/shell structure because of its immobilization on substrate. [585–587] When silver is used as the dopant in the core/shell structure we can achieve both the advantages of core/shell structure as well as the advantages of silver doping in the base material.

Semiconductor nanoparticles have been utilized for different advanced applications especially for the detection of anions in recent years. Detection of anions has attracted much research interest recent years because of their chemical, biological, and environmental importance. [424] Particularly, sensing of fluoride ions is very important because of its unique biological and chemical properties, such as high charge density, small in size, high polarizing ability, high electronegativity, and hard lewis basic nature. [405-407] Fluoride ions are widely used as additives in toothpaste for protecting the dental health and as pharmaceutical agents to treat dental cavities, [408] osteoporosis. [409,410] It is added in the drinking water to maintain the optimum level of the fluoride ion in the human body. [411] Fluoride is also used for manufacturing nuclear weapons. [412,413] In addition, the increasing number of industries on fluorine products is causing the fluorine contamination in the environment. However, high concentration of fluoride may cause fluorosis, [414,415] urolithiasis, [416] kidney failure, [417] cancer, [418] and even leading to death. The maximum permissible limit of fluoride ion in drinking water is 1.5 mg/L according to World Health Organization (WHO). [419] Hence precise detection of fluoride detection is necessary in drinking water and biological sample. So far, different methods are available for fluoride detection, such as ion-selective electrode, [588] chromatography, [589,590] spectrophotometry, [591] Willard and Winter methods. But these methods are complicated and high cost effective. Recently some fluoride probes have been reported based on different sensing mechanism, namely desilylation, [420-422] fluoride-hydrogen bonding, [424] boron-fluoride complexation, [405,426] colorimetric changes, [427-429] fluorescence quenching, [430] and fluorescence enhancing. [419,421,432,433] However, fluorescence based fluoride anion sensing method is important because of its low cost, simplicity, sensitivity, and high selectivity towards the anion species. Different material, such as Au, [592] CdSe/ZnS, [593] silica, [594] C dots, [595] Si Nanowires, [428] etc have been used as the fluorescence probe for the fluoride ions detection. However, requirement of fluoride probe with high selectivity for very ultra low level detection of fluoride ions is still a desired interest.

Herein, one fluorometric method is developed based on L-cysteine functionalized Ag doped CdS/ZnS core/shell (Ag-CdS/Ag-ZnS) nanoparticles for the detection of fluoride ions.

The method is tested in aqueous media at different pH and it is seen that pH 7 is the optimum for detecting the fluoride ions. This new fluorescence probe is highly selective and sensitive towards fluoride ions. By this method we can detect the fluoride ion with a detection limit as low as 96.15 µg/L. This approach of fluoride ion detection is noble because it is easy, inexpensive, highly selective and sensitive, and low time consuming method.

6.2 Materials and Methods

6.2.1 Materials

Reagent-grade $AgNO_3$ was purchased from Rankem, $(CH_3COO)_2Zn.2H_2O$, $(CH_3COO)_2Cd.2H_2O$, Na_2S, NaF, KNO_3, NaCl, $MgSO_4$, $NaHCO_3$, $Na_2HPO_4.2H_2O$, NaOH, $NaH_2PO_4.2H_2O$, and KBr were purchased from Merck; and NaI from Central Drug House. Dimethyl sulfoxide-d_6 (DMSO-d_6), and L-cysteine were obtained from Sigma Aldrich. All the chemicals were used as received without any further purification. Ultrapure water of 18.2 MΩ.cm resistivity and pH 6.4–6.5 was used for all the experiments.

6.2.2 Synthesis of Ag Doped CdS/ZnS Nanoparticles

In the first step, the core of Ag doped CdS nanoparticles were synthesized, where cadmium acetate (final concentration, c_f = 0.5 mM) and silver nitrate (c_f = 0.0075 mM) solutions were mixed in aqueous media and followed by drop wise addition of Na_2S (c_f = 0.5 mM). The reaction was continued with constant stirring for 45 min under the irradiation of a 200 watts incandescent lamp at 30°C temperature. After completion of reaction, the particles suspension was sonicated for 20 min for proper dispersion. In the second step, the Zinc acetate (c_f = 0.125 mM) and $AgNO_3$ (c_f = 0.00156 mM) solutions were mixed drop wise to the preformed suspension, followed by drop wise addition of Na_2S (c_f = 0.125 mM). The final mixture was kept under constant stirring and light irradiation conditions for another 45 min at 30°C temperature. Finally, the formed particles (termed as Ag-CdS/Ag-ZnS) were separated by centrifugation at 25000 rpm for 20 min. Then, the Ag-CdS/Ag-ZnS nanoparticles were washed thrice using alcohol-water mixture (2:1 ratio) and dried in a hot air oven at 60 °C for overnight. Similarly, the Ag-ZnS/Ag-CdS nanoparticles were also synthesized just by changing addition sequence according to the scheme 6.1.
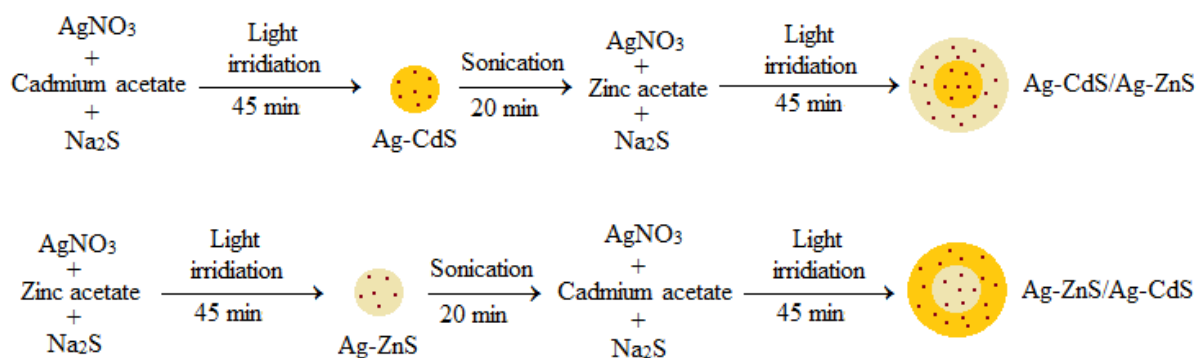
Scheme 6.1. Details synthesis procedure to form different types of radial position Ag-CdS/Ag-ZnS and Ag-ZnS/Ag-CdS nanoparticles.

6.2.3 Characterization of the Nanoparticles

The measurement of particle size and zeta potential was carried out by dynamic light scattering (DLS) using Malvern Zeta Size analyzer, (Nano ZS). The crystallinity of synthesized particles was characterized using X-ray diffraction (XRD) (Philips, PW 1830 HT) with scanning rate of 0.01°/S in the 2θ range from 15 to 75°. The morphologies of Ag-CdS/Ag-ZnS particles were investigated in transmission electron microscope (TEM) and high resolution-TEM (HR-TEM) (FEI, Tecnai S-twin and JEOL, JEM 2100). The optical absorption and fluorescence emission properties of the particles were tested by UV–Vis–NIR Spectroscopy (Shimadzu-3600), and fluorescence spectroscopy (Hitachi-7000) respectively. The chemical composition of the samples and the valence states of various elements were analyzed by X-ray photoelectron spectroscopy (XPS) (PHI 5000 VersaProbe II, ULVAC-PHI, Inc.). The quantum yield (QY) of these particles were calculated using phenol as a standard material (QY=0.14) using UV-Vis spectroscopy and fluorescence spectroscopy method.

6.2.4 Detection of fluoride ions

The fluoride ion concentration was detected by measuring the fluorescence emission intensity. Initially, the nanoparticles were functionalized by capping with L-cysteine. Then fluorescence response of the functionalized nanoparticles was recorded upon addition of fluoride ion as well as excited at 220 nm wavelength. The limit of detection (LOD) was obtained based on the calibration data as 3σ/k, where σ is the standard deviation from the blank measurements and k is the slope of the calibration curve (the plot of concentration of F⁻ vs. enhanced fluorescence intensity).

To evaluate the selectivity of the measurement in the presence of other associated anions, experiment was conducted in the presence of different anions, such as Cl^-, Br^-, I^-, OH^-, NO_3^-, SO_4^{2-}, HCO_3^-, HPO_4^{2-}, CH_3COO^-, $H_2PO_4^-$ with their associated cations Na^+, K^+, Mg^{2+}, and Zn^{2+}. A 30 mg/L concentration of each ion was taken for the selectivity test.

6.3 Results and Discussion

6.3.1 Characterization of Particle by UV-Vis Spectroscopy

The light absorption properties of the synthesized nanoparticles were studied by UV-Vis spectroscopy and the absorption spectra of CdS, ZnS, Ag-CdS/Ag-ZnS, and Ag-ZnS/Ag-CdS nanoparticles are presented in Figure 6.1. The Figure shows pure CdS nanoparticles donot have any sharp peak but there is a broad absorption in the rage of 200-450 nm wavelength, whereas, ZnS NPs is having a sharp peak in the UV region at 270 nm. In case of Ag-CdS/Ag-ZnS NPs there is a broad absorption band in the visible region and a sharp peak in the UV region (220 nm). The high absorbance intensity in the visible region might be because of Ag doping and the presence of sharp peak is because of the ZnS shell layer. However, the absorbance intensity again reduced when ZnS is present inside the core and CdS in the shell, which is mainly because of the difference in band gaps of CdS (2.5 eV) and ZnS (3.6 eV) NPs. This result clearly shows low band gap material in the inner layer and high band gap material in the outer layer gives better optical properties compared to reverse case.
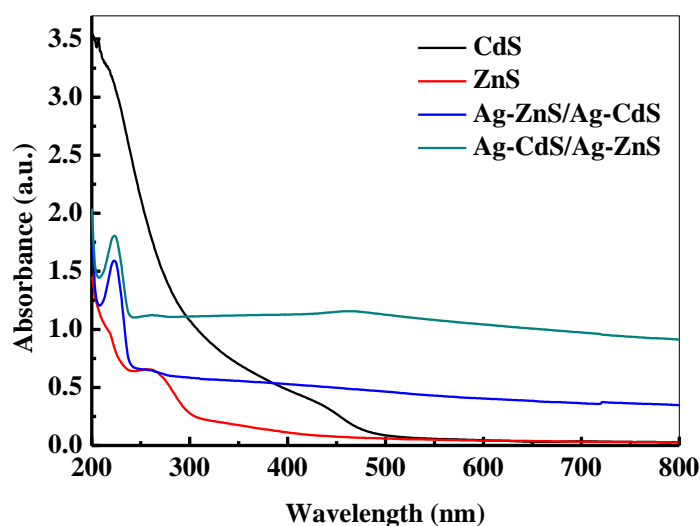
Figure 6.1. UV-Vis spectra of as synthesized CdS, ZnS, Ag-CdS/Ag-ZnS, and Ag-ZnS/Ag-CdS nanoparticles.

6.3.2 Characterization of Particles by XRD

The crystallinity and phases of the nanoparticles were analyzed by XRD analysis. The XRD patterns of Ag-CdS/Ag-ZnS and Ag-ZnS/Ag-CdS nanoparticles are shown in Figure 6.2. For Ag-CdS/Ag-ZnS nanoparticles the XRD pattern displays peaks for CdS at 2θ value of 26.59, 43.97, 52.17, and 54.25° corresponding to the plane (111), (220), (311), and (222) of cubic structure (JCPDS card no.75-1546); and peaks for ZnS were obtained at 2θ value of 28.11, 47.3, and 69.7° corresponding to the plane (111), (220), and (400) of cubic structure (JCPDS card no. 77-2100). In spite of ZnS coating on the CdS, the peaks for CdS are coming might be because of thin coating of ZnS on CdS core. For Ag-ZnS/Ag-CdS nanoparticles the peaks for CdS were obtained at 2θ values of 26.75, 43.84, 64.63, 69.80, and 70.47° corresponding to the plane (111), (220), (400), (331), and (420) of cubic structure (JCPDS card no. 02-0454); and peaks for ZnS were obtained at 2θ values of 28.78 and 68.99° corresponding to the plane (111) and (400) of cubic structure (JCPDS card no. 77-2100). More number of CdS peak compared to ZnS confirming the coating of CdS on ZnS layer. Noteworthy to mention that, there is no peak present for pure elemental silver in any of these core/shell particles. The absence of pure elemental silver peak imply there is no deposition of elemental Ag on the particles surface, however, shifting of XRD peaks are attributed to the substitution of principle reactants by Ag atom. In general, the substitution doping is favourable when the ionic radii of two elements are comparable. The ionic radii of Ag^{2+}, Cd^{2+}, Zn^{2+} and S^{2-} are 0.94, 0.95, 0.74 and 1.84 Å, respectively. As the ionic radius of Ag^{2+} is very close to Cd^{2+} and Zn^{2+} compared to S^{2-}, the silver can easily substitute the Cd or Zn in the CdS and ZnS lattices.
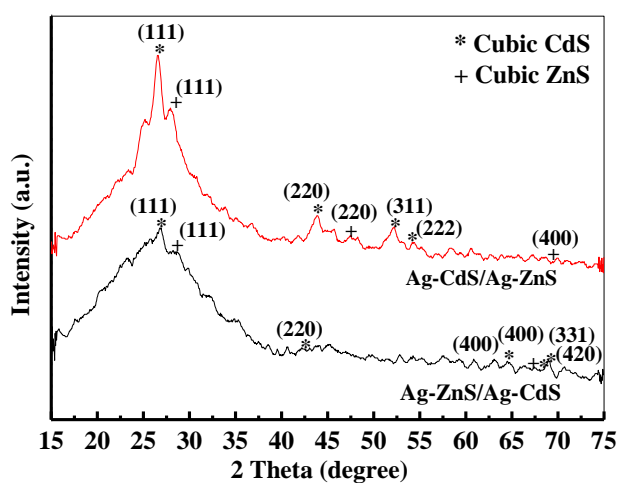
Figure 6.2. XRD patterns of Ag-CdS/Ag-ZnS and Ag-ZnS/Ag-CdS nanoparticles.

6.3.3 Characterization of Particles by FTIR Spectroscopy

Figure 6.3 represents the IR spectra of Ag-CdS/Ag-ZnS and Ag-ZnS/Ag-CdS nanoparticles in the range 4000-400 cm^{-1}. For Ag-CdS/Ag-ZnS nanoparticle the peaks at 1123.67, 682.4, and 570.85 cm^{-1} are because of the vibrational stretching of Zn-S. One peak at 735.96 cm^{-1} is for the Zn-S bond. In addition there is only one peak at 1599.7 cm^{-1} because of bending vibration of Cd-S bond. Low number of peak for Cd-S bond is indicating the coating of ZnS layer on CdS core. For Ag-ZnS/Ag-CdS nanoparticle the peaks at 1609.53 and 733.94 cm^{-1} are because of bending vibration of Cd-S bond. The peak at 556.67 cm^{-1} is for the stretching frequency of Cd-S bond. One peak at 1110.6 cm^{-1} is because of the vibration of Zn-S bond. In this case the number of peaks for Zn-S bond is low compared to Cd-S bond, which confirming the CdS coating on ZnS core.
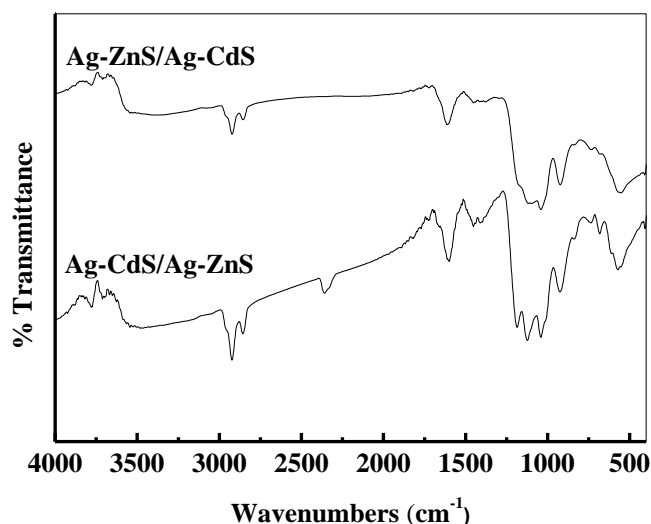
Figure 6.3. FTIR spectra of Ag-CdS/Ag-ZnS and Ag-ZnS/Ag-CdS nanoparticles.

6.3.4 Characterization of Particle by FE-SEM and TEM

The size and morphology of the Ag-CdS/Ag-ZnS and Ag-ZnS/Ag-CdS nanoparticles were studied by transmission electron microscopy. The TEM image of Ag-CdS/Ag-ZnS nanoparticles (Figure 6.4a) shows the small size particles are of spherical shape and the distribution of the particle size is in the range of 5.92 ± 0.76 nm with a shell thickness of about 0.75 nm. The high resolution TEM image of Ag-CdS/Ag-ZnS nanoparticles in Figure 6.4b shows the lattice fringes spacing of 0.33 nm corresponding to the (111) plane for cubic CdS and the lattice fringes spacing of 0.31 nm corresponding to the plane for cubic ZnS. The structure confirmed by HR-TEM is consistent with the XRD data also. Noteworthy to

120

mention that there is no lattice fringes presence because of silver, which confirms that there is no surface deposition of elemental silver. Figure 6.4c shows the selected area electron diffraction (SAED) pattern of this particle obtained by focusing the electron beam on individual nanoparticles. The ring like diffraction pattern with scattered spot which confirms the nanoparticles were poly crystalline in nature. The TEM image of Ag-ZnS/Ag-CdS nanoparticles is presented in Figure 6.4d, the obtained particle size is almost same as that of Ag-CdS/Ag-ZnS. The SAED pattern (Figure 6.4e) shows concentric circles pattern of cubic phase reveal the small size of the obtained nanoparticles.
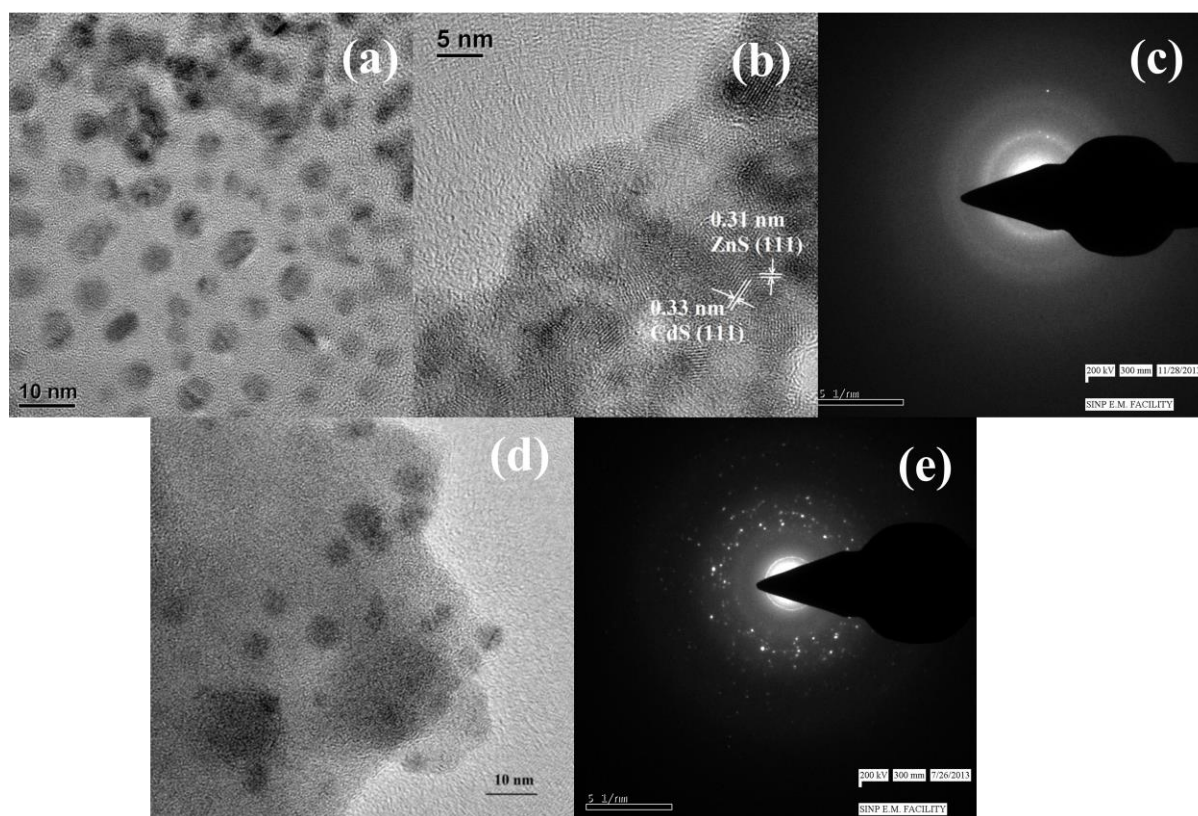
Figure 6.4. (a) TEM image, (b) high resolution TEM image, and (c) SAED pattern of Ag-CdS/Ag-ZnS NPs. (d) TEM image and (e) SAED pattern of Ag-ZnS/Ag-CdS nanoparticles.

6.3.5 Characterization of Particles by XPS

The chemical composition and the chemical state of the Ag-CdS/Ag-ZnS nanoparticles were analyzed by XPS. The high resolution peak of Ag 3d is presented in Figure 6.5a. The Ag $3d_{5/2}$ and Ag $3d_{3/2}$ peaks appear at binding energies of 366.375 and 372.75 eV, respectively with a slitting of 6.375 eV, confirming the presence of ionic silver instead of metallic form. Figure 6.5b shows the high resolution peak of Cd 3d level, where the detected major peaks at 410.625 and 404 eV are because of the Cd $3d_{3/2}$ and Cd $3d_{5/2}$ signal, and the spin-orbit separation of 6.625 eV is because of the Cd^{2+} formation. The scan for Zn 2p comprises two

peaks at the binding energies of 1044 and 1020.875 eV becuse of Zn $2p_{1/2}$ and Zn $2p_{3/2}$ with a spin-orbit splitting of 23.1 eV (Figure 6.5c), confirming the presence of Zn^{2+}. Figure 5d confirms S 2p level at the binding energy 160.625 eV. Now there are three possible location of dopant in the bi-layer structure- (i) surface of the host material, (ii) principle reactant of the host material, and (iii) interstitial sites of the host material. From FE-SEM or TEM image it is clear that there is no surface deposition of silver on the surface. If interfacial doping is there then the silver peak should come in the XRD data, but there is no peak of individual silver. XPS data shows the presence of silver is in ionic form. So, the only possibility of silver doping is by the replacement of principle reactant in CdS/ZnS bi-layer structure. From the XRD data it is also clear that silver doping is achieved by the substitution of Cd^{2+} and Zn^{2+} by silver in the CdS and ZnS lattices.
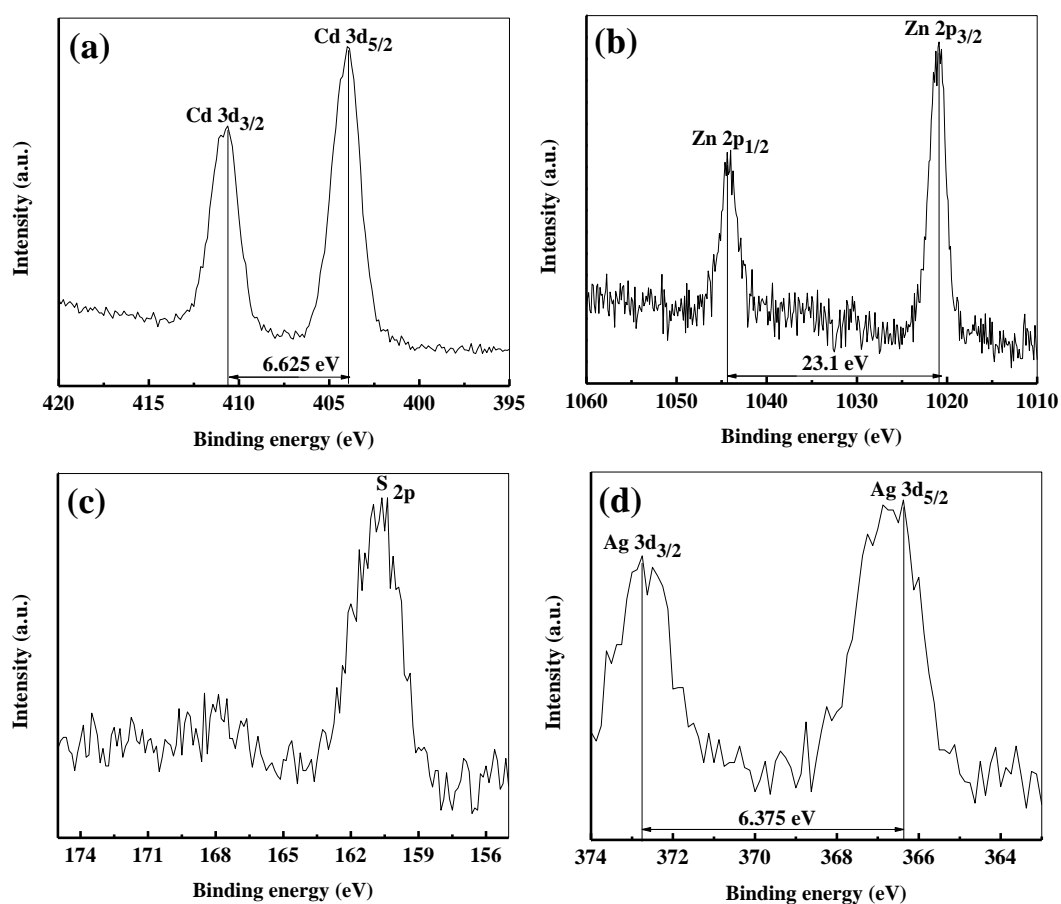
Figure 6.5. High resolution XPS narrow scan spectrum of (a) Ag(3d), (b) Cd(3d), (c) Zn(2p) and S(2p) for Ag-h-CdS/ZnS nanoparticles.

6.3.6   Characterization of Particle by Fluorescence Spectroscopy

The fluorescence emission property of the nanoparticles was examined by exciting at 220 nm wavelength and the emission spectra are presented in Figure 6.6. It has been seen that there

are two peaks of emission, one is in the UV (289 nm) region and another is in visible region (443.8 nm). It is noteworthy to mention that the emission peak at 289 nm is more prominent compared to 443.8 nm. While comparing the emission of Ag-CdS/Ag-ZnS and Ag-ZnS/Ag-CdS nanoparticles, it is notable that the emission intensity of Ag-CdS/Ag-ZnS is more compared to Ag-ZnS/Ag-CdS. This is because of different electron affinity and band configuration in the core/shell structure. The quantum yield (QY) was also calculated for the nanoparticles using phenol as the standard material and the obtained QY values are 77.57 and 69.6% for Ag-CdS/Ag-ZnS and Ag-ZnS/Ag-CdS nanoparticles (Figure 6.7 and Table 6.1). The QY is also high when the CdS is coated by ZnS, which is because of the coating of a high band gap material (ZnS) on low band gap material (CdS). In the core/shell structure, because of passivation of the core (CdS) surface and elimination of the surface trap, the electrons are located only in the core and holes are located throughout the core and shell layers (ZnS), as a result quantum yield increases in the Ag-CdS/Ag-ZnS nanoparticles. [596]
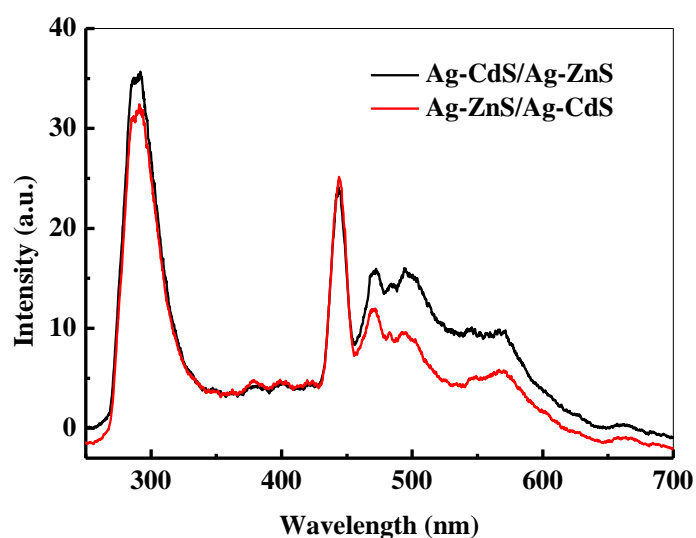
Figure 6.6. Light emission spectra of Ag-CdS/Ag-ZnS and Ag-ZnS/Ag-CdS nanoparticles in the range 250-700 nm.
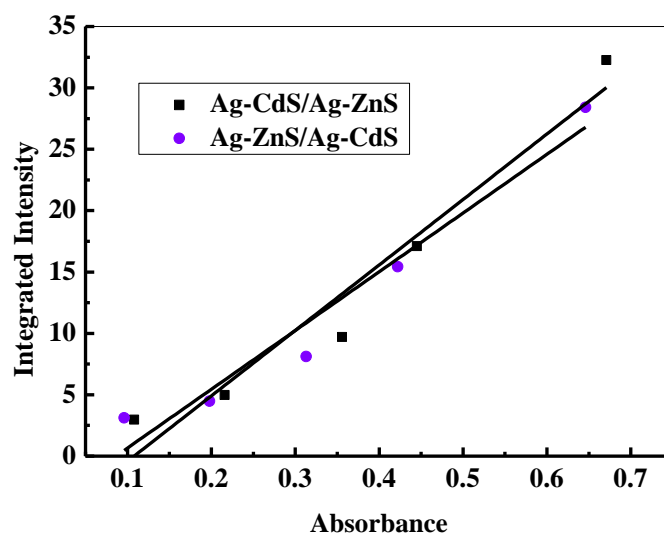
Figure 6.7. The plot of absorbance vs. integrated intensity of Ag-CdS/Ag-ZnS and Ag-ZnS/Ag-CdS nanoparticles.

Table 6.1. The fitting equation and R^2 value of integrated intensity (from fluorescence spectra) vs. absorbance (from UV spectra) line and the QY of phenol and Ag-CdS/Ag-ZnS nanoparticles.

Material	Fitting equation	R^2 value	Quantum yield (QY)
Phenol (reference)	y=26.72x+0.315	0.997	0.140
Ag-CdS/Ag-ZnS	y=53.33x-5.758	0.935	0.776
Ag-ZnS/Ag-CdS	y=47.86x-4.126	0.943	0.696

6.3.7 Detection of Fluoride Ions

The Ag-CdS/Ag-ZnS nanoparticles were utilized for rapid and selective detection of fluoride ions in aqueous media. The nanoparticles were first functionalized by capping with L-cysteine and then fluoride ions were added to the reaction media. The changes in fluorescence emission of the functionalized nanoparticles were tested after in situ addition of fluoride ions in different concentrations.

6.3.7.1 Effect of pH

To see the effect of pH on the fluorescence emission property of the nanoparticles, the emission efficiency was studied at three different pHs (pH 3, 7, and 10) and the results are presented in Figure 6.8. Figure 6.8a shows the fluorescence emission spectra of the

nanoparticles after functionalized with L-cysteine. In acidic pH (3) there is almost no emission at 289 nm but a small peak at 443.8 nm. While at pH 7 slight quenching of the fluorescence emission at 289 nm wavelength is observed, in contrast, there is an enhancement of the emission spectrum at 289 nm wavelength at pH 10. The intensity of fluorescence emission enhancement or quenching is mainly because of the interaction between the nanoparticles and L-cysteine molecules. In acidic media, because of protonation of the thiol group there is a weak interaction between the thiol group and the nanoparticles, as a result, quenching of fluorescence emission occurs. In contrast, in alkaline media due to deprotonation of the thiol groups there is a chance of strengthening the interaction between nanoparticles and the thiol groups, as a result enhancement of the fluorescence emission. Figure 6.8b shows the fluorescence emission spectra of the functionalized nanoparticles after addition of F$^-$ ions (2000 µg/L) at the three different pHs. It can be seen that there is no significant change of the fluorescence emission in acidic (pH=3) as well as basic media (pH=10), but a significant fluorescence emission enhancement in neutral media (pH=7). For this reason further study was conducted in neutral media only.
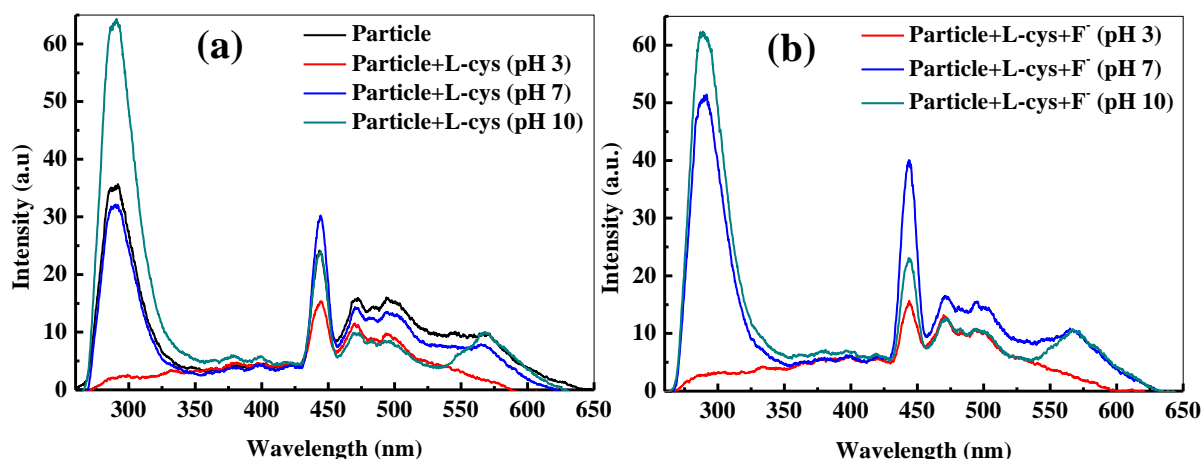
Figure 6.8. pH dependent fluorescence emission spectra of the nanoparticles after (a) L-cysteine capping, (b) F$^-$ ions addition to the L-cysteine capped nanoparticles.

6.3.7.2 Calibration Curve for Fluoride Ion Detection

The fluorescence emission spectra of the L-cysteine capped nanoparticles after the addition of different concentration of F$^-$ ions in the neutral media are presented in Figure 6.9. The concentrations of the F$^-$ ions were taken 190 – 22,800 µg/L. Results show that there is a gradual enhancement in the fluorescence emission intensity with the increasing concentration of F$^-$ ion. A plot of fluorescence intensity versus fluoride ion concentration is found to be linear (R^2 = 0.985, inset of Figure 6.9). The LOD is calculated as 99.7 µg/L. The permissible

limit of fluoride ion in the drinking water is 1,500 µg/L, [597] which is ~ 15 times higher that LOD of this method. So this fluorescence probe can be utilized for sensing the fluoride ions in water samples even at very low concentration.
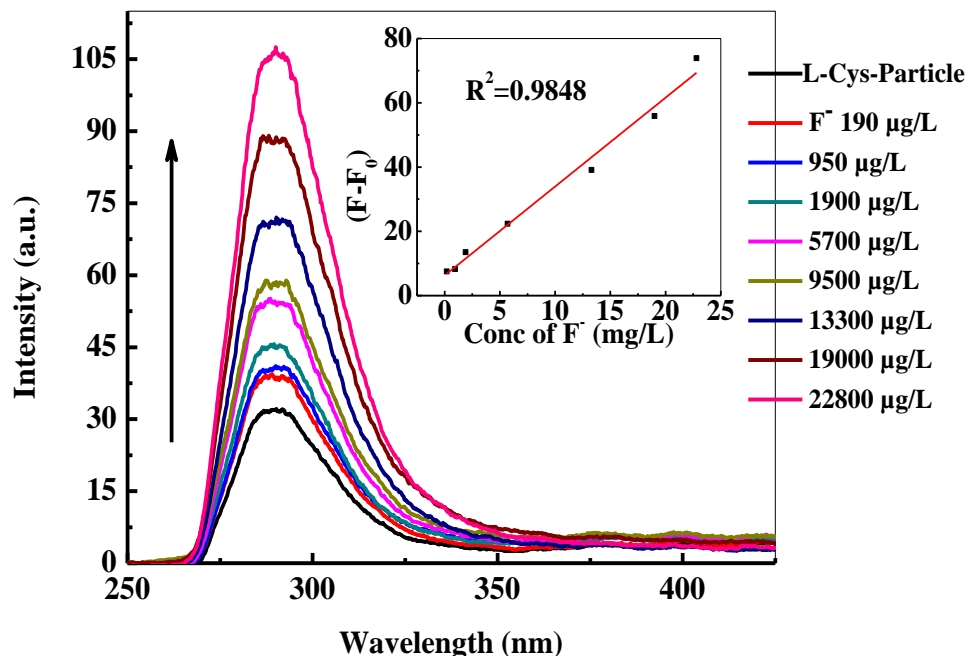
Figure 6.9. Fluorescence enhancement spectra of L-cysteine capped Ag-CdS/Ag-ZnS nanoparticles after the addition of fluoride ions in neutral media. The concentration of the fluoride ions was in the range of 190 – 22,800 µg/L. Inset is the linear plot of enhanced fluorescence intensity of the L-cysteine capped Ag-CdS/Ag-ZnS nanoparticles with the concentration of fluoride ions. F_0 and F are the fluorescence intensities of L-cysteine capped Ag-CdS/Ag-ZnS nanoparticles in the absence and presence of fluoride ions.

6.3.7.3 Anion Selectivity Test

The selectivity of the present fluorescence probe for fluoride ion detection was tested against other common background anions in the presence of their associated cations, such as Cl^- (Na^+), Br^- (K^+), I^- (Na^+), OH^- (Na^+), NO_3^- (K^+), SO_4^{2-} (Mg^{2+}), HCO_3^- (Na^+), HPO_4^{2-} (Na^+), CH_3COO^- (Zn^{2+}), $H_2PO_4^-$ (Na^+), 30 mg/L concentration each. These anions were mainly chosen because of their possibility of presence in the drinking water. Figure 6.10 shows that there is no change in fluorescence intensity in the presence of these anions but a significant fluorescence enhancement is there in the presence of F^- (22.8 mg/L). This result confirms that the fluorescence probe can selectively detect the fluoride ions in the presence of different interference ions.
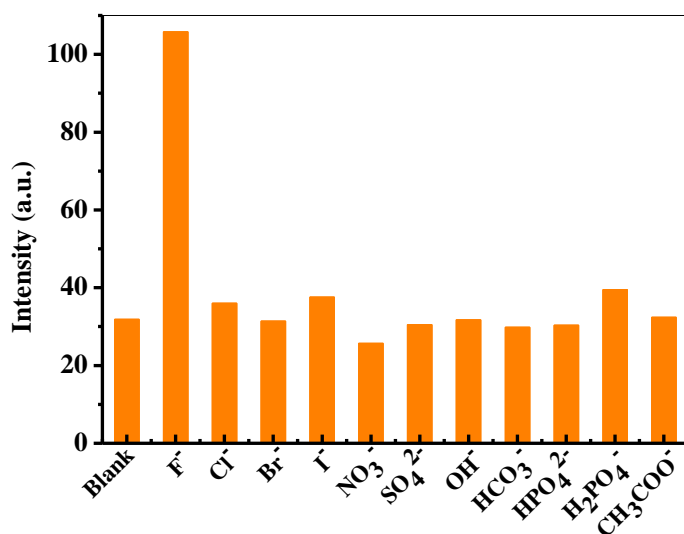
Figure 6.10. The change in fluorescence emission intensity of L-cysteine capped Ag-CdS/Ag-ZnS nanoparticles in the presence of F^- (22.8 mg/L) and other anions with their associated cations (Cl^-, Br^-, I^-, OH^-, NO_3^-, SO_4^{2-} HCO_3^-, HPO_4^{2-}, CH_3COO^-, $H_2PO_4^-$, Na^+, K^+, Mg^{2+}, and Zn^{2+}) (30 mg/L each).

6.3.7.4 Basic Mechanism

To understand the basic mechanism of fluoride ion detection by the L-cysteine fuctionalized nanoparticles the FT-IR study was done for pure L-cysteine, L-cysteine capped nanoaparticles, and fluoride added L-cysteine capped nanoparticles. The FT-IR spectra of pure L-cysteine (Figure 6) are having peaks at 3156, 2958, 2901, 2780 cm^{-1} for $-NH_3^+$; and 2633, 2547 cm^{-1} for –SH group. The peak of C=O appears at 1577 cm^{-1} and the peaks at 1293, 1136, 1060 cm^{-1} are of C-O bond. In FT-IR spectra of L-cysteine capped nanoparticles (Figure 6.11) there is no peak of –SH group but the peaks of NH_3^+ are present, which confirms the cleavage of thiol group (-SH) and the particles are attached through the thiol group of the L-cysteine. After addition of fluoride ions to the functionalized nanoparticles, broadening of the amine peaks (Figure 6.11) confirms the attachment of F^- ions to the amide group of pre-attached L-cystine molecules through the formation of N-H·····F^- hydrogen bonds. [598] The fluorescence enhancement of the functionalized nanoparticles after F^- addition is because of the strongest basicity nature of the F^- anions, and the effective hydrogen bonding and deprotonation with amide group of the binding side. [599] The mechanism of particle attachment with L-cysteine and F^- ion attachment with L-cysteine functionalized nanoparticles is presented in Scheme 6.2.
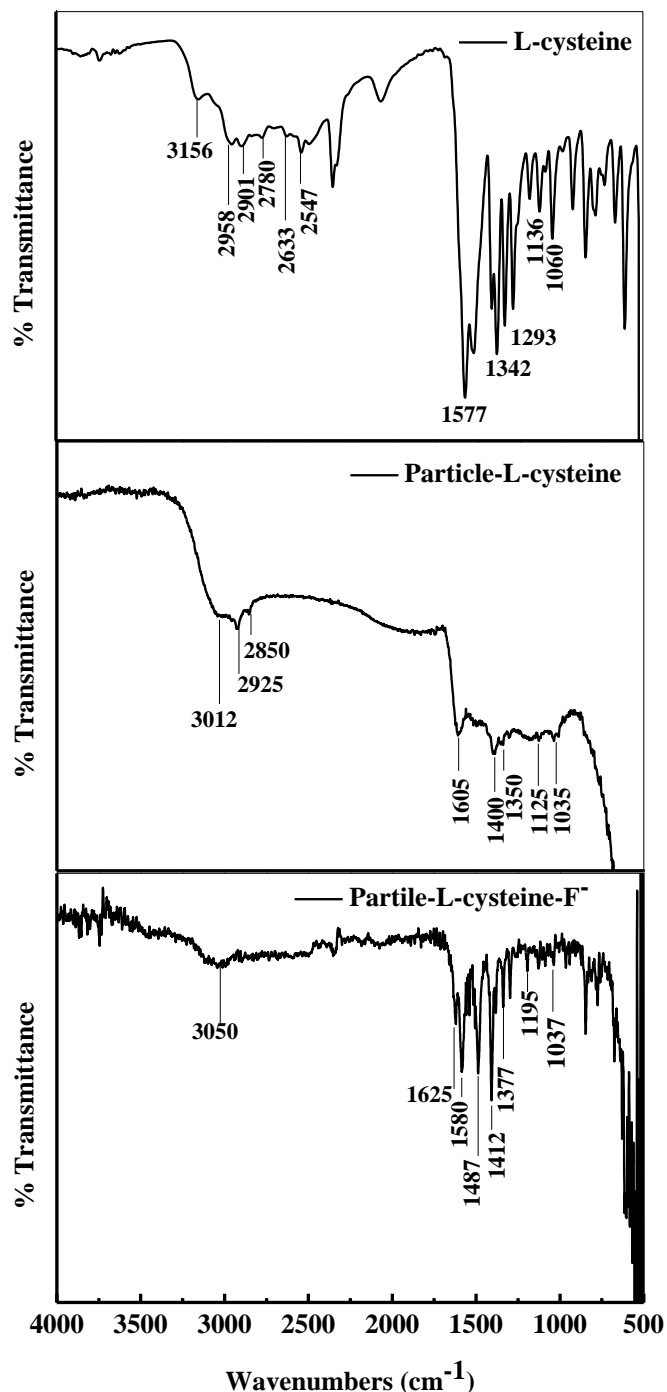
Figure 6.11. The FT-IR spectra of pure L-cysteine, L-cysteine capped nanoparticles, and L-cysteine capped nanoparticles after F⁻ ions addition.

To further support, the zeta potential measurement was also conducted for these three samples. The surface charge of the Ag-CdS/Ag-ZnS nanoparticles (-8.8 mV) was increased after capping of L-cysteine (-13.3 mV) because of the presence of free carboxylic groups of of L-cysteine molecules. A slight decrease (-11.4 mV) in surface charge of the capped nanoparticles after the addition of F⁻ is attributed to the presence of counter ion (Na⁺).
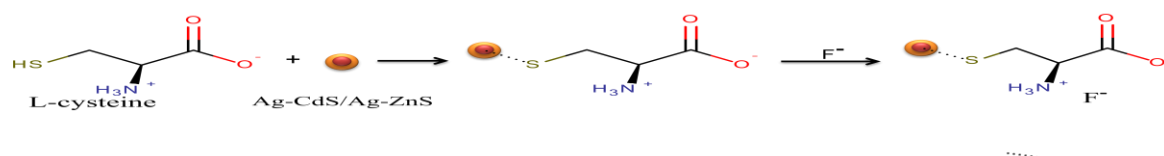
Scheme 6.2. Basic mechanism of particle attachment with L-cysteine and F^- ion attachment with L-cysteine functionalized nanoparticles.

Further, the mechanism of F^- binding with L-cysteine capped nanoparticles was also confirmed by the proton NMR study and the spectra are presented in Figure 6.12a. The ^1H NMR spectra of L-cysteine shows singlet at 10.217 ppm is because of the N-H proton, multiplets between 2.742 – to 2.9 ppm are because of C-H and C-H$_2$ protons, and singlet at 1.231 ppm is because of S-H proton. Whereas, the ^1H NMR spectra of L-cysteine with F^- (Figure 6.12b) shows a downfield shifting of the N-H proton signal from 10.217 to 10.253 ppm. To our belief, this is because of the deshielding effect of N-H proton. When F^- is attaching with amide group there is formation of N-H·····F^-. Because of interaction between N-H hydrogen bonding and F- the electron density gets reduced. The reduction in electron density causes deshielding effect in N-H bond and finally promotes the downfield shifting of the N-H proton signal.
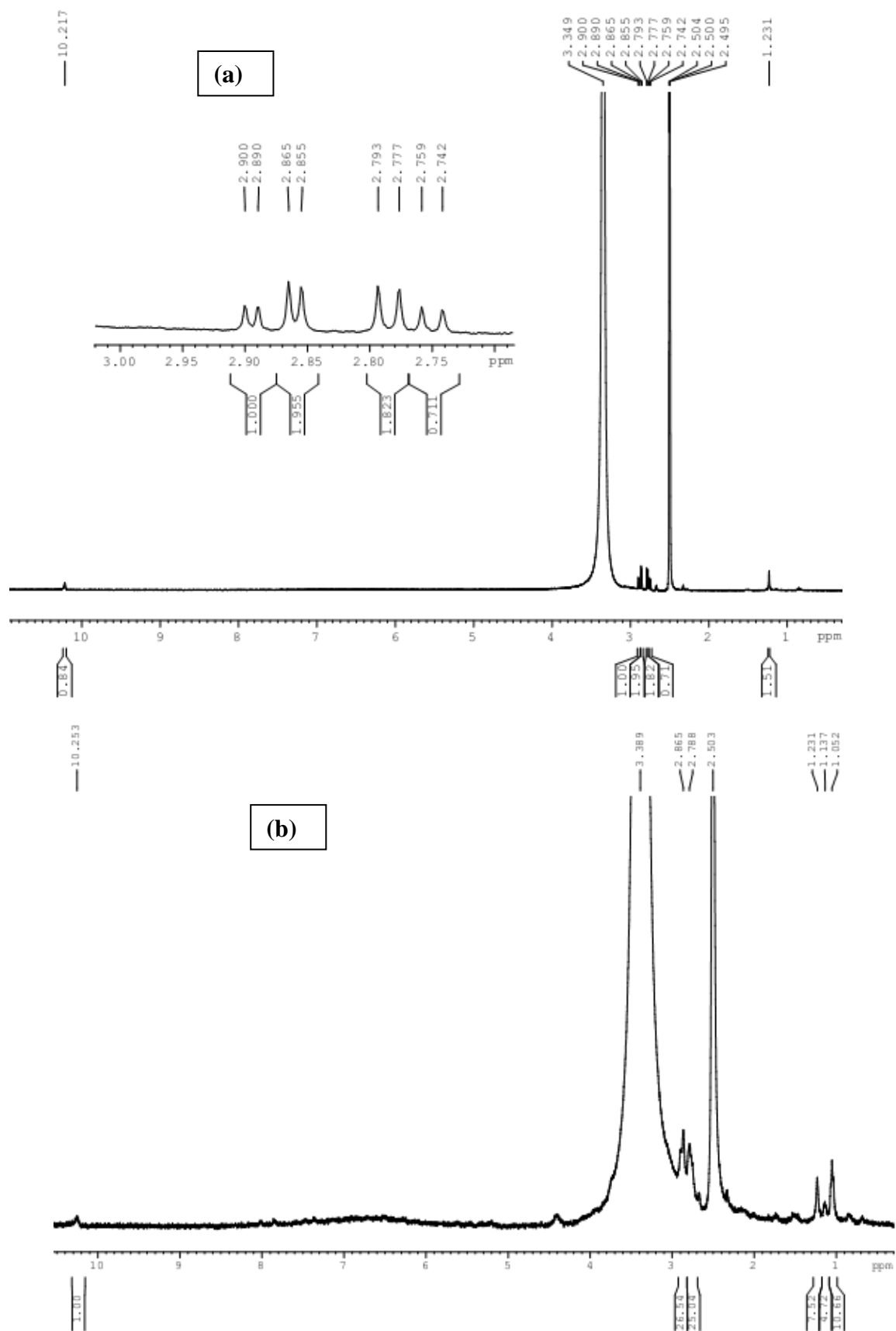
Figure 6.12. 1H NMR spectra of (a) L-cysteine and (b) L-cysteine with F⁻ in DMSO.

To get a comparative idea, our results are compared with the reported fluorometric/colormetric approaches for F$^-$ ion detection in Table 6.2. It can be seen that the reported methods of fluoride ion detection are in different media, such as water, acetonitrile, CH$_2$Cl$_2$, CHCl$_3$, CH$_3$CN, dimethyl sulfoxide (DMSO), and dichloromethane (DCM). Among these methods pure aqueous based analysis using NPs are limited. Noteworthy to mention, since the F$^-$ present in aqueous media, water-based detection methods are always preferable and economic. In that context, our method is applicable for neutral aqueous media, cheap, highly selective, and the detection limit (96.15 µg/L) is much lower compared to the available literature methods as well as the permissible limit of F$^-$ in drinking water.

Table 6.2. Comparison with the reported analytical methods for the detection of F$^-$ ions

Methods	Media	Materials	LOD (µg/L)
Fluorescent	water	Ag-CdS/Ag-ZnS	96.15 (our method)
		TU, [600] CMP, [601] Fe(III)-complex, [602] BTTPB, [422] QAM [603]	1900, [600] 199.479, [601] 2659.72, [602] 100, [422] 570 [603]
	Acetonitrile	BTD, [604] OC, [605]	3,458, [604] 4,750, [605]
	DMSO+water	HNCA, [606] ATPS [607]	162.24, [606] 100 [607]
	CHCl$_3$	BPT, [608] CdSe/ZnS [593]	46.2×10^6, [608] 1405.85×10^3 ±2.089×10^3 [593]
	CH$_2$Cl$_2$	OBC	284.97, 379.96 [426]
	DCM solution	PDIs	2659.72 [609]
	ethanol+water	ICTC	1519.84 [610]
Colorimetric	Water	SiNWs	1,000 [428]
	DMSO	PHC	3799.6, 379.96 [611]
	CH$_3$CN	CTAAM	189.98 [612]
	CH$_2$Cl$_2$+water	SPC	4,000 [613]

Triazolium units (TU), carbohydrate modified probe (CMP), N-(3-(benzo[d]thiazol-2-yl)-4-(tert-butyldiphenyl silyloxy)phenyl)-benzamide (BTTPB), quaternary ammonium moiety (QAM), Binaphthol thioureido derivative (BTD), organic compound (OC), dimethyl sulfoxide (DMSO), hydroxylnaphthalene 2-cyanoacrylate (HNCA), 9-anthryltriphenylstibonium (ATPS), bispyrenyl thioureas (BPT), organoboron compound (OBC), dichloromethane (DCM), perylene diimide derivatives (PDIs), internal charge

transfer based chemodosimeter (ICTC), Si Nanowires (SiNWs), pyrrole–hemiquinone compounds (PHC), chromogenic tripodal appended to azophenol moiety (CTAAM), Stibine–Palladium Complexes (SPC).

6.4   Conclusions

Ag-CdS/Ag-ZnS and Ag-ZnS/Ag-CdS nanoparticles were synthesized in aqueous media by chemical precipitation method. The size of the nanoparticles is in the range 5.92 ± 0.76 nm with 0.75 nm shell thickness. The obtained QY are 77.57 and 69.6% for Ag-CdS/Ag-ZnS and Ag-ZnS/Ag-CdS nanoparticles. A fluorescence probe has successfully developed based on L-cysteine functionalized Ag-CdS/Ag-ZnS nanoparticles. There is fluorescence enhancement of the functionalized nanoparticles after fluoride ion addition. A linear calibration curve is obtained with detection capability as low as 99.7 µg/L in aqueous and neutral media. This probe can selectively detect fluoride ions in the presence of different anions. The proposed method is simple, inexpensive, sensitive, and high selective towards fluoride ion detection, and can be used for F^- detection in the drinking water as well biological and environmental science.

Chapter 7

Synthesis and Characterization of Ag Doped Hollow CdS/ZnS Bi-layer Nanoparticles for Fluorometric Detection of Ultralow Arsenic Concentrations

7.1 Introduction

Multilayer hollow nanoparticles are attracting much attention in recent years over the core/shell or simple hollow particles because of their excellent optical, catalytic, and other properties. The nanoparticles under this class are important because they are having advantages of both core/shell and hollow structures. While analyzing the combination of materials for multi core/shell nanoparticles, it has been found that combinations of II-IV semiconductor materials, such as CdS and ZnS have attracted considerable research interest because of their potential applications in various fields, such as nonlinear optical devices, sensors, flat displays, and lasers. [614–616] Recently, hollow nanostructures with single shelled, double-shelled, and multi-shelled have been attracted considerable interest because of its unique properties, such as low density, high specific surface area, and controllable surface permeability, [617–619] and their potential applications in various fields of biotechnology, chemistry, and advanced functional materials. [620–625] The photoluminescence studies have been reported for different tri-layers (core/shell/shell) semiconductor nanoparticles, such as CdS/HgS/CdS, [626] Al doped ZnO/Al/Al doped ZnO thin film; [627] and hollow bi-layers nanoparticles such as ZnS/Ag_2S, [628] PSA/SiO_2. [629] Further, doping of core/shell or hollow structures help to enhance or develop new properties. Recently, doped multilayer nanoparticles have been studied by different researchers, such as $NaYF_4$:Yb,Er(Tm)/$NaYF_4$/Polymer, [630] $NaYF_4$:Er, Yb, Gd/$NaYF_4$:Tm,Yb/$NaGdF_4$:Gd. [631] Doped hollow structure single shell nanoparticles, such as rare -earth (RE)-doped gadolinium oxide (Gd_2O_3) hollow nanospheres has been studied as a promising platform for simultaneous bioimaging and drug delivery because of its combined presence of efficient optical and MR imaging capabilities, as well as the hollow structure. [632]

The semiconductor nanoparticles are also very useful for the application of sensing of metal ions in solution. Different fluorescence material, such as C, [379,633,634] Au, [402,635] SiO_2, [403,404,436,437] CdSe, [438,639] CdS, [640,641] ZnS, [642] zeolite, [643] SBA-15 [644–646] were used for different inorganic metal ion detection. Among different metal ions, detection of arsenic in water sample is very important because of its toxicity in nature. The contamination of arsenic in the surface (lakes, rivers) and groundwater occurs mainly because of its abundance natural availability (As_2S_2, As_2S_3, and As_2O_3). [647,648] Apart from these, the by-product of burning of waste and fossil fuels, E-wastes, gold mining, volcanism, pesticides, etc. also contribute to the environment. Arsenic is predominantly present in two major ionic forms in the ground water, such as arsenite (As(III)) and arsenate (As(V)). [490] The permissible limit of total arsenic in drinking water is 0.01 − 0.05 mg/L as prescribed by WHO. [650] It has been also

reported that As(III) is 25-60 times more toxic than As(V). [651,652] Elevated levels of arsenic in drinking water can cause various human diseases, such as skin damage, heart disease, and respiratory problem; moreover, because of mutagenic nature it can also lead to cancer in skin, lungs, liver, and kidney. [391,392] Because of these reasons, easy and low level detection of arsenic in water is become a challenge in recent years. Different analytical methods have been used for the detection of arsenic, such as atomic absorption spectroscopy (AAS), [393] hydride generation atomic absorption spectrometry (HG-AAS), [394] polarographic technique, [395] inductively coupled plasma (ICP), [396] ICP atomic emission spectrometry (ICP-AES), ICP mass spectrometry (ICP-MS), [397] high performance liquid chromatography (HPLC) with optical spectrometer detection, [398] and voltammetry study. [399,400] Here in the ICP-MS methods can detect up to a very low concentration of arsenic (~0.01 μg/L) but the ICP is very costly and the sample preparation for this method is complicated and time consuming. However, the other existing methods are expensive because of the high cost instruments, time consuming, difficult to detect at low level, interference of different associated ions; because of these reasons the in situ determination of at ultra-trace level arsenic species is still a challenging job.

In the present study, Ag doped hollow CdS/ZnS bi-layer (Ag-h-CdS/ZnS) nanoparticles are synthesized with improved photoluminescence property. The hollow structure is formed by a sacrificial core method using AgBr as the core. Ag doping is achieved during the removal of core by dissolution in ammonium hydroxide solution. The light emission properties of these nanoparticles in terms of quantum yield (QY) are studied using phenol as the reference. It was found that the fluorescence of the synthesized nanoparticles is selectively sensitive to the As(III) ions. Accordingly we proposed a new methods for sensing As(III) ions with a limit of detection as low as 226 ng/L, which is much lower than the reported literature till now. Compared to other nanoparticles-based arsenic sensors our approach is easy, selective, sensitive, and low cost for ultra trace level detection.

7.2   Materials and Methods

7.2.1   Materials

Reagent-grade silver nitrate (99.9%) and NaCl were purchased from Ranbaxy. Anionic surfactant sodium dodecyl benzene sulphonate (SDBS) (technical grade, Cat No. 28995-7), cetyltrimethyl ammonium bromide (CTAB) with 99% purity, and L-cysteine were obtained from Sigma Aldrich. Zinc acetate, cadmium acetate, sodium sulphide (Na_2S), ammonium hydroxide (25%), KNO_3, $CaCl_2$, $FeCl_3$, $FeSO_4.7H_2O$, $Al_2(SO_4)_3$, and $MgSO_4$ were purchased

from Merck. Arsenic tri-oxide (As_2O_3), $Na_2HAsO_4.7H_2O$, $Cr(NO_3)_3.9H_2O$ was taken from Loba Chemie. $HgCl_2$, $SnCl_2.2H_2O$ was taken from Fisher Scientific. All the chemicals were used as it was received without any further purification. Ultrapure water of 18.2 MΩ.cm resistivity and pH 6.4–6.5 was used for all the experiments.

7.2.2 Methods

The details procedure for silver doped hollow CdS/ZnS bi-layer nanoparticles synthesis is presented in scheme 7.1. AgBr nanoparticles were used as the core to synthesize silver doped hollow bi-layer nanoparticles. AgBr nanoparticles were synthesized in aqueous media following the reported protocol. [527] The equimolar concentrations of $AgNO_3$ and KBr were maintained (0.1 mM each) for the synthesis of core. After the equlibrium time (~30 min) for AgBr formation, the particles were dispersed in SDBS (concentration 1.5 times of CMC)and sonicated using a bath sonicator for 20 min. Cadmium acetate solution was then added to the suspension under constant stirring condition to get the final concentration of 0.025 mM. Then sodium sulphide solution was added drop wise to this reaction mixture to maintain final concentration of 0.025 mM. The reaction was continued for 45 min for the complete formation of AgBr/CdS core/shell nanoparticles. These core/shell nanoparticles were then sonicated again for 20 min. Then zinc acetate was added to this suspension under constant stirring condition (final conc. = 0.025 mM), sodium sulphide (final conc. = 0.025 mM) was then added drop wise. The reaction was continued for another 45 min to complete the formation of AgBr/CdS/ZnS core/shell/shell nanoparticles. The final particles were separated from the reaction mixture by centrifugation at 25000 rpm for 20 min. These particles were then suspended in ammonium hydroxide solution (final conc. 2.5 mM) for 48 hrs to remove the core. Finally Ag-h-CdS/ZnS nanoparticles were again centrifuged and washed three times with alcohol-water solution. For Ag doped hollow ZnS/CdS (Ag-h-ZnS/CdS) nanoparticles synthesis the same method was followed instead AgBr is dispersed in the CTAB media (concentration 1.5 times of CMC). The particles were then dried in oven at 60°C for overnight. For quantum yield (QY) calculation of the synthesized nanoparticles, phenol was used as a standard material (QY=0.14).
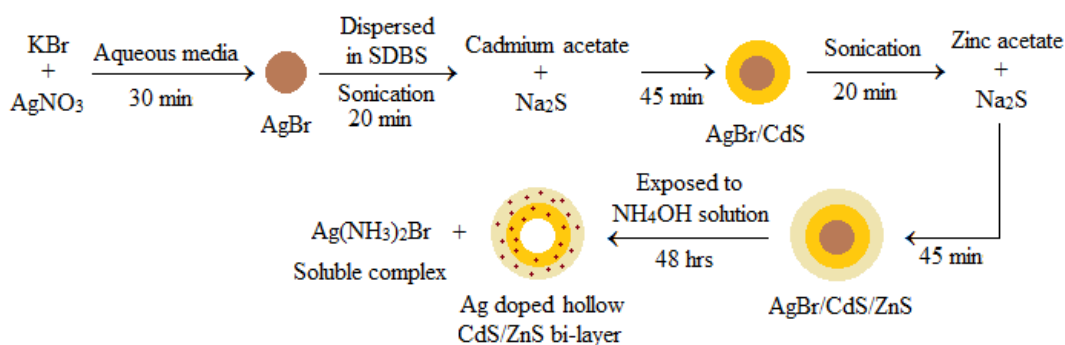
Scheme 7.1. Schematic synthesis route of silver doped hollow CdS/ZnS bi-layer nanoparticles.

7.2.3 Particles Characterization

The measurement of particle size and the zeta potential was carried out by dynamic light scattering (DLS) using Malvern Zeta Size analyzer, (Nano ZS). The crystallinity of synthesized particles was characterized using X-ray diffraction (XRD) (Philips, PW 1830 HT) with scanning rate of 0.01°/s in the 2θ range of 20 to 80°. The size and shape of the particles were observed in field emission scanning electron microscope (FE-SEM) (Nova NanoSEM NPE212) and transmission electron microscope (TEM) (Tecnai S-twin). The optical absorption and fluorescence emission properties of the particles were studied by UV–Vis–NIR Spectroscopy (Shimadzu-3600) and fluorescence spectroscopy (Hitachi- 7000), respectively. The particles were also characterized by fourier transform infrared spectroscopy (FT-IR, Thermo Fisher Scientific, Nicolet iS10). The chemical composition of the samples and the valence states of various elements were analyzed by X-ray photoelectron spectroscopy (PHI 5000 VersaProbe II scanning XPS microprobe, ULVAC-PHI) employing a monochromatic Al Kα X-ray source (hv=1486.6 eV). ^{1}H NMR spectra were collected with a Bruker Ultra shield 400 MHz spectrometer using SiMe$_4$ as an internal standard.

7.2.4 Determination of As(III) ions

For As(III) sensing purpose the as synthesized Ag-h-CdS/ZnS nanoparticles were initially capped with L-cysteine (0.0016 g/ml). After addition of L-cysteine to the nanoparticles solution it was kept for 2 hrs and then the analyte was added to the solution. The fluorescence intensity of the solution was then recorded after exciting at 220 nm wavelength. The fluorescence measurement was also taken for pure nanoparticles and L-cysteine functionalized nanoparticles.

7.2.4.1 Determination of Limits of Detection (LOD)

The limit of detection (LOD) of the fluorescence probe was calculated as $3\sigma/k$, where σ is the standard deviation from the blank measurements and k is the slope of the calibration curve.

7.2.4.2 Selectivity Test

To evaluate the selectivity of the fluorescence probe towards other ions, experiment was conducted in the presence of different ions, such as Na^+, K^+, Ca^{2+}, Mg^{2+}, Sn^{2+}, Hg^{2+}, Fe^{2+}, Fe^{3+}, Cr^{3+}, Al^{3+}, As(V), Cl^-, NO_3^-, SO_4^{2-}. The concentration of Na^+, K^+, Ca^{2+}, Mg^{2+}, Sn^{2+}, Fe^{2+}, Fe^{3+}, Cr^{3+}, Al^{3+}, Cl^-, NO_3^-, SO_4^{2-} ions was maintained 900 µg/L each, where as the concentration of Hg^{2+} and As(V) were 562.5, 675, 900 µg/L and 675, 900 µg/L with As(III) concentration of 22.5 µg/L.

7.3   Results and Discussion

7.3.1   Characterization of Particles by UV-Vis Spectroscopy

To investigate the optical absorption properties of the nanoparticles UV-Vis spectroscopy study was done and the results are presented in Figure 7.1. There is a sharp absorption peak in pure AgBr at 237 nm wavelength; whereas the broad absorption is notable in case of pure CdS and ZnS nanoparticles (inset Figure 7.1). After subsequent coatings of CdS and ZnS on AgBr the sharp peak of AgBr becomes broad absorption in the range of 350 to 650 nm wavelengths, which gives an indirect support of coating of CdS and ZnS layers on the AgBr core. After removal of the AgBr core the absorbance intensity has been improved both in UV and visible regions for Ag-h-CdS/ZnS nanoparticles, which could be because of the silver doping to the hollow bi-layer structure. But, the visible absorbance intensity again reduced when ZnS and CdS are in inner and outer layer, respectively in Ag-h-ZnS/CdS nanostructure. So, the optical absorption properties depend on the position of low band gap semiconductor CdS (2.5 eV) and the high band gap semiconductor ZnS (3.6 eV). The low band gap material in the inner layer gives better absorption properties in the bi-layer structure.
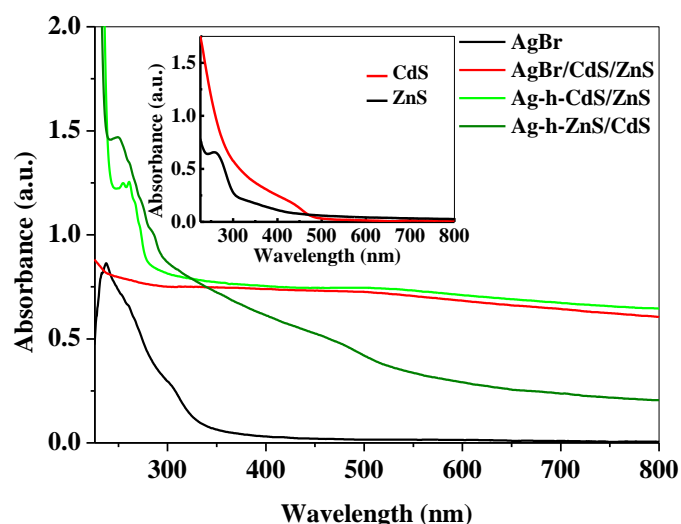
Figure 7.1. UV–vis absorbance spectra of AgBr, AgBr/CdS/ZnS, Ag-h-CdS/ZnS and Ag-h-ZnS/CdS nanoparticles.

7.3.2 Characterization of Particles by XRD

The crystallographic phases of the particles were identified by the X-ray diffraction (XRD) studies. The XRD patterns of pure AgBr, AgBr/CdS/ZnS, Ag-h-CdS/ZnS, and Ag-h-ZnS/CdS nanoparticles are shown in Figure 7.2. The peaks of AgBr were found at (2θ) 30.9, 44.3, 55.2, 64.5, and 73.3°, corresponding to the planes (200), (220), (222), (400), and (420) of cubic structure (JCPDS card no.79-0149). In the case of AgBr/CdS/ZnS core/shell/shell particles the AgBr peaks were suppressed to low intensity at the same 2θ; the peaks of CdS were obtained at (2θ) 26.69, 44.02, 52.13, and 63.63°, corresponding to (111), (220), (311) and (400) planes of cubic structure (JCPDS card no. 75-1546); and the peaks (2θ) at 28.91, 33.43, 48.27, 56.53 and 59.65° for ZnS, corresponding to the planes (111), (200), (220), (311) and (222) of cubic structural phase (JCPDS card no. 80-0020). The presences of AgBr and CdS peaks in the tri-layer particles are mainly because of the lower shell thickness of CdS and ZnS on AgBr nanoparticles. The absence of AgBr XRD peaks in Ag-h-CdS/ZnS and Ag-h-ZnS/CdS particles indicates the complete removal of AgBr core. However, there is a shifting of CdS and ZnS peaks from their previous positions that of before dissolution. That shifting of XRD peaks are mainly because of doping of Ag by during dissolution of core. In general, doping on nanoparticles may be of three types: (i) surface of the host material, (ii) replacement of the principle component of the host material, and (iii) interstitial sites of the host material. Since there is no peak of pure metal silver, the possibility of silver doping is because of the replacement of principle components in CdS/ZnS bi-layer structure. In general, the substitutional doping is favourable when the ionic radii of two elements are comparable. The ionic radii of Ag^{2+}, Cd^{2+}, Zn^{2+}, and S^{2-} are 0.94, 0.95, 0.74, and 1.84 Å

139

respectively. As the ionic radius of Ag^{2+} is very close to Cd^{2+} and Zn^{2+} compared to S^{2-}, the silver can easily substitute the Cd or Zn of the CdS and ZnS lattices. It can also to be noted that, the ZnS peak is more prominent in Ag-h-CdS/ZnS compared to Ag-h-ZnS/CdS because of the ZnS in outer shell layer.
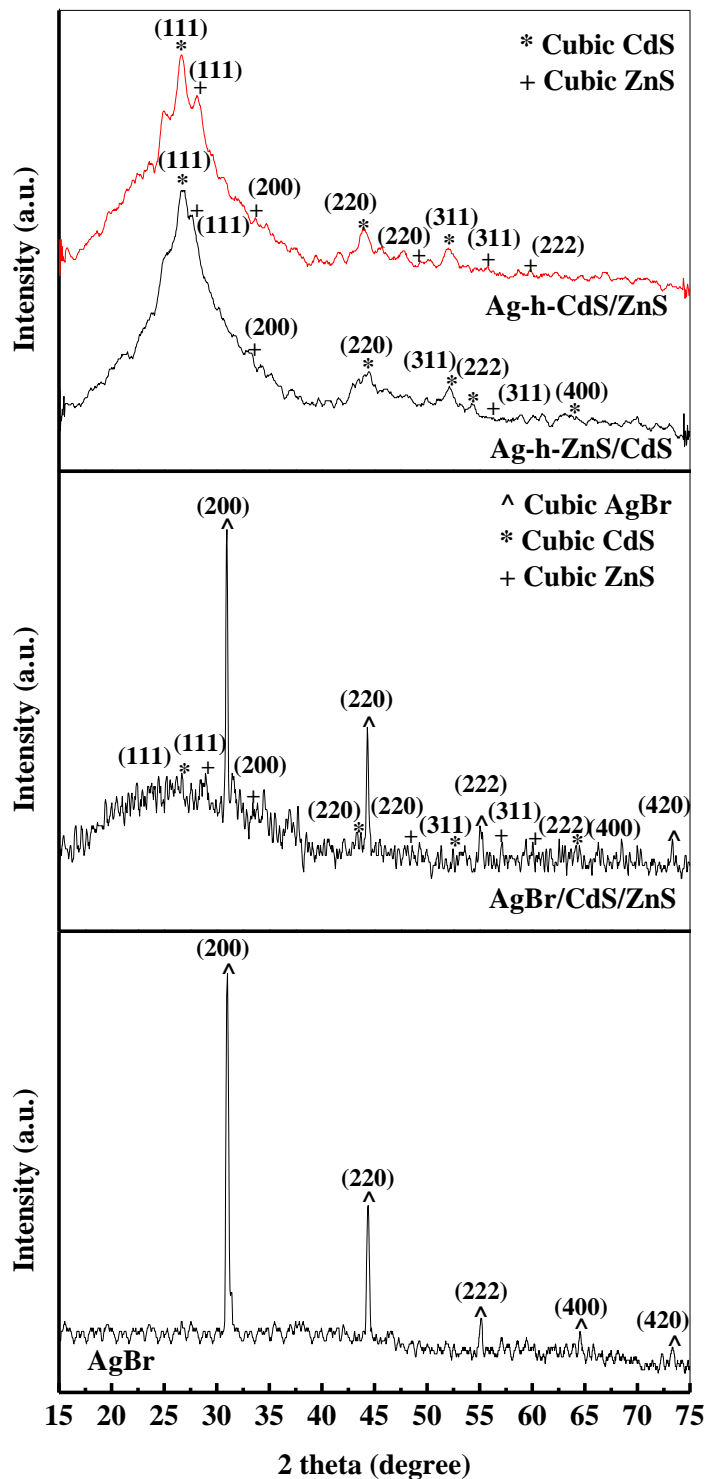
Figure 7.2. X-ray diffraction patterns of pure AgBr, AgBr/CdS/ZnS, Ag-h-CdS/ZnS and Ag-h-ZnS/CdS nanoparticles.

7.3.3 Characterization of Particles by FT-IR Spectroscopy

The FT-IR spectra of Ag-h-CdS/ZnS and Ag-h-ZnS/CdS double shell nanoparticles were recorded in the range 4000-400 cm^{-1}, as shown in Figure 7.3. In Ag-h-CdS/ZnS the major peaks at 1131.33, 611.12, and 582.69 cm^{-1} are because of the stretching vibration of Zn-S. One weak peak at 1600.05 cm^{-1} is for the bending vibration of Cd-S bond, but there is no other peak of CdS might be because of ZnS coating on CdS. For Ag-h-ZnS/CdS the peaks at 1612 and 738.37 cm^{-1} are because of the bending vibration of Cd-S bond. The major peak at 554.78 cm^{-1} is for the stretching frequency of Cd-S bond. The major peaks of Zn-S bond are not noticeable here, which confirms the coating of CdS layer on ZnS.
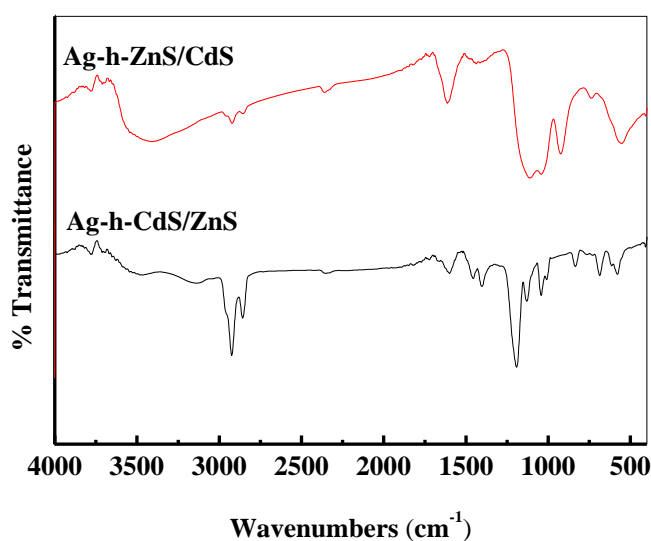
Figure 7.3. FT-IR spectra of Ag-h-CdS/ZnS and Ag-h-ZnS/CdS nanoparticles.

7.3.4 Characterization of Particles by Transmission Electron Microscopy (TEM)

The TEM characterization was done to study the morphology and the nanostructure of the particles. Figure 7.4a shows the high magnified TEM image of AgBr/CdS/ZnS tri-layer nanoparticle before dissolution in ammonium hydroxide solution. The contrast difference in layer in individual particle clearly indicates the formation of tri-layer nanoparticles of size 76.02 ± 2.47 nm with shell thickness of CdS layer was 1.5 nm and outside ZnS layer was 1.8 nm. The high resolution TEM image of AgBr/CdS/ZnS in Figure 7.4b clearly indicates the lattice fringes spacing of 0.28 nm corresponding to the (200) plane for cubic AgBr (JCPDS card no.79-0149), the lattice fringes spacing of 0.33 nm corresponding to the (111) plane for cubic CdS (JCPDS card no.75-1546) and the lattice fringes spacing of 0.31 nm corresponding to the plane for cubic ZnS (JCPDS card no. 80-0020). The TEM micrograph of Ag-h-CdS/ZnS particles is presented in Figure 7.4c. The Figure 7.4c clearly shows the absence of

141

dark core, which confirm the formation of hollow structure, and two layers at the edge because of two shells. Figure 7.4d shows the high magnified image of Ag-h-CdS/ZnS NPs. The high resolution TEM image (Figure 7.4e) shows the lattice fringes of cubic phase CdS and ZnS. The selected area electron diffraction (SAED) pattern of this particle was obtained by focusing the electron beam on individual nanoparticles and is presented in Figure 7.4f. The ring like diffraction pattern shows the concentric Debye-Scherrer rings which can be indexed to the (111) of CdS, (200), (220) of ZnS in synthesized CdS/ZnS hollow double shell nanoparticles.
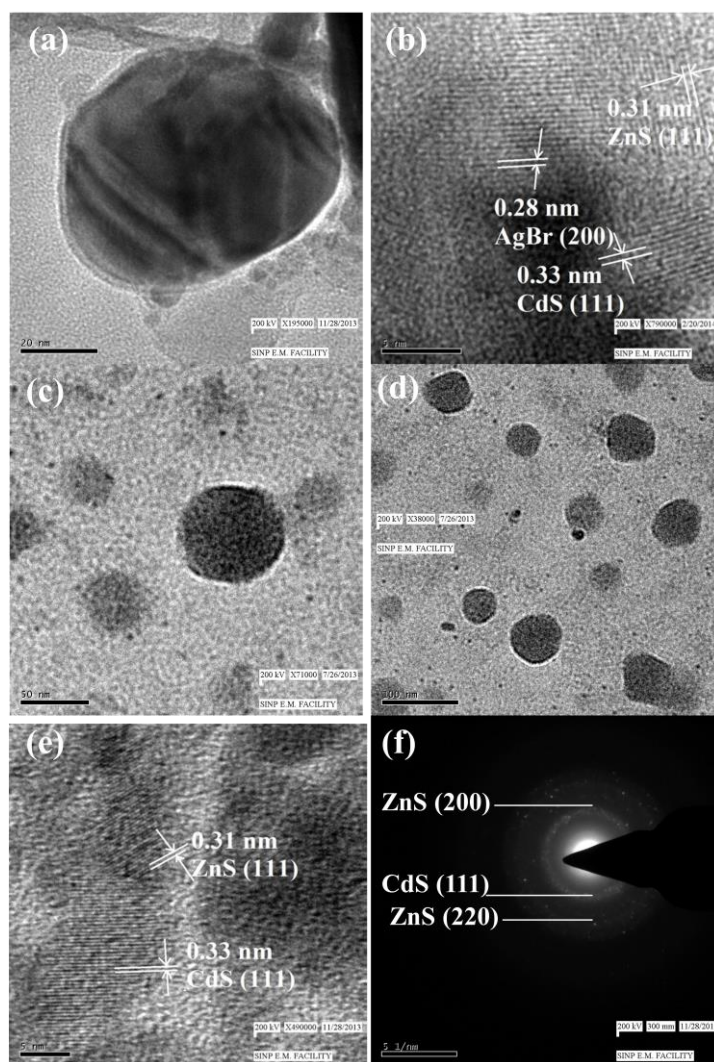
Figure 7.4. (a) TEM and (b) HR-TEM images of AgBr/CdS/ZnS tri-layer nanoparticles. (c, d) TEM images, (e) HR-TEM, and (f) SAED pattern of Ag-h-CdS/ZnS nanoparticles.

7.3.5 Characterization of Particle by XPS

The surface composition and the chemical states of Ag-h-CdS/ZnS nanoparticles were confirmed by X-ray photoelectron spectroscopy (XPS) studies. Figure 7.5a shows the high

resolution peak of Cd 3d level spectra of the sample. The strong peak of Cd $3d_{3/2}$ and Cd $3d_{5/2}$ could be seen at the binding energy of 411.1 and 404.6 eV, respectively, with spin orbit separation of 6.5 eV. The high resolution peak of Zn 2p in Figure 7.5b exhibits two strong peaks at 1021.4 and 1044.1 eV are assigned to the binding energy of Zn $2p_{3/2}$ and Zn $2p_{1/2}$, respectively with a slitting of 22.7 eV, confirming the formation of Zn^{2+}. The peak of S 2p came at the binding energy of 160.25 eV as presented in Figure 7.5c. The XPS spectra of Ag 3d level is presented in Figure 7.5d which shows the strong peaks of Ag $3d_{5/2}$ and Ag $3d_{3/2}$ at the binding energy of 366.9 and 372.8 eV, respectively with a slitting of the 3d doublet of 5.9 eV, confirming the presence of ionic silver instead of metallic silver, which supports the XRD data. So, the silver doping is achieved on both shell layers during dissolution by the substitution of Cd^{2+} and Zn^{2+} in the CdS and ZnS lattices.
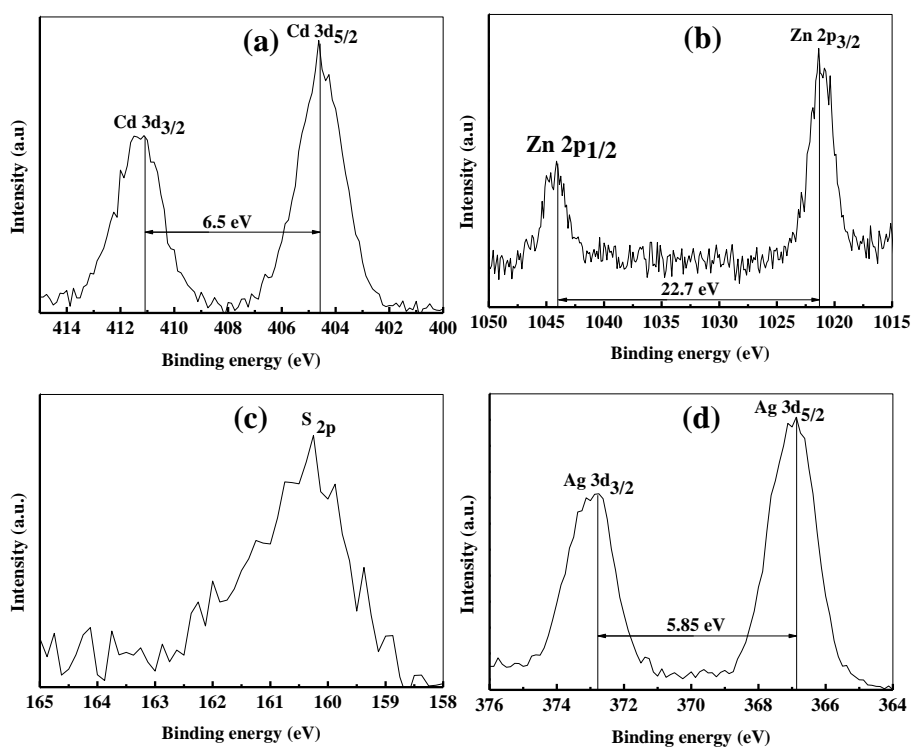
Figure 7.5. High resolution XPS narrow scan spectra of (a) Cd(3d), (b) Zn(2p), (c) S(2p) and (d) Ag(3d) for Ag-h-CdS/ZnS nanoparticles.

7.3.6 Characterization of Particles by Fluorescence Spectroscopy

Fluorescence properties of the synthesized nanoparticles were studied and the emission spectra of the Ag-h-CdS/ZnS and Ag-h-ZnS/CdS nanoparticles after excitation at 220 nm wavelength are presented in Figure 7.6. The major peaks were obtained in the visible region at the wavelengths of 443.8 and 443.6 nm for Ag-h-CdS/ZnS and Ag-h-ZnS/CdS, respectively. The emission intensity of Ag-h-CdS/ZnS is higher compared to Ag-h-ZnS/CdS.

This type of behaviour was also obtained in case of Ag doped CdS/ZnS and ZnS/CdS nanoparticles as discussed in the chapter 6. This behaviour is obtained mainly because of different electron affinity and band configuration due to the position variation of CdS and ZnS in the bi-layer structure. The quantum yield (QY) is also one of important parameters of any fluorescence material. The QY was also calculated for this sample using phenol as the standard material having QY of 0.14. The QY of Ag-h-CdS/ZnS was calculated as 88.14%, where as the quantum yield of Ag-h-ZnS/CdS is 80.34% (Table 7.1). The QY of the bi-layer nanoparticles is high when the CdS is in the outer layer, which is because of the low band gap material (CdS) is coated by a high band gap material (ZnS). In this type of structure, because of passivation of the core (inner layer) surface and elimination of the surface trap, the electrons are located only in the core and holes are located throughout the core and shell layers, as a result quantum yield increases. [628]
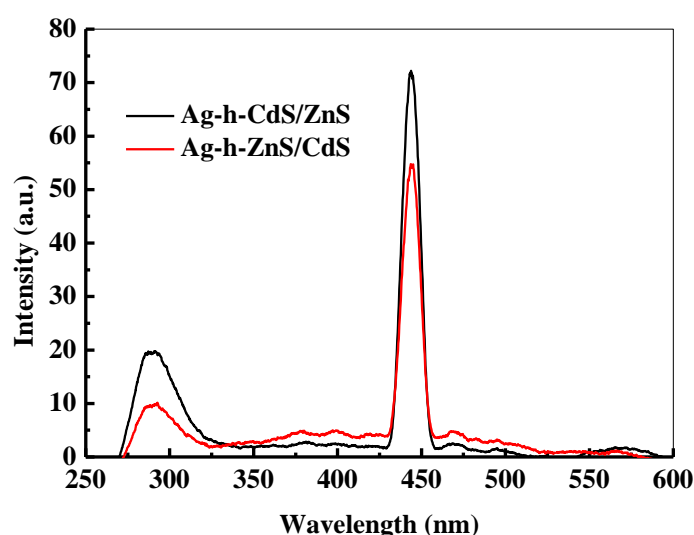
Figure 7.6. Emission spectra of Ag-h-CdS/ZnS and Ag-h-ZnS/CdS nanoparticles in the range 250-600 nm wavelength. The particles were excited at 220 nm wavelength.
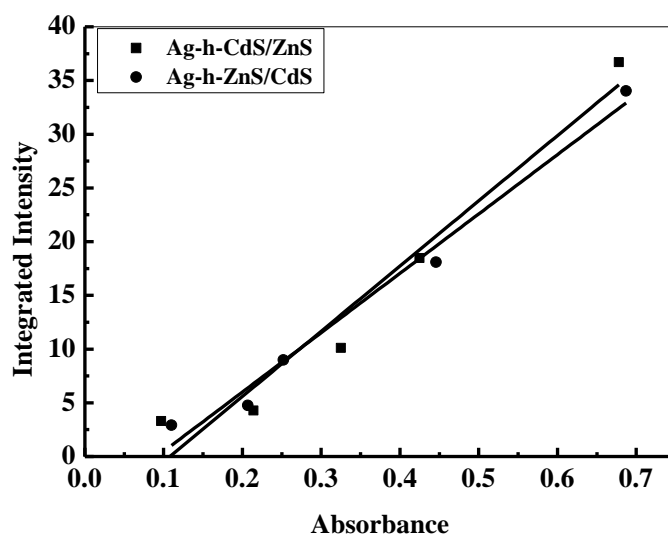
Figure 7.7. The plot of absorbance vs. integrated intensity of Ag-h-CdS/ZnS, Ag-h-ZnS/CdS nanoparticles.

Table 7.1. The fitting equation and R^2 value of integrated intensity (from fluorescence spectra) vs. absorbance (from UV spectra) line and the QY of phenol, Ag-h-CdS/ZnS and Ag-h-ZnS/CdS nanoparticles.

Material	Fitting equation	R^2 value	Quantum yield (QY)
Phenol (reference)	y=26.72x+0.3154	0.9973	0.14
Ag-h-CdS/ZnS	y=60.6x-6.5	0.93	0.8814
Ag-h-ZnS/CdS	y=55.24x-5.046	0.98	0.8034

7.3.7 Detection of As(III) Ions

The synthesized Ag-h-CdS/ZnS nanoparticles was used for the detection of As(III) ions. The nanoparticles were first functionalized by capping with L-cysteine and the fluorescence emission spectra were recorded upon addition of different concentrations of As(III) ions. Figure 7.8a shows the fluorescence quenching spectra of Ag-h-CdS/ZnS nanoparticles in the presence of As(III) ions in the neutral media. Initially there is a reduction in the fluorescence intensity after capping with L-cysteine, then with the addition of As(III) there is a gradual quenching of the fluorescence emission with increasing the As(III) ions. The fluorescence quenching of the nanoparticles is mainly because of the change in electron, charge and energy transfer during interaction between nanoparticles, and As(III). The functional groups

145

of L-cysteine selectively interact with the metal ions (As(III)) and form complex which subsequently change the electronic structure and accelerates the non-radiative recombination of the excitons in the nanoparticles, as a results there is quenching in the fluorescence. [633]
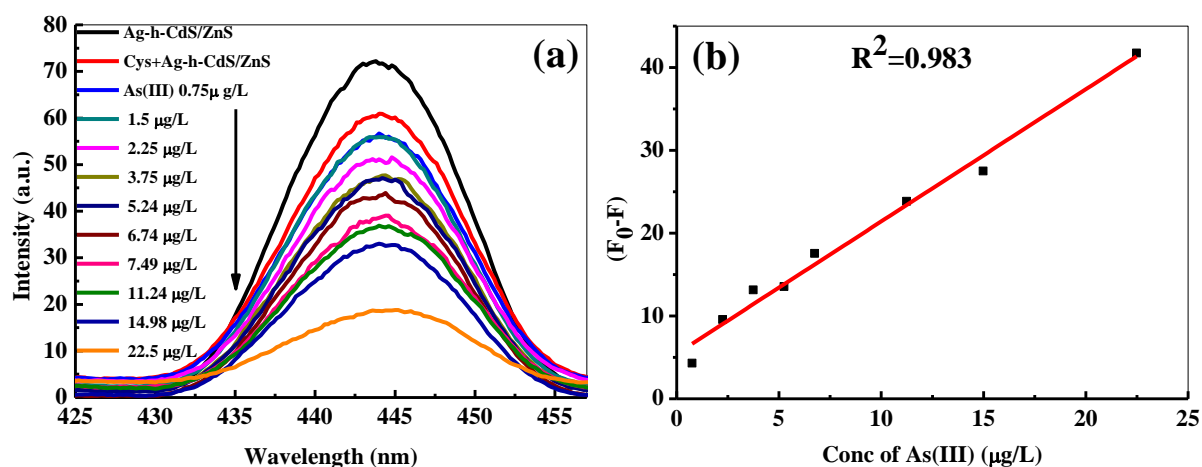
Figure 7.8. Fluorescence quenching of Ag-h-CdS/ZnS nanoparticles after capping with L-cysteine and the addition of As(III) ions in neutral media. The concentration of the As(III) ions are in the range of 750 – 22500 ng/L. Linear plot of quenched fluorescence intensity of the L-cysteine capped Ag-h-CdS/ZnS nanoparticles with the increasing concentration of As(III) is shown in the inset. F_0 and F are the fluorescence intensities of L-cysteine capped Ag-h-CdS/ZnS nanoparticles in absence and presence of As(III) ions.

To understand the mechanism of interaction of nanoparticles with L-cysteine, and As(III) ions FT-IR analysis was done. Figure 7.9 represents the FT-IR spectra of pure L-cysteine, L-cysteine capped nanoparticles, and L-cysteine capped nanoparticles with As(III). Pure L-cysteine shows the IR bands of $-NH_3^+$ (3141, 3002, and 2778 cm^{-1}), -SH (2546 and 2591 cm^{-1}), C=O (1574 cm^{-1}), and C-O (1060–1293 cm^{-1}). In L-cysteine capped nanoparticles the absence of –SH band is attributed to the cleavage of S-H bond and subsequent attachment with the nanoparticles surface. The peak for C=O also shifts to 1612 cm^{-1}. After As(III) addition, the shifting of C=O peak (1610 cm^{-1}), and the peak for C-O bond almost vanishes because of attachment of As(III) ion to COO- group of caped L-cysteine. The mechanism of L-cysteine attachment to the nanopaticles surface and subsequent attachment of As(III) ions is presented in Scheme 7.2. As shown in the scheme three L-cysteine caped nanoparticles can be attached to the tri-valance arsenic ion, which in turn leads to agglomeration of nanoparticles. To probe the hypothesis, the particle size analysis was done using DLS and FE-SEM, in spite of difference in size between two methods, both analysis shows increase in size after L-cysteine and subsequent As(III) addition (Figures 7.10 and 7.11). The FESEM

results indicate the final particle size increases to 199.5±54.2 nm, which again support the above hypothesis. The quenching effect of fluorescence emission is also because of larger particle size in the presence of As(III) ions. The zeta potential of the nanoparticles was also measured in its pure form, after L-cysteine capping, and after As(III) addition. The zeta potential was -15.8, -22, and -15.7 mV for pure nanoparticles, L-cysteine functionalized nanoparticles, and L-cysteine functionalized nanoparticles after As(III) addition. The surface charge increased after L-cysteine addition mainly because of O⁻ of L-cysteine and then the surface charge again reduced because of As(III) ion attachment with O⁻. To support the mechanism further, ^{1}H NMR study was done for pure L-cysteine and L-cysteine with As(III). The proton NMR spectra (Figure 7.12a) of pure L-cysteine shows the peak at 10.217 ppm is because of the N-H proton, multiplets between 2.742 – 2.9 ppm are because of CH and CH_2 protons, and singlet at 1.231 ppm is because of S-H proton. The NMR spectrum of L-cysteine in the presence of As(III) (Figure 7.12b) shows the downfield shifting of CH and CH_2 peaks. When As(III) ions are attached to the carboxylate group of L-cysteine molecules, then the carboxylate group will try to pull the electrons from C-H and $C-H_2$ carbon atoms, which in turn causes deshielding of protons. Finally, because of deshielding effect there is a downfield shifting of these protons peaks.
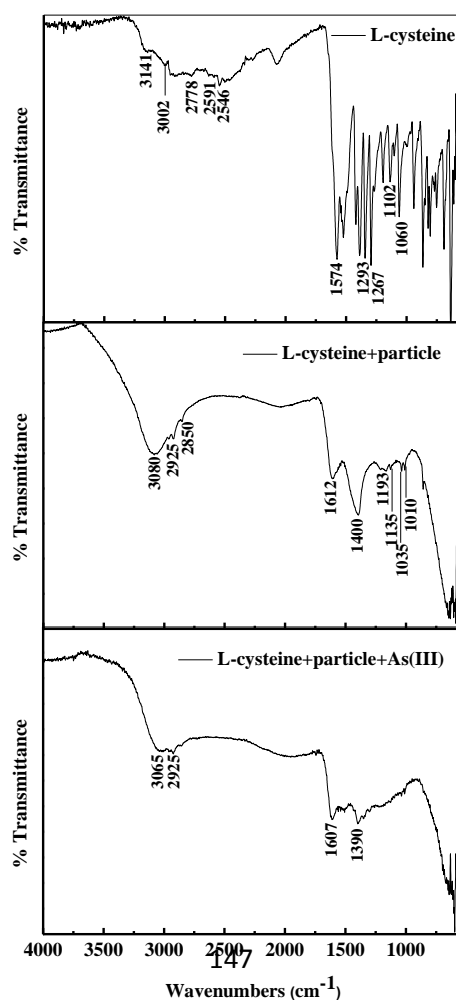
Figure 7.9. FTIR spectra of L-cysteine, L-cysteine capped nanoparticles, and L-cysteine capped nanoparticles in presence of As(III) ions.
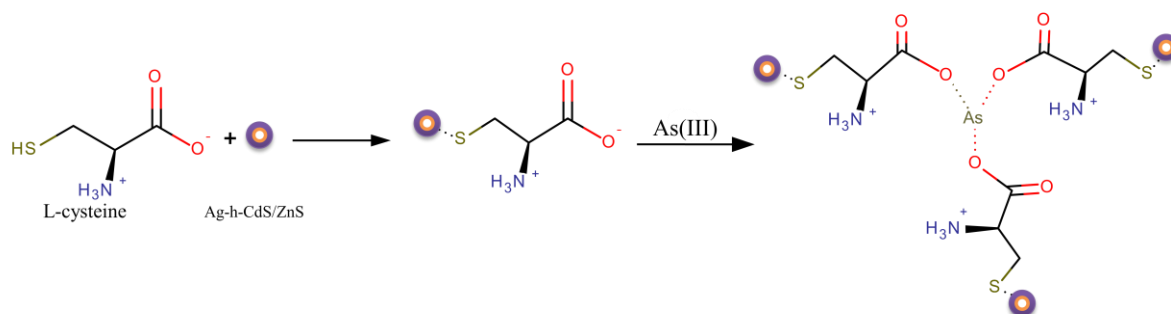
Scheme 7.2. Schematic diagram shows the mechanism of As(III) binding with the L-cysteine capped Ag-h-CdS/ZnS nanoparticles.
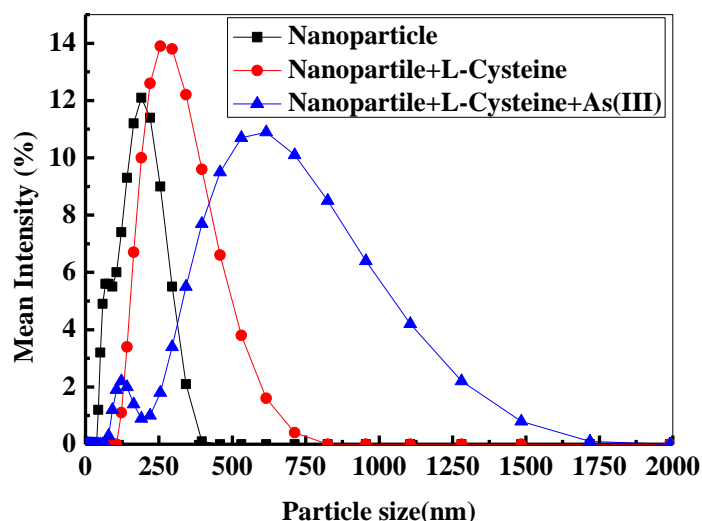
Figure 7.10. Particle size distribution of Ag-h-CdS/ZnS nanoparticles in pure form, L-cysteine capping, and L-cysteine capping in presence of As(III) measured by dynamic light scattering (DLS).
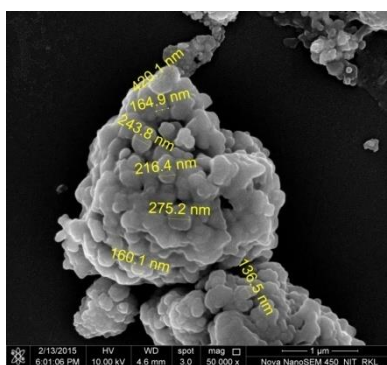
Figure 7.11. Field emission scanning electron microscopic (FE-SEM) image of L-cysteine capped Ag-h-CdS/ZnS nanoparticles after As(III) addition.
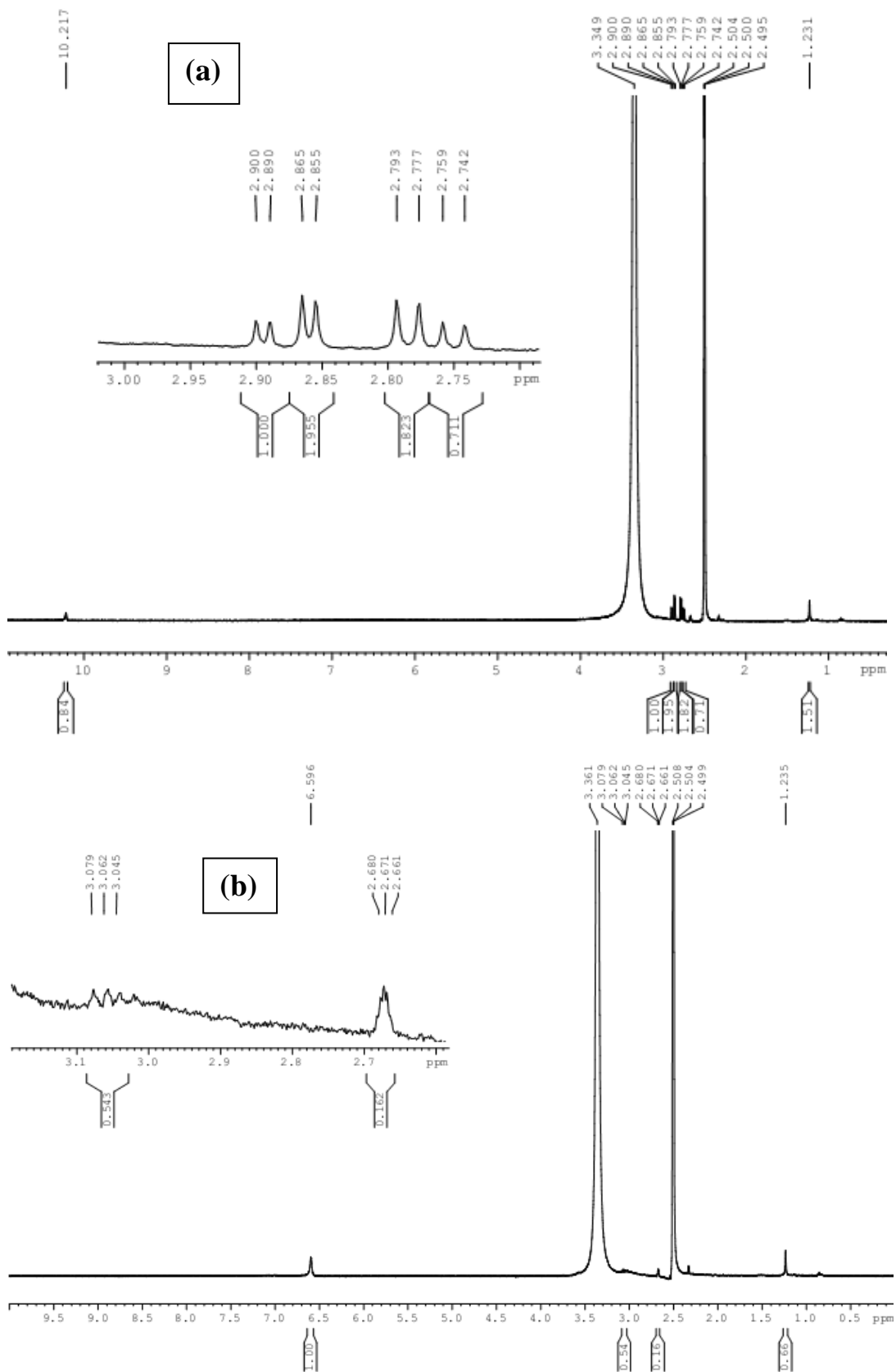
Figure 7.12. ^{1}H NMR spectra of (a) pure L-cysteine, (b) L-cysteine with As(III).

7.3.7.1 Effect of pH

To see the effect of pH, the quenching was also studied at acidic (pH 3) and basic (pH 10) pHs as presented in (a) and (b) parts of Figure 7.13. It can be seen that Ag-h-CdS/ZnS nanoparticles have strong quenching effect in the acidic media compared to that of neutral as well as basic media. This can be attributed to the fact that at acidic pH, L-cysteine molecules dissociates from the nanoparticles surface because of weak interaction between the thiol group and nanoparticles after protonation of the thiol group; as a result quenching of the fluorescence intensity. In case of alkaline pH there is a chance of strengthening the interaction between thiol group and nanoparticles because of deprotonation of the thiol groups, as a result the fluorescence intensity enhanced. [641] As the L-cysteine molecules are dissociated from the nanoparticles surface in acid media, after addition of As(III) further quenching is not significant.
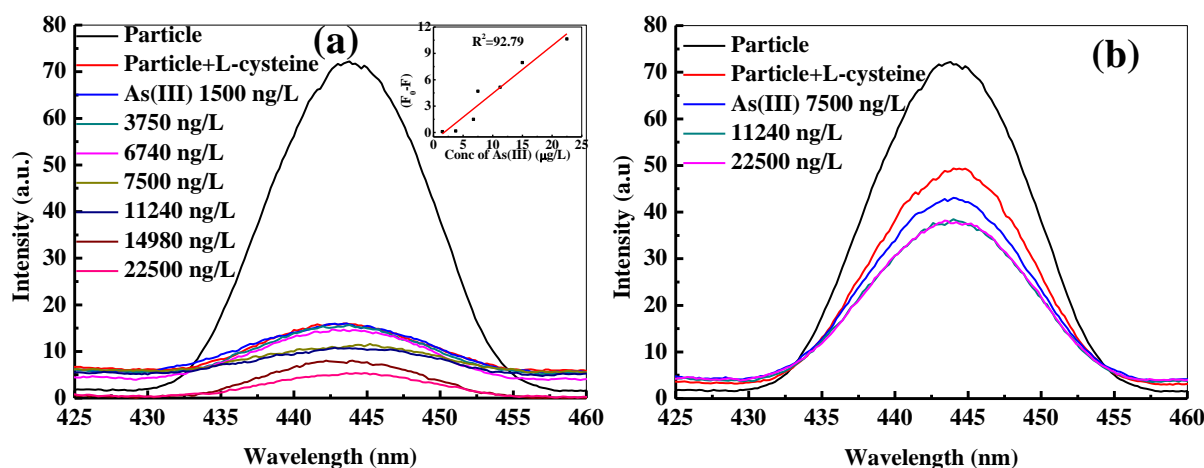
Figure 7.13. Fluorescence quenching of Ag-h-CdS/ZnS nanoparticles after capping with L-cysteine and the addition of As(III) ions in (a) acidic media (As(III) ions concentration 1500 – 22500 ng/L), (b) basic media (As(III) ions concentration 7500 – 22500 ng/L). Inset is the linear plot of quenched fluorescence intensity of the L-cysteine capped Ag-h-CdS/ZnS nanoparticles with the concentration of As(III) species in acidic media.

A linear relationship (R^2 = 0.983) between the quenched fluorescence intensity of L-cysteine capped Ag-h-CdS/ZnS nanoparticles with the concentration of As(III) ion in neutral media is observed, as shown in Figure 7.8b. The limit of detection (LOD) was also calculated to know the sensitivity of the method. The estimated LOD is 226 ng/L (3.015 nM), which is much lower than the permissible level (10,000-50,000 ng/L) of total arsenic content in drinking water as specified by World Health Organization (WHO). [650] The LOD was also

estimated in acidic media (pH 3) and the value is 666 ng/L (inset Figure 13a). So, in this proposed method we can detect very low level As(III) concentrations in neutral media only.

7.3.7.2 Selectivity Test

To know the selectivity of the method, the analysis was done in the presence of different ions present in surface, ground, and drinking water such as Na^+, K^+, Ca^{2+}, Mg^{2+}, Sn^{2+}, Hg^{2+}, Fe^{2+}, Fe^{3+}, Al^{3+}, Cr^{3+}, As(V), Cl^-, SO_4^{2-}, NO_3^- and the change in the fluorescence emissions are presented in Figure 7.14. It is seen that there is a negligible change in fluorescence emission upon addition of these ions except As(V) and Hg^{2+} but a significant quenching of emission happens after addition of As(III) with these ions. In the presence of Hg^{2+} there is a fluorescence enhancement up to a certain limit of Hg^{2+} (675 µg/L) concentration and after that there is no effect of Hg^{2+} on the fluorescence properties of nanoparticles. In the case of As(V) there is a little bit fluorescence quenching of the functionalized nanoparticles. This indicates that the present method can detect total arsenic (As(III) + As(V)) selectively in the presence of possible interference ions with a tolerance ratio of 25 for Hg^{2+} .
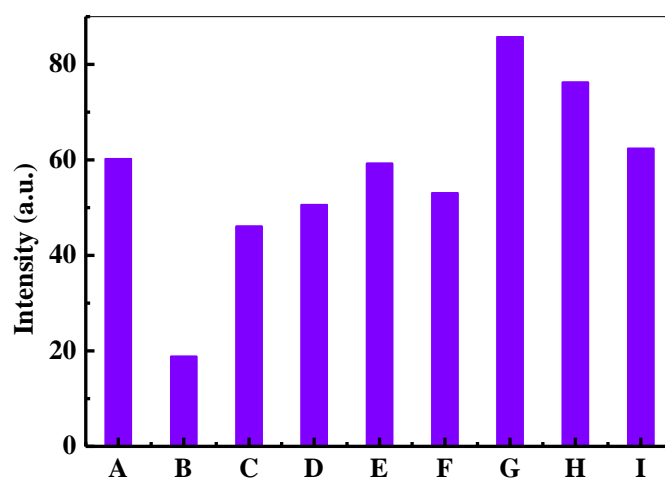
Figure 7.14. The change in fluorescence emission intensity of L-cysteine capped Ag-h-CdS/ZnS nanoparticles in the presence of A: blank, B: As(III) (22.5 µg/L), C: As(V) (900 µg/L), D: As(V) (675 µg/L), E: ions-1 (Na^+, Ca^{2+}, Mg^{2+}, Fe^{3+}, Cl^-, SO_4^{2-}) (900 µg/L each), F: ions-2 (K^+, Fe^{2+}, Sn^{2+}, Cr^{3+}, Al^{3+}, NO_3^-) (900 µg/L each), G: Hg^{2+} (900 µg/L), H: Hg^{2+} (675 µg/L) I: Hg^{2+} (562.5 µg/L).

A comparison study of different analytical methods reported earlier for the detection of As(III) is presented in Table 7.2. It shows that our approach of As(III) detection is superior

compared to literature in terms of LOD and lower cost of instrument used. Apart from this our approach is simple and can be implemented in neutral pH media.

Table 7.2. Comparison of the performance of various analytical methods for detecting As(III)/As(v) ions.

Methods [As(III)/(V)]	Materials	LOD (ng/L)
Our method	Ag-h-CdS/ZnS	226
Electrochemical [As(III)]	Au, [653] Pt NPs modified BDD [654]	250, [653] 500 [654]
Voltammetric[As(III)]	Ibu-Au, [400] Ag–GO, [655] Pt-Fe(III)/MWCNT/GCE [656]	18, [400] 20, [655] 750 [656]
Fluorescent [As(III)]	Au clusters	4020 [657]
Colorimetric [As(III)]	Au	5300 [658]
SERS [As(III)]	GSH/4-MPY-AgNPs	760 [659]
PME [As(III)]	IIPs	37,460 [660]
LDI-MS [As(III)]	Au-MCEM	187.3 [661]
Fluorescent [As(V)]	CdS, [640] DDC NPs [662]	400, [640] 750 [662]
PBS [As(V)]	Au	750 [663]
UVS [As(V)]	NPs of EVMITC	500 [664]

Boron doped diamond (BDD), ibuprofen (Ibu), graphene oxide (GO), multiwalled carbon nanotube/glassy carbon electrode (MWCNT/GCE), surface-enhanced Raman scattering (SERS), glutathione/4-mercaptopyridine (GSH/4-MPY), potentiometric membrane electrode (PME), ion imprinted polymers (IIPs), laser-induced desorption/ionization mass spectrometry (LDI-MS), mixed cellulose ester membrane (MCEM), Dy_2O_3-doped CeO_2 (DDC), Plasmon-based spectroscopy (PBS), UV-Vis spectrophotometry (UVS), ethyl violet with a molybdate-iodine tetrachloride complex (EVMITC).

7.4 Conclusions

Silver doped hollow CdS/ZnS and ZnS/CdS bi-layer nanoparticles are synthesized by AgBr templated sacrificial core removal technique. Silver doping is achieved by the substitution of principle reactant in the CdS and ZnS lattices during the removal of AgBr core. The particle size of Ag-h-CdS/ZnS nanoparticles is 76.02 ± 2.47nm with the shell thickness of CdS layer is 1.5 nm and ZnS layer is 1.8 nm. The QY of Ag-h-CdS/ZnS and Ag-h-ZnS/CdS NPs are

88.14 and 80.34%, respectively. The position of CdS in the inner layer is more effective than in the outer layer of the bi-layer structure for getting higher light emission efficiency (7.8% more). The Ag-h-CdS/ZnS NPs were used sensing of As(III) ions selectively by fluorescence spectrometric technique, and found to be capable of detecting As(III) ions at very low level concentration with a 226 ng/L limit of detection. This approach of As(III) detection is novel because of its simplicity, low LOD, high selectivity and sensitivity, and inexpensive.

Chapter 8

Conclusions and Suggestions for Future Work

8.1   Conclusions

The pure and Ag doped TiO_2, CdS, and ZnS nanoparticles were synthesized in aqueous surfactant media. Ag doping is achieved through substitution of principle reactant component of the host material. The Ag doped hollow TiO_2 (Ag-h-TiO_2) nanoparticles were synthesized by a sacrificial core method using AgBr as sacrificial core. During the removal of core, Ag was doped in the interstitial sites of the host TiO_2. The obtained Ag-h-TiO_2 nanoparticles are purely in anatase phase and good crystalline in nature. Ag-CdS/Ag-ZnS and Ag-ZnS/Ag-CdS nanoparticles were synthesized in aqueous media by chemical precipitation method. For this nanoparticle the Ag doping is achieved by the substitution of principle reactants component of the host material. Silver doped hollow CdS/ZnS bi-layer (Ag-h-CdS/ZnS) and ZnS/CdS bi-layer (Ag-h-ZnS/CdS) nanoparticles were synthesized by AgBr templated sacrificial core removal technique. Silver doping is achieved by the substitution of principle reactant in the CdS and ZnS lattices during the removal of AgBr core.

The particle size was in the range of 33.39 ± 1.67 and 27.6 ± 2.08 nm for pure and Ag doped TiO_2, 4.06 ± 0.63 and 3.44 ± 0.76 nm for pure CdS and 1.5-Ag-CdS, and 5.85 ± 0.5 nm and 4.91 ± 0.45 nm for pure and Ag doped ZnS nanoparticles respectively. The mean particle size of Ag-h-TiO_2 nanoparticles was 17.76 ± 2.85 nm with wall thickness of ~ 2.5 nm. The hollow structured nanoparticles have the specific surface area of 198.3 m^2/g, where as solid TiO_2 nanoparticles have the specific surface area of 95.1 m^2/g. Apart from the surface area, the quantum yield of Ag-h-TiO_2 nanoparticles also increased to 18.7% compared to that of pure solid TiO_2 nanoparticles. The size of the Ag-CdS/Ag-ZnS nanoparticles is in the range 5.92 ± 0.76 nm with 0.75 nm shell thickness. The obtained QY are 77.57 and 69.6% for Ag-CdS/Ag-ZnS and Ag-ZnS/Ag-CdS nanoparticles. The particle size of Ag-h-CdS/ZnS nanoparticles was 76.02 ± 2.47 nm with the shell thickness of CdS layer is 1.5 nm and ZnS layer is 1.8 nm. The QY of Ag-h-CdS/ZnS and Ag-h-ZnS/CdS NPs are 88.14 and 80.34%, respectively. The position of CdS in the inner layer is more effective than in the outer layer of the bi-layer structure for getting higher light emission efficiency (7.8% more).

The TiO_2, CdS, and ZnS nano catalysts showed 80.78, 82.46, and 81.66% MTZ degradation and 49.73, 41.4, and 34.9% MBD degradation efficiency under visible light irradiation. The degradation efficiency of these particles enhanced drastically while doped with silver, however, the optimum doping percentage is crucial to get highest efficiency. The maximum degradation efficiencies of 1.00, 1.5, and 1.25% Ag doped TiO_2, CdS, and ZnS nanoparticles were 94.39, 95.11, and 94.9% for MTZ and 95.9, 95.33, and 94.99% for MBD.

In spite of the fact that, the maximum degradation efficiencies are similar for all three catalysts at the optimum doping content, but for TiO_2 low dopant concentration is required. Since TiO_2 is nontoxic and cheap, Ag doped TiO_2 will be useful for photodegradation of antibiotics and dye in waste water compared to other two catalysts studied here. The catalyst recycling study for the MTZ degradation also shows 10-12% reduction in degradation efficiency of the catalyst after sixth cycle of photodegradation, which indicates the re-usability of the catalyst.

The Ag-h-TiO_2 nanoparticles as photocatalyst were tested for the photocatalytic degradation of three important different classes of organic compounds such as nitrobenzene (NB), metronidazole (MTZ) antibiotic, and methylene blue dye (MBD) in aqueous solution under irradiation of visible light. The maximum NB degradation was obtained 95.5% under visible light irradiation for 3.5 hr. The metronidazole degradation efficiency was found to be 96.55 and 94.77% under the irradiation of visible light for the initial MTZ concentration of 15 and 30 mg/L with catalyst dose of 0.5 g/L. The Ag-h-TiO_2 NPs show only 10.47% decrease in degradation efficiency even after sixth cycle of reuse. The synthesized Ag-h-TiO_2 nanoparticles may also be useful for dye sensitized solar cells and other electrochemical applications.

Overall our approach in the degradation of metronidazole antibiotics, nitrobenzene, and methylene blue dye using different doped nanoparticles is expected to be an important technique for the remediation of antibiotic and dye contaminated waste water treatment. Additionally, as the degradation is possible in visible light, the process can also be considered as environmentally friendly or green.

The photocatalytic degradation property of Ag doped TiO_2 NPs has been successfully exploited for controlling the growth of *F.solani* and *V.inaquaelis* phytopathogens under the exposure of visible light. Fungal growth inhibition potency of three tested NPs under dark are showing the following order: Ag-h-TiO_2 > Ag-s-TiO_2 > TiO_2. At very low concentration (0.015 mg/plate), the Ag-h-TiO_2 NPs not only inhibit the growth of *F.solani* but also the production of orange color phytotoxic naphthoquinone during the growth. The MICs of the Ag-h-TiO_2 NPs for *F.solani* and *V.inaquaelis* are found to be 0.43 and 0.75 mg/plate respectively. At higher concentration, the NPs inhibit the sporulation process of *V.inaquaelis*. The antifungal activity of the used NPs is enhanced under the exposure of visible light and highly dependent on the intensity of the exposed light. A comparison of the fungal growth under complete darkness and 4 h/day visible light exposure (13,500 lux) shows the growth inhibition capacity of Ag-h-TiO_2 NPs is enhanced upto 15 and 50 % in case of *F.solani* and

V.inaquaelis repectively with respect to the control experiments. The photo generated $^\bullet$OH radicals damage the compact chitin and β-glucan structure of the fungal cell wall, because of this intracellular proteins release out and leading to cell death. In case of Ag doped TiO_2 the formation of stable Ag-S bond and di-sulfide bond (R-S-S-R) in cellular protein also plays key role in cell damage. It is expected to improve the antifungal activity of the NPs to a much higher extend and complete inhibition of the fungal pathogens can be achieved at much lower concentrations than the laboratory-based results under the exposure of sunlight for agricultural field applications. It is evident from the above research work that, Ag-h-TiO_2 NPs can effectively control both the phytopathogens at very low concentration, so this NPs can be utilized as a green fungicide for controlling a wide range phytopathogens. Additionally, the Ag-h-TiO_2 NPs can also be used effectively to prevent rotting of crops (potato, tomato etc.) because of fungal attacks during the storage.

A fluorescence probe has successfully developed based on L-cysteine functionalized Ag-CdS/Ag-ZnS nanoparticles. There is fluorescence enhancement of the functionalized nanoparticles after fluoride ion addition. A linear calibration curve is obtained with detection capability as low as 99.7 μg/L in aqueous and neutral media. This probe can selectively detect fluoride ions in the presence of different anions. The proposed method is simple, sensitive, and high selective towards fluoride ion detection, and can be used for F^- detection in the drinking water as well biological and environmental science.

The Ag-h-CdS/ZnS NPs were used sensing of As(III) ions selectively by fluorescence spectrometric technique, and found to be capable of detecting As(III) ions at very low level concentration with a 226 ng/L limit of detection. This approach of As(III) detection is novel because of its simplicity, low LOD, high selectivity and sensitivity.

8.2   Suggestions for Future Work

Some suggestions are listed here as the future scope of work which can be continued.

1. Further studied of TiO_2, CdS, and ZnS nanoparticles in the presence of other transition metals or lanthanides as the dopant can be carried out.

2. Doped core/shell structure can be studied between TiO_2 and CdS, ZnO and CdS nanoparticles as the heterostructure.

3. In catalysis applications the synthesized nanoparticles can be utilized for the degradation of other organic compounds. Apart from degradation studies Ag-h-TiO_2 nanoparticles can also be studied for dye sensitized solar cell (DSSC) applications.

4. As the Ag-CdS/Ag-ZnS core/shell and Ag-h-CdS/ZnS bi-layer nanoparticles are having good fluorescence properties, these can be utilized for bioimaging applications.

References

1. Nag, A.; Sapra, S.; Nagamani, C.; Sharma, A.; Pradhan, N.; Bhat, S. V.; Sarma, D. D. A Study of Mn^{2+} Doping in CdS Nanocrystals. *Chem. Mater.* **2007**, *19*, 3252-3259.

2. Bryan, J. D.; Gamelin, D. R. Doped Semiconductor Nanocrystals: Synthesis, Characterization, Physical Properties, and Applications. *Prog. Inorg. Chem.* **2005**, *54*, 47-126.

3. Laguna, O. H.; Pérez, A.; Centeno, M. A.; Odriozola, J. A. Synergy Between Gold and Oxygen Vacancies in Gold Supported on Zr-doped Ceria Catalysts for the CO Oxidation. *Appl. Catal., B: Environmental* **2015**, *176-177*, 385-395.

4. Mahmed, N.; Larismaa, J.; Heczko, O.; Cura, M. E.; Hannula, S. P. Influence of Sintering Temperature on the Properties of Pulsed Electric Current Sintered Hybrid Coreshell Powders. *J. Eur. Ceram. Soc.* **2013**, *33*, 2233-2239.

5. Zhang, J.; Ma, L.; Gan, M.; Yang, F.; Fu, S.; Li, X. Well-Dispersed Platinum Nanoparticles Supported on Hierarchical Nitrogen-Doped Porous Hollow Carbon Spheres with Enhanced Activity and Stability for Methanol Electrooxidation. *J. Power Sources* **2015**, *288*, 42-52.

6. Sealy, C. Nanocrystal Doping Follows the Dots. doi:10.1016/j.nantod.2011.04.005.

7. Wallentin, J.; Mergenthaler, K.; Ek, M.; Wallenberg, R.; Samuelson, L.; Deppert, K.; Pistol, M.-E.; Borgström, M. T. Probing the Wurtzite Conduction Band Structure Using State Filling in Highly Doped InP Nanowires. *Nano Lett.* **2011**, *11*, 2286–2290.

8. Erwin, S. C.; Zu, L.; Haftel, M. I.; Efros, A. L.; Kennedy, T. A.; Norris, D. J. Doping Semiconductor Nanocrystals. *Nature* **2005**, *436*, 91-94.

9. Buonsanti, R.; Milliron, D. J. Chemistry of Doped Colloidal Nanocrystals. *Chem. Mater.* **2013**, *25*, 1305−1317.

10. He, R.; Hocking, R. K. Local Structure and Photocatalytic Property of Sol–gel Synthesized ZnO Doped with Transition Metal Oxides. *J. Mater. Sci.* **2012**, 3150-3158.

11. Yang, Y.; Chen, O.; Angerhofer, A.; Cao, Y. C. Radial-Position-Controlled Doping in CdS/ZnS Core/Shell Nanocrystals. *J. Am. Chem. Soc.* **2006**, *128*, 12428-12429.

12. Mall, M.; Kumar, L. Optical Studies of Cd^{2+} and Mn^{2+} Co-Doped ZnS Nanocrystals. *J. Lumin.* **2010**, *130*, 660–665.

13. Hammad, T. M.; Salem, J. K. Synthesis and Characterization of Mg-Doped ZnO Hollow Spheres. *J. Nanopart. Res.* **2011**, *13*, 2205–2212.

14. Mammen, N.; Narasimhan, S.; Gironcoli, S. D. Tuning the Morphology of Gold Clusters by Substrate Doping. *J. Am. Chem. Soc*. **2011**, *133*, 2801–2803.

15. Liu, Y.; Liu, C.-y.; Rong, Q.-h.; Zhang, Z. Characteristics of the Silver-Doped TiO_2 Nanoparticles. *Appl. Surf. Sci.* **2003**, *220*, 7–11.

16. Varadhaseshan, R.; Sundar, S. M. Existence of Ferromagnetism and Structural Characterization of Nickel Doped ZnO Nanocrystals. *Appl. Surf. Sci.* **2012**, *258*, 7161-7165.

17. Xu, J.; Chen, M.; Fu, D. Study on Highly Visible Light Active Bi-doped TiO_2 Composite Hollow Sphere. *Appl. Surf. Sci.* **2011**, *257*, 7381–7386.

18. Jia, G.; You, H.; Song, Y.; Huang, Y.; Yang, M.; Zhang, H. Facile Synthesis and Luminescence of Uniform Y_2O_3 Hollow Spheres by a Sacrificial Template Route. *Inorg. Chem*. **2010**, *49*, 7721–7725.

19. Cao, Y. W.; Banin, U. Growth and Properties of Semiconductor Core/Shell Nanocrystals with InAs Cores. *J. Am. Chem. Soc*. **2000**, *122*, 9692-9702.

20. Amato, M. Ossicini, S.; Rurali, R. Band-Offset Driven Efficiency of the Doping of SiGe Core-Shell Nanowires. *Nano Lett*. **2011**, *11*, 594–598.

21. Yogamalar, N. R.; Bose, A. C. Burstein–Moss Shift and Room Temperature Near-Band-Edge Luminescence in Lithium-Doped Zinc Oxide. *Appl. Phys. A* **2011**, *103*, 33–42.

22. Xiao, Q.; Tang, X.; Liu, Y.; Zhong, Y.; Zhu, W. Citrate Route to Prepare K-Doped Li_2ZrO_3 Sorbents with Excellent CO_2 Capture Properties. *Chem. Eng. J.* **2011**, *174*, 231–235.

23. Sato, T.; Katakura, T.; Yin, S.; Fujimoto, T.; Yabe, S. Synthesis and UV-Shielding Properties of Calcia-Doped Ceria Nanoparticles Coated with Amorphous Silica. *Solid State Ionics* **2004**, *172*, 377–382.

24. Li, J.; Cai, D.; Song, J.; Jin, D.; Yu, S.; Cheng, J. Synthesis and Photocatalytic Property of Ba-Doped $BiFeO_3$ Nanoparticles. *Mater. Sci.* **2010**, 3-6.

25. Wang, B.; Wang, S.; Gong, L.; Zhou, Z. Structural, Magnetic and Photocatalytic Properties of Sr^{2+}-Doped $BiFeO_3$ Nanoparticles Based On An Ultrasonic Irradiation Assisted Self-Combustion Method. *Ceram. Int*. **2012**, *38*, 6643-6649.

26. Pathak, C. S.; Mishra, D. D.; Agarwala, V.; Mandal, M. K. Blue Light Emission From Barium Doped Zinc Sulfide Nanoparticles. *Ceram. Int*. **2012**, *38*, 5497-5500.

27. Hao, E.; Zhang, H.; Yang, B.; Ren, H.; Shen, J. Preparation of Luminescent Polyelectrolyte/Cu-Doped ZnSe Nanoparticle Multilayer Composite Films. *J. colloid interface sci.* **2001**, *238*, 285-290.

28. Andronenko, S. I.; Leo, A.; Stiharu, I.; Misra, S. K. EPR/FMR Investigation of Mn-Doped SiCN Ceramics. *Appl. Magn. Reson.* **2010**, *39*, 347-356.

29. Nazari, A. G.; Tahari, A.; Moztarzadeh, F.; Mozafari, M.; Bahrololoom, M. E. Ion exchange behaviour of silver-doped apatite micro- and nanoparticles as antibacterial biomaterial. *Micro Nano Lett.* **2011**, *6*, 713–717.

30. Zhi, G.; Song, J.; Mei, B.; Zhou, W. Synthesis and Characterization of Er^{3+} Doped CaF_2 Nanoparticles. *J. Alloys Compd.* **2011**, *509*, 9133-9137.

31. Secu, M. Nanoparticles Size Effects in Thermoluminescence of Oxyfluoride Glass-Ceramics Containing Sm^{3+}-doped CaF_2 nanocrystals. *J. Nanopart. Res.* **2011**, *13*, 2727–2732.

32. Jose, G.; Jose, G.; Thomas, V.; Joseph, C.; Ittyachen, M. A.; Unnikrishnan, N. V. Optical Characterization of Eu^{3+} Ions in CdSe Nanocrystal Containing Silica Glass. *J. fluores.* **2004**, *14*, 733-738.

33. Bednarkiewicz, A.; Wawrzynczyk, D.; Nyk, M.; Strek, W. Synthesis and Spectral Properties of Colloidal Nd^{3+} Doped $NaYF_4$ Nanocrystals. *Opt. Mater.* **2011**, *33*, 1481–1486.

34. Asapu, R.; Palla, V. M.; Wang, B.; Guo, Z.; Sadu, R.; Chen, D. H. Phosphorus-Doped Titania Nanotubes with Enhanced Photocatalytic Activity. *J. Photochem. Photobiol., A: Chemistry* **2011**, *225*, 81-87.

35. Li, D.; Haneda, H.; Hishita, S.; Ohashi, N.; Labhsetwar, N. Fluorine-Doped TiO_2 Powders Prepared by Spray Pyrolysis and Their Improved Photocatalytic Activity for Decomposition of Gas-Phase Acetaldehyde. *J. Fluorine Chem.* **2005**, *126*, 69–77.

36. Avadhut, Y. S.; Weber, J.; Hammarberg, E.; Feldmann, C.; Schellenberg, I.; Pöttgen, R. Gunne, J. S. A. D. Study on the Defect Structure of SnO_2:F Nanoparticles by High-Resolution Solid-State NMR. *Chem. Mater.* **2011**, *23*, 1526–1538.

37. Zeng, D. W.; Xie, C. S.; Zhu, B. L.; Song, W. L.; Wang, A. H. Synthesis and Characteristics of Sb-Doped ZnO Nanoparticles. *Mater. Sci. Eng., B.* **2003**, *104*, 68-72.

38. Bui, D.-N. Kang, S.-Z.; Li, X.; Mu, J. Effect of Si Doping on the Photocatalytic Activity and Photoelectrochemical Property of TiO_2 Nanoparticles. *Catal. Commun.* **2011**, *13*, 14–17.

39. Combe, E.; Chubilleau, C.; Berardan, D.; Guilmeau, E.; Maignan, A.; Raveau, B. Citrate Gel Process and Thermoelectric Properties of Ge-Doped In_2O_3 Bulk Ceramics. *Powder Technol.* **2011**, *208*, 503–508.

40.   Ashton, T. S.; Moore, A. L. Three-Dimensional Foam-Like Hexagonal Boron Nitride Nanomaterials Via Atmospheric Pressure Chemical Vapor Deposition. *J. Mater. Sci*. **2015**, *50*, 6220–6226.

41.   Al-Agel, F. A.; Akhtar, M. S.; Alshammari, H.; Alshammari, A.; Khan, S. A. Solution Processed ZnO Rectangular Prism as an Effective Photoanode Material for Dye Sensitized Solar Cells. *Mater. Lett*. **2015**, *147*, 119–122.

42.   Umar, A.; Akhtar, M. S.; Al-Hajry, A.; Al-Assiri, M. S.; Dar, G. N.; Islam, M. S. Enhanced Photocatalytic Degradation of Harmful Dye and Phenyl Hydrazine Chemical Sensing Using ZnO Nanourchins. *Chem. Eng. J*. **2015**, *262*, 588–596.

43.   Deshmukh, R. G.; Badadhe, S. S.; Vaishampayan, M. V.; Mulla, I. S. Facile Synthesis and Gas Sensing Properties of Nanotriangular Tin Oxide. *Mater. Lett*. **2008**, *62*, 4328–4331.

44.   Li, J.; Liu, Z.; Zhu, Z. Enhanced photocatalytic activity in $ZnFe_2O_4$–ZnO–Ag_3PO_4 hollow nanospheres through the cascadal electron transfer with magnetical separation. *J. Alloys Compd.* **2015**, *636*, 229–233.

45.   Cui, L.; Wang, Y.; Niu, M.; Chen, G.; Cheng, Y. Synthesis and Visible Light Photocatalysis of Fe-Doped TiO_2 Mesoporous Layers Deposited on Hollow Glass Microbeads. *J. Solid State Chem.* **2009**, *182*, 2785–2790.

46.   Xu, J.; Chen, M.; Fu, D. Study on Highly Visible Light Active Bi-Doped TiO_2 Composite Hollow Sphere. *Appl. Surf. Sci*. **2011**, *257*, 7381–7386.

47.   Zhang, Y.; Li, Y. Synthesis and Characterization of Monodisperse Doped ZnS Nanospheres with Enhanced Thermal Stability. *J. Phys. Chem. B* **2004**, *108*, 17805-17811.

48.   Nair, M. G.; Nirmala, M.; Rekha, K.; Anukaliani, A. Structural, Optical, Photo Catalytic and Antibacterial Activity of ZnO and Co Doped ZnO Nanoparticles. *Mater. Lett*. **2011**, *65*, 1797–1800.

49.   Li, H.; Zhang, Z.; Huang, J.; Liu, R.; Wang, Q. Optical and Structural Analysis of Rare Earth and Li Co-Doped ZnO Nanoparticles. *J. Alloys Compd*. **2013**, *550*, 526–530.

50.   Wang, X.; Tang, Y.; Leiw, M.-Y.; Lim, T.-T. Solvothermal Synthesis of Fe–C Codoped TiO_2 Nanoparticles for Visible-Light Photocatalytic Removal of Emerging Organic Contaminants in Water. *Appl. Catal., A: General* **2011**, *409–410*, 257–266.

51.   Lin, S. E.; Borgohain, K.; Wei, W. C. J. Praseodymium-Doped Photo-Luminescent Strontium Indate Nanoparticles by Ultrasonic Spray Pyrolysis. *J. Am. Ceram. Soc*. **2006**, *89*, 3266–3269.

52.   Sathyaseelan, B.; Senthilnathan, K.; Alagesan, T.; Jayavel, R.; Sivakumar, K. A Study on Structural and Optical Properties of Mn- and Co-doped SnO_2 Nanocrystallites. *Mater. Chem. Phys.* **2010**, *124*, 1046–1050.

53.   Liu, J.; Zhao, Z.; Chen, Y.; Xu, C.; Duan, A.; Jiang, G. Different Valent Ions-Doped Cerium Oxides and Their Catalytic Performances for Soot Oxidation. *Catal. Today* **2011**, *175*, 117–123.

54.   Alemi, A.; Hanifehpour, Y.; Joo, S. W.; Min, B.-K. Synthesis of Novel $Ln_xSb_{2-x}Se_3$(Ln: Lu^{3+}, Ho^{3+}, Nd^{3+}) Nanomaterials Via Co-reduction Method and Investigation of their Physical Properties. *Colloids Surf. A: Physicochem. Eng. Aspects* **2011**, *390*, 142–148.

55.   Niu, N.; Yang, P.; Liu, Y.; Li, C.; Wang, D.; Gai, S.; He, F. Controllable Synthesis and Up-conversion Properties of Tetragonal $BaYF_5$:Yb/Ln (Ln=Er, Tm, and Ho) Nanocrystals. *J. Colloid Interface Sci.* **2011**, *362*, 389–396.

56.   Janssens, S.; Williams, G. V. M.; Clarke, D. Synthesis and Characterization of Rare Earth and Transition Metal Doped $BaMgF_4$ Nanoparticles. *J. Lumin.* **2013**, *134*, 277–283.

57.   Liu, Q.; Sun, Y.; Yang, T.; Feng, W.; Li, C.; Li, F. Sub-10 nm Hexagonal Lanthanide-Doped $NaLuF_4$ Upconversion Nanocrystals for Sensitive Bioimaging in Vivo. *J. Am. Chem. Soc.* **2011**, *133*, 17122–17125.

58.   Zhou, J.-C.; Yang, Z.-L.; Dong, W.; Tang, R.-J.; Sun, L.-D.; Yan, C.-H.; Bioimaging and Toxicity Assessments of Near-Infrared Upconversion Luminescent $NaYF_4$:Yb,Tm Nanocrystals. *Biomater.* **2011**, *32*, 9059-9067.

59.   Xu, A. The Preparation, Characterization, and their Photocatalytic Activities of Rare-Earth-Doped TiO_2 Nanoparticles. *J. Catal.* **2002**, *207*, 151-157.

60.   Sutradhar, N.; Sinhamahapatra, A.; Pahari, S.; Jayachandran, M.; Subramanian, B.; Bajaj, H. C.; Panda, A. B. Facile Low-Temperature Synthesis of Ceria and Samarium-Doped Ceria Nanoparticles and Catalytic Allylic Oxidation of Cyclohexene. *J. Phys. Chem. C* **2011**, *115*, 7628–7637.

61.   El-bially, A. B.; Seoudi, R.; Eisa, W.; Shabha, A. A.; Soliman, S. I.; Ei-Hamid, R. K. A.; Ramanad, R. A. Preparation, Characterization and Physical Properties of CdS Nanoparticles with Different Sizes. Journal of Applied Sciences Research. *J. Appl. Sci. Res.* **2012**, *8*, 676-685.

62.   Dumbrava, A.; Badea, C.; Prodan, G.; Ciupina, V. Synthesis and Characterization of Cadmium Sulfide obtained at Room Temperature. *Chalcogenide Lett.* **2010**, *7*, 111-118.

63.   Rao, B. S.; Kumar, B. R.; Reddy, V. R.; Rao, T. S. Preparation and Characterization of CdS Nanoparticles by Chemical Co-precipitation Technique. *Chalcogenide Lett.* **2011**, *8*, 177-185.

64.   Hu, K.; Brust, M.; Bard, A. J. Characterization and Surface Charge Measurement of Self-Assembled CdS Nanoparticle Films. *Chem. Mater.* **1998**, *10*, 1160-1165.

65.   Brus, L. Electronic Wave Functions in Semiconductor Clusters: Experiment and Theory. *J. Phys. Chem.* **1986**, *90*, 2555-2560.

66.   Henglein, A. Small-Particle Research: Physicochemical Properties of Extremely Small Colloidal Metal and Semiconductor Particles. *Chem. Rev.* **1989**, *89*, 1861-1873.

67.   Querner, C.; Reiss, P.; Sadki, S.; Zagorska, M.; Pron, A. Size and Ligand Effects on the Electrochemical and Spectroelectrochemical Responses of CdS Nanocrystals. *Phys. Chem. Chem. Phys.* **2005**, *7*, 3204-3209.

68.   Pan, D.; Wang, Q.; Pang, J.; Jiang, S.; Ji, X.; An, L. Semiconductor "Nano-Onions" with Multifold Alternating CdS/CdSe or CdSe/CdS Structure. *Chem. Mater.* **2006**, *18*, 4253-4258.

69.   Zhuang, J.; Zhang, X.; Wang, G.; Li, D.; Yang, W.; Li, T. Synthesis of Water-Soluble ZnS: Mn^{2+} Nanocrystals by using Mercaptopropionic Acid as Stabilizer. *J. Mater. Chem.* **2003**, *13*, 1853-1857.

70.   Liu, S.-M.; Liu, F.-Q.; Guo, H.-Q.; Zhang, Z.-H.; Wang, Z.-G. Surface States Induced Photoluminescence from Mn^{2+} Doped CdS Nanoparticles. *Solid State Commun.* **2000**, 115, 615-618.

71.   Esakkiraj, E.; Kadhar, S. P. S. A.; Henry, J.; Mohanraj, K.; Kannan, S.; Barathan, S.; G. Sivakumar, Optostructral and Vibrational Characteristics of Cu:CdS Nanoparticles by Precipitation Method. *Optik* **2013**, *124*, 5229-5231.

72.   Tamrakar, R. K.; Bisen, D. P. Optical and Kinetic Studies of CdS:Cu Nanoparticles. *Res. Chem. Intermed.* **2013**, *39*, 3043-3048.

73.   Mercy, A.; Murugesan K. S.; Boaz, B. M.; Anandhi, A. J.; Kanagadurai, R. Synthesis and Structural and Optical Characterization of Mn^{2+} Doped Cadmium Sulphide Nanoparticles Stabilized in DETA Matrix. *J. Alloys Compd.* **2013**, *554*, 189-194.

74.   Salimian, S.; Shayesteh, S. F. Structural, Optical and Magnetic Properties of Mn-Doped CdS Diluted Magnetic Semiconductor Nanoparticles. *J. Supercond. Nov. Magn.* **2012**, *25*, 2009-2014.

75. Rao, B. S.; Kumar, B. R.; Reddy, V. R.; Rao, T. S.; Chalapathi, G. V. Influence on Optical Properties of Nickel Doped Cadmium Sulfide. *Chalcogenide Lett.* **2011**, *8*, 39-44.

76. Thambidurai, M.; Muthukumarasamy, N.; Velauthapillai, D.; Murugan, N.; Chaudhuri, J.; Parameswaran, S.; Marathe, A.; Agilan, S.; Balasundaraprabhu, R. Effect of Cr-Doping on the Structural and Optical Properties of CdS Nanoparticles Prepared by Chemical Precipitation Method. *J. Mater. Sci.: Mater. Electron* **2012**, *23*, 618-624.

77. Wang, C.-C.; Wu, S.-Y.; Yuan, L.-Y. Study on the Zn(II)-Doped CdS Luminescent Nanoparticles Formation on the Chelating Polymer Microsphere. *Macromol. Symp.* **2008**, *270*, 135-142.

78. Giribabu, G.; Murali, G.; Reddy, D. A.; Liu, C.; Vijayalakshmi, R. P. Structural, Optical and Magnetic Properties of Co Doped CdS Nanoparticles. *J. Alloys Compd.* **2013**, *581*, 363-368.

79. Zhu, G.; Drozdowicz-Tomsia, K.; Yu, H.; Goldys, E. M. Synthesis and Characterization of Disodium Ethylenediaminetetraacetic Acid Capped and Europium Doped CdS Nanoparticles. *Solid State Commun.* **2006**, *137*, 503-506.

80. Saravanan, L.; Pandurangan, A.; Jayavel, R. Synthesis and Luminescence Enhancement of Cerium Doped CdS Nanoparticles. *Mater. Lett.* **2012**, *66*, 343-345.

81. Otaqsara, S. M. T.; Yousef, M. H.; Khosravim, A. A. Optical Characterization of Fe^{3+} Doped CdS Nanoparticles Synthesized by Wet-Chemical Route. *Turk J Phys.* **2011**, *35*, 341-347.

82. Kumar, K. S.; Divya, A.; Reddy, P. S. Synthesis and Characterization of Cr Doped CdS Nanoparticles Stabilized with Polyvinylpyrrolidone. *Appl. Surf. Sci.* **2011**, *257*, 9515-9518.

83. Thambidurai, M.; Muthukumarasamy, N.; Velauthapillai, D.; Lee, C. Quantum Confinement Effects in Gd-Doped CdS Nanoparticles Prepared by Chemical Precipitation Technique. *J. Mater. Sci. Mater. Electron.* **2013**, *24*, 4535-4541.

84. Ma, X.; Song, J.; Yu, Z. The Light Emission Properties of ZnS:Mn Nanoparticles. *Thin Solid Films* **2011**, *519*, 5043-5045.

85. Uda, H.; Yonezawa, H.; Ohtsubo, Y.; Kosaka, M.; Sonomura, H. Thin CdS Films Prepared by Metalorganic Chemical Vapor Deposition. *Sol. Energy Mater. Sol. Cells* **2003***, 75*, 219-226.

86. Rai, S.; Bokatial, L.; Dihingia, P. J. Effect of CdS Nanoparticles on Fluorescence from Sm^{3+} Doped SiO_2 Glass. *J. Lumin.* **2011**, *131*, 978-983.

87. Rai, S.; Bokatial, L. Effect of CdS Nanoparticles on Photoluminescence Spectra of Tb^{3+} in Sol–Gel-Derived Silica Glasses. *Bull. Mater. Sci.* **2011**, *34*, 227-231.

88. Kumar, A.; Chaudhary, V. Optical and Photophysical Properties of Ag/CdS Nanocomposites—An Analysis of Relaxation Kinetics of the Charge Carriers. *J. Photochem. Photobiol A: Chemistry* **2007**, *189*, 272-279.

89. Kamat, P. V. Photoinduced Transformations in Semiconductor–Metal Nanocomposite Assemblies. *Pure Appl. Chem.* **2002**, *74*, 1693-1706.

90. Gong, H.-M.; Wang, X.-H.; Du, Y.-M.; Wang, Q.-Q. Optical Nonlinear Absorption and Refraction of CdS and CdS-Ag Core-Shell Quantum Dots. *J. Chem. Phys.* **2006**, *125*, 024707.

91. Honma, I.; Sano, T.; Komiyama, H. Surface-Enhanced Raman Scattering (SERS) for Semiconductor Microcrystallites Observed in Ag-CdS Hybrid Particles. *J. Phys. Chem.* **1993**, *97*, 6692-6695.

92. Shen, Q.; Liu, Y.; Xu, J.; Meng, C.; Liu, X. Microwave Induced Center-Doping of Silver Ions in Aqueous CdS Nanocrystals with Tunable, Impurity and Visible Emission. *Chem. Commun.* **2010**, *46*, 5701-5703.

93. Thakur, P.; Joshi, S. S.; Kapoor, S.; Mukherjee, T. Fluorescence Behavior of Cysteine-Mediated Ag@CdS Nanocolloids. *Langmuir* **2009***, 25*, 6377-6384**.**

94. Kumar, M. R.; Murugadoss, G. Synthesis and Study of Optical and Thermal Properties of Mn Doped CdS Nanoparticles using Polyvinylpyrrolidone. *J. Lumin.* **2014**, *146*, 325 − 332.

95. Mishra, S. K.; Srivastava, R. K.; Prakash, S. G.; Yadav, R. S.; Panday, A. C. Structural, Optical and Photoconductivity Characteristics of Manganese Doped Cadmium Sulfide Nanoparticles Synthesized by Co-Precipitation Method. *J. Alloys Compd.* **2012**, *513*, 118–124.

96. Giribabu, G.; Murali, G.; Reddy, D. A.; Sambasivam, S.; Vijayalakshmi, R. P. Structural, Optical and Magnetic Properties of Cobalt and Aluminum Codoped CdS Nanoparticles. *Mater. Lett.* **2014**, *126*, 119–122

97. Morales, R. L.; Moreno, O. P.; Tomásc, S. A.; Angel, O. Z. Influence of Internal Stress On the Optical Properties of CdS:Cu Nanoparticles. *Opt. Mater.* **2013**, *35*, 1023–1028.

98. Bokatial, L.; Rai, S. Structural and Upconversion Studies of Er^{3+} Codoped with CdS Nanoparticles in Sol-Gel Glasses. *J. Fluoresc.* DOI 10.1007/s10895-012-1108-3.

99. Nisha, K. D.; Navaneethan, M.; Hayakawa, Y.; Ponnusamy, S.; Muthamizhchelvan, C. Influence of Lanthanide ion on the Morphology and Luminescence Properties of Cadmium Sulphide Nanocrystals. *J. Alloys Compd*. **2011**, *509*, 5816–5821.

100. Li, Y.; Ding, Y.; Zhang, Y.; Qian, Y. Photophysical Properties of ZnS Quantum Dots. *J. Phys. Chem. Solids* **1999**, *60*, 13-15.

101. Zhang, H.; Wang, Z.; Zhang, L.; Li, Y.; Yuan, J. Chemical Synthesis and Characterization of Cu Doped ZnS Nano-Powder. *J. Mater. Sci. Lett.* **2002**, *21*, 1031-1033.

102. Kumar, S.; Verma, N. K.; Singla, M. L. Reflective Characteristics of Ni doped ZnS Nanoparticle-Pigment and their Coatings. *Chalcogenides Lett.* **2011**, *8*, 561-569.

103. Sahai, S.; Husain, M.; Shanker, V.; Singh, N.; Haranath, D. Facile Synthesis and Step by Step Enhancement of Blue Photoluminescence from Ag-Doped ZnS Quantum Dots. *J. colloid interface sci.* **2011**, *357*, 379-383.

104. Pathak, C. S.; Mishra, D. D.; Agarwala, V.; Mandal, M. K. Blue Light Emission from Barium Doped Zinc Sulfide Nanoparticles. *Ceram. Int.* **2012**, *38*, 5497-5500.

105. Xu, Z.; Li, B.; Tanga, W.; Chen, T.; Zhanga, H.; Wang, Q. Glycopolypeptide-Encapsulated Mn-Doped ZnS Quantum Dots for Drug Delivery: Fabrication, Characterization, and in Vitro Assessment. *Colloids surf., B* **2011**, *88*, 51-57.

106. Wei, S.; Lee, B. I.; Lin, Z.; Tong, W.; Wagner, B. K.; Park, W.; Summers, C. J. Synthesis and Photoluminescence Enhancement of Mn^{2+}-doped ZnS Nanocrystals. *J. Lumin.* **2001**, *92*, 73-78.

107. Chung, J. H.; Ah, C. S.; Jang, D. -j. Formation and Distinctive Decay Times of Surface- and Lattice-Bound Mn^{2+} Impurity Luminescence in ZnS Nanoparticles. *J. Phys. Chem. B* **2001**, *105*, 4128-4132.

108. Liu, L.; Yang, L.; Pu, Y.; Xiao, D.; Zhu, J. Optical Properties of Water-Soluble Co^{2+}:ZnS Semiconductor Nanocrystals Synthesized by a Hydrothermal Process. *Mater. Lett.* **2012**, *66*, 121-124.

109. Yang, P.; Lü, M.; Xü, D.; Yuan, D.; Song, C.; Zhou, G. The Effect of Co^{2+} and Co^{3+} on Photoluminescence Characteristics of ZnS Nanocrystallines. *J. Phys. Chem. Solids* **2001**, *62* 1181-1184.

110. Reddy, D. A.; Divya, A.; Murali, G.; Vijayalakshmi, R. P. & Reddy, B. K. Synthesis and Optical Properties of Cr Doped ZnS Nanoparticles Capped by 2-Mercaptoethanol. *Physica B: Condensed Matter* **2011**, *406*, 1944-1949.

111. Eryong, N.; Donglai, L.; Yunsen, Z.; Xue, B.; Liang, Y.; Yong, J.; Zhifeng, J.; Xiaosong, S. Photoluminescence and Magnetic Properties of Fe-Doped ZnS Nano-Particles Synthesized by Chemical Co-Precipitation. *Appl. Surf. Sci.* **2011**, *257*, 8762-8766.

112. Kuppayee, M.; Vanathi Nachiyar, G. K.; Ramasamy, V. Synthesis and Characterization of Cu^{2+} Doped ZnS Nanoparticles using TOPO and SHMP as Capping Agents. *Appl. Surf. Sci.* **2011**, *257*, 6779-6786.

113. Wang, M.; Sun, L.; Fu, X.; Liao, C.; Yan, C. Synthesis and Optical Properties of ZnS : Cu(II) Nanoparticles. *Solid State Commun.* **2000**, *115*, 493-496.

114. Yang, P.; Lü, M.; Xu, D.; Yuan, D.; Song, C.; Zhou, G. Photoluminescence Characteristics of ZnS Nanocrystallites Doped with Ti^{3+} and Ti^{4+}. *Appl. Phys. A: Mater. Sci. Process.* **2002**, *74*, 525-528.

115. Yang, P.; Lü, M.; Xü, D.; Yuan, D.; Chang, J.; Zhou, G.; Pan, M. Strong Green Luminescence of Ni^{2+} -Doped ZnS Nanocrystals. *Appl. Phys. A: Mater. Sci. Process.* **2002**, *74*, 257-259.

116. Kumar, S.; Chen, C. L.; Dong, C. L.; Ho, Y. K.; Lee, J. F.; Chan, T. S.; Thangavel, R.; Chen, T. K.; Mok, B. H.; Rao, S. M.; Wu, M. K. Room Temperature Ferromagnetism in Ni Doped ZnS Nanoparticles. *J. Alloys Compd.* **2013**, *554*, 357-362.

117. Borse, P. H.; Vogel, W.; Kulkarni, S. K. Effect of pH on Photoluminescence Enhancement in Pb-Doped ZnS Nanoparticles. *J. colloid interface sci.* **2006**, *293*, 437-442.

118. Manzoor, K.; Vadera, S.; Kumar, N.; Kutty, T. R. Synthesis and Photoluminescent Properties of ZnS Nanocrystals Doped with Copper and Halogen. *Mater. Chem. Phys.* **2003**, *82*, 718-725.

119. Huang, C. -M.; Cheng, K. -W.; Jhan, Y. -R.; Chung, T.-W. Preparation of Visible-Light-Active Ag and In-Doped ZnS Thin Film Photoelectrodes by Reactive Magnetron Co-Sputtering. *Thin Solid Films* **2007**, *515*, 7935-7944.

120. Hao, E.; Sun, Y.; Yang, B.; Zhang, X.; Liu, J.; Shen, J. Synthesis and Photophysical Properties of ZnS Colloidal Particles Doped with Silver. *J. colloid interface sci.* **1998**, *204*, 369-373.

121. Sharma, R.; Bisen, D. P.; Dhoble, S. J.; Brahme, N.; Chandra, B. P. Mechanoluminescence and Thermoluminescence of Mn doped ZnS Nanocrystals. *J. Lumin.* **2011**, *131*, 2089–2092.

122. Wang, Z.; Zhang, H.; Zhang, L.; Yuan, J.; Yan, S.; Wang, C. Synthesis and Size Control of Monodisperse Manganese-Doped ZnS Nanoparticles by Methacrylate Polymer. *Colloid Polym. Sci*. **2003**, *281*, 178-181.

123. Gan, L. M.; Liu, B.; Chew, C. H.; Xu, S. J.; Chua, S. J.; Loy, G. L.; Xu, G. Q. Enhanced Photoluminescence and Characterization of Mn-Doped ZnS Nanocrystallites Synthesized in Microemulsion. *Langmuir* **1997**, *13*, 6427-6431.

124. Cao, S.; Yeung, K. L.; Yue, P. L. An Investigation of Trichloroethylene Photocatalytic Oxidation on Mesoporous Titania-Silica Aerogel Catalysts. *Appl. Catal., B: Environmental* **2007**, *76*, 64-72.

125. Hoffmann, M. R.; Martin, S. T.; Choi, W.; Bahnemann, D. W. Environmental Applications of Semiconductor Photocatalysis. *Chem. Rev.* **1995**, *95*, 69-96.

126. Zaleska, A. Doped-TiO_2 : A Review. *Rec. Pat. Eng*. **2008**, *2*, 157-164.

127. Zhang, W. F.; Zhang, M. S.; Yin, Z.; Chen, Q. Photoluminescence in Anatase Titanium Dioxide Nanocrystals. *Appl. Phys. B: Lasers Opt.* **2000**, *70*, 261-265.

128. Vorontsov, A. V.; Stoyanova, I. V.; Kozlov, D.V.; Simagina, V. I.; Savinov, E. N. Kinetics of the Photocatalytic Oxidation of Gaseous Acetone over Platinized Titanium Dioxide. *J. Catal.* **2000**, *189*, 360-369.

129. Zhu, J.; Chen, F.; Zhang, J.; Chen, H.; Anpo, M. Fe^{3+}-TiO_2 Photocatalysts Prepared by Combining Sol–gel Method with Hydrothermal Treatment and their Characterization. *J. Photochem. Photobiol., A* **2006**, *180*, 196-204.

130. Jaimy, K. B.; Ghosh, S.; Sankar, S.; Warrier, K. G. K. An Aqueous Sol–gel Synthesis of Chromium (III) Doped Mesoporous Titanium Dioxide for Visible Light Photocatalysis. *Mater. Res. Bull.* **2011**, *46*, 914-921.

131. Mohamed, R. M.; Aazam, E. S. Preparation and Characterization of Platinum Doped Porous Titania Nanoparticles for Photocatalytic Oxidation of Carbon Monoxide. *J. Alloys Comp.* **2011**, *509*, 10132-10138.

132. Iwasaki, M.; Hara, M.; Kawada, H.; Tada, H.; Ito, S. Cobalt Ion-Doped TiO_2 Photocatalyst Response to Visible Light. *J. Colloid Interface Sci.* **2000**, *224*, 202-204.

133. Liqiang, J.; Honggang, F.; Baiqi, W.; Dejun, W.; Baifu, X.; Shudan, L.; Jiazhong, S. Effects of Sn Dopant on the Photoinduced Charge Property and Photocatalytic Activity of TiO_2 Nanoparticles. *Appl. Catal., B* **2006**, *62*, 282-291.

134. Herrmanna, J. -M.; Tahiri, H.; Ait-Ichou, Y.; Lassaletta, G.; González-Elipe, A. R.; Fernbdez, A.; Characterization and Photocatalytic Activity in Aqueous Medium of TiO_2 and Ag-TiO_2 Coatings on Quartz. *Appl. Catal., B* **1997**, *13*, 219-228.

135. Li, Y.; Ma, M.; Chen, W.; Li, L.; Zen, M. Preparation of Ag-doped TiO_2 Nanoparticles by a Miniemulsion Method and their Photoactivity in Visible Light Illuminations. *Mater. Chem. Phys.* **2011**, *129*, 501-505.

136. Binitha, N. N.; Yaakob, Z.; Reshmi, M. R.; Sugunan, S.; Ambili, V. K.; Zetty, A. A. Preparation and Characterization of Nano Silver-Doped Mesoporous Titania Photocatalysts for Dye Degradation. *Catal. Today* **2009**, *147*, S76-S80.

137. Liu, Y., Wang, X., Yang, F. & Yang, X. Excellent Antimicrobial Properties of Mesoporous Anatase TiO_2 and Ag/TiO_2 Composite Films. *Microporous Mesoporous Mater.* **2008**, *114*, 431-439.

138. Pang, H.; Yang, H.; Guo, C. X.; Lu, J.; Li, C. M. Nanoparticle Self-Assembled Hollow TiO_2 Spheres with well Matching Visible Light Scattering for High Performance Dye-Sensitized Solar Cells. *Chem. Commun.* **2012**, *48*, 8832-8834.

139. Zhao, J.; Wu, T.; Wu, K.; Oikawa, K.; Hidaka, H.; Serpone, N. Photoassisted Degradation of Dye Pollutants. 3. Degradation of the Cationic Dye Rhodamine B in Aqueous Anionic Surfactant/TiO_2 Dispersions under Visible Light Irradiation﹕ Evidence for the Need of Substrate Adsorption on TiO_2 Particles. *Environ. Sci. Technol.* **1998**, *32*, 2394-2400.

140. Wu, T.; Liu, G.; Zhao, J.; Hidaka, H.; Serpone, N. Photoassisted Degradation of Dye Pollutants. V. Self-Photosensitized Oxidative Transformation of Rhodamine B under Visible Light Irradiation in Aqueous TiO_2 Dispersions. *J. Phys. Chem. B* **1998**, *102,* 5845-5851.

141. Vinu, R.; Madras, G. Photocatalytic Activity of Ag-Substituted and Impregnated Nano-TiO_2. *Appl. Catal., A* **2009**, *366*, 130-140.

142. Young, C.; Lim, T. M.; Chiang, K.; Scott, J.; Amal, R. Photocatalytic Oxidation of Toluene and Trichloroethylene in the Gas-Phase by Metallised (Pt, Ag) Titanium Dioxide. *Appl. Catal., B* **2008**, *78*, 1-10.

143. Bansal, A.; Madhavi, S.; Tan, T. T. Y.; Lim, T. M. Effect of Silver on the Photocatalytic Degradation of Humic Acid. *Catal. Today* **2008**, *131*, 250-254.

144. Sharma, V. K.; Yngard, R. A.; Lin, Y. Silver nanoparticles: Green Synthesis and their Antimicrobial Activities. *Adv. Colloid Interface Sci.* **2009**, *145*, 83–96.

145. Sondi, I.; Salopek-Sondi, B. Silver Nanoparticles as Antimicrobial Agent: a Case Study on E. coli as a Model for Gram-negative Bacteria. *J. Colloid Interface Sci.* **2004**, *275*, 177-182.

146. Smetana, A. B.; Klabunde, K. J.; Marchin, G. R.; Sorensen, C. M. Biocidal Activity of Nanocrystalline Silver Powders and Particles. *Langmuir* **2008**, *24*, 7457-7464.

147. Li, Q.; Mahendra, S.; Lyon, D. Y.; Brunet, L.; Liga, M. V.; Li, D.; Alvarez, P. J. J. Antimicrobial Nanomaterials for Water Disinfection and Microbial Control: Potential Applications and Implications. *Water Res.* **2008**, *42*, 4591-4602.

148. Zhang, L.; Yu, J. C.; Yip, H. Y.; Li, Q.; Kwong, K. W.; Xu, A. W.; Wong, P. K. Ambient Light Reduction Strategy to Synthesize Silver Nanoparticles and Silver-Coated TiO_2 with Enhanced Photocatalytic and Bactericidal Activities. *Langmuir* **2003**, *19*, 10372-10380.

149. Guin, D.; Manorama, S. V.; Latha, J. N. L.; Singh, S. Photoreduction of Silver on Bare and Colloidal TiO_2 Nanoparticles/Nanotubes : Synthesis, Characterization, and Tested for Antibacterial Outcome. *J. Phys. Chem. C* **2007**, *111*, 13393-13397.

150. Seery, M. K.; George, R.; Floris, P.; Pillai, S. C. Silver Doped Titanium Dioxide Nanomaterials for Enhanced Visible Light Photocatalysis. *J. Photochem. Photobiol., A* **2007**, *189*, 258-263.

151. Wang, C.-y.; Böttcher, C.; Bahnemann, D. W.; Dohrmann, J. K. In Situ Electron Microscopy Investigation of Fe(III)-Doped TiO_2 Nanoparticles in an Aqueous Environment. *J. Nanopart. Res*. **2004**, *6*, 119–122.

152. Wang, W.; Zhang, J.; Chen, F.; He, D.; Anpo, M. Preparation and Photocatalytic Properties of Fe^{3+}-Doped Ag@TiO_2 Core–Shell Nanoparticles. *J. Colloid Interface Sci*. **2008**, *323*, 182–186.

153. Patel, S. K. S.; Kurian, S.; Gajbhiye, N. S. Room-Temperature Ferromagnetism of Fe-Doped TiO_2 Nanoparticles Driven by Oxygen Vacancy. *Mater. Res. Bull.* **2013**, *48*, 655–660.

154. Deng, Q.R.; Xia, X. H.; Guo, M. L.; Gao, Y.; Shao, G. Mn-doped TiO_2 Nanopowders with Remarkable Visible Light Photocatalytic Activity. *Mater. Lett.* **2011**, *65*, 2051–2054.

155. Maensiri, S.; Laokul, P.; Klinkaewnarong, J. A simple Synthesis and Room-Temperature Magnetic Behavior of Co-Doped Anatase TiO_2 Nanoparticles. *J. Magn. Magn. Mater*. **2006**, *302*, 448–453.

156. Pan, D.; Xu, G.; Wan, J.; Shi, Z.; Han, M.; Wang, G. Tuning the Solubility of TiO_2 Nanoparticles in Apolar Solvents by Doping with Co^{2+}. *Langmuir* **2006**, *22*, 5537-5540.

157. Rahulan, K. M.; Stephen, L. D.; Kanakam, C. C. Spectral and Nonlinear Optical Transmission Studies of Zr^{4+}-Doped TiO_2 Nanoparticles. *Appl. Surf. Sci*. **2013**, *266*, 326– 331.

158. Chauhan, R.; Kumar, A.; Chaudhary, R. P. Structural and Optical Characterization of Zn Doped TiO_2 Nanoparticles Prepared by Sol–Gel Method. *J. Sol-Gel Sci. Technol*. **2012**, *61*, 585–591.

159. Liu, Y.; Szeifert, J. M.; Rohlfing, D. F.; Bein, T. Niobium-Doped Titania Nanoparticles: Synthesis and Assembly into Mesoporous Films and Electrical Conductivity. *ACS Nano* **2010**, *4*, 5373-5381.

160. Xinshu, N.; Sujuan, L.; Huihui, C.; Jianguo, Z. Preparation, Characterization of Y^{3+}-Doped TiO_2 Nanoparticles and their Photocatalytic Activities for Methyl Orange Degradation. *J. Rare Earth.* **2011**, *29*, 225-229.

161. Li, C.; Shi, L.; Xie, D.; Du, H. Morphology and Crystal Structure of A1-Doped TiO_2 Nanoparticles Synthesized by Vapor Phase Oxidation of Titanium Tetrachloride. *J. Non-Cryst. Solids* **2006**, *352*, 4128–4135.

162. Mattsson, A.; Lejon, C.; Bakardjieva, S.; Štengl, V.; Osterlund L. Characterisation, Phase Stability and Surface Chemical Properties of Photocatalytic Active Zr and Y Co-Doped Anatase TiO_2 Nanoparticles. *J. Solid State Chem*. **2013**, *199*, 212–223.

163. Zhang, C.; Ikeda, M.; Isobe, M.; Uchikoshi, T.; Li, J.-G.; Watanabe, T.; Ishigaki, T. Phase Composition and Magnetic Properties of Niobium–Iron Codoped TiO_2 Nanoparticles Synthesized in Ar/O_2 Radio-Frequency Thermal Plasma. *J. Solid State Chem*. **2011**, *184*, 2525–2532.

164. Sun, T.; Fan, J.; Liu, E.; Liu, L.; Wang, Y.; Dai, H.; Yang, Y.; Hou, W.; Hu, X.; Jiang, Z. Fe and Ni Co-doped TiO_2 Nanoparticles Prepared by Alcohol-Thermal Method: Application in hydrogen evolution by water Splitting under Visible Light Irradiation. *Powder Technol*. **2012**, *228*, 210–218.

165. Xiaoping Wang, Yuxin Tang, Ming-Yian Leiw, Teik-Thye Lim. Solvothermal Synthesis of Fe–C Codoped TiO_2 Nanoparticles for Visible-Light Photocatalytic Removal of Emerging Organic Contaminants in Water. *Appl. Catal., A* **2011**, *409– 410*, 257– 266.

166. Xiao, Q.; Si, Z.; Yu, Z.; Qiu, G. Sol–Gel Auto-Combustion Synthesis of Samarium-Doped TiO_2 Nanoparticles and their Photocatalytic Activity Under Visible Light Irradiation. *Mater. Sci. Eng., B* **2007**, *137*, 189–194.

167. Li, J.-G.; Wang, X.; Watanabe, K.; Ishigaki, T. Phase Structure and Luminescence Properties of Eu^{3+}-Doped TiO_2 Nanocrystals Synthesized by Ar/O_2 Radio Frequency Thermal Plasma Oxidation of Liquid Precursor Mists. *Phys. Chem. B* **2006**, *110*, 1121-1127.

168. Xiao, J.; Peng, T.; Lia, R.; Peng, Z.; Yan, C. Preparation, Phase Transformation and Photocatalytic Activities of Cerium-Doped Mesoporous Titania Nanoparticles. *J. Solid State Chem.* **2006**, *179*, 1161–1170.

169. Chiou, C.-H.; Juang, R.-S. Photocatalytic Degradation of Phenol in Aqueous Solutions by Pr-Doped TiO_2 Nanoparticles. *J. Hazard. Mater*. **2007**, *149*, 1–7.

170. Huixian, S.; Tianyong, Z.; Hongliang, W. Preparation and Photocatalytic Activity of La^{3+} and Eu^{3+} Co-Doped TiO_2 Nanoparticles: Photo-Assisted Degradation of Methylene Blue. *J. Rare Earth*. **2011**, *29*, 746-752.

171. Zhao, Q.; Liu, Y.; Zhao, N.; Penner, S.; Ma, Z. A Novel Approach for Efficient Ni Nanoparticle Doping of MgB_2 by Liquid-Assisted Sintering. *IEEE Transac. Nanotechnol*. **2011**, *10*, 331-337.

172. Secu, M. Nanoparticles Size Effects in Thermoluminescence of Oxyfluoride Glass-Ceramics Containing Sm^{3+}-Doped CaF_2 Nanocrystals. *J. Nanopart. Res.* **2011**, *13*, 2727–2732.

173. Zhi, G.; Song, J.; Mei, B.; Zhou, W. Synthesis and Characterization of Er^{3+} Doped CaF_2 Nanoparticles. *J. Alloys Compd*. **2011**, *509*, 9133-9137.

174. Wang, J.; Wang, Z.; Li, X.; Wang, S.; Mao, H.; Li, Z. Energy Transfer from Benzoic Acid to Lanthanide Ions in Benzoic Acid-Functionalized Lanthanide-Doped CaF_2 Nanoparticles. *Appl. Surf. Sci.* **2011**, *257*, 7145–7149.

175. Bender, C. M.; Burlitch, J. M. Duane Barber and Clifford Pollock. Synthesis and Fluorescence of Neodymium-Doped Barium Fluoride Nanoparticles. *Chem. Mater*. **2000**, *12*, 1969-1976.

176. El-Himri, A.; Pérez-Coll, D.; Núñez, P.; Martín, I. R.; Lavín, V.; Rodríguez, V. D. Preparation and Optical Spectroscopy of Eu^{3+}-Doped GaN Luminescent Semiconductor from Freeze-Dried Precursors. *J. Solid State Chem.* **2004**, *177*, 4213–4220.

177. Fan, X.; Pi, D.; Wang, F.; Qiu, J.; Wang, M. Hydrothermal Synthesis and Luminescence Behavior of Lanthanide-Doped GdF_3 Nanoparticles. *IEEE Transac. Nanotechnol.* **2006**, *5*, 123-128.

178. Bednarkiewicz, A.; Wawrzynczyk, D.; Nyk, M.; Strek, W. Synthesis and Spectral Properties of Colloidal Nd^{3+} Doped $NaYF_4$ Nanocrystals. *Opt. Mater.* **2011**, *33*, 1481–1486.

179. Yi, G.; Lu, H.; Zhao, S.; Ge, Y.; Yang, W. Synthesis, Characterization, and Biological Application of Size-Controlled Nanocrystalline $NaYF_4$:Yb,Er Infrared-to-Visible Up-Conversion Phosphors. *Nano Lett.* **2004**, *4,* 2191-2196.

180. Vorsthove, M.; Kynast, U. Efficiency Issues in Ce^{3+} doped YAG Nanocrystals. *Mater. Res. Bull.* **2011**, *46,* 1761–1765.

181. Zhu, L.; Liu, Y.; Fan, X.; Yang, D.; Cao, X. Facile Synthesis and Luminescence Properties of Uniform and Monodisperse KY_3F_{10}:Ln^{3+} (Ln=Eu, Ce, Tb) Nanospheres. *J. Lumin.* **2011**, *131*, 1380–1385.

182. Ma, M.; Xu, C.; Yang, L.; Ren, G.; Lin, J.; Yang, Q. Intense Ultraviolet and Blue Upconversion Emissions in Yb^{3+}–Tm^{3+} Codoped Stoichiometric $Y_7O_6F_9$ Powder. *Physica B* **2011**, *406*, 3256–3260.

183. Nazari, A. G.; Tahari, A.; Moztarzadeh, F.; Mozafari, M.; Bahrololoom, M. E. Ion Exchange Behaviour of Silver-Doped Apatite Micro- and Nanoparticles as Antibacterial Biomaterial. *Micro Nano Lett.* **2011**, *6*, 713–717.

184. Andronenko, S. I.; Leo, A.; Stiharu, I.; Misra, S. K. EPR/FMR Investigation of Mn-Doped SiCN Ceramics. *Appl. Magn. Reson.* **2010**, *39*, 347-356.

185. Pandurangappa, C.; Lakshminarasappa, B. N.; Nagabhushana, B. M. Synthesis and Optical studies of Gamma Irradiated Eu Doped Nanocrystalline CaF_2. *J. Alloys Compd.* **2011**, *509*, 7671– 7673.

186. Bensalah, A.; Mortier, M.; Patriarche, G.; Gredin, P.; Vivien, D. Synthesis and optical characterizations of undoped and rare-earth-doped CaF_2 nanoparticles. *J. Solid State Chem.* **2006**, *179*, 2636–2644.

187. Liu, Q.; Sun, Y.; Yang, T.; Feng, W.; Li, C.; Li, F. Sub-10 nm Hexagonal Lanthanide-Doped $NaLuF_4$ Upconversion Nanocrystals for Sensitive Bioimaging in Vivo. *J. Am. Chem. Soc.* **2011**, *133*, 17122–17125.

188. Chaudhuri, R. G.; Paria, S. A Novel Method for the Templated Synthesis of Ag_2S Hollow Nanospheres in Aqueous Surfactant Media. *J. Colloid Interface Sci.* **2012**, *369*, 117–122.

189. Hu, M.; Belik, A. A.; Imura, M.; Mibu, K.; Tsujimoto, Y.; Yamauchi, Y. Synthesis of Superparamagnetic Nanoporous Iron Oxide Particles with Hollow Interiors by Using Prussian Blue Coordination Polymers. *Chem. Mater.* **2012**, *24*, 2698−2707.

190. Wang, F.; Tang, Y.; Zhang, B.; Chen, B.; Wang, Y. Preparation of Novel Magnetic Hollow Mesoporous Silica Microspheres and their Efficient Adsorption. *J. Colloid Interface Sci*. **2012**, *386*, 129–134.

191. Chen, M.; Xie, L.; Li, F.; Zhou, S.; Wu, L. Capillary-Force-Induced Formation of Luminescent Polystyrene/(Rare-Earth-Doped Nanoparticle) Hybrid Hollow Spheres. *ACS Appl. Mater. Interfaces* **2010**, *2*, 2733-2737.

192. Cui, L.; Wang, Y.; Niu, M.; Chen, G.; Cheng, Y. Synthesis and Visible Light Photocatalysis of Fe-doped TiO_2 Mesoporous Layers Deposited on Hollow Glass Microbeads. *J. Solid State Chem.* **2009**, *182*, 2785–2790.

193. Jia, G.; You, H.; Song, Y.; Huang, Y.; Yang, M.; Zhang, H. Facile Synthesis and Luminescence of Uniform Y_2O_3 Hollow Spheres by a Sacrificial Template Route. *Inorg. Chem.* **2010**, *49*, 7721–7725.

194. Jia, G.; Zhang, C.; Wang, L.; Ding, S.; You, H. Preparation and Luminescence Properties of Lutetium Oxide Hollow Spheres by a Template-Directed Route. *J. Alloys Compd*. **2011**, *509*, 6418–6422.

195. Ma, G.; Jia, R.; Zhao, J.; Wang, Z.; Song, C.; Jia, S.; Zhu, Z. Nitrogen-Doped Hollow Carbon Nanoparticles with Excellent Oxygen Reduction Performances and Their Electrocatalytic Kinetics. *J. Phys. Chem. C* **2011**, *115*, 25148–25154.

196. Shu, Z.; Jiao, X.; Chen, D. Template-Free Solvothermal Synthesis of Size-Controlled Yttria-Stabilized-Zirconia Hollow Spheres. *J. Alloys Compp*. **2011**, *509*, 9200– 9206.

197. Hammad, T. M.; Salem, J. K. Synthesis and Characterization of Mg-Doped ZnO Hollow Spheres. *J. Nanopart. Res.* **2011**, *13*, 2205–2212.

198. Li, Y.; Li, G.; Peng, H.; Chen, K. Synthesis and Electrochemical Properties of Self-Doped Poly(Aniline-co-3-Aminobenzeneboronic Acid) Hollow Micro/Nanostructures. *Mater. Lett*. **2011**, *65*, 1218–1221.

199. Tian, G.; Gu, Z.; Liu, X.; Zhou, L.; Yin, W.; Yan, L.; Jin, S.; Ren, W.; Xing, G.; Li, S.; Zhao, Y. Facile Fabrication of Rare-Earth-Doped Gd_2O_3 Hollow Spheres with Upconversion Luminescence, Magnetic Resonance, and Drug Delivery Properties. *J. Phys. Chem. C* **2011**, *115*, 23790–23796.

200. Wang, C.; Ao, Y.; Wang, P.; Hou, J.; Qian, J. Preparation of Cerium and Nitrogen Co-Doped Titania Hollow Spheres with Enhanced Visible Light Photocatalytic Performance. *Powder Tech*. **2011**, *210*, 203–207.

201. Wang, C.; Ao, Y.; Wang, P.; Hou, J.; Qian, J. Preparation, Characterization and Photocatalytic activity of the Neodymium-Doped TiO$_2$ Hollow Spheres. *Appl. Surf. Sci*. **2010**, *257*, 227–231.

202. Wang, P.; Wu, J.; Ao, Y.; Wang, C.; Hou, J.; Qian, J. Preparation and Enhanced Photocatalytic Performance of Sn Ion Modified Titania Hollow Spheres. *Mater Lett*. **2011**, *65*, 3278–3280.

203. Wu, M.; Yang, B.; Lv, Y.; Fu, Z.; Xu, J.; Guo, T.; Zhao, Y. Efficient One-Pot Synthesis of Ag Nanoparticles Loaded on N-Doped Multiphase TiO$_2$ Hollow Nanorod Arrays with Enhanced Photocatalytic Activity. *Appl. Surf. Sci*. **2010**, *256*, 7125–7130.

204. Xu, J.; Chen, M.; Fu, D. Study on Highly Visible Light Active Bi-Doped TiO$_2$ Composite Hollow Sphere. *Appl. Surf. Sci*. **2011**, *257*, 7381–7386.

205. Spanhel, L.; Weller, H.; Henglein, A. Photochemistry of Semiconductor Colloids. 22. Electron Injection from Illuminated CdS into Attached Ti0$_2$ and ZnO Particles. *J. Am. Chem. Soc.* **1987**, *109*, 6632-6635.

206. Youn, H.-C.; Baral, S.; Fendler, J. H. Dihexadecyl Phosphate, Vesicle-Stabilized and in Situ Generated Mixed Cadmium Sulfide and Zinc Sulfide Semiconductor Particles: Preparation and Utilization for Photosensitized Charge Separation and Hydrogen Generation. *J. Phys. Chem.* **1988***, 92*, 6320-6327.

207**.** Zhou, H. S.; Sasahara, H.; Honma, I.; Komiyama, H.; Haus, J. W. Coated Semiconductor Nanoparticles: the CdS/PbS System's Photoluminescence Properties. *Chem. Mater*. **1994**, *6*, 1534-1541.

208. Oldenberg, S. J.; Averitt, R. D.; Westcott, S. L.; Halas, N. Nanoengineering of Optical Resonances. *J. Chem. Phys. Lett.* **1998**, *288*, 243-247.

209. Liu, Y. F.; Yu, J. S. J. Selective Synthesis of CdTe and high Luminescence CdTe/CdS Quantum Dots: the Effect of Ligands. *Colloid Interface Sci.* **2009***, 333*, 690-698.

210. Kortan, A. R.; Hull, R.; Opila, R. L.; Bawendi, M. G.; Steigerwald, M.L.; Carroll,P.J.; Brus, L. E. Nucleation and Growth of Cadmium Selenide on Zinc Sulfide Quantum Crystallite Seeds, and Vice Versa, in Inverse Micelle Media. *J. Am. Chem. Soc.* **1990**, *112*, 1327-1332.

211. Zhang, F.; Che, R.; Li, X.; Yao, C.; Yang, J.; Shen, D.; Hu, P.; Li, W.; Zhao, D. Direct Imaging the Upconversion Nanocrystal Core/Shell Structure at the Subnanometer Level: Shell Thickness Dependence in Upconverting Optical Properties. *Nano Lett.* **2012**, *12*, 2852−2858.

212. Ren, Y.; Chen, M.; Zhang, Y.; Wu, L. Fabrication of Rattle-Type TiO_2/SiO_2 Core/Shell Particles with Both High Photoactivity and UV-Shielding Property. *Langmuir* **2010**, *26*, 11391–11396.

213. Mahmed, N.; Jiang, H.; Heczko, O.; Söderberg, O.; Hannula, S.-P. Influence of Different Synthesis Approach on Doping Behavior of Silver Nanoparticles Onto the Iron Oxide–Silica Coreshell Surfaces. *J. Nanopart. Res.* **2012**, *14*, 987-1002.

214. Pinho, S. L C.; Pereira, G. A.; Voisin, P.; Kassem, J.; Etienne, L.; Peters, J. A.; Carlos, L. Fine Tuning of the Relaxometry of γ-Fe_2O_3@SiO_2 Nanoparticles by Tweaking the Silica Coating Thickness. *ACS Nano* **2010**, *4*, 5339-5349.

215. Wang, Z. L.; Quan, Z. W.; Jia, P. Y.; Lin, C. K.; Luo, Y.; Chen, Y.; Fang, J.; Zhou, W.; Connor, C. J. O.; Lin, J. A Facile Synthesis and Photoluminescent Properties of Redispersible CeF_3, CeF_3:Tb^{3+}, and CeF_3:Tb^{3+}/LaF_3 (Core/Shell) Nanoparticles. *Chem. Mater.* **2006**, *18*, 2030-2037.

216. Wang, Y.; Liu, K.; Liu, X.; Gregorkiewicz, T.; Kong, X.; Aalders, M. C. G.; Buma, W. J.; Zhang, H. Critical Shell Thickness of Core/Shell Upconversion Luminescence Nanoplatform for FRET Application. *J. Phys. Chem. Lett.* **2011**, *2*, 2083–2088.

217. Cao, Y. W.; Banin, U. Growth and Properties of Semiconductor Core/Shell Nanocrystals with InAs Cores. *J. Am. Chem. Soc.* **2000**, *122*, 9692-9702.

218 Amato, M.; Ossicini, S.; Rurali, R. Band-Offset Driven Efficiency of the Doping of SiGe Core-Shell Nanowires. *Nano Lett.* **2011**, *11*, 594–598.

219. Yi, G.-S.; Chow, G.-M.; Water-Soluble $NaYF_4$:Yb,Er(Tm)/$NaYF_4$/Polymer Core/Shell/Shell Nanoparticles with Significant Enhancement of Upconversion Fluorescence. *Chem. Mater.* **2007**, *19*, 341-343.

220. Yi, F.; Bu, W.; Zhang, S.; Liu, X.; Liu, J.; Xing, H.; Xiao, Q.; Zhou, L.; Peng, W.; Wang, L.; Shi, J. Positive and Negative Lattice Shielding Effects Co-existing in Gd (III) Ion Doped Bifunctional Upconversion Nanoprobes. *Adv. Funct. Mater.* **2011**, *21*, 4285–4294.

221. Kömpe, K.; Borchert, H.; Storz, J.; Lobo, A.; Adam, S.; Möller, T.; Haase, M. Green-Emitting $CePO_4$:Tb/$LaPO_4$ Core–Shell Nanoparticles with 70% Photoluminescence Quantum Yield. *Angew. Chem. Int. Ed.* **2003**, *42*, 5513 –5516.

222. Runowski, M.; Grzyb, T.; Lis, S. Bifunctional Luminescent and Magnetic Core/Shell Type Nanostructures Fe_3O_4@CeF_3:Tb^{3+}/SiO_2. *J. Rare Earth*. 2011, *29*, 1117-1122.

223. Yang, Y.; Chen, O.; Angerhofer, A.; Cao, Y. C. On Doping CdS/ZnS Core/Shell Nanocrystals with Mn. *J. Am. Chem. Soc.* **2008**, *130*, 15649–15661.

224. Chen, O.; Shelby, D. E.; Yang, Y.; Zhuang, J.; Wang, T.; Niu, C.; Omenetto, N.; Cao, Y. C. Excitation-Intensity-Dependent Color-Tunable Dual Emissions from Manganese-Doped CdS/ZnS Core/Shell Nanocrystals. *Angew. Chem. Int. Ed*. **2010**, *49*, 10132 –10135.

225. Thakar, R.; Chen, Y.; Snee, P. T. Efficient Emission from Core/(Doped) Shell Nanoparticles: Applications for Chemical Sensing. *Nano Lett.* **2007**, *7*, 3429-3432.

226. Ehlert, O.; Osvet, A.; Batentschuk, M.; Winnacker, A.; Nann, T. Synthesis and Spectroscopic Investigations of Cu- and Pb-Doped Colloidal ZnS Nanocrystals. *J. Phys. Chem. B* **2006**, *110*, 23175-23178.

227. Zhao, Y.; Smith, J. T.; Appenzeller, J.; Yang, C. Transport Modulation in Ge/Si Core/Shell Nanowires through Controlled Synthesis of Doped Si Shells. *Nano Lett*. **2011**, *11*, 1406–1411.

228. Lee, H.; Choi, H. J. Single-Impurity Scattering and Carrier Mobility in Doped Ge/Si Core-Shell Nanowires. *Nano Lett*. **2010**, *10*, 2207–2210.

229. Lehmann, O.; Kömpe, K.; Haase, M. Synthesis of Eu^{3+}-Doped Core and Core/Shell Nanoparticles and Direct Spectroscopic Identification of Dopant Sites at the Surface and in the Interior of the Particles. *J. Am. Chem. Soc*. **2004**, *126*, 14935-14942.

230. Buissette, V.; Moreau, M.; Gacoin, T.; Boilot, J.-P. Luminescent Core/Shell Nanoparticles with a Rhabdophane $LnPO_4$-xH_2O Structure: Stabilization of Ce^{3+}-Doped Compositions. *Adv. Funct. Mater*. **2006**, *16*, 351–355.

231. Vlaskin, V. A.; Beaulac, R.; Gamelin, D. R. Dopant-Carrier Magnetic Exchange Coupling in Colloidal Inverted Core/Shell Semiconductor Nanocrystals. *Nano Lett*. **2009**, *9*, 4376-4382.

232. Khan, A. F.; Yadav, R.; Mukhopadhya, P. K.; Singh, S.; Dwivedi, C.; Dutta, V.; Chawla, S. Core–shell Nanophosphor with Enhanced NIR–Visible Upconversion as Spectrum Modifier for Enhancement of Solar Cell Efficiency. *J. Nanopart. Res*. **2011**, *13*, 6837–6846.

233. Wang, Y.; Liu, K.; Liu, X.; Gregorkiewicz, T.; Kong, X.; Aalders, M. C. G.; Buma, W. J.; Zhang, H. Critical Shell Thickness of Core/Shell Upconversion Luminescence Nanoplatform for FRET Application. *J. Phys. Chem. Lett*. **2011**, *2*, 2083–2088.

234. Vetrone, F.; Naccache, R.; Mahalingam, V.; Morgan, C. G.; Capobianco, J. A. The Active-Core/Active-Shell Approach: A Strategy to Enhance the Upconversion Luminescence in Lanthanide-Doped Nanoparticles. *Adv. Funct. Mater*. **2009**, *19*, 2924–2929.

235. Boyer, J.-C. Gagnon, J.; Cuccia, L. A.; Capobianco, J. A. Synthesis, Characterization, and Spectroscopy of $NaGdF_4:Ce^{3+},Tb^{3+}/NaYF_4$ Core/Shell Nanoparticles. *Chem. Mater*. **2007**, *19*, 3358-3360.

236. Wang, Q.; Yang, X.; Yu, L.; Yang, H. Magnetic and Luminescent Properties of $Fe/Fe_3O_4@Y_2O_3:Eu$ Nanocomposites. *J. Alloys Compd*. **2011**, *509*, 9098– 9104.

237. Gautam, A.; Veggel, F. C. J. M. V. Blue Electroluminescence from Eu^{2+}-Doped $GaN@SiO_2$ Nanostructures Tuned to Industrial Standards. *Chem. Mater.* **2011**, *23*, 4817–4823.

238. Zhang, X.-y.; Han, L.-q.; Wang, C.-y.; Chen, M.-m. Double-Shelled MnO_2 Hollow Spheres for Supercapacitors. *Mater. Lett.* **2014**, *136*, 78–80.

239. Rivera, M. C.; Pinheiro, A. C.; Bourbon, A. I.; Cerqueira, M. A.; Vicente, A. A. Hollow Chitosan/Alginate Nanocapsules for Bioactive Compound Delivery. *Int. J. Biol. Macromol.* **2015**, *79*, 2015, 95–102.

240. Zhao, X.; Du, P.; Liu, P. Preparation of Aggregation-Resistant Biocompatible Superparamagnetic Noncovalent Hybrid Multilayer Hollow Microspheres for Controlled Drug Release. *Mol. Pharmaceutics* **2012**, *9*, 3330−3339.

241. Rahman, M. M.; Wang, J. Z.; Wexler, D.; Zhang, Y. Y.; Li, X. J.; Chou, S. L.; Liu, H. K. "Silver-Coated TiO_2 Nanostructured Anode Materials for Lithium Ion Batteries. *J. Solid State Electrochem.* **2010**, *14*, 571–578.

242. Chiou, J. W.; Ray, S. C.; Tsai, H. M.; Pao, C. W.; Chien, F. Z.; Pong, W. F.; Tseng, C. H.; Wu, J. J.; Tsai, M. H.; Chen, C.H.; Lin, H. J.; Lee, J. F.; Guo, J. H. Correlation between Electronic Structures and Photocatalytic Activities of Nanocrystalline-(Au, Ag, and Pt) Particles on the Surface of ZnO Nanorods. *J. Phys. Chem. C* **2011***, 115*, 2650– 2655.

243. Chen, C.; Xie, Y.; Ali, G.; Yoo, S. H.; Cho, S. O. Improved Conversion Efficiency of CdS Quantum Dots-Sensitized TiO_2 Nanotube Array Using ZnO Energy Barrier Layer. *Nanotechnology* **2011**, *22*, 015202.

244. Wu, M.; Yang, B. F.; Lv, Y.; Fu, Z. P.; Xu, J. A.; Guo, T.; Zhao, Y. X. Efficient One-Pot Synthesis of Ag Nanoparticles Loaded on N-Doped Multiphase TiO_2 Hollow Nanorod Arrays with Enhanced Photocatalytic Activity. *Appl. Surf. Sci*. **2010**, *256*, 7125– 7130.

245. Gao, Y.; Fang, P.; Chen, F.; Liu, Y.; Liu, Z.; Wang, D.; Dai, Y. Enhancement of Stability of N-Doped TiO_2 Photocatalysts with Ag Loading. *Appl. Surf. Sci*. **2013**, *265*, 796–801.

246. Malashkevich, G. E.; Shevchenko, G. P.; Serezhkina, S. V.; Pershukevich, P. P.; Semkova, G. I.; Glushonok, G. K. Effect of the Chemical State of Silver on the Luminescence Properties of GeO_2–Eu_2O_3–Ag Films. *Phys. Solid State* **2007**, *49*, 1891–1902.

247. Dolgov, L.; Reedo, V.; Kiisk, V.; Pikker, S.; Sildos, I.; Kikas, J. Structure and Fluorescent Properties of TiO_2:Sm^{3+}–Ag Composite. *Opt. Mater.* **2010**, *32*, 1540–1544.

248. Bokare, A.; Sanap, A.; Pai, M.; Sabharwal, S.; Athawale, A. A. Antibacterial Activities of Nd Doped and Ag Coated TiO_2 Nanoparticles Under Solar Light Irradiation. *Colloids Surf., B* **2013**, *102*, 273–280.

249. Akhavan, O. Lasting Antibacterial Activities of Ag–TiO_2/Ag/a-TiO_2 Nanocomposite Thin Film Photocatalysts Under Solar Light Irradiation. *J. Colloid Interface Sci.* **2009**, *336*, 117–124.

250. Yu, C.; Wei, L.; Li, X.; Chen, J.; Fan, Q.; Yu, J. C. Synthesis and Characterization of Ag/TiO_2-B Nanosquares with High Photocatalytic Activity Under Visible Light Irradiation. *Mater. Sci. Eng. B* **2013**, *178*, 344–348.

251. Shi, Z.-L.; Du, C.; Yao, S.-H. Preparation and Photocatalytic Activity of Cerium Doped Anatase Titanium Dioxide Coated Magnetite Composite. *J. Taiwan Inst. Chem. Eng.* **2011**, *42*, 652–657.

252. Zhang, S.; Peng, F.; Wang, H.; Yu, H.; Zhang, S.; Yang, J.; Zhao, H. Electrodeposition Preparation of Ag Loaded N-Doped TiO_2 Nanotube Arrays with Enhanced Visible Light Photocatalytic Performance. *Catal. Commun.* **2011**, *12*, 689–693.

253. Reisfeld, R.; Gaft, M.; Saridarov, T.; Panczer, G.; Zelner, M. Nanoparticles of Cadmium Sulfide with Europium and Terbium in Zirconia Films having Intensified Luminescence. *Mater. Lett.* **2000**, *45*, 154.

254. Rai, S.; Bokatial, L.; Dihingia, P. J. Effect of CdS Nanoparticles on Fluorescence from Sm^{3+} Doped SiO_2 Glass. *J. Lumin.* **2011**, *131*, 978–983.

255. Chen, C.; Wang, L.; Li, F.; Ling, L. Improving Conversion Efficiency of CdS Quantum Dots-Sensitized TiO_2 Nanotube Arrays by Doping with Zn^{2+} and Decorating with ZnO Nanoparticles. *Mater. Chem. Phys.* **2014**, *146*, 531-537.

256. Kumar, S.; Kumar, S.; Verma, N. K.; Chakarvarti, S. K. Room Temperature Magnetism in Ni-Doped CdSe Nanoparticles. *J. Mater. Sci: Mater Electron* **2011**, *22*, 901–904.

257. Sethi, R.; Kumar, L.; Sharma, P. K.; Pandey, A. C. Tunable Visible Emission of Ag-Doped CdZnS Alloy Quantum Dots. *Nanoscale Res. Lett.* **2010**, *5*, 96–102.

258. Nair, M. G.; Nirmala, M.; Rekha, K.; Anukaliani, A. Structural, Optical, Photo CAtalytic and Antibacterial Activity of ZnO and Co Doped ZnO Nanoparticles. *Mater. Lett.* **2011**, *65*, 1797–1800.

259. Goswami, N.; Sahai, A. Structural Transformation in Nickel Doped Zinc Oxide Nanostructures. *Mater. Res. Bull.* **2013**, *48*, 346–351.

260. Jiang, H.; Liu, X. F.; Zou, Z. Y.; Wu, Z. B.; He, B.; Yu, R. H. The Effect of Surfactants on the Magnetic and Optical Properties of Co-Doped SnO_2 Nanoparticles. *Appl. Surf. Sci.* **2011**, *258*, 236–241.

261. Tagaya, M.; Ikoma, T.; Yoshioka, T.; Motozuka, S.; Xu, Z.; Minami, F.; Tanaka, J. Synthesis and Luminescence Properties of Eu(III)-Doped Nanoporous Silica Spheres. *J. Colloid Interface Sci.* **2011**, *363*, 456–464.

262. Prakash, R.; Kumar, S.; Ahmed, F.; Lee, C. G.; Song, J. I. Room Temperature Ferromagnetism in Ni Doped In_2O_3 Nanoparticles. *Thin Solid Films* **2011**, *519*, 8243–8246.

263. Jose, G.; Jose, G.; Thomas, V.; Joseph, C.; Ittyachen, M. A.; Unnikrishnan, N. V. Optical Characterization of Eu^{3+} Ions in CdSe Nanocrystal Containing Silica Glass. *J. fluores.* **2004**, *14*, 733-738.

264. Zhang, J.; Gao, D.; Yang, G.; Zhang, J.; Shi, Z.; Zhang, Z.; Zhu, Z.; Xue, D. Synthesis and Magnetic Properties of Zr Doped ZnO Nanoparticles. *Nanoscale Res. Lett.* **2011**, *6*, 587(1-7).

265. Arshad, M.; Azam, A.; Ahmed, A. S.; Mollah, S.; Naqvi, A. H. Effect of Co Substitution on the Structural and Optical Properties of ZnO Nanoparticles Synthesized by sol–gel route. *J. Alloys Compd.* **2011**, *509*, 8378–8381.

266. Fu, M.; Li, Y.; Wu, S.; Lu, P.; Liu, J.; Dong, F. Sol–gel Preparation and Enhanced Photocatalytic Performance of Cu-Doped ZnO Nanoparticles. *Appl. Surf. Sci.* **2011**, *258*, 1587–1591.

267. Tseng, Y.-C.; Lin, Y.-J.; Chang, H.-C.; Chen, Y.-H.; Liu, C.-J.; Zou, Y.-Y. Effects of Ti content on the Optical and Structural Properties of the Ti-Doped ZnO Nanoparticles. *J. Lumin.* **2012**, *132*, 491–494.

268. Zhang, D.; Zeng, F. Visible Light-Activated Cadmium-Doped ZnO Nanostructured Photocatalyst for the Treatment of Methylene Blue Dye. J. Mater. Sci. DOI 10.1007/s10853-011-6016-4.

269. Kumar, S.; Mukherjee, S.; Kr. Singh, R.; Chatterjee, S.; Ghosh, A. K. Structural and Optical Properties of Sol-Gel Derived Nanocrystalline Fe-Doped ZnO. *J. Appl. Phys.* **2011**, *110*, 103508-7.

270. Slama, R.; Ghribi, F.; Houas, A.; Barthou, C.; Mir, L. E. Photocatalytic and Optical Properties of Vanadium Doped Zinc Oxide Nanoparticles. *Int. J. Nanoelectron. Mater.* **2010**, *3*, 133-142.

271. Ahmed, A. S.; Shafeeq M. M.; Singla, M. L.; Tabassum, S.; Naqvi, A. H.; Azam, A. Band Gap Narrowing and Fluorescence Properties of Nickel Doped SnO_2 Nanoparticles. *J. Lumin.* **2011**, *131*, 1–6.

272. Gu, F.; Wang, S. F.; Lü, M. K.; Qi, Y. X.; Zhou, G. J.; Xu, D.; Yuan, D. R. Luminescent Properties of Mn^{2+}-Doped SnO_2 Nanoparticles. *Inorg. Chem. Commun.* **2003**, *6*, 882-885.

273. Ha, H.-W.; Kim, K.; Borniol, M. D.; Toupance, T. Fluorine-Doped Nanocrystalline SnO_2 Powders Prepared Via a Single Molecular Precursor Method as Anode Materials for Li-ion Batteries. *J. Solid State Chem.* **2006**, *179*, 702–707.

274. Sambasivam, S.; Paul J. D.; Jeong, J. H.; Choi, B. C.; Lim, K. T.; Kim, S. S.; Song, T. K. Antiferromagnetic Interactions in Er-doped SnO_2 DMS Nanoparticles. *J. Nanopart. Res.* **2011**, *13*, 4623–4630.

275. Koao, L. F.; Swart, H. C.; Obed, R. I.; Dejene, F. B. Synthesis and Characterization of Ce^{3+} Doped Silica (SiO_2) Nanoparticles. *J. Lumin.* **2011**, *131*, 1249–1254.

276. Lucio-Ortiz, C. J.; Rosa, J. R.; Ramirez, A. H.; Reyes Heredia, J. A.; Angel, P.; Muñoz-Aguirre, S.; León-Covián, L. M. Synthesis and Characterization of Fe Doped Mesoporous Al_2O_3 by Sol–Gel Method and its Use in Trichloroethylene Combustion. *J. Sol-Gel Sci. Technol.* **2011**, *58*, 374–384.

277. Cheng, H.; Lu, Z.; Liu, Y.; Yang, H.; Gu, Y.; Li, W.; Tang, Y. Sol-gel Synthesis and Photoluminescence Characterization of $La_2Ti_2O_7$:Eu^{3+} Nanocrystals. *Rare Metal* **2011**, *30*, 602-606.

278. Hreniak, D.; Strek, W.; Amami, J.; Guyot, Y.; Boulon, G.; Goutaudier, C.; Pazik, R. The Size-Effect on Luminescence Properties of $BaTiO_3$:Eu^{3+} Nanocrystallites Prepared by the Sol–gel Method. *J. Alloys Compd.* **2004**, *380*, 348–351.

279. Ameen, S.; Akhtar, M. S.; Seo, H.-K. Kim, Y. S.; Shin, H. S. Influence of Sn Doping on ZnO Nanostructures from Nanoparticles to Spindle Shape and Their Photoelectrochemical Properties for Dye Sensitized Solar Cells. *Chem. Eng. J.* **2012**, *187*, 351-356.

280.   Jin, H.; Xu, Y.; Pang, G.; Dong, W.; Wan, Q.; Sun, Y.; Feng, S. Al-Doped SnO_2 Nanocrystals from Hydrothermal Systems. *Mater. Chem. Phys.* **2004**, *85*, 58–62.

281.   Sabari Arul, N.; Mangalaraj, D.; Chen, P. C.; Ponpandian, N.; Viswanathan, C. Self Assembly of Co Doped CeO_2 Microspheres from Nanocubes by Hydrothermal Method and their Photodegradation Activity on AO7. *Mater. Lett.* **2011**, *65*, 3320–3322.

282.   Kimura, T.; Dong, Q.; Yin, S.; Hashimoto, T.; Sasaki, A.; Sato, T. Synthesis and Piezoelectric Properties of Li-Doped $BaTiO_3$ by a Solvothermal Approach. *J. Eur. Ceram. Soc.* **2013**, *33*, 1009–1015.

283.   Lu, F.; Zhou, Y.; Liu, J.; Pan, Y. Enhancement of F-Doping on the Electrochemical Behavior of Carbon-Coated $LiFePO_4$ Nanoparticles Prepared by Hydrothermal Route. *Electrochim. Acta* **2011**, *56*, 8833– 8838.

284. Lin, M.; Zhao, Y.; Wang, S.; Liu, M.; Duan, Z. F.; Chen, Y. M.; Li, F.; Xu, F.; Lu, T. J. Recent Advances in Synthesis and Surface Modification of Lanthanide-Doped Upconversion Nanoparticles for Biomedical Applications. *Biotechnol. Adv.* **2012**, *30*, 1551–1561.

285.   Dziembaj, R.; Molenda, M.; Chmielarz, L.; Zaitz, M. M.; Piwowarska, Z.; Rafalska-Łasocha, A. Optimization of Cu Doped Ceria Nanoparticles as Catalysts for Low-Temperature Methanol and Ethylene Total Oxidation. *Catal. Today* **2011**, *169*, 112–117.

286.   Lee, M.-H.; Oh, S.-G.; Yi, S.-C. Preparation of Eu-Doped Y(2)O(3) Luminescent Nanoparticles in Nonionic Reverse Microemulsions. *J. colloid interface sci.* **2000**, *226*, 65-70.

287.   Bensalah, A.; Mortier, M.; Patriarche, G.; Gredin, P.; Vivien, D. Synthesis and Optical Characterizations of Undoped and Rare-Earth-Doped CaF_2 Nanoparticles. *J. Solid State Chem.* **2006**, *179*, 2636–2644.

288.   Bender, C. M.; Burlitch, J. M. Duane Barber and Clifford Pollock. Synthesis and Fluorescence of Neodymium-Doped Barium Fluoride Nanoparticles. *Chem. Mater.* **2000**, *12*, 1969-1976.

289.   Burianova, S.; Poltierova Vejpravova, J.; Holec, P.; Plocek, J.; Niznansky, D. Surface Spin Effects in La-Doped $CoFe_2O_4$ Nanoparticles Prepared by Microemulsion Route. *J. Appl. Phys.* **2011**, *110*, 073902-7.

290.   Wang, X.-K.; Wang, C.; Guo, W.-L.; Wang, J.-G. A Novel Single-Step Synthesis of N-Doped TiO_2 Via a Sonochemical Method. *Mater Res. Bull.* **2011**, *46*, 2041–2044.

291.   Yang, H.; Shi, J.; Gong, M.; Cheah, K. W. Synthesis and Photoluminescence of Eu^{3+}-or Tb^{3+}-Doped Mg_2SiO_4 Nanoparticles Prepared by a Combined NOvel Approach. *J. Lumin.* **2006**, *118*, 257–264.

292.   Bai, W.; Choy, K. L.; Stelzer, N. H. J.; Schoonman, J. Thermophoresis-Assisted Vapour Phase Synthesis of CeO_2 and $CexY_{12}xO_{22}d$ Nanoparticles. *Solid State Ionics* **1999**, *116*, 225-228.

293.   Winterer, M.; Fischer, R. A.; Hahn, H.; Seggern, H. V. Photoluminescence Properties of Nanocrystalline Y_2O_3: Eu^3 in Different Environment. *Acta Materialia* **2001**, *44*, 1213-1217.

294.   Zeng, D. W.; Xie, C. S.; Zhu, B. L.; Song, W. L.; Wang, A. H. Synthesis and Characteristics of Sb-Doped ZnO Nanoparticles. *Mater. Sci. Eng., B* **2003**, *104*, 68-72.

295.   Yan, W.; Chen, Y.; Yin, M. Quenching Mechanism of Er^{3+} Emissions in Er^{3+}- and Er^{3+}/Yb^{3+}-Doped $SrAl_{12}O_{19}$ Nanophosphors. *J. Rare Earths.* **2011**, *29*, 202-206.

296.   Duan, L.; Zhao, X.; Liu, J.; Geng, W.; Xie, H.; Chen, S. Structural, thermal and Magnetic Investigations of Heavily Mn-Doped ZnO Nanoparticles. *J. Magnetism Magnetic Mater.* **2011**, *323*, 2374–2379.

297.   Barros, B. S.; Melo, P. S.; Kiminami, R. H. G. A.; Costa, A. C. F. M.; Sá, G. F.; Alves, S. Photophysical Properties of Eu^{3+} and Tb^{3+}-Doped $ZnAl_2O_4$ Phosphors Obtained by Combustion Reaction. *J. Mater. Sci.* **2006**, *41*, 4744-4748.

298.   Lee, S. Y.; Lee, S. W.; Kim, S. M.; Yu, W. J.; Jo, Y. W.; Lee, Y. H.; Scalable Complementary Logic Gates with Chemically Doped Semiconducting Carbon Nanotube transistors. *ACS Nano* **2011**, *5*, 2369-75.

299.   Lei, Z.; Bai, D.; Zhao, X. S. Improving the ELectrocapacitive Properties of Mesoporous CMK-5 Carbon with Carbon Nanotubes and Nitrogen Doping. *Microporous Mesoporous Mater.* **2012**, *147*, 86–93.

300   Yu, W. J.; Kim, U. J.; Kang, B. R.; Lee, I. H.; Lee, E.-H.; Lee, Y. H. Adaptive Logic Circuits with Doping-Free Ambipolar Carbon Nanotube Transistors. *Nano lett.* **2009**, *9*, 1401-1405.

301.   Nduwimana, A.; Wang, X.-Q. Charge Carrier Separation in Modulation Doped Coaxial Semiconductor Nanowires. *Nano Lett*. **2009**, *9*, 283-286.

302.   Sato, K.; Castaldini, A.; Fukata, N.; Cavallini, A. Electronic Level Scheme in Boron- and Phosphorus-Doped Silicon Nanowires. *Nano Lett.* **2012**, *12*, 3012−3017.

303. Vallett, A. L.; Minassian, S.; Kaszuba, P.; Datta, S.; Redwing, J. M.; Mayer, T. S. Fabrication and Characterization of Axially Doped Silicon Nanowire Tunnel Field-Effect Transistors. *Nano Lett.* **2010**, *10*, 4813–4818.

304. Luo, D.; Wu, L.; Zhi, J. Fabrication of Boron-Doped Diamond Nanorod Forest Electrodes and Their Application in Nonenzymatic Amperometric Glucose Biosensing. *ACS Nano* **2009**, *3*, 2121-2128.

305. Deng, Z.; Tong, L.; Flores, M.; Lin, S.; Cheng, J.-X.; Yan, H.; Liu, Y. High-quality manganese-doped zinc sulfide quantum rods with tunable dual-color and multiphoton emissions. *J. Am. Chem. Soc.* **2011**, *133*, 5389–5396.

306. Fan, Y.; Wang, Y.; Lou, J.; Xu, S.; Zhang, L.; An, L.; Heinrich, H. Formation of Silicon-Doped Boron Nitride Bamboo Structures Via Pyrolysis of a Polymeric Precursor. *J. Am. Ceramic Soc.* **2006**, *89*, 740-742.

307. Seong, H.-K.; Kim, J.-Y.; Kim, J.-J.; Lee, S.-C.; Kim, S.-R.; Kim, U.; Park, T.-E.; Choi, H.-J. Room-temperature Ferromagnetism in Cu Doped GaN Nanowires. *Nano Lett.* **2007**, 7, 3366-71.

308. Su, R. Jin, Y.; Liu, Y.; Tong, M.; Kim, H. Bactericidal Activity of Ag-Doped Multi-Walled Carbon Nanotubes and the Effects of Extracellular Polymeric Substances and Natural organic matter. *Colloids surf., B* **2012**, *104C,* 133-139.

309. An, X.; Meng, G.; Zhang, M.; Tian, Y.; Sun, S.; Zhang, L. Synthesis and Optical Absorption Property of Ordered Macroporous Titania Film Doped with Ag Nanoparticles. *Mater. Lett*. **2006**, *60*, 2586–2589.

310. Liu, Y.; Wei, J. H.; Xiong, R.; Pan, C. X.; Shi, J. Enhanced Visible Light Photocatalytic Properties of Fe-doped TiO_2 Nanorod Clusters and Monodispersed nanoparticles. *Appl. Surf. Sci.* **2011**, *257*, 8121–8126.

311. Asapu, R.; Palla, V. M.; Wang, B.; Guo, Z.; Sadu, R.; Chen, D. H. Phosphorus-Doped Titania Nanotubes with Enhanced Photocatalytic Activity. *J. Photochem. Photobiol., A* **2011**, *225*, 81-87.

312. Mercado, C.; Seeley, Z.; Bandyopadhyay, A.; Bose, S.; McHale, J. L. Photoluminescence of Dense Nanocrystalline Titanium Dioxide Thin Films: Effect of Doping and Thickness and Relation to Gas Sensing. *ACS Appl. Mater. Interfaces* **2011**, *3*, 2281–2288.

313. Mercado, C.; Seeley, Z.; Bandyopadhyay, A.; Bose, S.; McHale, J. L. Photoluminescence of Dense nanocrystalline Titanium Dioxide Thin FIlms: EFfect of

Doping and Thickness and Relation to Gas Sensing. *ACS Appl. Mater. Interfaces* **2011**, *3*, 2281–2288.

314. Babapour, A.; Akhavan, O.; Moshfegh, A. Z.; Hosseini, A. A. Size Variation and Optical Absorption of Sol-Gel Ag Nanoparticles Doped SiO_2 Thin Film. *Thin Solid Films* **2006**, *515*, 771–774.

315. Buso, D.; Guglielmi, M.; Martucci, A.; Cantalini, C.; Post, M. L.; Haché, A. Porous Sol Gel Silica Films Doped with Crystalline NiO Nanoparticles for Gas Sensing Applications. *J. Sol-Gel Sci. Techn*. **2006**, *40*, 299–308.

316. Pedrueza, E.; Valdés, J. L.; Chirvony, V.; Abargues, R.; Hernández-Saz, J.; Herrera, M.; Molina, S. I.; Martínez-Pastor, J. P. Novel Method of Preparation of Gold-Nanoparticle-Doped TiO_2 and SiO_2 Plasmonic Thin Films: Optical Characterization and Comparison with Maxwell-Garnett Modeling. *Adv. Funct. Mater*. **2011**, *21*, 3502–3507.

317. Wang, Z.; Xin, Y.; Zhang, Z.; Li, Q.; Zhang, Y.; Zhou, L. Synthesis of Fe-Doped CeO_2 nanorods by a Widely Applicable Co-precipitation Route. *Chem. Eng. J*. **2011**, *178*, 436–442.

318. Chu, X.; Zhou, S.; Dong, Y.; Sun, W.; Ge, X. Trimethylamine Gas Sensor Based on Cr^{3+} Doped ZnO Nanorods/Nanoparticles Prepared Via Solvothermal Method. *Mater. Chem. Phys*. **2011**, *131*, 27–31.

319. Wu, C.; Shen, L.; Zhang, Y-C.; Huang, Q. Solvothermal Synthesis of Cr-Doped ZnO Nanowires with Visible LIght-Driven Photocatalytic Activity. *Mater. Lett*. **2011**, *65*, 1794–1796.

320. Hong, C.-S.; Park, H.-H.; Moon, J.; Park, H.-H.. Effect of Metal (Al, Ga, and In)-Dopants and/or Ag-Nanoparticles on the Optical and Electrical Properties of ZnO Thin Films. *Thin Solid Films* **2006**, *515*, 957–960.

321. Elilarassi, R.; Chandrasekaran, G. Microstructural and Photoluminescence Properties of Co-Doped ZnO Films Fabricated using a Simple Solution Growth Method. *Mater. Sci. Semiconductor Process.* **2011**, *14*, 179–183.

322. Hari, P.; Spencer, D.; Hor, A.; Liang, H.; Roberts, K.; Teeters, D. Cobalt Doping, Etching, and Attachment of Gold Nanoparticles and Quantum Dots on ZnO Nanorods. *Phys. Status Solidi C* **2011**, *8*, 2814–2817.

323. Yakuphanoglu, F. Preparation of Nanostructure Ni Doped CdO thin Films by Sol Gel Spin Coating Method. *J. Sol-Gel Sci. Technol*. **2011**, *59*, 569–573.

324. Misra, A.; Tyagi, P. K.; Singh, M. K.; Misra, D. S. FTIR Studies of Nitrogen Doped Carbon Nanotubes. *Diamond Relat. Mater*. **2006**, *15*, 385 – 388.

325.   Ren, G.; Zeng, S.; Hao, J. Tunable Multicolor Upconversion Emissions and Paramagnetic Property of Monodispersed Bifunctional Lanthanide-Doped NaGdF$_4$ Nanorods. *J. Phys. Chem. C* **2011**, *115*, 20141–20147.

326.   Zamudio, A.; Elías, A. L.; Rodríguez-Manzo, J. A.; Manzo, R.; López-Uríus, F.; Rodríguez- Gattorno, G.; Lupo, F.; Rühle, M.; Smith, D. J.; Terrones, H.; Díaz, D.; Terrone, M. Efficient Anchoring of Silver Nanoparticles on N-Doped Carbon Nanotubes. *Small* **2006**, *2*, 346–350.

327.   Habibi, M. H.; Mokhtari, R. Novel Sulfur-Doped Niobium Pentoxide Nanoparticles: Fabrication, Characterization, Visible Light Sensitization and Redox Charge Transfer Study. *J. Sol-Gel Sci. Technol.* **2011**, *59*, 352–357.

328.   Hamal, D. B.; Klabunde, K. J. Synthesis, Characterization, and Visible Light Activity of New Nanoparticle Photocatalysts Based on Silver, Carbon, and Sulfur-Doped TiO$_2$. *J. Colloid Interface Sci.* **2007**, *311*, 514–522.

329.   Regan, W.; Byrnes, S.; Gannett, W.; Ergen, O.; Vazquez-Mena, O.; Wang, F.; Zettl, A. Screening-Engineered Field-Effect Solar Cells. *Nano Lett.* **2012**, *12*, 4300-4304.

330.   Iwashina, K.; Kudo, A. Rh-Doped SrTiO$_3$ Photocatalyst Electrode Showing Cathodic Photocurrent for Water Splitting under Visible-Light Irradiation. *J. Am. Chem. Soc*. **2011**, *133*, 13272–13275.

331.   Kruefu, V.; Peterson, E.; Khantha, C.; Siriwong, C.; Phanichphant, S.; Carroll, D. L. Flame-Made Niobium Doped Zinc Oxide Nanoparticles in Bulk Heterojunction Solar Cells. *Appl. Phys. Lett.* **2010**, *97*, 053302-3.

332.   Hensel, J.; Wang, G.; Li, Y.; Zhang, J. Z. Synergistic Effect of CdSe Quantum Dot Sensitization and Nitrogen Doping of TiO$_2$ Nanostructures for Photoelectrochemical Solar Hydrogen Generation. *Nano Lett*. **2010**, *10*, 478-483.

333.   Yang, W.; Fellinger, T.-P.; Antonietti, M. Efficient Metal-Free Oxygen Reduction in Alkaline Medium on High-Surface-Area Mesoporous Nitrogen-Doped Carbons Made from Ionic Liquids and Nucleobases. *J. Am. Chem. Soc.* **2011**, *133*, 206–209.

334.   Yang, X.; Wolcott, A.; Wang, G.; Sobo, A.; Fitzmorris, R. C.; Qian, F.;Zhang, J. Z.; Li, Y. Nitrogen-Doped ZnO Nanowire Arrays for Photoelectrochemical Water Splitting. *Nano Lett.* **2009**, *9*, 2331-2336.

335.   Alivisatos, A. P. Perspectives on the Physical Chemistry of Semiconductor Nanocrystals. *J. Phys. Chem.* **1996**, *100*, 13226-13239.

336.   Chen, P.-C.; Shen, G.; Chen, H.; Ha, Y.-g.; Wu, C.; Fu, Y.; Liu, J.; Facchetti, A.; Marks, T. J.; Thompson, M. E.; Sukcharoenchoke, S.; Zhou, C. High-Performance

Single-Crystalline Arsenic-Doped Indium Oxide Nanowires for Transparent Thin-Film Transistors and Active Matrix Organic Light- Emitting Diode Displays. *ACS. Nano.* **2009**, *3*, 3383-3390.

337. Nag, A.; Sarma, D. D. White Light from Mn^{2+}-Doped CdS Nanocrystals: A New Approach. *J. Phys. Chem. C*, **2007**, *111*, 13641-13644.

338. Stouwdam, J. W.; Hebbink, G. A.; Huskens, J.; Veggel, F. C. J. M. V. Lanthanide-Doped Nanoparticles with Excellent Luminescent Properties in Organic Media. *Chem. Mater.* **2003,** *15*, 4604-4616.

339. Demir-Cakan, R.; Morcrette, M.; Nouar, F.; Davoisne, C.; Devic, T.; Gonbeau, D.; Dominko, R.; Serre, C.; Férey, G.; Tarascon, J.-M.; Cathode Composites for Li-S Batteries via the Use of Oxygenated Porous Architectures. *J. Am. Chem. Soc*. **2011**, *133*, 16154-60.

340. Liu, N.; Hu, L.; McDowell, M. T.; Jackson, A.; Cui, Y. Prelithiated Silicon Nanowires as an Anode for Lithium Ion Batteries. *ACS Nano,* **2011**, *5*, 6487-93.

341. Elmolla, E. S.; Chaudhuri, M. Degradation of the Antibiotics Amoxicillin, Ampicillin and Cloxacillin in Aqueous Solution by the Photo-Fenton Process. *J. Hazard. Mater.* **2009**, *172*, 1476–1481.

342. Rysz, M.; Alvarez, P. J. J. Amplification and Attenuation of Tetracycline Resistance in Soil Bacteria: Aquifer Column Experiments. *Water Res.* **2004**, *38*, 3705–3712.

343. Gilliver, M. A.; Bennett, M.; Begon, M.; Hazel, S. M.; Hart, C. A. Enterobacteria: Antibiotic Resistance Found in Wild Rodents. *Nature* **1999**, *401*, 233–234.

344. Goni-Urriza, M.; Capdepuy, M.; Arpin, C.; Raymond, N.; Caumette, P.; Quentin, C. Impact of an Urban Effluent on Antibiotic Resistance of Riverine Enterobacteriaceae and Aeromonas spp. *Appl. Environ. Microbiol.* **2000**, *66*, 125–132.

345. Muruganandham, M.; Shobana, N.; Swaminathan, M. Optimization of Solar Photocatalytic Degradation Conditions of Reactive Yellow 14 Azo Dye in Aqueous TiO$_2$. *J. Mol. Catal. A* **2006**, *246*, 154–161.

346. Chun, H.; Yizhong, W. Decolorization and Biodegradability of Photocatalytic Treated Azo Dyes and Wool Textile Wastewater. *Chemosphere* **1999**, *39*, 2107-2115.

347. Ehrampoush, M. H.; Moussavi, G. R.; Ghanian, M. T.; Rahimi, S.; Ahmadian, M. Removal of Methylene Blue Dye from Textile Simulated Sample using Tubular Reactor and TiO$_2$ /UV-C Photocatalytic Process. *Iran. J. Environ. Health Sci. Eng.* **2011**, *8*, 35–40.

348. Natarajan, T. S.; Thomas, M.; Natarajan, K.; Bajaj, H. C.; Tayade, R. J. Study on UV-LED/TiO_2 Process for Degradation of Rhodamine B Dye. *Chem. Eng. J.* **2011**, *169*, 126–134.

349. Li, Z.; Shen, W.; He, W.; Zu, X. Effect of Fe-Doped TiO_2 Nanoparticle Derived from Modified Hydrothermal Process on the Photocatalytic Degradation Performance on Methylene Blue. *J. Hazard. Mater.* **2008**, *155*, 590–594.

350. Ni, Y.; Zhu, Y.; Ma, X. A Simple Solution Combustion Route for the Preparation of Metal-Doped TiO_2 Nanoparticles and their Photocatalytic Degradation Properties. *Dalton Trans.* **2011**, *40*, 3689–3694.

351. Chauhan, R.; Kumar, A.; Chaudhary, R. P. Photocatalytic Degradation of Methylene Blue with Cu Doped ZnS Nanoparticles. *J. Lumin.* **2014**, *145*, 6–12.

352. Ghosh Chaudhuri, R.; Paria, S. Visible Light Induced Photocatalytic Activity of Sulfur Doped hollow TiO_2 Nanoparticles, Synthesized Via a Novel Route. *Dalton Trans.* **2014**, *43*, 5526–5534.

353. Piccinini, P.; Minero, C.; Vincenti, M.; Pelizzetti, E. Photocatalytic Mineralization of Nitrogen-Containing Benzene Derivatives. *Catal. Today* **1997**, *39*, 187-195.

354. Bhatkhande, D. S.; Pangarkar, V. G.; Beenackers, A. A. C. M. Photocatalytic Degradation of Nitrobenzene using Titanium Dioxide and Concentrated Solar Radiation: Chemical Effects and Scaleup. *Water res.* **2003**, *37*, 1223-1230.

355. ElShafei, G. M. S.; Yehia, F. Z.; Dimitry, O. I. H.; Badawi, A. M.; Eshaq, G. Degradation of Nitrobenzene at Near Neutral pH using Fe^{2+} –Glutamate Complex as a Homogeneous Fenton Catalyst. *Appl. Catal., B* **2010**, *99*, 242-247.

356. O'connor, O. A.; Young, L. Y. Toxicity and Anaerobic Biodegradability of Substituted Phenols under Methanogenic Conditions. *Environ. Toxicol. Chem.* **1989**, *8*, 853-862.

357. Zhao, L.; Ma, J.; Sun, Z. -z.; Zhai, X. -d. Catalytic Ozonation for the Degradation of Nitrobenzene in Aqueous Solution by Ceramic Honeycomb-Supported Manganese. *Appl. Catal., B* **2008**, *83*, 256-264.

358. Zhu, J.; Chen, F.; Zhang, J.; Chen, H.; Anpo, M. Fe^{3+}-TiO_2 Photocatalysts Prepared by Combining Sol–Gel Method with Hydrothermal Treatment and their Characterization. *J. Photochem. Photobiol., A* **2006**, *180*, 196–204.

359. Kiraz, N.; Burunkaya, E.; Kesmez, Ö.; Çamurlu, H. E.; Asiltürk, M.; Yeşil, Z.;Arpaç, E. Preparation of Sn Doped Nanometric TiO_2 Powders by Reflux and Hydrothermal Syntheses and their Characterization. *J. Sol-Gel Sci. Technol.* **2011**, *59*, 381-386.

360. Li, F.; Yin, X.; Yao, M.-m.; Li, J. Investigation on F–B–S Tri-Doped Nano-TiO$_2$ Films for the Photocatalytic Degradation of Organic Dyes. *J Nanopart Res.* DOI 10.1007/s11051-011-0461-5.

361. Lu, X.; Liu, Z.; Zhu, Y.; Jiang, L. Sonochemical Synthesis and Photocatalytic Property of Zinc Oxide Nanoparticles Doped with Magnesium(II). *Mater. Res. Bull.* **2011**, *46*, 1638–1641.

362. Rao, K. J.; Paria, S. Use of Sulfur Nanoparticles as a Green Pesticide on *Fusarium Solani* and *Venturia Inaequalis* Phytopathogens. *RSC Adv.* **2013**, *3*, 10471-10478.

363. Suyana, P.; Kumar, S. N.; Kumar, B. S. D.; Nair, B. N.; Pillai, S. C.; Mohamed, A. P.; Warrier, K. G. K.; Hareesh, U. S. Antifungal Properties of Nanosized ZnS Particles Synthesised by Sonochemical Precipitation. *RSC Adv.* **2014**, *4*,8439 –8445.

364. Jiang, Y.; O'Neill, A. J.; Ding, Y.; Zinc Oxide Nanoparticle-Coated Films: Fabrication, Characterization, and Antibacterial Properties. *J. Nanopart. Res.* **2015**, *17*, 180-189.

365. Kruk, T.; Szczepanowicz, K.; Stefańska, J.; Socha, R. P.; Warszyński, P.; Synthesis and Antimicrobial Activity of Monodisperse Copper Nanoparticles. *Colloids Surf., B: Biointerfaces,* **2015**, *128*, 17-22.

366. Haghighi, N.; Abdi, Y.; Haghighi, F. Light-Induced Antifungal Activity of TiO$_2$ Nanoparticles/ZnO Nanowires. *Appl. Surf. Sci.* **2011**, *257*, 10096–10100.

367. Haghighi, F.; Mohammadi, S. R.; Mohammadi, P.; Hosseinkhani, S.; Shidpour, R. Antifungal Activity of TiO$_2$ Nanoparticles and EDTA on Candida Albicans Biofilms. *Infect. Ep. Med.* **2013**, *1*, 33-38.

368. Gholami-Shabani, M.; Shams-Ghahfarokhi, M.; Gholami-Shabani, Z.; Akbarzadeh, A.; Riazi, G.; Ajdari, S.; Amani, A.; Razzaghi-Abyaneh, M. Enzymatic Synthesis of Gold Nanoparticles using Sulfite Reductase Purified from Escherichia Coli: A Green Eco-Friendly Approach. *Process Biochem.* **2015**, *50*, 1076–1085.

369. Bober, P.; Liu, J.; Mikkonen, K. S.; Ihalainen, P.; Pesonen, M.; Plumed-Ferrer, C.; Wright, A.; Lindfors, T.; Xu, C.; Latonen, R.-M. Biocomposites of Nanofibrillated Cellulose, Polypyrrole, and Silver Nanoparticles with Electroconductive and Antimicrobial Properties. *Biomacromolecules* **2014**, *15*, 3655−3663.

370. Badireddy, A. R.; Hernandez-Delgadillo, R.; Sánchez-Nájera, R. I.; Chellam, S.; Cabral-Romero, C. Synthesis and Characterization of Lipophilic Bismuth Dimercaptopropanol Nanoparticles and Their Effects on Oral Microorganisms Growth and Biofilm Formation. *J. Nanopart. Res.* **2014**, *16*, 2456-2468.

371. Gowri, S.; Gandhi, R. R.; Sundrarajan, M. Structural, Optical, Antibacterial and Antifungal Properties of Zirconia Nanoparticles by Biobased Protocol. *J. Mater. Sci. Technol.* **2014**, *30*, 782-790.

372. Panáček, A.; Kolář, M.; Večeřova, R.; Prucek, R.; Soukupová, J.; Kryštof, V.; Hamal, P.; Zbořil, R.; Kvítek, L. Antifungal Activity of Silver Nanoparticles Against Candida Spp. *Biomater.* **2009**, *30*, 6333–6340.

373. Jiang, Y.; Zhao, H.; Zhu, N.; Lin, Y.; Yu, P.; Mao, L. A Simple Assay for Direct Colorimetric Visualization of Trinitrotoluene at Picomolar Levels Using Gold Nanoparticles. *Angew. Chem. Int. Ed.* **2008**, *47*, 8601–8604.

374. Tu, R.; Liu, B.; Wang, Z.; Gao, D.; Wang, F.; Fang, Q.; Zhang, Z. Amine-Capped ZnS-Mn^{2+} Nanocrystals for Fluorescence Detection of Trace TNT Explosive. *Anal. Chem.* **2008**, *80*, 3458-3465.

375. Li, Q.; Tan, X.; Fu, L.; Liu, Q.; Tang, W. A Novel Fluorescence and Resonance Rayleigh Scattering Probe Based on Quantum Dots for the Detection of Albendazole. *Anal. Methods*, **2015**, *7*, 614–620.

376. Li, L.; Lu, Y.; Ding, Y.; Cheng, Y.; Xu, W.; Zhang, F. Determination of Paracetamol Based on ite Quenching Effect on the Photoluminescence of CdTe Fluorescence Probes. *J. Fluoresc.* **2012**, *22*, 591-596.

377. Singh, D.; Nagaraja, C. M. A luminescent 3D Interpenetrating Metal–Organic Framework for Highly Selective Sensing of Nitrobenzene. *Dalton Trans.* **2014**, *43*, 17912–17915.

378. Dar, R. A.; Khare, N. G.; Cole, D. P.; Karna, S. P.; Srivastava, A. K. Green Synthesis of a Silver Nanoparticle–Grapheme Oxide Composite and its Application for As(III) Detection. *RSC Adv.* **2014**, *4*, 14432–14440.

379. Cao, B.; Yuan, C.; Liu, B.; Jiang, C.; Guan, G.; Han, M.-Y. Ratiometric Fluorescence Detection of Mercuric Ion Based on the Nanohybrid of Fluorescence Carbon Dots and Quantum Dots. *Anal. Chim. Acta.* **2013**, *786*, 146–152.

380. Huang, H.; Lv, J.-J.; Zhou, D.-L.; Bao, N.; Xu, Y.; Wang, A.-J.; Feng, J.-J. One-Pot Green Synthesis of Nitrogen-Doped Carbon Nanoparticles as Fluorescent Probes for Mercury Ions. *RSC Adv.* **2013**, *3*, 21691-21696.

381. Lu, W.; Qin, X.; Liu, S.; Chang, G.; Zhang, Y.; Luo, Y.; Asiri, A. M.; Al-Youbi, A. O.; Sun, X. Economical, Green Synthesis of Fluorescent Carbon Nanoparticles and Their Use as Probes for Sensitive and Selective Detection of Mercury(II) Ions. *Anal. Chem.* **2012**, *84*, 5351−5357.

382. Koneswaran, M.; Narayanaswamy, R. L-Cysteine-Capped ZnS Quantum Dots Based Fluorescence Sensor for Cu^{2+} Ion. *Sens. Actuators, B* **2009**, *139*, 104–109.

383. Meng, Q.; Zhang, X.; He, C.; He, G.; Zhou, P.; Duan, C. Multifunctional Mesoporous Silica Material Used for Detection and Adsorption of Cu^{2+} in Aqueous Solution and Biological Applications in Vitro and in Vivo. *Adv. Funct. Mater.* **2010**, *20*, 1903–1909.

384. Seo, S.; Lee, H. Y.; Park, M.; Lim, J. M.; Kang, D.; Yoon, J.; Jung, J. H. Fluorescein-Functionalized Silica Nanoparticles as a Selective Fluorogenic Chemosensor for Cu^{2+} in Living Cells. *Eur. J. Inorg. Chem.* **2010**, 843–847.

385. Sun, W.; Du, Y.; Wang, Y. Study on Fluorescence Properties of Carbogenic Nanoparticles and Their Application for the Determination of Ferrous Succinate. *J. Lumin.* **2010**, *130*, 1463–1469.

386. Guo, Y.; Zhang, L.; Zhang, S.; Yang, Y.; Chen, X.; Zhang, M. Fluorescent Carbon Nanoparticles for the Fluorescent Detection of Metal Ions. *Biosens. Bioelectron.* **2015**, *63*, 61–71.

387. Dong, Z.; Dong, Z.; Wang, P.; Tian, X.; Geng, H.; Li, R.; Ma, J. A Fluorescent Probe for Zinc Detection Based on Organically Functionalized SBA-15. *Appl. Surf. Sci.* **2010**, *257*, 802–806.

388. Tan, J.; Wang, H.-F.; Yan, X.-P. A Fluorescent Sensor Array Based on Ion Imprinted Mesoporous Silica. *Biosens. Bioelectron.* **2009**, *24*, 3316–3321.

389. Kumar, M.; Puri, A. A Review of Permissible Limits of Drinking Water. *Indian J. Occup. Environ. Med.* **2012**, *16*, 40-44.

390. World Health Organisation (WHO), Guidelines for Drinking Water Quality, **1993**, p. 41.

391. Chakraborti, D.; Rahman, M. M.; Raul, K.; Chowdhyry, U. K.; Sengupta, M. K.; Lodh, D.; Chanda, C. R.; Saha, K. C.; Mukherjee, S. C. Arsenic Calamity in the Indian Subcontinent: What Lessons have been Learned? *Talanta* **2002**, *58*, 3-22.

392. Chatterjee, A.; Das, D.; Mandal, B. K.; Chowdhury, T. R.; Samanta, G.; Chakraborti, D. Arsenic in Ground Water in Six Districts of West Bengal, India: the Biggest Arsenic Calamity in the World. Part I Arsenic Species in Drinking Water and Urine of the Affected People. *Analyst* **1995**, *120,* 643-650.

393. Hsieh, C.-J.; Yen, C.-H.; Kuo, M.-S, Determination of Trace Amount Arsenic(III) and Arsenic(v) in Drinking Water and Arsenic(III) Vapour in Air by Graphite-Furnace Atomic Absorption Spectrometry using 2, 3 Dimercaptopropane-1-Sulfonate as a Complexing Agent. *Anal. Sci.* **1999**, *15*, 669-673.

394.   Anawar, H. M. Arsenic Speciation in Environmental Samples by Hydride Generation and Electrothermal Atomic Absorption Spectrometry. *Talanta* **2012**, *88*, 30− 42.

395.   Sharma, P.; Sanganeria, S.; Rawat, C.; Polarographic Determination of Arsenic in Aquatic Environment. *Chem. Environ. Res.* **1993**, *2*, 95–99.

396.   Marawi, I.; Wang, J.; Caruso, J. A. Graphite furnace Hydride Preconcentration and Subsequent Detection by Inductively Coupled Plasma Mass Spectrometry. *Anal. Chim. Acta.* **1994**, *291*, 127-136.

397.   Hymer, C. B.; Caruso, J. A. Arsenic and its Speciation Analyses using High-Performance Liquid Chromatography and Inductively Coupled Plasma Mass Spectrometry. *J. Chromatogr. A* **2004**, *1045*, 1–13.

398.   Al-Assaf, K. H.; Tyson, J. F; Uden, P. C. Determination of Four Species in Soil by Sequential and with Post-Column Generation and Detection. *J. Anal. Atom. Spectrom.* **2009**, *24*, 376–384.

399.   Holak, W. Determination of Arsenic by Cathodic Stripping Voltammetry with a Hanging Mercury Drop Electrode. *Anal. Chem.* **1980**, *52*, 2189-2192.

400.   Hassan, S. S.; Sirajuddin; Solangi, A. R.; Kazi, T. G.; Kalhoro, M. S.; Junejo, Y.; Tagar, Z. A.; Kalwar, N. H. Nafion Stabilized Ibuprofen-Gold Nanostructures Modified Screen Printed Electrode as Arsenic(III) Sensor. *J. Electroanal. Chem.* **2012**, *682*, 77-82.

401.   Cao, B.; Yuan, C.; Liu, B.; Jiang, C.; Guan, G.; Han, M.-Y. Ratiometric Fluorescence Detection of Mercuric Ion Based on the Nanohybrid of Fluorescence Carbon Dots and Quantum Dots. *Anal. Chim. Acta* **2013**, *786*, 146-152.

402.   Watanabe, S.; Seguchi, H.; Yoshida, K.; Kifune, K.; Tadaki, T.; Shiozaki, H. Colorimetric Detection of Fluoride Ion in an Aqueous Solution using a Thioglucose-Capped Gold Nanoparticle. *Tetrahedron Lett.* **2005**, *46*, 8827-8829.

403.   Tan, J.; Wang, H.-F.; Yan, X.-P. A fluorescent Sensor Array Based on Ion Imprinted Mesoporous Silica. *Biosens. Bioelectron.* **2009**, *24*, 3316-3321.

404.   Seo, S.; Lee, H. Y.; Park, M.; Lim, J. M.; Kang, D.; Yoon, J.; Jung, J. H. Fluorescein-Functionalized Silica Nanoparticles as a Selective Fluorogenic Chemosensor for Cu^{2+} in Living Cells. *Eur. J. Inorg. Chem.* **2010**, 843–847.

405.   Chiu, C.-W.; Gabbaï, F. P. Fluoride Ion Capture from Water with a Cationic Borane. *J. Am. Chem. Soc.* **2006**, *128*, 14248 − 14249.

406.   Wade, C. R.; Broomsgrove, A. E. J.; Aldridge, S.; Gabbaï, P. Fluoride Ion Complexation and Sensing Using Organoboron Compounds. *Chem. Rev.* **2010**, *110*, 3958 − 3984.

407. Zhou, Y.; Zhang, J. F.; Yoon, J. Fluorescence and Colorimetric Chemosensors for Fluoride-Ion Detection. *Chem. Rev.* **2014**, *114*, 5511 − 5571.

408. Kirk, K. L. Biochemistry of the Halogens and Inorganic Halides; Plenum Press: New York, **1991**; p 58.

409. Farley, J. R.; Wergedal, J. E.; Baylink, D. J. Fluoride Directly Stimulates Proliferation and Alkaline Phosphatase Activity of Bone-Forming Cells. *Science* **1983**, *222*, 330–332.

410. Dambacher, M. A.; Ittner, J.; Ruegsegger, P. Long-term Fluoride Therapy of Postmenopausal Osteoporosis. *Bone* **1986**, *7*, 199–205.

411. Lennon, M. A. One in a Million : the First Community Trial of Water Fluoridation. *Bull. World Health Organization* **2006**, *84*, 759 − 760.

412. Dale, T.J.; Rebek, J. J. Fluorescent Sensors for Organophosphorus Nerve Agent Mimics. *J. Am. Chem. Soc.* **2006**, *128*, 4500 − 4501.

413. Xu, S.; Chen, K. C.; Tian, H. A Colorimetric and Fluorescent Chemodosimeter: Fluoride Ion Sensing by An Axial-Substituted Subphthalocyanine. *J. Mater. Chem.* **2005**, *15*, 2676-2680.

414. Wiseman, A. Handbook of Experimental Pharmacology XX/2, Springer-Verlag, Berlin, **1970**, Part 2, pp. 48–97.

415. Ayoob, S.; Gupta, A. K. Fluoride in Drinking Water: A Review on the Status and Stress Effects Crit. Rev. *Env. Sci. Tech.* **2006**, *36*, 433-487.

416. Singh, P. P.; Barjatiya, M. K.; Dhing, S.; Bhatnagar, R.; Kothari, S.; Dhar, V. Evidence Suggesting that High Intake of FLuoride Provokes Nephrolithiasis in Tribal Population. *Urol. Res.* **2001**, *29*, 238-244.

417. Cittanova, M.L.; Lelongt, B.; Verpont, M.C. Fluoride Ion Toxicity in Human Kidney Collecting Duct Cells. *Anesthesiology* **1996**, *84*, 428–435.

418. Bassin, E. B.; Wypij, D.; Davis, R.B. Age-Specific Fluoride Exposure in Drinking Water and Osteosarcoma (United States). *Cancer Cause. Control* **2006**, *17*, 421–428.

419. Baruah, U.; Gogoi, N.; Majumdar, G.; Chowdhury, D. β-Cyclodextrin and Calix[4]Arene-25,26,27,28-Tetrol Capped Carbon Dots for Selective and Sensitive Detection of Fluoride. *Carbohydr. Polym.* **2015**, *117*, 377 − 383.

420. Kim, T.-hyun & Swager, T.M. A Fluorescent Self-Amplifying Wavelength-Responsive Sensory Polymer for Fluoride Ions. *Angew. Chem. Int. Ed.* **2003**, *42*, 4803 − 4806.

421. Ke, B.; Chen, W.; Ni, N.; Cheng, Y.; Dai, C.; Dinh, H.; Wang, B. A Fluorescent Probe for Rapid Aqueous Fluoride Detection and Cell Imaging. *Chem. Commun.* **2013**, *49*, 2494 – 2496.

422. Hu, R.; Feng, J.; Hu, D.; Wang, S.; Li, S.; Li, Y.; Yang, G. A Rapid Aqueous Fluoride Ion Sensor with Dual Output Modes. *Angew. Chem. Int. Ed.* **2010**, *49*, 4915 – 4918.

423. Cametti, M.; Rissanen, K. Recognition and Sensing of Fluoride Anion. *Chem. Commun.* **2009**, 2809 – 2829.

424. Cho, E. J.; *Moon, J. W.; Ko, S. W.; Lee, J. Y.; Kim, S. K.; Yoon, J.; Nam, K. C.* A New Fluoride Selective Fluorescent as Well as Chromogenic Chemosensor Containing a Naphthalene Urea Derivative. *J. Am. Chem. Soc.* **2003**, *125*, 12376 – 12377.

425. Chiu, C.-W.; Gabbaï, F. P. Fluoride Ion Capture from Water with a Cationic Borane. *J. Am. Chem. Soc.* **2006**, *128*, 14248 – 14249.

426. Liu, X. Y.; Bai, D. R.; Wang, S. Charge-Transfer Emission in Nonplanar Three-Coordinate Organoboron Compounds for Fluorescent Sensing of Fluoride. *Angew. Chem. Int . Ed.* **2006**, *45*, 5475 – 5478.

427. Yang, X. Xie, L.; Ning, R.; Gong, X.; Liu, Z.; Li, Y.; Zheng, L.; Zhang, G.; Gao, B.; Cui, Y.; Sun, G.; Zhang, G. A Diketopyrrolopyrrole-Based Near-Infrared Sensor for Selective Recognition of Fluoride Ions. *Sens. Actuators, B* **2015**, *210*, 784 – 794.

428. Wang, H.; Fan, P.-H.; Tong, B.; Dong, Y.-P.; Ou, X.-M.; Li, F.; Zhang, X.-H. Hydrogen-Terminated Si Nanowires as Label-Free Colorimetric Sensors in the Ultrasensitive and Highly Selective Detection of Fluoride Anions in Pure Water Phase. *Adv. Funct. Mater.* **2015**, *25*, 1506 – 1510.

429. Kim, H. Y.; Im, H. G.; Chang, S.-K. Colorimetric and Fluorogenic Signaling of Fluoride Ions by Thiophosphinated Dichlorofluorescein. *Dyes Pigments* **2015**, *112*, 170 – 175.

430. Ghosh, K.; Kar, D.; Fröhlich, R.; Chattopadhyay, A. P.; Samadder, A.; Khuda-Bukhsh, A. R. O-Tert-Butyldiphenylsilyl Coumarin and Dicoumarol: a Case Toward Selective Sensing of F⁻ Ions in Organic and Aqueous Environments. *Analyst,* **2013,** *138,* 3038 – 3045.

431. Ke, B.; Chen, W.; Ni, N.; Cheng, Y.; Dai, C.; Dinh, H.; Wang, B. A Fluorescent Probe for Rapid Aqueous Fluoride Detection and Cell Imaging. *Chem. Commun.* **2013**, *49*, 2494 – 2496.

432. Hu, B.; Lu, P.; Wang, Y. A highly Selective and Real-Time Ratiometric Fluorescent Chemosensor for Fluoride Anion Detection under Either Neutral or Basic Condition. *Sens. Actuators, B* **2014**, *195*, 320 − 323.

433. Jun, E. J.; Swamy, K. M. K.; Bang, H.; Kim, S.-Jin Anthracene Derivatives Bearing Thiourea Group as Fluoride Selective Fluorescent and Colorimetric Chemosensors. *Tetrahedron Lett.* **2006**, *47*, 3103 − 3106.

434. Watkinson, A. J.; Murby, E. J.; Kolpin, D. W.; Costanzo, S. D. The Occurrence of Antibiotics in an Urban Watershed: From Wastewater to Drinking Water. *Sci. Total Environ.* **2009**, *407*, 2711−2723.

435. Carlson, K.; Kim, S. C. Occurrence of Ionophore Antibiotics in Water and Sediments of a Mixed-landscape Watershed. *Water Res.* **2006**, *40*, 2549−2560.

436. Larsson, D. G. J.; de Pedro, C.; Paxeus, N. Effluent from Drug Manufacturers Contains Extremely High Levels of Pharmaceuticals. *J. Hazard. Mater.* **2007**, *148*, 751– 755.

437. Langford, K. H.; Thomas, K. V. Determination of Pharmaceutical Compounds in Hospital Effluents and their Contribution to Wastewater Treatment Works. *Environ. Int*. **2009**, *35*, 766–770.

438. Giger, W.; Alder, A. C.; Golet, E. M.; Kohler, H. P. E.; McArdell, C. S.; Molnar, E.; Siegrist, H.; Suter, M. J. F. Occurrence and Fate of Antibiotics as Trace Contaminants in Wastewaters, Sewage Sludges, and Surface Waters. *Chimia*. **2003**, *57*, 485–491.

439. Kim, S.-C.; Carlson, K. Temporal and Spatial Trends in The Occurrence of Human and Veterinary Antibiotics in Aqueous and River Sediment Matrices. *Environ. Sci. Technol*. **2007**, *41*, 50–57.

440. Thiele-Bruhn, S. Pharmaceutical Antibiotic Compounds in Soils - A Review. *J. Plant Nutr. Soil Sci.* **2003**, *166*, 145−167.

441. Elmolla, E. S.; Chaudhuri, M. Degradation of Amoxicillin, Ampicillin and Cloxacillin Antibiotics in Aqueous Solution by the UV/ZnO Photocatalytic Process. *J. Hazard. Mater*. **2010**, *173*, 445–449.

442. Luo, Y.; Mao, D. Q.; Rysz, M.; Zhang, H. J.; Xu, L.; Alvarez, P. J. J. Trends In Antibiotic Resistance Genes Occurrence in the Haihe River, China. *Environ. Sci. Technol*. **2010**, *44*, 7220–7225.

443. Chee-Sandford, J. C.; Mackie, R. I.; Koike, S.; Krapac, I. G.; Lin, Y.-F.; Yannarell, A. C.; Maxwell, S.; Aminov, R. I. Fate and Transport of Antibiotic Residues and Antibiotic

Resistance Genes Following Land Application of Manure Waste. *J. Environ. Qual*. **2009**, *38*, 1086–1108.

444. Richardson, M.L.; Bowron, J.M. The fate of pharma-ceutical chemicals in the aquatic environment. *J. Pharm. Pharmacol*. **1985**, *37*, 1–12.

445. Rabølle, M.; Spliid, N. H. Sorption and mobility of metronidazole, olaquindox, oxytetracycline and tylosin in soil. *Chemosphere* **2000**, *40*, 715–722.

446. Daeseleire, E.; Ruyck, H.; Van Renterghem, R. Rapid Confirmatory Assay for the Simultaneous Detection of Ronidazole, Metronidazole and Dimetridazole in Eggs Using Liquid Chromatography–Tandem Mass Spectrometry. *Analyst* **2000**, *125*, 1533–1535.

447. Prados-Joya, G.; Sánchez-Polo, M.; Rivera-Utrilla, J.; Ferro-garcía, M. Photodegradation of the Antibiotics Nitroimidazoles in Aqueous Solution by Ultraviolet Radiation. *Water Res*. **2011**, *45*, 393–403.

448. Shemer, H.; Kunukcu, Y. K.; Linden, K. G. Degradation of the Pharmaceutical Metronidazole via UV, Fenton and Photo-Fenton processes. *Chemosphere* **2006**, *63*, 269–276.

449. Johnson, M. B.; Mehrvar, M. Aqueous Metronidazole Degradation by UV/H_2O_2 Process in Single-and Multi-Lamp Tubular Photoreactors: Kinetics and Reactor Design. *Ind. Eng. Chem. Res*. **2008**, *47*, 6525–6537.

450. Alexy, R.; Kümpel, T.; Kümmerer, K. Assessment of Degradation of 18 Antibiotics in the Closed Bottle Test. *Chemosphere* **2004**, *57*, 505–512.

451. Kümmerer, K.; Al-Ahmad, A.; Mersch-Sundermann, V. Biodegradability of some Antibiotics, Elimination of the Genotoxicity and Aection of Wastewater Bacteria in a Simple Test. *Chemosphere* **2000**, *40*, 701–710.

452. Ingerslev, F.; Toräng, L.; Loke, M. L.; Halling-Sørensen, B.; Nyholm, N. Primary Biodegradation of Veterinary Antibiotics in Aerobic and Anaerobic Surface Water Simulation Systems. *Chemosphere* **2001**, *44*, 865–872.

453. Tong, L.; Pérez, S.; Gonçalves, C.; Alpendurada, F.; Wang, Y.; Barceló, D. Kinetic and Mechanistic Studies of the Photolys is of Met Ronidazole in Simulated Aqueous Environmental Matrices Using a Mass Spectrometric Approach. *Anal. Bioanal. Chem*. **2011**, *399*, 421–428.

454. Liu, J.; Zhang, G.; Jimmy C. Yu, J. C.; Guo, Y. In Situ Synthesis of Zn_2GeO_4 Hollow Spheres and their Enhanced Photocatalytic Activity for the Degradation of Antibiotic Metronidazole. *Dalton Trans*. **2013**, *42*, 5092–5099.

455. Dong, S.; Sun, J.; Li, Y.; Yu, C.; Li, Y.; Sun, J. $ZnSnO_3$ Hollow Nanospheres/Reduced Graphene Oxide Nanocomposites as High-Performance Photocatalysts for Degradation of Metronidazole. *Appl. Catal., B* **2014**, *144*, 386–393.

456. Fang, Z.; Qiu, X.; Chen, J.; Qiu, X. Degradation of Metronidazole by Nanoscale Zero-Valent Metal Prepared from Steel Pickling Waste Liquor. *Appl. Catal., B* **2010**, *100*, 221–228.

457. Zollinger, H. Synthesis, Properties and Applications of Organic Dyes and Pigments. Colour Chemistry, John Wiley e VCH Publishers, New York, 2002, pp. 92–100.

458. Hu, C.; Wang, Y. Z. Decolorization and biodegradability of photocatalytic treated azo dyes and wool textile wastewater. *Chemosphere* **1999**, *39*, 2107–2115.

459. Li, J.; Xu, Y.; Liu, Y.; Wu, D.; Sun, Y. Synthesis of Hydrophilic ZnS Nanocrystals and their Application in Photocatalytic Degradation of Dye Pollutants. *Chin. Particuol.* **2004**, *2*, 266–269.

460. Borker, P.; Salker, A. V. Photocatalytic Degradation of Textile Azo Dye Over $Ce_{1-x}Sn_xO_2$ Series. *Mater. Sci. Eng. B* **2006**, *133*, 55–60.

461. Buvaneswari, N.; Kannan, C. Plant toxic and Non-Toxic Nature of Organic Dyes through Adsorption Mechanism on Cellulose Surface. *J. Hazard. Mater.* **2011**, *189*, 294–300.

462. Patil, S. S.; Shlnde, V. M. Biodegradation Studies of Aniline and Nitrobenzene in Aniline Plant Waste Water by Gas Chromatography, *Environ. Scl. Technol.* **1988**, *22*, 1160–1165.

463. Moore, A. T.; Vira, A.; Fogel, S. Biodegradation of Trans-l,2-Dichloroethylene by Methane-Utilizing Bacteria in an Aquifer Simulator. *Environ. Sci. Technol.* **1989**, *23*, 403–406.

464. Slokar, Y. M.; Marechal, A. M. L. Methods of Decoloration of Textile Wastewaters, *Dyes Pigments.* **1998**, *37*, 335–356.

465. Hoffmann, M. R.; Martin, S. T.; Choi, W.; Bahneman, D. W. Environmental Applications of Semiconductor Photocatalysis. *Chem. Rev.* **1995**, *95*, 69–96.

466. Xiao, Q.; Si, Z.; Zhang, J.; Xiao, C.; Tan, X. Photoinduced Hydroxyl Radical and Photocatalytic Activity of Samarium-Doped TiO_2 Nanocrystalline. *J. Hazard. Mater.* **2008**, *150*, 62–67.

467. Xiao, Q.; Zhang, J.; Xiao, C.; Si, Z.; Tan, X. Solar Photocatalytic Degradation of Methylene Blue in Carbon-Doped TiO_2 Nanoparticles Suspension. *Solar Energy*, **2008**, *82*, 706–713.

468. Chauhan, R.; Kumar, A.; Chaudhary, R. P. Visible-Light Photocatalytic Degradation of Methylene Blue with Fe Doped CdS Nanoparticles. *Appl. Surf. Sci.* **2013**, *270*, 655–660.

469. Lv, Y.; Ding, Y.; Zhou, J.; Xiao, W.; Feng, Y. Preparation, Characterization, and Photocatalytic Activity of N, S-Codoped TiO_2 Nanoparticles. *J. Am. Ceram. Soc.* **2009**, *92*, 938–941.

470. Pouretedal, H. R.; Norozi, A.; Keshavarz, M. H.; Semnani, A. Nanoparticles of Zinc Sulfide Doped with Manganese, Nickel and Copper as Nanophotocatalyst in the Degradation of Organic Dyes. *J. Hazard. Mater.* **2009**, *162*, 674–681.

471. Di, L.; Xu, Z.; Wang, K.; Zhang, X. A Facile Method for Preparing Pt/TiO_2 Photocatalyst with Enhanced Activity using Dielectric Barrier Discharge. *Catal. Today* **2013**, *211*, 109–113.

472. Lin, Y.; Jiang, Z.; Zhu, C.; Hu, X.; Zhang, X.; Zhu, H.; Fan, J.; Lin, S. H. Electronic and Optical Performances of Si and Fe-Codoped TiO_2 Nanoparticles: A Photocatalyst for the Degradation of Methylene blue. *Appl. Catal., B* **2013**, *142–143*, 38–44.

473. Tang, Y.; Di, W.; Zhai, X.; Yang, R.; Qin, W. NIR-Responsive Photocatalytic Activity and Mechanism of $NaYF_4$:Yb,Tm@TiO_2 Core–Shell Nanoparticles. *ACS Catalysis*, **2013**, *3*, 405–412.

474. Hamal, D. B.; Klabunde, K. J. Synthesis, Characterization, and Visible Light Activity of New Nanoparticle Photocatalysts Based on Silver, Carbon, and Sulfur-Doped TiO_2. *J. Colloid Interface Sci.* **2007**, *311*, 514-522.

475. Zhang, H.; Wang, G.; Chen, D.; Lv, X.; Li, J. Tuning Photoelectrochemical Performances of $Ag-TiO_2$ Nanocomposites via Reduction/Oxidation of Ag. *Chem. Mater.* **2008**, *20,* 6543–6549.

476. Ni, Y.; Zhu, Y.; Ma, X. A Simple Solution Combustion Route for the Preparation of Metal-Doped TiO_2 Nanoparticles and their Photocatalytic Degradation Properties. *Dalton Trans.* **2011**, *40*, 3689-3694.

477. Kumar, K.; Chitkara, M.; Sandhu, I. S.; Mehta, D.; Kumar, S. Photocatalytic, Optical and Magnetic Properties of Fe-Doped ZnO Nanoparticles Prepared by Chemical Route. *J. Alloys Compd.* **2014**,*588*, 681-689.

478. Bayal, N.; Jeevanandam, P. Sol–Gel Synthesis of SnO_2–MgO Nanoparticles and Their Photocatalytic Activity Towards Methylene Blue Degradation. *Mater. Res. Bull.* **2013**, *48*, 3790-3799.

479. Esparza, P.; Hernández, T.; Borges, M. E.; Álvarez-Galván, M. C.; Ruiz-Morales, J. C.; Fierro, J. L. G. TiO$_2$ Modifications by Hydrothermal Treatment and Doping to Improve its Photocatalytic Behaviour Under Visible Light. *Catal. Today* **2013**, *210*, 135-141.

480. Jiang, X., Yang, L., Liu, P., Li, X. & Shen, J. The Photocatalytic and Antibacterial Activities of Neodymium and Iodine Doped TiO$_2$ Nanoparticles. *Colloids surf., B* **2010**, *79*, 69-74.

481. Wang, Q.; Jiang, Z.; Wang, Y.; Chen, D.; Yang, D. Photocatalytic Properties of Porous C-doped TiO$_2$ and Ag/C-Doped TiO$_2$ Nanomaterials by Eggshell Membrane Templating. *J. Nanopart. Res.* **2009**, 11, 375-384.

482 Zeng, H.; Cai, W.; Liu, P.; Xu, X.; Zhou, H.; Klingshirn, C.; Kalt, H. ZnO-Based Hollow Nanoparticles by Selective Etching: Elimination and Reconstruction of MetalSemiconductor Interface, Improvement of Blue Emission and Photocatalysis. *ACS Nano* **2008**, *2*, 1661-1670.

483. He, W.; Kim, H. k.; Wamer, W. G.; Melka, D.; Callahan, J. H. Photogenerated Charge Carriers and Reactive Oxygen Species in ZnO/Au Hybrid Nanostructures with Enhanced Photocatalytic and Antibacterial Activity. *J. Am. Chem. Soc.* **2014**, *136*, 750 - 757.

484. Jose, R.; Thavasi, V.; Ramakrishna, S. Metal Oxides for Dye-Sensitized Solar Cells. *J. Am. Ceram. Soc.* **2009**, *301*, 289-301.

485. Guo, J.; She, C.; Lian, T. Ultrafast Electron Transfer between Conjugated Polymer and Antimony-Doped Tin Oxide (ATO) Nanoparticles. *J. Phys. Chem. C* **2008**, *112*, 4761-4766.

486. Tubtimtae, A.; Arthayakul, K.; Teekwang, B.; Hongsith, K. MnTe Semiconductor-Sensitized Boron-Doped TiO$_2$ and ZnO Photoelectrodes for Solar Cell Applications. *J. Colloid Interface Sci.* **2013**, *405*, 78-84.

487. Reddy, A. L. M.; Shaijumon, M. M.; Gowda, S. R.; Ajayan, P. M. Coaxial MnO$_2$/Carbon Nanotube Array Electrodes for High-Performance Lithium Batteries. *Nano Lett.* **2009**, *9*, 1002-1006.

488. Chan, C. K.; Peng, H.; Twesten, R. D.; Jarausch, K. Zhang, X. F.; Cui, Y. Fast, Completely Reversible Li Insertion in Vanadium Pentoxide Nanoribbons. *Nano* Lett **2007**, *7*, 490-495.

489. Kimura, T., Dong, Q.; Yin, S.; Hashimoto, T.; Sasaki, A.; Sato, T. Synthesis and Piezoelectric Properties of Li-doped $BaTiO_3$ by a Solvothermal Approach. *J. Eur. Ceram. Soc.* **2013**, *33*, 1009-1015.

490. Yang, Q.; Guo, X.; Wang, W.; Zhang, Y.; Xu, S.; Lien, D. H.; Wang, Z. L. Enhancing Sensitivity of a Single ZnO Micro-/Nanowire Photodetector by Piezo-phototronic Effect. *ACS Nano* **2010**, *4*, 6285-6291.

491. Kamat, P.V. Graphene-Based Nanoarchitectures. Anchoring Semiconductor and Metal Nanoparticles on a Two-Dimensional Carbon Support. *J. Phys. Chem. Lett.* **2010**, *1*, 520–527.

492. Sun, Y. F.; Liu, S. B.; Meng, F. L.; Liu, J. Y.; Jin, Z.; Kong, L. T.; Liu, J. H. Metal Oxide Nanostructures and Their Gas Sensing Properties: A Review. *Sensors* **2012**, *12*, 2610-2631.

493. Hassan, H. S.; Kashyout, A. B.; Soliman, H. M. A.; Uosif, M. A.; Afify, N. Effect of Reaction Time and Sb Doping Ratios on the Architecturing of ZnO Nanomaterials for Gas Sensor Applications. *Appl. Surf. Sci.* **2013**, *277*, 73-82.

494. Zaleska, A. Doped-TiO_2: A Review. *Rec. Patents Eng.* **2008**, *2*, 157-164.

495. Liu, Y.; Li, J.; Zhou, B.; Chen, H.; Wang, Z.; Cai, W. A TiO_2-Nanotube-Array-Based Photocatalytic Fuel Cell using Refractory Organic Compounds as Substrates for Electricity Generation. *Chem. Commun.* **2011**, *47*, 10314–10316.

496. Wang, W.; Zhang, J.; Chen, F.; He, D.; Anpo, M. Preparation and Photocatalytic Properties of Fe^{3+}-Doped Ag@TiO_2 Core–shell Nanoparticles. *J. colloid interface sci.* **2008**, *323*, 182-186.

497. Deng, Q. R.; Xia, X. H.; Guo, M. L.; Gao, Y.; Shao, G. Mn-doped TiO_2 Nanopowders with Remarkable Visible Light Photocatalytic Activity. *Mater. Lett.* **2011**, *65*, 2051-2054.

498. Behnajady, M. A.; Alizade, B.; Modirshahla, N. Synthesis of Mg-Doped TiO2 Nanoparticles under Different Conditions and its Photocatalytic Activity. *Photochem. photobiol.* **2011**, *87*, 1308-1314.

499. Xiao, Q.; Si, Z.; Yu, Z.; Qiu, G. Sol–gel Auto-combustion Synthesis of Samarium-Doped TiO2 Nanoparticles and their Photocatalytic Activity under Visible Light Irradiation. *Mater. Sci. Eng. B* **2007**, *137*, 189-194.

500. Hewer, T. L. R.; Souza, E. C. C.; Martins, T. S.; Muccillo, E. N. S.; Freire, R. S. Influence of Neodymium Ions on Photocatalytic Activity of TiO_2 Synthesized by Sol–gel and Precipitation Methods. *J. Mol. Catal., A* **2011**, *336*, 58-63.

501. Ji, L.; Wang, Z.; Li, Z.; Liang, J. Preparation of Aligned Titania Nanowires with an Aligned Carbon Nanotube Composite Template. *Mater. Lett.* **2008**, *62,* 1979-1982.

502. Grandcolas, M.; Ye, J.; Hanagata, N. Combination of Photocatalytic and Antibacterial Effects of Silver Oxide Loaded on Titania Nanotubes. *Mater. Lett.* **2011**, *65*, 236-239.

503. Zhang, Y.; Gao, Y.; Xia, X. H.; Deng, Q. R.; Guo, M. L.; Wan, L.; Shao, G. Structural Engineering of Thin Films of Vertically Aligned TiO_2 Nanorods. *Mater. Lett.* **2010**, *64*, 1614-1617.

504. Morey, M. S.; Bryan, J. D.; Schwarz, S.; Stucky, G. D. Pore Surface Functionalization of MCM-48 Mesoporous Silica with Tungsten and Molybdenum Metal Centers: Perspectives on Catalytic Peroxide Activation. *Chem. Mater.* **2000**, *12*, 3435-3444.

505. Okada, K.; Shimai, A.; Takei, T.; Hayashi, S.; Yasumori, A.; MacKenzie, K. J. D. Preparation of Microporous Silica From Metakaolinite by Selective Leaching Method. *Microporous Mesoporous Mater.* **1998**, *21*, 289-296.

506. Cochran, J. K. Ceramic Hollow Spheres and their Applications. *Curr. Opin. Solid State Mater. Sci.* **1998**, *3*, 474 –479.

507. Syoufian, A.; Inoue, Y.; Yada, M.; Nakashima, K. Preparation of Submicrometer-Sized Titania Hollow Spheres by Templating Sulfonated Polystyrene Latex Particles. *Mater. Lett.* **2007**, *61*, 1572-1575.

508. Cui, L.; Wang, Y.; Niu, M.; Chen, G.; Cheng, Y. Synthesis and visible light photocatalysis of Fe-doped TiO_2 mesoporous layers deposited on hollow glass microbeads. *J. Solid State Chem.* **2009**, *182*, 2785-2790.

509. Wang, C.; Ao, Y.; Wang, P.; Hou, J.; Qian, J. Preparation, Characterization and Photocatalytic Activity of the Neodymium-Doped TiO_2 Hollow Spheres *J. Appl. Surf. Sci.* **2010**, *257*, 227-231.

510. Wang, C.; Ao, Y.; Wang, P.; Hou, J.; Qian, J. Preparation of Cerium and Nitrogen Co-Doped Titania Hollow Spheres with Enhanced Visible Light Photocatalytic Performance. *Powder Technol.* **2011**, *210*, 203-207.

511. Wang, P.; Wu, J.; Ao, Y.; Wang, C.; Hou, J.; Qian, J. Preparation and Enhanced Photocatalytic Performance of Sn Ion Modifi ed Titania Hollow Spheres. *Mater. Lett.* **2011**, *65*, 3278-3280.

512. Xu, J.; Chen, M.; Fu, D. Study on Highly Visible Light Active Bi-Doped TiO_2 Composite Hollow Sphere. *Appl. Surf. Sci.* **2011**, *257*, 7381-7386.

513. An, G.; Yang, C.; Jin, S.; Chen, G.; Zhao, X. Hollow TiO_2:Sm^{3+} Spheres with Enhanced Photoluminescence Fabricated by a Facile Method using Polystyrene as Template. *J. Mater. Sci.* **2013**, *48*, 5483-5488.

514. Chaudhuri, R.G.; Paria, S. Visible Light Induced Photocatalytic Activity of Sulfur Doped Hollow TiO_2 Nanoparticles, Synthesized Via a Novel Route. *Dalton Trans.* **2014**, *43*, 5526-5534.

515. Awazu, K.; Fujimaki, M.; Rockstuhl, C.; Tominaga, J.; Murakami, H.; Ohki, Y.; Yoshida, N.; Watanabe, T. A Plasmonic Photocatalyst Consisting of Silver Nanoparticles Embedded in Titanium Dioxide. *J. Am. Chem. Soc.* **2008**, *130*, 1676-1680.

516. Tian, Y.; Tatsuma, T. Mechanisms and Applications of Plasmon-Induced Charge Separation at TiO_2 Films Loaded with Gold Nanoparticles. *J. Am. Chem. Soc.* **2005**, *127*, 7632-7637.

517. Smetana, A. B.; Klabunde, K. J.; Marchin, G. R.; Sorensen, C. M. Biocidal Activity of Nanocrystalline Silver Powders and Particles. *Langmuir* **2008**, *24*, 7457-7464.

518. Li, Q.; Mahendra, S.; Lyon, D. Y.; Brunet, L.; Liga, M. V.; Li, D.; Alvarez, P. J. J. Antimicrobial Nanomaterials for Water Disinfection and Microbial Control: Potential Applications and Implications. *Water res.* **2008**, *42*, 4591-602.

519. Xiang, Q.; Yu, J.; Cheng, B.; Ong, H. C. Microwave-Hydrothermal Preparation and Visible-Light Photoactivity of Plasmonic Photocatalyst Ag-TiO_2 Nanocomposite Hollow Spheres *Chem. Asian J.* **2010**, *5*, 1466 – 1474.

520. Song, C.; Wang, D.; Gu, G.; Lin, Y.; Yang, J.; Chen, L.; Fu, X.; Hu, Z. Preparation and Characterization of Silver/TiO_2 Composite Hollow Spheres. *J. colloid interface sci.* **2004**, *272*, 340-344.

521. Ji, P. L.; Kong, X. Z.; Wang, J. G.; Zhu, X. L. Characterization and Photocatalytic Properties of Silver and Silver Chloride Doped TiO_2 Hollow Nanoparticles. *Chin. Chem. Lett.* **2012**, *23*, 1399-1402.

522. Guo, H.; Tian, D.; Liu, L.; Wang, Y.; Guo, Y.; Yang, X. Core–shell TiO_2 Microsphere with Enhanced Photocatalytic Activity and Improved Lithium Storage. *J. Solid State Chem.* **2013**, *201*, 137-143.

523. Karan, N.S.; Agrawal, A.; Pandey, P. K.; Smitha, P.; Sharma, S. J.; Mishra, D. P.; Gajbhiye, N. S. Diffusion Flame Synthesis of Hollow , Anatase TiO_2 Nanoparticles. *Mater. Sci. Eng., B* **2009**, *163,* 128–133.

524. Li, X.; Lv, K.; Deng, K.; Tang, J.; Su, R.; Sun, J.; Chen, L. Synthesis and Characterization of ZnO and TiO_2 Hollow Spheres with Enhanced Photoreactivity. *Mater. Sci. Eng., B* **2009**, *158*, 40–47.

525. Song, C.; Yu, W.; Zhao, B.; Zhang, H.; Tang, C.; Sun, K.; Wu, X.; Dong, L.; Chen, Y. Efficient Fabrication and Photocatalytic Properties of TiO_2 Hollow Spheres. *Catal. Commun.* **2009**, *10*, 650-654.

526. Zhang, F.; Zhang, Y.; Song, S.; Zhang, H. Superior Electrode Performance of Mesoporous Hollow TiO_2 Microspheres Through Efficient Hierarchical Nanostructures. *J. Power Sources* **2011**, *196*, 8618-8624.

527. Ray, M. Paria, S. Growth Kinetics of Silver Bromide Nanoparticles in Aqueous Nonionic Surfactant Solutions. *Ind. Eng. Chem. Res.* **2011**, *50*, 11601-11607.

528. Kawamura, G.; Sato, S.; Muto, H.; Sakai, M.; Lim, P. B.; Watanabe, K.; Inoue, M.; Matsuda, A. AgBr Nanocrystal-Dispersed Silsesquioxane– Titania hybrid Films for Holographic Materials. *Mater. Lett.* **2010**, *64*, 2648-2651.

529. Behnajady, M. A.; Eskandarloo, H.; Modirshahla, N.; Shokri, M. Investigation of the Effect of Sol – gel Synthesis Variables on Structural and Photocatalytic Properties of TiO_2 Nanoparticles. *Desalination* **2011**, *278*, 10-17.

530. Du, J.; Zhang, J.; Liu, Z.; Han, B.; Jiang, T.; Huang, Y. Controlled Synthesis of Ag/TiO_2 Core-Shell Nanowires with Smooth and Bristled Surfaces via a One-Step Solution Route. *Langmuir* **2006**, *22*, 1307-1312.

531. Boxi, S. S.; Paria, S. Effect of Silver Doping on TiO_2, CdS, and ZnS Nanoparticles for the Photocatalytic Degradation of Metronidazole under Visible Light. *RSC Adv.* **2014**, *4*, 37752-37760.

532. Hoffmann, M. R.; Martin, S. T.; Choi, W.; Bahnemannt, D. W. Environmental Applications of Semiconductor Photocatalysis. *Chem. Rev.* **1995**, *95*, 69-96.

533. Choi, W.; Termin, A.; Hoffmann, M. R. The Role of Metal Ion Dopants in Quantum-Sized TiO_2: Correlation between Photoreactivity and Charge Carrier Recombination Dynamics. *J. Phys. Chem.* **1994**, *98*, 13669-13679.

534. Liqiang, J.; Honggang, F.; Baiqi, W.; Dejun, W.; Baifu, X.; Shudan, L.; Jiazhong, S. Effects of Sn Dopant on the Photoinduced Charge property and Photocatalytic Activity of TiO_2 Nanoparticles. *Appl. Catal., B* **2006**, *62*, 282-291.

535. Shen, X. –Z.; Liu, Z. –C.; Xie, S. –M.; Guo, J. Degradation of Nitrobenzene using Titania Photocatalyst Co-doped with Nitrogen and Cerium under Visible Light Illumination. *J. Hazard. Mater.* **2009**, *162*, 1193–1198.

536. Whang, T. –J.; Hsieh, M. –T.; Shi, T. –E.; Kuei, C. –H. UV-Irradiated Photo catalytic Degradation of Nitrobenzene by Titania Binding on Quartz Tube. *Int. J. Photoenergy.* **2012**, 1-8, doi:10.1155/2012/681941.

537. Tayade, R. J.; Kulkarni, R. G.; Jasra, R. V. Photocatalytic Degradation of Aqueous Nitrobenzene by Nanocrystalline TiO_2. *Ind. Eng. Chem. Res.* **2006**, *45*, 922-927.

538. Ellappan, P.; Miranda, L. R. Synthesis and Characterization of Cerium Doped Titanium Catalyst f or the Degradation of Nitrobenzene Using Visible Light. *Int. J. Photoenergy*. **2014**, 1-9, doi:10.1155/2014/756408.

539. Baeissa, E. S. $Pt/Cd_2Sb_2O_{6.8}$ Nanoparticles for Efficient Visible Light Photocatalysis. *Ceram. Int.* **2014**, *40*, 7195-7201.

540. Shen, X.; Zhu, L.; Wang, N.; Zhang, T.; Tang, H. Selective Photocatalytic Degradation of Nitrobenzene Facilitated by Molecular Imprinting with a Transition State Analog. *Catal. Today* **2014**, *225*, 164–170.

541. Hajipour, M. J.; Fromm, K. M.; Ashkarran, A. A.; Aberasturi, D. J. d.; Larramendi, I. R. d.; Rojo, T.; Serpooshan, V.; Parak, W. J.; Mahmoudi, M. Antibacterial Properties of Nanoparticles. *Trends Biotechnol.* **2012**, *30*, 499-511.

542. Li, Q.; Mahendra, S.; Lyon, D. Y.; Brunet, L.; Liga, M. V.; Li, D.; Alvarez, P. J. J. Antimicrobial Nanomaterials for Water Disinfection and Microbial Control: Potential Applications and Implications. *Water Res.* **2008**, *42*, 4591–4602.

543. Raffi, M.; Mehrwan, S.; Bhatti, T. M.; Akhter, J. I.; Hameed, A.; Yawar, W.; Hasan, M. M. Investigations into the antibacterial behavior of copper nanoparticles against *Escherichia coli. Ann. Microbiol*. **2010**, *60*, 75–80.

544. Kim, J. S.; Kuk, E.; Yu, K. N.; Kim, J. H.; Lee, H. J.; Kim, S. H.; Park, Y. K.; Hwang, C. Y.; Kim, Y. K.; Lee, Y. S.; Jeong, D. H.; Cho, M. H. Antimicrobial effects of silver nanoparticles. *Nanomed. Nanotechnol., Biol. Med.*, **2007**, *3*, 95–101.

545. Gong, P.; Li, H.; He, X.; Wang, K.; Hu, J.; Tan, W.; Zhang, S.; Yang, X. Preparation and Antibacterial Activity of $Fe_3O_4@Ag$ Nanoparticles. *Nanotechnology* **2007**. *18*, 285604.

546. Yasa, I.; Lkhagvajav, N.; Koizhaiganova, M.; Celik, E.; Sarı, O.; Assessment of Antimicrobial Activity of Nanosized Ag Doped TiO_2 Colloids. *World J. Microb. Biot.* **2012**, *28*, 2531–2539.

547. Rupa, V.; Manikandan, D.; Divakar, D.; Sivakumar, T. Effect of Deposition of Ag on TiO_2 Nanoparticles on the Photodegradation of Reactive Yellow-17. *J. Hazard. Mater.* **2007**, *147*, 906–913.

548. Gupta, K.; Singh, R. P.; Pandey A.; Pandey, A. Photocatalytic Antibacterial Performance of TiO$_2$ and Ag-Doped TiO$_2$ Against *S. aureus*. *P. aeruginosa* and *E. coli. Beilstein J. Nanotechnol.* **2013,** *4,* 345–351.

549. Lin, Y.; Qiqiang,W.; Xiaoming, Z.; Zhouping, W.; Wenshui, X.; Yuming, D. Synthesis of Ag/TiO$_2$ Core/Shell Nanoparticles with Antibacterial Properties. *Bull. Korean Chem. Soc.* **2011**, *32*, 2607-10.

550. Sun, S. Q.; Sun, B.; Zhang, W.; Wang, D.; Preparation and Antibacterial Activity of Ag–TiO$_2$ Composite Film by Liquid Phase Deposition (LPD) Method. *Bull. Mater. Sci.***2008**, *31*, 61–66.

551. Hwang, E. T.; Lee, J. H.; Chae, Y. J.; Kim, Y. S.; Kim, B. C.; Sang, B. I.; Gu, M.B. Analysis of Toxic Mode of Action of Silver Nanoparticles Using Stress-Specific bioluminescent bacteria. *Small* **2008**, *4*, 746-750.

552. Kim, J. S.; Kuk, E.; Yu, K. N.; Kim, J.-H.; Park, S. J.; Lee, H. J.; Kim, S. H.; Park, Y. K.; Park, Y. H.; Hwang, C.-Y.; Kim, Y.-K.; Lee, Y.-S.; Jeong, D. H.; Cho, M.-H. Antimicrobial Effects of silver Nanoparticles. *Nanomed.: Nanotech. Biol. Med.* **2007,** *3,* 95–101.

553. Steponkus, P. L., Lanphear, F. O. Refinement of the Triphenyl Tetrazolium Chloride Method of Determining Cold Injury. *Plant Physiol*. **1967**, *42*, 1423-1426.

554. Radheshkumar, C.; Münstedt, H. Antimicrobial Polymers from Polypropylene/Silver Composites—Ag$^+$ Release Measured by Anode Stripping Voltammetry. *React. Funct. Polym.* **2006**, *66*, 780–788.

555. Klueh, U.; Wagner, V.; Kelly, S.; Johnson, A.; Bryers, J. D. Efficacy of Silver-Coated Fabric to Prevent Bacterial Colonization and Subsequent Device-Based Biofilm Formation. *J Biomed. Mater. Res. Part B Appl. Biomater.* **2000**, *53*, 621-631.

556. Davies, R. L.; Etris, S. F. The Development and Functions of Silver in Water Purification and Disease Control. *Catal. Today* **1997**, *36*, 107-114.

557. Duarte, M. L. R.; Archer, S. A. *In Vitro* Toxin Production by *Fusarium solani* f. sp. *piperis. Fitopatol. Bras.* **2003**, *28*, 229-235.

558. Medentsev, A. G.; Akimenko, V. K. Mechanism of Phytotoxic Action of Naphthoquinone Pigments of the Fungus *Fusarium decemcellulare*. *Phytochemistry* **1992**, *31*, 77-79.

559. Nemec, S.; Phelps, D.; Baker, R. Effect of Dihydrofusarubin and Isomatricin from *Fusarium Solani* on Carbohydrate STatus and Metabolism of rough Lemon Seedling. *Phytopathology*, **1989**, *79*, 6, 700-705.

560.   Costa, B.; Nahas, C. Growth and Enzymatic Responses of Phytopathogenic Fungi to Glucose in Culture Media and Soil. *Braz. J. microbiol.* **2012**, *43*, 332-340.

561.   Luo, L.; Chen, H.; Zhang, L.; Xu, K.; Lv, Y. A Cataluminescence Gas Sensor for Carbon Tetrachloride Based on Nanosized ZnS. *Analytica Chimica Acta* **2009**, *635*, 183–187.

562.   Tong, H.; Zhu, Y. -J.; Yang, L. -X.; Li, L.; Zhang, L.; Chang, J.; An, L. -Q.; Wang, S. -W. Self-Assembled ZnS Nanostructured Spheres：Controllable Crystal Phase and Morphology. *J. Phys. Chem. C* **2007**, *111*, 3893-3900.

563.   Toyama, T.; Yoshimura, K.; Fujii, M.; Haze, H.; Okamoto, H. Novel Green Thin-Film Electroluminescent Devices Utilizing ZnS Nanocrystals Doped with Tb Compounds. *Appl. Surface Sci.* **2005**, *244*, 524-527.

564.   Wang, Q.; Chen, G.; Zhou, C.; Jin, R.; Wang, L. Sacrificial Template Method for the Synthesis of CdS Nanosponges and their Photocatalytic Properties. *J. Alloys Compd.* **2010**, *503*, 485-489.

565.   Liu, S. -M.; Guo, H. -Q.; Zhang, Z. -H.; Li, R.; Chen, W.; Zhan-Guo Wang, Z. -G. Characterization of CdSe and CdSe/CdS Core/Shell Nanoclusters Synthesized in Aqueous Solution. *Physica E* **2000**, *8*, 174-178.

566.   Peng, X.; Schlamp, M. C.; Kadavanich, A. V.; Alivisatos, A. P. Epitaxial Growth of Highly Luminescent CdSe/CdS Core/Shell Nanocrystals with Photostability and Electronic Accessibility. *J. Am. Chem. Soc.* **1997**, *119,* 7019-7029.

567.   Shao, M.; Li, Q.; Xie, B.; Wu, J.; Qian, Y. The Synthesis of CdS/ZnO and CdS/Pb_3O_4 Composite Materials Via Microwave Irradiation. *Mater. Chem. Phys.* **2002**, *78*, 288-291.

568.   Zhang, J.; Xiao, M.; Liu, Z.; Han, B.; Jiang, T.; He, J.; Yang, G. Preparation of ZnS/CdS Composite Nanoparticles by Coprecipitation from Reverse Micelles using CO_2 as Antisolvent. *J. Colloid Interface Sci.* **2004**, *273*, 160-164.

469.   Malik, M. A.; Brien, P. O.; Revaprasadu, N. A. Simple Route to the Synthesis of Core/Shell Nanoparticles of Chalcogenides. *Chem. Mater.* **2002**, *14*, 2004-2010.

570.   Caruso, R.A.; Antonietti, M. Sol-Gel Nanocoating：An Approach to the Preparation of Structured Materials. C*hem. Mater.* **2001**, *13,* 3272-3282*.*

571.   Li, F.; Jiang, Y.; Hu, L.; Liu, L.; Li, Z.; Huang, X. Structural and Luminescent Properties of ZnO Nanorods and ZnO/ZnS Nanocomposites. *J. Alloys Compd.* **2009**, *474*, 531-535.

572. Yang, H.; Holloway, P. H. Enhanced Photoluminescence from CdS：Mn/ZnS Core/Shell Quantum Dots. *Appl. Phys. Lett.* **2011**, *82*, 1965-1967.

573. Hines, M.A.; Guyot-sionnest, P. Synthesis and Characterization of Strongly Luminescing ZnS-Capped CdSe Nanocrystals. *J. Phys. Chem.* **1996**, *100*, 468-471.

574. Dabbousi, B.O.; Rodriguez-Viejo, J.; Mikulec, F. V.; Heine, J. R.; Mattoussi, H.; Ober, R.; Jensen, K. F.; Bawendi*et,* M. G. (CdSe)ZnS Core-Shell Quantum Dots：Synthesis and Characterization of a Size Series of Highly Luminescent Nanocrystallites. *J. Phys. Chem. B* **1997**, *101*, 9463-9475.

575. Yang, B. H.; Holloway, P. H. Efficient and Photostable ZnS-Passivated CdS：Mn Luminescent Nanocrystals. *Adv. Funct. Mater.* **2004**, *14*, 152-156.

576. Yang, Y.; Chen, O.; Angerhofer, A.; Cao, Y. C. Radial-Position-Controlled Doping in CdS/ZnS Core/Shell Nanocrystals. *J. Am. Chem. Soc.* **2006**, *128*, 12428-12429 .

577. Thakar, R.; Chen, Y.; Snee, P. T. Efficient Emission from Core/(Doped) Shell Nanoparticles: Applications for Chemical Sensing. *Nano Lett.* **2007**, *7*, 3429-3432.

578. Wang, S.; Jarrett, B. R.; Kauzlarich, S. M.; Louie, A. Y. Core/Shell Quantum Dots with High Relaxivity and Photoluminescence for Multimodality Imaging. *J. Am. Chem. Soc.* **2007**, *129*, 3848-3856.

579. Ithurria, S.; Guyot-sionnest, P.; Mahler, B.; Dubertret, B. Mn^{2+} as a Radial Pressure Gauge in Colloidal Core/Shell Nanocrystals. *Phys. Rev. Lett.* **2007**, *99*, 265501-265504.

580. Archer, P. I.; Santangelo, S. A.; Gamelin, D. R. Inorganic Cluster Syntheses of TM^{2+}-Doped Quantum Dots (CdSe, CdS, CdSe/CdS): Physical Property Dependence on Dopant Locale. *J. Am. Chem. Soc.* **2007**, *129*, 9808-9818.

581. Murugadoss, G. Synthesis of High Quality and Monodisperse CdS：Mn^{2+}/ZnS and CdS：Mn^{2+}/CdS Core–Shell Nanoparticles. *Superlattices Microstruct.* **2012**, *52*, 1026-1042.

582. Chen, O.; Shelby, D. E.; Yang, Y.; Zhuang, J.; Wang, T.; Niu, C.; Omenetto, N.; Cao, Y. C.; Excitation-Intensity-Dependent Color-Tunable Dual Emissions from Manganese-Doped CdS/ZnS Core/Shell Nanocrystals. *Angew. Chem. Int. Ed.* **2010**, *49*, 10132–10135.

583. Ehlert, O.; Osvet, A.; Batentschuk, M.; Winnacker, A.; Nann, T. Synthesis and Spectroscopic Investigations of Cu- and Pb-Doped Colloidal ZnS Nanocrystals. *J. Phys. Chem. B* **2006**, *110*, 23175-23178.

584. Vetrone, F.; Naccache, R.; Mahalingam, V.; Morgan, C. G.; Capobianco, J. A. The Active-Core/Active-Shell Approach: A Strategy to Enhance the Upconversion Luminescence in Lanthanide-Doped Nanoparticles. *Adv. Funct. Mater.* **2009**, *19*, 2924-2929.

585. Raheman, F.; Deshmukh, S.; Ingle, A.; Gade, A.; Rai, M. Article Nano Biomed Eng Silver Nanoparticles : Novel Antimicrobial Agent Synthesized from an Endophytic Fungus Pestalotia sp. Isolated from Leaves of Syzygium cumini (L). *Nano Biomed. Eng.* **2011**, *3*, 174-178.

586. Siekkinen, A.; Xia, Y. Maneuvering the Surface Plasmon Resonance of Silver Nanostructures through Shape-Controlled Synthesis. *J. Phys. Chem. B* **2006**, *110*, 15666-15675.

587. Jiang, Z. -J.; Liu, C. -Y.; Sun, L. -W. Catalytic Properties of Silver Nanoparticles Supported on Silica Spheres. *J. Phys. Chem. B* **2005**, *109*, 1730-1735.

588. Frant, M. S.**;** Ross, J. W. Electrode for Sensing Fluoride Ion Activity in Solution. *Science* **1966**, *154,* 1553-1555.

589. Stefan, R. I.; van Staden, J. F.; Aboul-Enein, H. Y. Determination of Fluoride in Toothpaste, Effluents Streams and Natural and Borehole Water Using a Flow Injection System with a FLuoride-Selective Membrane Electrode. *Pharm. Acta Helv*. **1999**, *73*, 307–310.

590. Ikenishi, R.**;** Kitagawa, T. Gas Chromatographic Method for the Determination of Fluoride ion in Biological Samples. II. Stability of Fluorine-Containing Drugs and Compounds in Human Plasma. *Chem. Pharm. Bull*. **1988**, *36*, 810-814.

591. Culik, B. Microdiffusion and Spectrophotometric Determination of Fluoride in Biological Samples. *Anal. Chim. Acta* **1986**, *189,* 329-337.

592. Watanabe, S.; Seguchi, H.; Yoshida, K.; Kifune, K. Colorimetric Detection of Fluoride Ion in an Aqueous Solution using a Thioglucose-Capped Gold Nanoparticle. *Tetrahedron Lett.* **2005**, *46*, 8827 – 8829.

593. Mulrooney, R. C.; Singh, N.; Kaur, N.; Callan, J. F. An "Off–On" Sensor for Fluoride using Luminescent CdSe/ZnS Quantum Dots. *Chem. Commun.* **2009**, 686 – 688.

594. Jha, G.; Anoop, N.; Rahaman, A.; Sarkar, M. Fluoride Ion Sensing in Aqueous Medium by Employing Nitrobenzoxadiazole-Postgrafted Mesoporous Silica Nanoparticles (MCM-41). *Phys. Chem. Chem. Phys.* **2015**, *17*, 3525 – 3533.

595. Basu, A.; Suryawanshi, A.; Kumawat, B.; Dandi, A.; Guin, D.; Ogale, S. B. Starch (Tapioca) to Carbon Dots: an Efficient Green Approach to an On–Off–On Photoluminescence Probe for Fluoride Ion Sensing. *Analyst* **2015**, *140*, 1837 – 1841.

596. Chaudhuri, R. G.; Paria, S. Optical Properties of Double-Shell Hollow ZnS−Ag₂S Nanoparticles. *J. Phys. Chem. C* **2013**, *117*, 23385−23390.

597. Helen, L.; Johnston, B. A. Rural Health Cooperatives. *Public Health Rep.* **1950**, *65*, 1383 – 1418.

598. Dey, S. K.; Datta, B. K.; Das, G. Binding Discrepancy of Fluoride in Quaternary Ammonium and Alkali Salts by a Tris(Amide) Receptor in Solid and Solution States. *Cryst. Eng. Comm.* **2012**, *14*, 5305–5314.

599. Lin, Q.; Yang, Q.-P.; Sun, B.; Lou, J.-C.; Wei, T.-B.; Zhang, Y.-M. A Highly Selective and Sensitive Fluorescence "Turn-on" Fluoride Ion Sensor. *RSC Adv.* **2015**, *5*, 11786 – 11790.

600. Sui, B.; Kim, B.; Zhang, Y.; Frazer, A.; Belfield, K. D. Highly Selective Fluorescence Turn-On Sensor for Fluoride Detection. *ACS Appl. Mater. Interfaces* **2013**, *5*, 2920 − 2923.

601. Wei, G.; Yin, J.; Ma, X.; Yu, S.; Wei, D.; Du, Y. A carbohydrate Modified Fluoride Ion Sensor and its Applications. *Anal. Chim. Acta.* **2011**, *703*, 219-225.

602. Lu, W.; Jiang, H.; Hu, F.; Jiang, L.; Shen, Z. A Novel Chemosensor Based on Fe(III)-Complexation for Selective Recognition and Rapid Detection of Fluoride Anions in Aqueous Media. *Tetrahedron* **2011**, *67*, 7909 – 7912.

603. Li, L.; Ji, Y.; Tang, X. Quaternary Ammonium Promoted Ultra Selective and Sensitive Fluorescence Detection of Fluoride Ion in Water and Living Cells. *Anal. Chem.* **2014**, *86*, 10006 – 10009.

604. Tang, L.; Wang, N.; Guo, J. Colorimetric and Fluorescent Recognition of Fluoride by a Binaphthol Thioureido Derivative. *Bull. Korean Chem. Soc.* **2012**, *33*, 2145 – 2148.

605. Bozdemir, O. A.; Sozmen, F.; Buyukcakir, O.; Guliyev, R.; Cakmak, Y.; Akkaya, E. U. Reaction-Based Sensing of Fluoride Ions Using Built-In Triggers for Intramolecular Charge Transfer and Photoinduced Electron Transfer. *Org. Lett.* **2010**, *12*, 1400 – 1403.

606. Liu, R.; Gao, Y.; Zhang, Q.; Yang, X.; Lu, X.; Ke, Z.; Zhou, W.; Qu, J. A Fluorescent Probe Based on Hydroxylnaphthalene 2-Cyanoacrylate: Fluoride Ion DEtection and its Bio-Imaging in Live Cells. *New J. Chem.*, **2014**, *38*, 2941-2945.

607. Ke, I.-S.; Myahkostupov, M.; Castellano, F. N.; Gabbaï, F. P. Stibonium Ions for the Fluorescence Turn-On Sensing of F⁻ in Drinking Water at Parts per Million Concentrations. *J. Am. Chem. Soc.* **2012**, *134*, 15309-15311.

608. Thongkum, D.; Tuntulani, T. Fluoride-Induced Intermolecular Excimer Formation of Bispyrenyl Thioureas LInked by Polyethylene Glycol Chains. *Tetrahedron* **2011**, *67*, 8102-8109.

609. Chen, Z.J.; Wang, L. M.; Zou, G.; Zhang, L.; Zhang, G. J.; Cai, X. F.; Teng, M. S. Colorimetric and Ratiometric Fluorescent Chemosensor for Fluoride Ion Based on Perylene Diimide Derivatives. *Dyes Pigments* **2012**, *94*, 410-415.

610. Zhu, B.; Yuan, F.; Li, R.; Li, Y.; Wei, Q.; Ma, Z.; Du, B.; Zhang, X. A Highly Selective Colorimetric and Ratiometric Fluorescent Chemodosimeter for Imaging Fluoride Ions in Living Cells. *Chem. Commun.* **2011**, *47*, 7098–7100.

611. Wang, Q.; Xie, Y.; Ding, Y.; Li, X.; Zhu, W. Colorimetric Fluoride Sensors based on Deprotonation of Pyrrole – Hemiquinone Compounds. *Chem. Commun.* **2010**, *46*, 3669 – 3671.

612. Mahapatra, A. K.; Manna, S. K.; Sahoo, P. Color Response of Tri-armed Azo Host Colorimetric Sensors and Test Kit for Fluoride. *Talanta* **2011**, *85*, 2673-2680.

613. Wade, C. R.; Ke, I.-S.; Gabbaï, F. P. Sensing of Aqueous Fluoride Anions by Cationic Stibine – Palladium Complexes. *Angew. Chem. Int. Ed.* **2012**, *51*, 478 – 481.

614. Moore, D.; Wang, Z. L. Growth of Anisotropic One-Dimensional ZnS Nanostructures. *J. Mater. Chem.* **2006**, *16*, 3898–3905.

615. Shen, G.; Bando, Y.; Golberg, D. Nanowires, C.-Coated S.-Crystalline Z.S. Carbon-Coated Single-Crystalline Zinc Sulfide Nanowires. *J. Phys. Chem. B* **2006**, *110*, 20777-20780.

616. Shi, Y.; Chen, J.; Shen, P. ZnS Micro-Spheres and Flowers : Chemically Controlled Synthesis and Template Use in Fabricating MS (Shell)/ZnS (Core) and MS (M = Pb, Cu) Hollow Microspheres. *J. Alloys Compd.* **2007**, *441*, 337-343.

617. Ras, R. H. A.; Kemell, M.; Wit, J. D.; Ritala, M.; Brinke, G. T.; Leskelä, M.; Ikkala, O. Hollow Inorganic Nanospheres and Nano Tubes with Tunable Wall Thicknesses by Atomic Layer Deposition on Self-Assembled Polymeric Templates. *Adv. Mater.* **2007**, *19*, 102-106.

618. Zhong, Z.; Yin, Y.; Gates, B.; Xia, Y. Preparation of Mesoscale Hollow Spheres of TiO_2 and SnO_2 by Templating Against Crystalline arrays of Polystyrene Beads. *Adv. Mater.* **2000**, *12*, 206-209.

619. Lou, X. W.; Wang, Y.; Yuan, C.; Lee, J. Y.; Archer, L. A. Template-Free Synthesis of SnO_2 Hollow Nanostructures with High Lithium Storage Capacity. *Adv. Mater.* **2006**, *18*, 2325-2329.

620. Xu, X. & Asher, S.A. Synthesis and Utilization of Monodisperse Hollow Polymeric Particles in Photonic Crystals. *J. Am. Chem. Soc.* **2004**, *126*, 7940-7945.

621. Wattendorf, U.; Kreft, O.; Textor, M.; Sukhorukov, G. B.; Merkle, H. P. Stable Stealth Function for Hollow Polyelectrolyte Microcapsules through a Poly (ethylene glycol) Grafted Polyelectrolyte Adlayer. *Biomacromolecules* **2008**, *9*, 100–108.

622. Li, B.; Xie, Y.; Jing, M.; Rong, G.; Tang, Y.; Zhang, G. In_2O_3 Hollow Microspheres : Synthesis from Designed $In(OH)_3$ Precursors and Applications in Gas Sensors and Photocatalysis. *Langmuir* **2006**, *22*, 9380-9385.

623. Zhao, Q.; Gao, Y.; Bai, X.; Wu, C.; Xie, Y. Facile Synthesis of SnO_2 Hollow Nanospheres and Applications in Gas Sensors and Electrocatalysts. *Eur. J. Inorg. Chem.* **2006**, 1643–1648.

624. Dai, Z.; Dähne, L.; Möhwald, H.; Tiersch, B. Novel Capsules with High Stability and Controlled Permeability by Hierarchic Templating. *Angew. Chem. Int. Ed.* **2002**, *41*, 4019-4022.

625. Li, H.; Bian, Z.; Zhu, J.; Zhang, D.; Li, G.; Huo, Y.; Li, H.; Lu, Y. Mesosporous Titania Spheres with Tunable Chamber Structure and Enhanced Photocatalytic Activity. *J. Am. Chem. Soc.* **2007**. *129*, 8406-8407.

626. Lifshitz, E.; Porteanu, H.; Glozman, A.; Weller, H.; Pflughoefft, M.; Echymüller, A. Optically Detected Magnetic Resonance Study of CdS/HgS/CdS Quantum Dot Quantum Wells. *J. Phys. Chem. B* **1999**, *103*, 6870-6875.

627. Lin, Y. -S.; Tseng, W. -C. Effect of Al Nanoparticles on the Microstructure, Electrical, and Optical Properties of AZO/Al/AZO Trilayer Thin Film. *J. Electronic Mater.* **2012**, *41*, 437-441.

628. Chaudhuri, R. G.; Paria, S. Optical Properties of Double-Shell Hollow ZnS−Ag_2S Nanoparticles. *J. Phys. Chem. C* **2013**, *117*, 23385−23390.

629. Chen, B.; Deng, J.; Yang, W. Hollow Two-Layered Chiral Nanoparticles Consisting of Optically Active Helical Polymer/Silica : Preparation and Application for Enantioselective Crystallization. *Adv. Funct. Mater.* **2011**, *21*, 2345-2350.

630. Yi, G.-S.; Chow, G. -M. Water-Soluble $NaYF_4$:Yb,Er(Tm)/$NaYF_4$/Polymer Core/Shell/Shell Nanoparticles with Significant Enhancement of Upconversion Fluorescence. *Chem. Mater.* **2007**, *19*, 341-343.

631. Chen, F.; Bu, W.; Zhang, S.; Liu, X.; Liu, J.; Xing, H.; Xiao, Q.; Zhou, L.; Peng, W.; Wang, L.; Shi, J. Positive and Negative Lattice Shielding Effects Co-existing in Gd (III) Ion Doped Bifunctional Upconversion Nanoprobes. *Adv. Funct. Mater.* **2011**, *21*, 4285-4294.

632. Tian, J.; Gu, Z.; Liu, X.; Zhou, L.; Yin, W.; Yan, L.; Jin, S.; Ren, W.; Xing, G.; Li, S.; Zhao, Y. Facile Fabrication of Rare-Earth-Doped Gd_2O_3 Hollow Spheres with Upconversion Luminescence, Magnetic Resonance, and Drug Delivery Properties. *J. Phys. Chem. C* **2011**, *115*, 23790-23796.

633. Guo, Y.; Zhang, L.; Zhang, S.; Yang, Y. Chen, X.; Zhang, M. Fluorescent Carbon Nanoparticles for the Fluorescent Detection of Metal Ions. *Biosens. Bioelectron.* **2015**, *63*, 61-71.

634. Lu, W.; Qin, X.; Liu, S.; Chang, G.; Zhang, Y.; Luo, Y.; Asiri, A. M.; Al-Youbi, A. O.; Sun, X. Economical, Green Synthesis of Fluorescent Carbon Nanoparticles and Their Use as Probes for Sensitive and Selective Detection of Mercury(II) Ions. *Anal. Chem.* **2012**, *84*, 5351−5357.

635. Obliosca, J. M.; Wang, P.-C.; Tseng, F.-G. Probing Quenched Dye Fluorescence of Cy3 − DNA − Au-Nanoparticle Hybrid Conjugates using Solution and Array Platforms. *J. Colloid Interface Sci.* **2012**, *371*, 34-41.

636. Meng, Q.; Zhang, X.; He, C.; He, G.; Zhou, P.; Duan, C. Multifunctional Mesoporous Silica Material Used for Detection and Adsorption of Cu^{2+} in Aqueous Solution and Biological Applications in vitro and in vivo. *Adv. Funct. Mater.* **2010**, *20*, 1903−1909.

637. Li, Y.-F.; Wei, Y.-F.; Tan, Y.; Kong, X.-F.; Zhou, K.; Wu, Z. -M.; Liu, Y.-J. Detection and Removal of Hg^{2+} Based on Mesoporous Silica Material Functionalized by Naphthalimide in Aqueous Solution. *Anal. Sci.* **2014**, *30*, 257-262.

638. Jin, W. J.; Costa-Fernández, J. M.; Pereiro, R.; Sanz-Medel, A. Surface-Modified CdSe Quantum Dots as Luminescent Probes for Cyanide Determination. *Anal. Chim. Acta* **2004**, *522*, 1-8.

639. Chen, J.; Gao, Y. C.; Xu, Z. B.; Wu, G. H.; Chen, Y. C.; Zhu, C. Q. A Novel Fluorescent Array for Mercury (II) Ion in Aqueous Solution with Functionalized Cadmium Selenide Nanoclusters. *Anal. Chim. Acta* **2006**, *577*, 77-84.

640. Hosseini, M. S.; Nazemi, S. Preconcentration Determination of Arsenic Species by Sorption of As(v) on Amberlite IRA-410 Coupled with Fluorescence Quenching of L-Cysteine Capped CdS Nanoparticles. *Analyst* **2013**, *138*, 5769-5776.

641. Koneswaran, M.; Narayanaswamy, R. Mercaptoacetic Acid Capped CdS Quantum Dots as Fluorescence Single Shot Probe for Mercury(II). *Sens. Actuators, A* **2009**, *139*, 91-96.

642. Koneswaran, M.; Narayanaswamy, R. Chemical l-Cysteine-Capped ZnS Quantum Dots Based Fluorescence Sensor for Cu^{2+} Ion. *Sens. Actuators, B* **2009**, *139*, 104-109.

643. Yin, M.; Li, Z.; Liu, Z.; Yang, X.; Ren, J. Magnetic Self-Assembled Zeolite Clusters for Sensitive Detection and Rapid Removal of Mercury(II). *ACS Appl. Mater. Interfaces* **2012**, *4*, 431−437.

644. Hosseini, M.; Gupta, V. K.; Ganjali, M. R.; Rafiei-Sarmazdeh, Z.; Faridbod, F.; Goldooz, H.; Badiei, A. R.; Norouzi, P. A Novel Dichromate-Sensitive Fluorescent Nano-Chemosensor using New Functionalized SBA-15. *Anal. Chim. Acta* **2012**, *715*, 80-85.

645. Wang, X.; Wang, P.; Dong, Z.; Ma, Z.; Jiang, J.; Li, R.; Ma, J. Highly Sensitive Fluorescence Probe Based on Functional SBA-15 for Selective Detection of Hg^{2+}. *Nanoscale Res. Lett.* **2010**, *5,* 1468–1473.

646. Dong, Z.; Dong, Z.; Wang, P.; Tian, X.; Geng, H.; Li, R.; Ma, J. A Fluorescent Probe for Zinc Detection Based on Organically Functionalized SBA-15. *Appl. Surf. Sci.* **2010**, *257*, 802-806.

647. Mandal, B. K.; Suzuki, K. T. Arsenic Round the World : a Review. *Talanta* **2002***, 58* 201–235.

648. Miller, W. H.; Schipper, H. M.; Lee, J. S.; Singer, J.; Waxman, S. Mechanisms of Action of Arsenic Trioxide. *Cancer Res.* **2002**, *62*, 3893-3903.

649. Ensafi, A. A.; Ring, A. C.; Fritsch, I. Highly Sensitive Voltammetric Speciation and Determination of Inorganic Arsenic in Water and Alloy Samples Using Ammonium 2-Amino-1-Cyclopentene-1-Dithiocarboxylate. *Electroanalysis*, **2010**, *22*, 1175-1185.

650. World Health Organisation (WHO), Guidelines for Drinking Water Quality, **1993**, p. 41.

651. Liu, B.; Wang, D.; Li, H.; Xu, Y.; Zhang, L. As(III) Removal from Aqueous Solution using α-Fe_2O_3 Impregnated Chitosan Beads with As(III) as Imprinted Ions. *Desalination* **2011**, *272*, 286–292.

652. Jena, B. K.; Raj, C. R. Gold Nanoelectrode Ensembles for the Simultaneous Electrochemical Detection of Ultratrace Arsenic, Mercury, and Copper. *Anal. Chem.* **2008**, *80*, 4836–4844.

653. Majid, E.; Hrapovic, S.; Liu, Y.; Male, K. B.; Luong, J. H. T. Electrochemical Determination of Arsenite Using a Gold Nanoparticle Modified Glassy Carbon Electrode and Flow Analysis. *Anal. Chem.* **2006**, *78*, 762-769.

654. Hrapovic, S.; Liu, Y.; Luong, J. H. T. Reusable Platinum Nanoparticle Modified Boron Doped Diamond Microelectrodes for Oxidative Determination of Arsenite. *Anal. Chem.* **2007**, *79,* 500 -507.

655. Dar, R. A. Khare, N. G.; Cole, D. P.; Karnac, S. P.; Srivastava, A. K. Green Synthesis of a Silver Nanoparticle–Graphene Oxide Composite and its Application for As(III) Detection. *RSC Adv.* **2014**, *4*, 14432-14440.

656. Shin, S.-H.; Hong, H.-G. Anodic Stripping Voltammetric Detection of Arsenic(III) at Platinum-Iron(III) Nanoparticle Modified Carbon Nanotube on Glassy Carbon Electrode. *Bull. Korean Chem. Soc.* **2010**, *31*, 3077-3083.

657. Roy, S.; Palui, G.; Banerjee, A. The as-Prepared Gold Cluster-Based Fluorescent Sensor for the Selective Detection of As III Ions in Aqueous Solution. *Nanoscale* **2012**, *4*, 2734-2740.

658. Wu, Y.; Zhan, S.; Wang, F.; He, L.; Zhi, W.; Zhou, P. Cationic Polymers and Aptamers Mediated Aggregation of Gold Nanoparticles for the Colorimetric Detection of Arsenic(III) in Aqueous Solution. *Chem. Commun.* **2012**, *48*, 4459–4461.

659. Li, J.; Chen, L.; Lou, T.; Wang, Y. Highly Sensitive SERS Detection of As^{3+} Ions in Aqueous Media using Glutathione Functionalized Silver Nanoparticles. *ACS Appl. Mater. Interfaces* **2011**, *3*, 3936–3941.

660. Alizadeh, T.; Rashedi, M. Synthesis of Nano-Sized Arsenic-Imprinted Polymer and its use as As^{3+} Selective Ionophore in a Potentiometric Membrane Electrode : Part 1. *Anal. Chim. Acta* **2014**, *843*, 7-17.

661. Weng, C.-I; Cang, J.-S.; Chang, J.-Y.; Hsiung, T.-M.; Unnikrishnan, B.; Hung, Y.-L.; Tseng, Y.-T.; Li, Y.-J.; Shen, Y.-W.; Huang, C.-C.; Detection of Arsenic(III) through Pulsed Laser-Induced Desorption/ Ionization of Gold Nanoparticles on Cellulose Membranes. *Anal. Chem.* **2014**, *86*, 3167−3173.

662. Hosseini, M. S.; Belador, F. A Novel Spectrofluorometric Method for the Determination of Arsenic in Human Hair Using Dy_2O_3-Doped CeO_2 Nanoparticles. *Analyst* **2014**, *139*, 5007-5013.

663. Hong, S.; Park, S.; Lee, S.; Yang, Y. I.; Song, H. D.; Yi, J. The Sensitive, Anion-Selective Detection of Arsenate with Poly (Allylamine Hydrochloride) by Single Particle Plasmon-Based Spectroscopy. *Anal. Chim. Acta* **2011**, *694*, 136-141.

664. Morita, K. & Kaneko, E. Spectrophotometric Determination of Trace Arsenic in Water Samples Using a Nanoparticle of Ethyl Violet with a Molybdate-Iodine Tetrachloride Complex as a Probe for Molybdoarsenate. *Anal. Chem.* **2006**, *78*, 7682-7688.

Appendix

1. Calibration Curve for Metronidazole Antibiotic Degradation
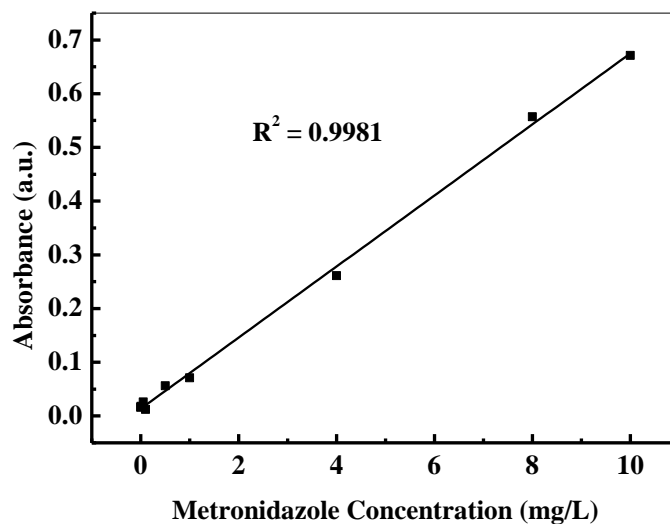

Figure A1. Plot of concentration of metronidazole vs. UV-Visible absorbance

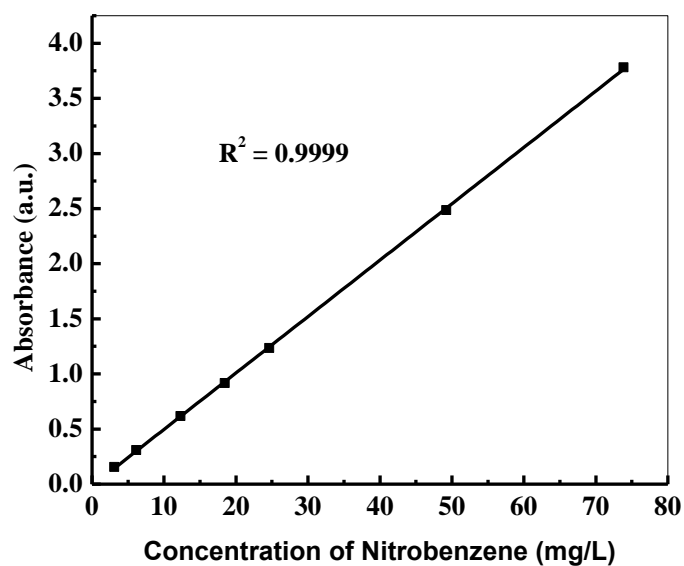## 2. Calibration Curve for Nitrobenzene Degradation

Figure A2. Plot of concentration of nitrobenzene vs. UV-Visible absorbance

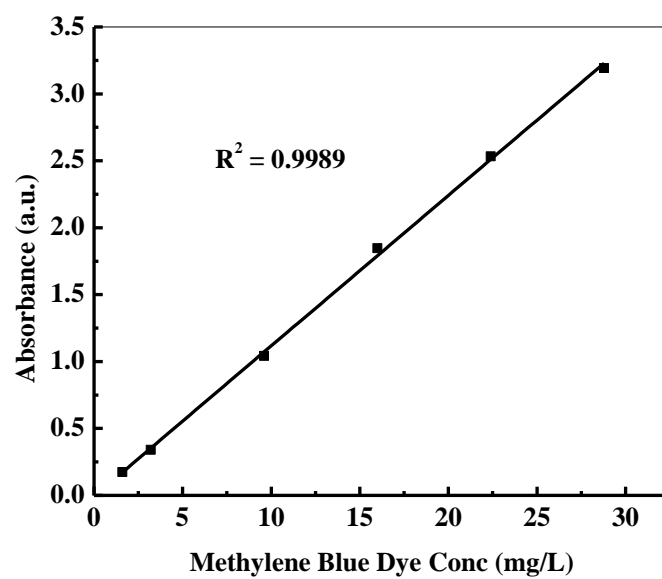## 3. Calibration Curve for Methylene Blue Dye Degradation

Figure A3. Plot of concentration of methylene blue dye vs. UV-Visible absorbance

CURRICULUM VITAE

SIDDHARTHA SANKAR BOXI

Mob: +91-9437797077, e-mail: ssboxich@gmail.com
Vill. +P.O.: Dhanyaghar, Dist.: Purba Medinipur, Pin-721643

PERSONAL DETAILS

Permanent Address	: S/O: Sri Banamali Boxi,
	Vill. + P.O.: Dhanyaghar, P. S.: Nanda Kumar
	Dist: Purba Medinipur, State: West Bengal, Pin: 721643
Date of Birth	: 25-05-1986
Nationality	: Indian
Religion	: Hinduism
Caste	: General
Sex	: Male
Marital Status	: Married
Languages proficiency: Bengali, English, and Hindi	

Areas of Research:

Synthesis of nanoparticles, doping of nanoparticles, photocatalysis, nanoparticles based fluorescence sensor, interficial and reheological behavior studies of fluids.

ACADEMIA

Course/ Degree	Board/University	Dissertation	Year of Passing	Marks Obtained
PhD	National Institute of Technology Rourkela	Synthesis, characterization and applications of doped nanoparticles	Dissertation submitted June, 2015	
M. Tech	University of Calcutta	Studies on Hydrolysis of starchy raw materials	2011	79.95 %
B. Tech	West Bengal University of Technology	Novel Absorption Tower Design	2008	8.14 (DGPA)
12th	West Bengal Board of Higher Secondary Education	-	2004	78.1 %
10th	West Bengal Council of Secondary Education	-	2002	74.38 %

Performance in GATE 2009:

All India Rank	: 296
GATE Score	: 430
Percentile Score	: 92.85

o Best Research Presentation award of the department of chemical engineering in Research Scholar Week-2015 organized by National Institute of Technology Rourkela.
o SRF fellowship funded by CSIR (July, 2011 to February, 2015).
o GATE scholarship funded by MHRD for pursuing M. Tech programme (2009-2011).

WORKING EXPERIENCE

1. **Calcutta Institute of Technology**, Department of Chemical Engineering, Uluberia, West Bengal, India. From 01.09.2010 to 30.04.2011, as Part time faculty.
2. **Gokul Refoils & Solvent Ltd.**, Haldia, West Bengal, India. From 01.03.2009 to 30.06.2009, as Trainee Engineer.

RESEARCH PUBLICATIONS

o **Siddhartha Sankar Boxi**, Santanu Paria. "Effect of silver doping on TiO_2, CdS, and ZnS nanoparticles for the photocatalytic degradation of metronidazole under visible light." *RSC Advances.* 2014, 4, 37752-37760.

o **Siddhartha Sankar Boxi**, Santanu Paria. "Visible light induced enhanced photocatalytic degradation of organic pollutants in aqueous media using Ag doped hollow TiO_2 nanospheres." *RSC Advances.* 2015, 5, 37657-37668.

o **Siddhartha Sankar Boxi**, Santanu Paria "Fluorometric detection of ultralow arsenic concentrations using Ag doped hollow CdS/ZnS bi-layer nanoparticles." Dalton Transactions, 2015, 44, 20464-20474.

o **Siddhartha Sankar Boxi**, Santanu Paria. "Fluorometric Selective Detection of Fluoride Ions in Aqueous Media Using Ag doped CdS/ZnS Core/Shell Nanoparticles." Dalton Transactions, 2016, 45, 811-819.

o **Siddhartha Sankar Boxi**, Khushi Mukherjee, Santanu Paria. "Applications of silver doped hollow TiO_2 nanoparticles as an effective green fungicide against *Fusarium solani* and *Venturia inaequalis* phytopathogens." Nanotechnology (IOP) Accepted, 2016.

International conferences

o **Siddhartha Sankar Boxi**, Santanu Paria. "Synthesis, characterization, and photoluminescence properties of Ag doped CdS nanoparticles." 3rd International Conference NANOCON 014, Bharati Vidyapeeth University, Pune, 14th, 15th October, 2014.

o **Siddhartha Sankar Boxi**, Santanu Paria. "Synthesis and characterization of Ag doped TiO_2 nanoparticles for photocatalytic application organic dye in the presence of solar light." 2nd International Conference on Nanotechnology ICNT 2015, Haldia Institute of Technology, Haldia, West Bengal, 19 – 22 February, 2015.